Corrosion and Cracking Susceptibility of Austenitic Alloys in Supercritical Water

by

Yashar Behnamian

A thesis submitted in partial fulfillment of the requirements for the degree of

Doctor of Philosophy

in

Materials Engineering

Department of Chemical and Materials Engineering
University of Alberta

Abstract

The present research has been done with the intent of evaluating the corrosion resistance and cracking susceptibility of some commercial candidate alloys that can be potentially used in Gen-IV supercritical water reactor (SCWR). The mechanism of the crack initiation in austenitic alloys exposed to SCW is not entirely understood and experimental data for performance in long-term exposure and upside down situation are not available yet.

Fundamentally, austenitic and nickel-base alloys have always attracted a significant attention in power generation industry. However, using these materials for such purposes is limited due to their susceptibility to stress corrosion cracking (SCC). With this in mind, this study was focused on investigation of oxidation of several grades of austenitic stainless steels, and nickel-based alloy exposed to the supercritical water (SCW) at 800 °C for 12 h. Morphology, microstructure, and chemical composition of oxide films formed on stainless steels (SS) 347H, 316L, and 310S, and alloys 625, 214, C2000, and 800H upon SCW exposure were studied using the weight measurement, X-ray diffraction (XRD) analysis, scanning electron microscopy (SEM), and energy dispersive spectroscopy (EDS). It was found that alloying elements can substantially influence the oxidation of austenitic alloys exposed to SCW at high temperature (800 °C) for around 12 h. Results confirmed the presence of a duplex oxide layer consisting of Fe-Cr and Cr-Ni spinel/Cr_2O_3 on the substrate surface.

In addition, the corrosion behavior of SS 316L capsules was investigated after 20,000 h SCW exposure at the temperature of 500 °C. Specimens were analyzed by electron microscopy, energy dispersive spectroscopy, electron energy loss spectroscopy, and X-ray diffraction technique. The film of the corrosion products was composed of an outer layer of magnetite and

an inner layer of spinel structure. By increasing the exposure time, a rougher surface and thicker oxide film was approached, which were identified as Fe_3O_4 + spinel/Cr_2O_3/Ni-enrichment + SS 316L from the outer to the inner layer. Microcrack initiation was evident around the oxidized grain boundaries. The possible oxidation mechanism was studied and discussed as well.

Furthermore, the oxidation behavior of capsules which were made of SS 310S was investigated after 20,000 h exposure to SCW at 500 °C. Later on, samples were analyzed using scanning electron microscopy, energy-dispersive X-rays, Auger electron spectroscopy (AES), and X-ray diffraction analysis. Results revealed that two distinct oxide layers including an outer layer of magnetite and an inner layer of spinel had been formed on the inner surface of the SS 310S capsules. Long exposure to SCW resulted in formation a rougher surface and thicker oxide scale, identified as Fe_3O_4 + spinel/Cr_2O_3/Ni-enrichment + SS 310S alloy from the outer to the inner layer. The most probable oxidation and microcrack susceptibility mechanism were proposed and discussed. By employing the complementary characterization techniques, such as transmission electron microscopy, conventional selected area electron diffraction analysis, energy-dispersive X-ray spectroscopy and advanced electron energy loss spectroscopy, it was recognized that the cracks tip were oxidized and had a three-layer morphology in which all the layers tapered toward the crack tip.

In the complementary step, the impact of SCW exposure time on the corrosion behavior of 304-ODS (oxide dispersion strengthened) steel in SCW (at the temperature of 650 °C) was investigated. The exposed coupons were analyzed by scanning/transmission electron microscopy equipped with energy dispersive spectroscopy, electron energy loss spectroscopy, X-ray diffraction, and time-of-flight secondary ion mass spectrometry (TOF-SIMS). The results

demonstrated that the weight gain increased by escalating the SCW exposure time, following a parabolic behavior. An oxide scale was formed on 304-ODS alloy which was made of two distinct layers, including an outer layer of magnetite (Fe_3O_4) and an inner layer of $FeCr_2O_4/(Fe,Cr)_2O_3$. Additionally, the oxidation mechanism was discussed.

Preface

Chapter 2 of this thesis has been submitted for publication in *Corrosion Science* as Yashar Behnamian, Amir Mostafaei, Mirjavad Geramian, Yifei Sun, Subia Liu, Babak Shalchi Amirkhiz, Yimin Zeng, Weixing Chen, Jingli Li Luo, Wenyue Zheng, and David Guzonas. "An Investigation of the Corrosion Resistance of Austenitic Steels and Nickle-Base Alloys in Supercritical Water at 800 °C". Amir Mostafaei, Mirjavad Geramian and Yiefe Sun, Subia Liu, contributed to the experimental data collection. Babak Shalchi Amirkhiz, Yimin Zeng contributed to microscopy data collection.

Chapter 4 of this thesis has been submitted for publication in *Corrosion Science* as Yashar Behnamian, Amir Mostafaei, Alireza Kohandehghan, Ermia Aghaie, Ramin Zahiri, Kai Cui, Jian Li, Weixing Chen, Jingli Li Luo, Wenyue Zheng, and David Guzonas. "Oxidation and Cracking Susceptibility of 310S Stainless Steel in Supercritical Water: Part I - Investigations by SEM, AES, and XRD". Amir Mostafaei, Ermia Aghaie, and Ramin Zahiri contributed to the experimental data collection, Alireza Kohandehghan, Kai Cui and Jian Li contributed to electron microscopy data collection.

Chapter 5 of this thesis has been submitted for publication in *Corrosion Science* as Yashar Behnamian, Amir Mostafaei, Alireza Kohandehghan, Ermia Aghaie, Kai Cui, Douglas Vick, Babak Shalchi Amirkhiz, Yimin Zeng, Jian Li, Weixing Chen, Jingli Li Luo, Wenyue Zheng, and David Guzonas. "Oxidation and Cracking Susceptibility of 310S Stainless Steel in Supercritical Water: Part II - Transmission Electron Microscopy Observations". Amir Mostafaei and Alireza Kohandehghan contributed to experimental data collection. Ermia Aghaie, Kai Cui,

Douglas Vick, Babak Shalchi Amirkhiz, Yimin Zeng and Jian Li contributed to electron microscopy data collection.

Chapter 6 of this thesis has been submitted for publication in *Corrosion Science* as Yashar Behnamian, Amir Mostafaei, Alireza Kohandehghan, Kai Cui, Douglas Vick, Babak Shalchi Amirkhiz, Ramin Zahiri, Ermia Aghaie, Zhanjiang Zhou, Yimin Zeng, Weixing Chen, Jingli Li Luo, Wenyue Zheng, and David Guzonas. "Investigation of the Oxidation Behavior of an Austenitic 304 - Oxide Dispersion Strengthened Steel in Supercritical Water at 650 °C". Amir Mostafaei, Zhanjiang Zhou, Ermia Aghaie and Ramin Zahiri contributed to experimental data collection. Kai Cui, Douglas Vick, Babak Shalchi Amirkhiz and Alireza Kohandehghan contributed to electron microscopy data collection.

I was responsible for the data collection, analysis and manuscript composition. Prof. Jing Li Luo and Prof. Weixing Chen have been the supervisory authors.

This thesis is dedicated to

My family

Acknowledgment

I express my heartfelt and utmost gratitude to two scientists who are also my supervisors, Prof. Weixing Chen and Prof. Jing Li Luo. They provided me with the opportunity and support to study under their supervision and work on this project. I am also grateful for their knowledge, encouragement, patience and invaluable helps during the entire course of my study. It is a great honor to be guided by them.

I express my deep appreciation to Dr. Hao Zhang as a member of my supervisory committee and his invaluable supervision. I would like to express my appreciation to the committee members Dr. Sheng-Hui Wang and Dr. Mohtada Sadrzadeh for reviewing my dissertation and giving valuable comments. It is a pleasure to thank those who made this thesis possible, Dr. Jian Li, Dr. Wenyue Zheng, Dr. Babak Shalchi Amirkhiz, and Dr. Yimin Zeng, of CanmetMATERIALS. Dr. David Guzonas of CNL. Dr. Alireza Kohandehghan, Mr. Ramin Zahiri, Dr. Dimitri Karpuzov, Dr. Shihong Xu, Dr. Dimitri Karpuzov, Dr. Nathan Gerein, and George Braybrook. Finally, thanks to all the technicians and staff members of the Chemical and Materials Engineering (CME) Department, Alberta Centre for Surface Engineering and Science (ACSES).

Table of Contents

List of Tables

List of Figures

List of Symbols

AES: Auger Electron Spectroscopy

BF: Bright Field

CANDU: Canadian Duterium Uranium

CERT: Constant Extension Rate Test

DF: Dark Field

DO: Dissolved Oxygen

EDS: Energy Dispersive Spectroscopy

EBSD: Electron Backscattered Diffraction

EELS: Electron Energy Loss Spectroscopy

F-M: Ferritic-Martensitic

FIB: Focused Ion Beam

FEG: Field Emission Gun

FFT: Fast Furrier Transform

GIF: Generation-IV International Forum

HT: High Temperature

HRTEM: High Resolution Transition Electron Microscopy

HAADF: High Angle Annular Dark Field

IGSCC: Intergranular Stress Corrosion Cracking

ID: Inner Diameter

ISE: Ion-induced Secondary Electron

MTC: Mill Test Certificate

MD: Magnetic Disc

ODS: Oxide Dispersion Strengthen

RD: Rolling Direction

SS: Stainless Steel

SCW: Supper Critical Water

SCC: Stress Corrosion Cracking

SE: Secondary Electron

SIMS: Secondary Ion Mass Spectroscopy

SSRT: Slow Strain Rate Test

SAED: Selected Area Electron Diffraction

SIO: Selective Internal Oxidation

SEM: Scanning Electron Microscopy

SCW: Supercritical Water

SCWR: Supercritical Water-Cooled Reactor

STEM: Scanning Transmission Electron Microscopy

SHS: Superheated Steam

TD: Transverse Direction

TT: Through Thickness

TGSCC: Transgranular Stress Corrosion Cracking

TEM: Transmission Electron Microscopy

WG: Weight Gain

WL: Weight Loss

XRD: X-ray Diffraction

Chapter 1: Introduction and Literature Review

1.1 Introduction

For the sake of the global warming which resulted from burning hydrocarbon fuels, green nuclear power has become crucial over the last few years.[1] Moreover, concerns regarding the availability and security of energy resources have lately intensified research for new energy sources and fostered the further development of nuclear energy.[1] While current nuclear power plants provide sustainable electricity, cutting-edge technologies could assist to meet the requirements regarding the demand for low-cost electricity. Current generation nuclear plants have many concerns regarding their safety, efficiency, and operating cost. In order to overcome the drawbacks, fourth generation of nuclear reactors has been proposed by the generation IV international forum (GIF).[2] Generation IV international forum (GIF) has proposed several promising nuclear reactor concepts for international collaborative research and development.

There are several kinds of generation IV nuclear reactor concept, such as very high temperature reactor (VHTR), sodium cooled fast reactor (SFR), supercritical water reactor (SCWR), gas cooled fast reactor (GFR), lead cooled fast reactor (LFR), molten salt reactor (MSR). Supercritical water (SCW) cooled reactor (SCWR) is an advanced type of the GIF reactor concepts. In addition, it is considered as one of the most promising nuclear reactor concept which Canada opted for working on its research and development.[3] As a matter of fact, switching the coolant of a nuclear reactor from steam to the SCW will increase its thermal efficiency to 45% compared to the 33% efficiency of current light water reactors. The use of

SCW will also simplify the heat transport circuit and the plant design by eliminating steam processing sections such as dryers, separators, and generators.[4] Based on the unique high thermal capacity of SCW, mass flow can be reduced to eight times less than that of modern subcritical water reactors to achieve the same efficiency in thermal channels. This switching is capable of reducing the capital cost of each kilowatt per hour to half of the current cost.[4] Thus, the SCWR has a specific potential to fulfill the proposed objectives of economics, sustainability, and safety of the GIF.

As Canada worked on the research and development of the generation IV energy technologies, defining the appropriate materials for in-core and out-of-core components is one of the major concerns for SCWR development, as still no single material has been proposed by researchers to fulfill all the requirements for application in an SCWR.[4] Indeed, two major concerns were recognized by the SCWR materials and chemistry project management board which must be overcome to guarantee the safety and reliability of the SCWR[4].

1. In order to ensure a reliable performance of any single alloy in a SCWR, there is not sufficient data and mechanism, especially concerning the alloys which can be used for in-core components.

2. Due to the significant changes in physical and chemical features of water above the thermodynamic critical point and the possible impact of the water radiolysis, adequate understanding of SCW chemistry does not exist to come up a comprehensive chemistry control strategy.

This study has been conducted with the intent of evaluating some commercial candidate alloys and a modified one for SCWR application in Canada. This study fundamentally has

focused on performance of the alloys after the long time SCW exposure. It is believed that the current study will propose a critical insight technology to the future development of Canada's nuclear industry.

Table 1-1: Critical thermodynamic data for various compounds.[6]

Solvents	Critical Temperature (°C)	Critical Pressure (MPa)
Propylene	91.6	4.62
Carbon dioxide	31.1	7.38
Water	374.2	22.05
Ethane	32.2	4.88
Propane	96.7	4.25
p-Xylene	343.1	3.52
Cyclohexane	280.3	4.07
Isopropanol	235.2	4.76
Benzene	289.0	4.89
Toluene	318.6	4.11

1.2 Literature Review

1.2.1 Supercritical Water Medium

While a compound is over to its thermodynamic critical point ($P > P_c$, $T > T_c$), this compound is in supercritical state which is at variance with a normal gas, liquid, or solid phases, normally called the supercritical phase.[5] Every stable compound has its critical point. The critical temperatures and pressures for different supercritical fluids are tabulated in Table 1-1.[5,6]

As can be found in Table 1-1, different chemical compounds have different thermodynamic critical points. SCW and supercritical carbon dioxide are the most widely used supercritical compounds in various industries including power generation industry, waste treatment, food production, and hazardous waste treatment.[5,7-10]

SCW is a dense gas with both liquid-like and gas-like properties, but it fundamentally illustrates a liquid-like density with gaseous transport features.[11] A SCW can be considered as a homogeneous phase because of not having definitive gas-liquid interface. On the other hand, from the microscopic point of view, SCW has clusters of solvent molecules and free spaces.[12]

SCW possesses adjustable physicochemical characteristics like density, viscosity, and diffusivity which can be continuously tuned at different levels of pressure and temperature.[13,14] These adjustable features enable SCW to be employed for some specific applications like the extractions in solvents, waste treatment, and power generations.[12]

1.3 Supercritical Water and its Properties

At temperatures above 374.15 °C and pressures higher than 22.1 MPa, water is in a supercritical state. Water in a supercritical state acts as a single, non-condensable phase with an intermediate density between gas and liquid.[15] Physical and chemical properties of SCW,[16-18] such as density, thermal conductivity, and heat capacity are significantly different from those of water that exists below the critical point. At a constant pressure greater than 22.1 MPa, as the temperature increases and reaches the critical temperature the density of water drops drastically due to the thermal expansion of water molecules. Additionally, supercritical fluids have the low

viscosity of a gas and the high density of a liquid. The dielectric constant and ionic products of liquid water decrease sharply as water enters the SCW stability window at pressures above 22.1 MPa. SCW at low density demonstrates unlimited solubility for non-condensable gases such as nitrogen, oxygen, and argon.[19,20]

Table 1-2: Comparison of thermo-physical properties for water in conditions of CANDU-SCWR, CANDU-6, and PWR.[21]

Parameter	Unit	CANDU-SCWR	CANDU-6	PWR
Pressure	MPa	25	10.5	15
Temperature Inlet-Outlet	°C	350–625	265–310	290–325
ΔT from inlet to outlet	°C	275	45	35
Density	kg/m^3	625.5–675.8	782.9–692.4	745.4–664.9
Enthalpy	kJ/kg	1624–3567	1159–1401	1285–1486
Increase in enthalpy	kJ/kg	1943	242	201
From inlet to outlet	kJ/kg·K	7.06	5.38	5.74
Specific heat	J/kg. K	6978–2880	4956–6038	5257–6460
Expansivity	1/K	$5.17 \cdot 10^{-3}$–$1.74 \cdot 10^{-3}$	$2.09 \cdot 10^{-3}$–$3.71 \cdot 10^{-3}$	2.54^{-3}–$4.36 \cdot 10^{-3}$
Thermal conductivity	W/m· K	0.481–0.107	0.611–0.530	0.580–0.508

1.4 Generations of Nuclear Reactors

Table 1-2 demonstrates the thermo-physical properties of water in three generations of CANDU (Canada Deuterium Uranium) reactors. Pressurized water reactors (PWRs) and CANDU-SCWRs have the lowest and the highest difference, respectively, in inlet and outlet temperatures. A CANDU-SCWR operates at a pressure of 25 MPa with an inlet temperature of 350 °C and outlet temperature of 625 °C which enables it to reach a high thermal efficiency. The

peak temperature can be as high as 800 °C in some sections in an upside down situation. The application of SCW in nuclear reactors can increase the thermal efficiency, but the high temperature and high pressure conditions promote an oxidizing hydrothermal condition leading to a severe material degradation. A moderate level of material degradation can be acceptable in boiler industry, although it is unacceptable in the nuclear power industry. Based on the latest concepts of flow pass,[22] the coolant inlet and outlet of high pressure tubes are located under the high pressure plenum. The pressurized plenum is connected to a calandria vessel (a heat exchanger) containing a moderator up to 80 °C. The calandria is a high pressure tube containing an insulated fuel bundle and a channel for SCW. The pressure tube containing the insulated fuel bundle is not in direct contact with SCW. However, the fuel cladding, the high pressure plenum, and the coolant inlet and outlet are in direct contact with SCW.

Figure 1-1a schematically demonstrates the Canadian pressurized tube SCWR design concept.[22] The coolant media flows down a tube located in the center of each fuel channel, which is a fuel assembly under the pressure (Figure 1-1b). At the bottom of the fuel channel, the coolant media flows upwards which is in contact with the fuel pins until it exists the outlet plenum as SCW. The represented fuel channel design (Figure 1-1b) which is composed of a pressure tube with the thickness of 12 mm, a 0.5 mm outer liner tube, a 5.5 mm non-porous insulator made of yttrium (Y)-stabilized zirconia (ZrO_2) and a 0.5 mm austenitic Fe-Cr-Ni alloy liner tube that holds the fuel pins together.

According to the recent reports, two fuel cycles were investigated in order to improve the performance: (i) 13.4% plutonium (Pu) in thorium (Th) and (ii) 39.7% uranium (U) in Th.[23] A bundle of fuel pins (62 in one channel) is located all over a central flow tube which is made of an

austenitic Fe-Cr-Ni alloy with 89 mm diameter. Selection of a material that performs appropriately within such circumstances with the minimum degradation rate is a considerable challenge.

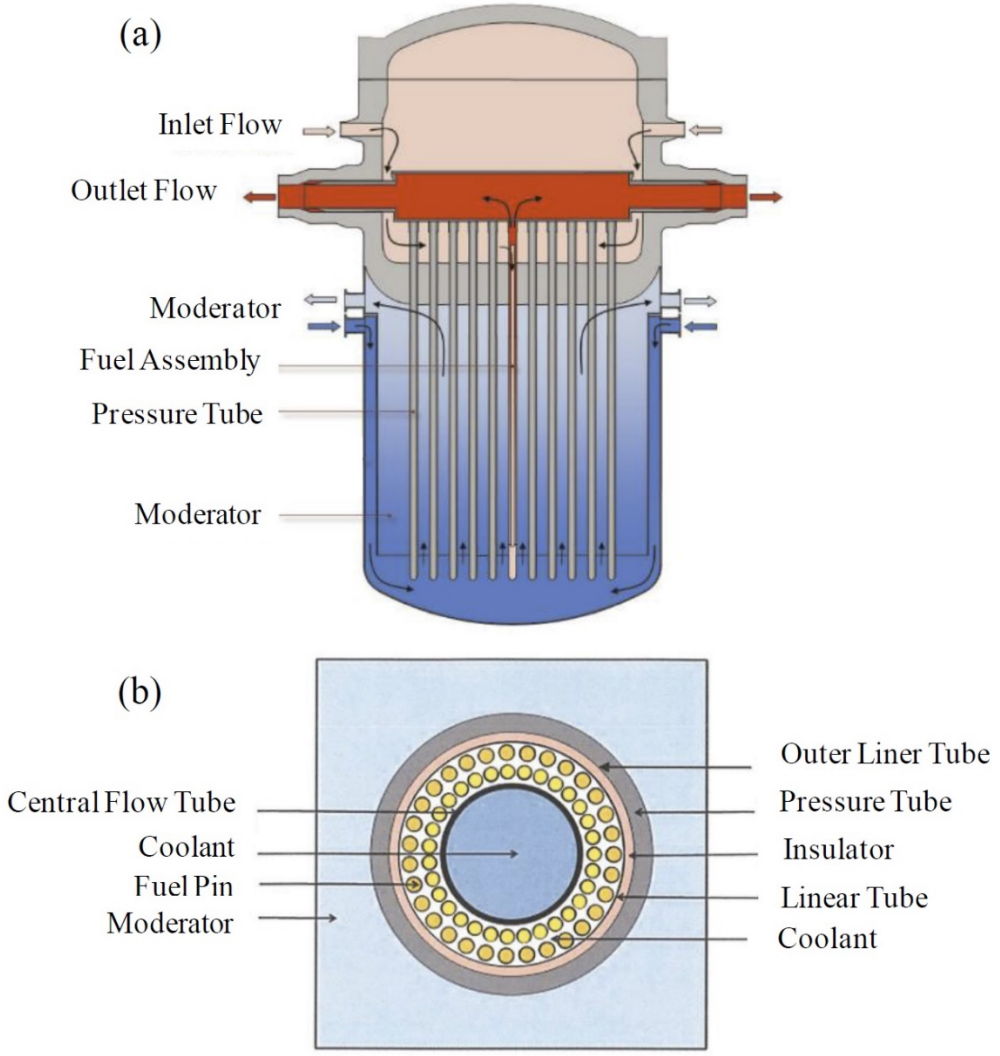

Figure 1-1: (a) Schematic of the in-core design of the Canadian pressurized tube SCWR concept and (b) cross-section schematic of the fuel channel design.[22]

Table 1-3: Pressure, inlet and outlet temperatures of coolant for the participating Generation-IV Forum countries.[24]

Country	Pressure (MPa)	Inlet Temperature (°C)	Outlet Temperature (°C)
EU/Japan	25	290	510
US	25	280	500
Russia	24.5	290	540
Korea	25	280	510
China	25	280	500
Canada	25	350	625

Table 1-3 lists pressure and the inlet and outlet temperatures of coolant for the participating generation-IV forum countries.

1.5 Challenges in Materials Selection

Because of the oxidizing nature of SCW, all parts in direct contact with SCW must have excellent corrosion and stress corrosion cracking (SCC) resistance. Moreover, they should demonstrate acceptable high temperature properties such as creep and irradiation resistivity.

1.5.1 Corrosion and Stress Corrosion Cracking in Supercritical Water

Since the 1960s many SCW power plants have contained ferritic-martensitic (F/M) steel boiler tubes. The maximum working temperature of a power plant with F/M boiler tubes is 550 °C. However, advanced F/M steels can be utilized at temperatures up to 620 °C and austenitic stainless steel (SS) tubes show acceptable performance up to 675 °C.[25] For temperatures over 675 °C, austenitic nickel based tubes would be generally preferred.[26] So far, no single alloy has

been selected for high temperature channels of SCWRs.[25,27] Due to the corrosive environment in SCWRs, a number of studies have been conducted to describe the corrosion and stress corrosion cracking susceptibility in an SCWR environment. Was et al.[28,29] pioneered the studies of F/M steel corrosion and SCC susceptibility in SCW environments. Coupons of three F/M alloys-T91, HCM12A, and HT-9 were exposed to SCW for up to 300 h at 500 °C containing 2 ppm dissolved oxygen (DO) and a pressure of 25 MPa inside a sealed metal capsule. Under these conditions, the alloys showed parabolic oxidation behaviour and a double oxide layer consisting of magnetite (outer layer) and Fe-Cr spinel (inner layer) developed on the substrate surface.

Figure 1-2 illustrates the SEM cross-section image of the cracks on HT-9 alloy after SCW exposure at different temperatures. In an investigation of SCC susceptibility,[29] under slow strain rate testing (SSRT) in SCW at conditions cited above, fractoghraphic analysis of exposed samples showed ductile ruptures, aside from HT-9 which failed by intergranular cracking. At similar exposure time, DO concentration, and temperatures of 500 °C, 550 °C, and 600 °C, Kim et al.[30] reported severe oxidation of alloys T91, T92, and T122, no SCC susceptibility was reported above 550 °C though. Despite the high SCC resistance of F/M alloys, Tanzosh et al.[25] and Fazio et al.[27] suggested that oxide thickening and corresponding spalling were a greater concern due to the fact that spalled materials in an SCWR can lodge in crevices and cause tubing or nasal blockage. Additionally, they mentioned that the transportation of irradiated spalled oxides to a steam turbine may cause both radioactive contamination and erosion damage to the steam turbine.

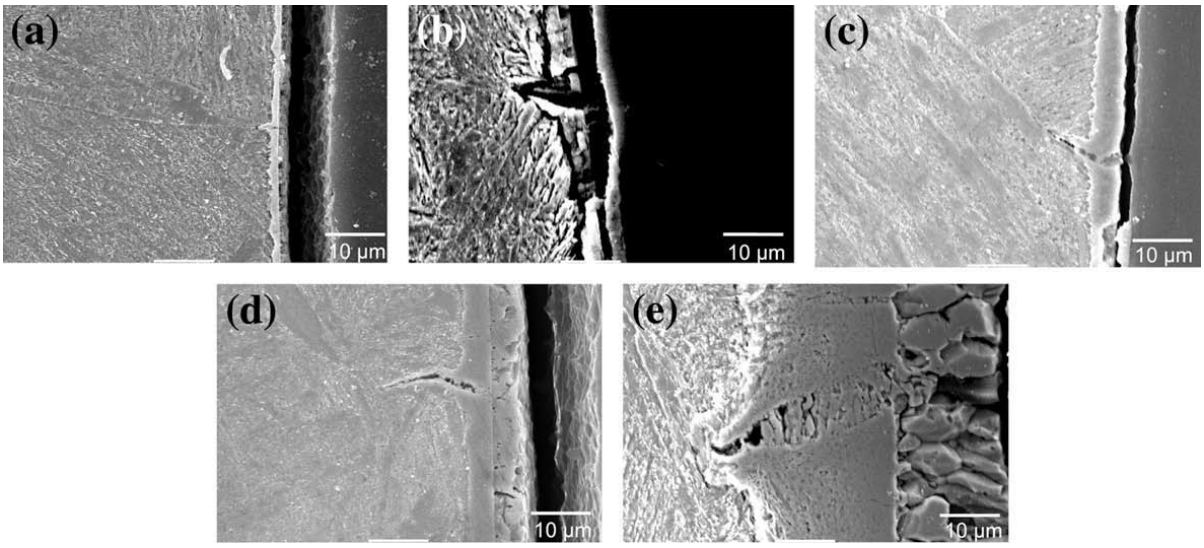

Figure 1-2: Cross-section images of crack on HT-9 at (a) 400 °C deaerated SCW, (b) 500 °C in Ar, (c) 500 °C deaerated SCW, (d) 500 °C with 300 appb DO, and (e) 600 °C deaerated SCW.[29]

Austenitic stainless steel alloys show good corrosion resistance in subcritical and supercritical steam.[25] In an early investigation, Boyd and Pray[31] exposed SS 310 and SS 316 alloys to an SCW environment at 30 MPa and 700 °C. A thick black tarnished oxide layer on SS 316 was reported and transgranular SCC (TGSCC) cracks were observed. Fine cracks in SS 316 exposed to degassed supercritical water at ~ 700 °C are shown in Figure 1-3.

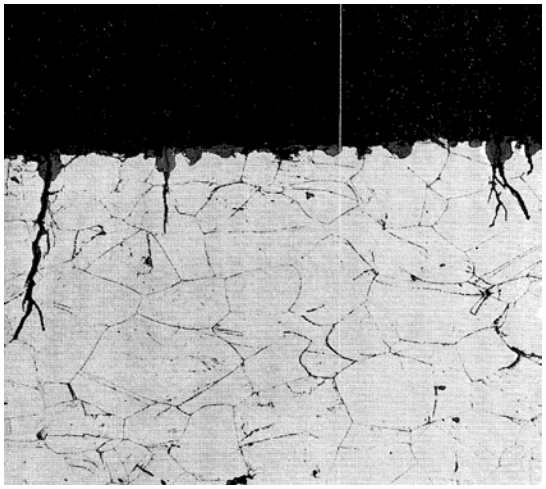

Figure 1-3: Light microscopy image illustrating fine cracks in SS 316 exposed to degassed supercritical water at 700 °C.[42]

Was et al.[32,33] studied the corrosion and SCC susceptibility of stainless steels using SSRT experiments in deaerated SCW for 570 h in a temperature range of 400 °C to 550 °C.

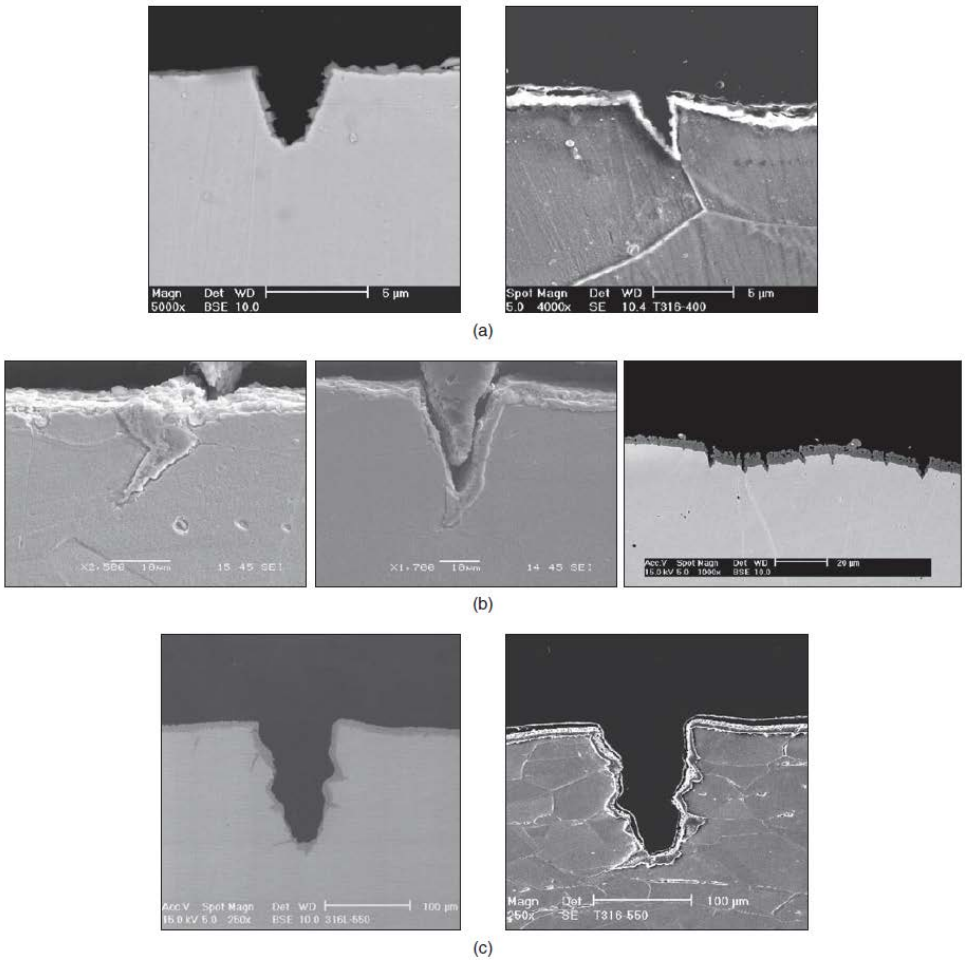

Figure 1-4: SEM cross-section micrographs of SS 316 L evaluated in deaerated SCW at: (a) 400 °C, (b) 500 °C, and (c) 550 °C.[33]

A mean weight gain of 0.3 mg/cm^2 at 500 °C and 24 MPa showed that there was considerable oxidation of the metal substrates. The SEM cross-section micrographs of SS 316 L examined in deaerated SCW at 400, 500, and 550 °C are depicted in Figure 1-4. It was observed that SS 304L suffered from severe intergranular SCC (IGSCC), whereas both TGSCC and

IGSCC were observed in SS 316L. Novotny et al.[33] investigated the SCC susceptibility of SS 316L in deaerated SCW from 400 °C to 650 °C and suggested that the highest temperature for usability of austenitic SS 316L in SCW was 550 °C.

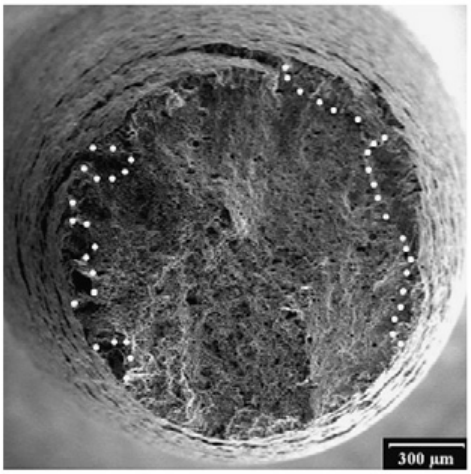

Figure 1-5: Fracture surfaces of SS 316L tested at the strain rate of 1×10^{-7} s^{-1}. Areas exhibiting stress corrosion cracking features are marked by dotted lines.[33]

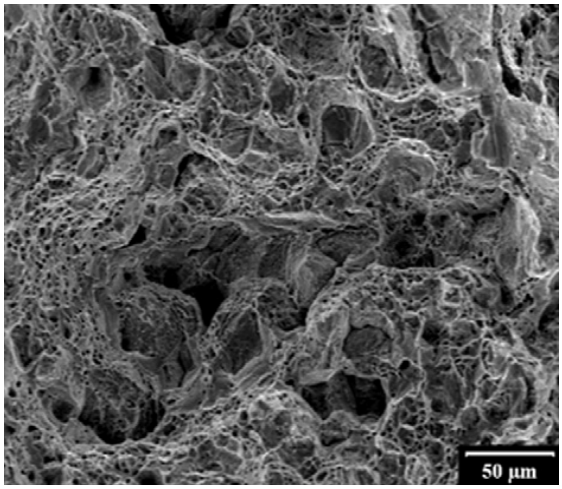

Figure 1-6: Facets of intergranular fracture surrounded by transgranular ductile dimples.[33]

The SEM image of the fracture surfaces of SS 316L which examined at the strain rate of 1×10^{-7} s^{-1} is demonstrated in Figure 1-5.[33] The fracture morphology of SS 316L after the SSRT test

can be seen in Figure 1-6. It was also reported that TG cracking and ductile fracture are the active mechanisms in pure SCW under SSRT.[33]

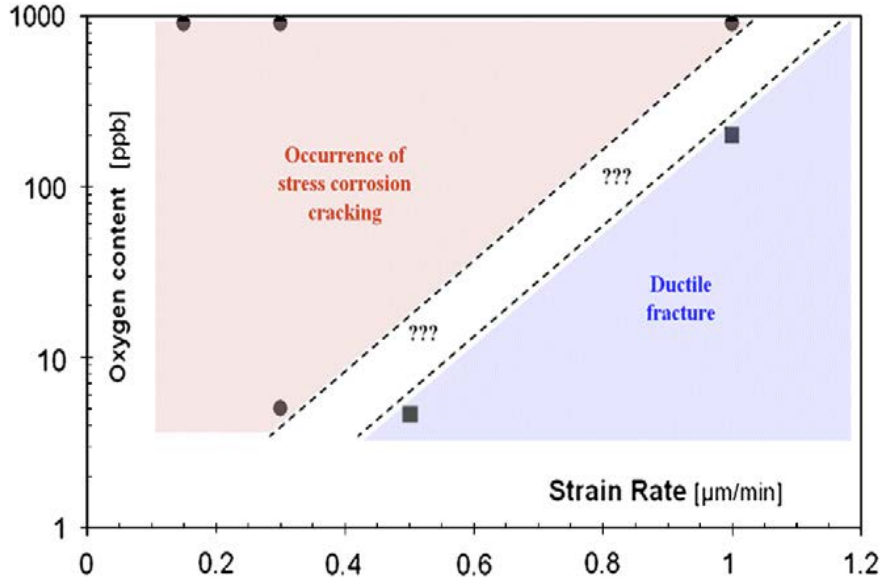

Figure 1-7: Oxygen content as a function of strain rate map delineating TGSCC occurrence in 550 °C SCW environment.[33]

The impact of the SSRT test parameters on the occurrence of SCC is illustrated in a map shown in Figure 1-7. Research conducted by Allen et al.[34] showed that austenitic nickel based alloys have the highest corrosion resistance in SCW. Inconel 625 and 718 tested in SCW containing up to 2 ppm DO for 550 h at 500 °C and 600 °C gained less than 0.1 mg/cm^2 weight. Delafosse et al.[35,36] observed some degree of IGSCC susceptibility in Inconel 718 using SSRT in SCW at 400 °C. SSRT experiment of Inconel 625 with a constant load at 500 °C for 500 h in low pH chlorinated SCW showed that this alloy was susceptible to IGSCC.[36] Was et al.[37] noticed that Inconel 625 suffered only from IGSCC, whereas Inconel 690 showed both IGSCC and TGSCC in slow strain rate tests at 500 °C for 570 h in SCW.

1.6 Materials Selection

Three classes of alloys such as austenitic stainless steel, ferritic-martensitic steel, and nickel-base alloys were selected for the SCWR application. Generally, nickel-base alloy and austenitic stainless steel demonstrate a moderate resistance to the general corrosion. However, they show a weak resistance to the stress corrosion cracking and irradiation induced swelling. Ferritic martensitic alloys show decent resistivity to the embrittlement, swelling, and SCC. One of the drawbacks of F/M alloys is that they do not retain their mechanical integrity at higher temperatures.

This study mostly focused on the corrosion behavior of the austenitic and nickel-base alloys and cracking susceptibility of the selected austenitic alloys. Generally, due to the low neutral capture cross-section, austenitic stainless steel would remain the main candidates. Regarding high temperature integrity consideration, nickel-base alloys can be considered in the list of the prime candidates for the Canadian supercritical water concepts.[38]

1.6.1 SS 347H

SS 347 is an austenitic stainless steel developed from the prototype 18Cr-8Ni alloy 302 with addition of Nb to improve the creep resistance. Nb is added to stabilize the stainless steel and the final production is called stabilized stainless steel. Grain boundary chromium depletion is avoided in stabilized stainless steel. Moreover, intergranular corrosion has been reported for unstabilized austenitic stainless steels.[39]

347H is considered as a higher carbon version of alloy 347 with improved high temperature and creep properties. SS 348 is a version of SS 347 with restricted cobalt and tantalum content for nuclear applications. SS 321 is a version of 18Cr-8Ni alloy with titanium added rather than niobium. A Russian alloy, 1Kh18N10T, with somewhat higher nickel content relative to SS 321 was utilized successfully in the nuclear channels at Beloyarsk.[40]

Ulmer et al.[41] found that SS 347 revealed a moderate weight gain after SCW exposure for 1500 h at 650 °C. Pray and Boyd[42] reported formation of a thick black layer onto its surface upon exposure of SS 347 alloy to supper heated steam at about 700 °C for ~1000 h.

1.6.2 SS 316L

By adding Mo to the prototype 18Cr-8Ni alloy 302, SS 316L can be obtained illustrating a high pitting corrosion resistance. Was et al.,[43] Briggs et al.,[44] Bailat et al.,[45] Alexandreanu et al.,[46] and Lehockey et al.[47] reported that multiple layers develop onto SS 316 surface when exposed to high temperatures. Moreover, Was et al.[43] found that the double oxide layer composed of two layers, an outer layer consisting mainly of iron oxide and an inner layer consisting of chromium oxide. Nickel oxide was not present and there was a near surface zone that contains small amount of Cr. In similar observation, magnetite was detected as the predominant phase in outer layer at 500°C in SCW.

Additionally, the absence of nickel in the oxide layer and the high concentration of nickel at the inner oxide layer was also observed by Was et al.[48] when SS 316 was oxidized at 600°C in a vacuum, consistent with the Ellingham diagram and other data in high temperature

environments. Despite the negligible tendency of the SS 316L towards the oxidation, it has been reported that 316 exposed to 400˚C SCW for 7 days showed no visible oxidation or pitting effects.[49-51] Betova reported that temperature increase alters the SS 316 oxide morphology significantly.[52] They recognized that the crystallite size of the outer oxide on SS 316L enlarged with temperature, and following a 100 h exposure at 700˚C, the oxide thickness measured approximately 27 μm.[53]

The oxides formed on stainless steel in low DO SCW generally form a double layer structure with an outer layer of iron-rich oxide and an inner layer of chromium-rich oxide.[48,49,51-53] The outer layer is a mixed magnetite-hematite layer and the inner layer consists of a mixed-spinel structure.[53,54,55] Electron backscatter diffraction (EBSD) analysis has illustrated that the crystallographic orientation of both the inner and outer oxide layers on SS 316L was consistent with the underlying grain.[55] Based on the quantitative and qualitative analysis, Was proposed an oxidation mechanism for austenitic stainless steels in SCW from 400 ˚C to 550˚C. The inner oxide layer of SS 316L alloy is not only a dense film, but also it includes orientations identical to the metal substrate. Furthermore, the interface between the two oxide layers has a very flat surface.[55]

1.6.3 SS 310S

SS 310S contains 19-22 wt.% Ni and 24-26 wt.% Cr and is alloyed with up to 2 wt.% Mn and 1.5 wt.% Si. Sanchez[56] reported that SS 310S alloy showed a slight weight gain after exposure to SCW for 1500 h at 538 °C. By increasing the exposure time up to ~3000 h, the

samples lost some weight. Additionally, Boyd [56] reported that SS 310S after ~2000 h exposure to the supper heated steam at ~700 °C represented a heavy weight gain.

1.6.4 Alloy 625

Alloy 625 is considered as a nickel-chromium-molybdenum-iron alloy which is a solid-solution-hardenable alloy. At high temperatures, a chromium-depleted zone could be formed at the interface of metal and oxide. As well, grain boundaries become the most viable pathway to supply chromium for the growth of the inner oxide layer, subsequently leading to the raised oxide topography along the grain boundaries. In vast number of studies, this alloy demonstrated incredibly higher corrosion resistance compared with austenitic stainless steels. The weight changes are typically quite small even at the highest temperatures which is really difficult to be measured.[57]

Many studies reported that the surface oxide formed by corrosion in SCW has a double-layer structure consisting of a nickel/iron-rich outer layer and a chromium-rich inner layer. Also, a diffusion layer is formed at the oxide layer/base alloy interface, where the element compositions gradually alter from that of the oxide to the bulk alloy concentration.[58]

1.6.5 Alloy 214

At only 16 wt.% Cr, this alloy is one of the most corrosion resistant candidate which can be used at high temperature service in burners. Alloy 214 contains 4.4 wt.% Al with high oxidation resistance owing to its tightly adherent alumina scale. Chromia scale usually provides a

considerable corrosion resistant in most alloys, but it is oxidized and evaporated in SCW.[58,59] It is typically occurred in SCW containing oxidizing radiolysis products. Nonetheless, alumina cannot oxidize and is stable in high-temperature neutral supercritical water. Deodeshmukh [60] reported the results of 8500 h corrosion tests of foils of alloy 214 and several nickel-base alloys in the air with 10 vol.% steam at 760 and 871 °C. At 760 °C, the metal loss was approximately 0.1 μm, while at 871 °C the metal loss was ~ 3 μm. Maximum internal oxide penetration was reported 8 μm at 760 °C and 23 μm at 871 °C. Furthermore, the thickness of inner layer of Al_2O_3 and the outer layer of $NiAl_2O_4$ spinel were measured less than 1 μm.

1.6.6 Alloy C2000

Alloy C2000 is considered as a nickel-chromium-molybdenum-copper alloy which contains copper under 2 wt.%. Copper increases the corrosion resistance of this alloy against the various corrosive chemical environment like hydrochloric, sulphuric, and hydrofluoric acids. The molybdenum and copper improve the corrosion resistance of this alloy in the reducing media and high content of chromium generally increases the corrosion resistance to oxidation.[61]

Zhang studied the protective oxide layer formed on alloy C2000 at different temperatures. He recognized that increasing the temperature up to the water boiling point resulted in a loss of Cr_2O_3 from the inner and of Mo/Cu from outer layers. However, a comprehensive study has not been conducted so far to comprehensively evaluate the corrosion resistance of this alloy at high temperature in an extreme hydrothermal condition.[61]

1.6.7 Alloy 800H

Alloy 800H is considered as a nickel-iron-chromium alloy demonstrating high resistance to carburization and oxidation at high temperature. Alloys consisting higher nickel have significantly taken into consideration because of the concerns about accumulation of the chloride and other impurities. Alloy 800H contains carbon ranging from 0.05 to 0.1 wt.%, and has a large grain size (>ASTM 5).

Alloy 800 is normally employed at temperatures up to approximately 593 °C, above which the alloy is utilized when resistance to creep and rupture is required. In addition, alloy 800 is considered as a promising candidate due to high temperature strength and chloride-induced SCC resistance. Ruther [62] reported that alloy 800 had an excellent performance in isothermal testing at the temperature of 650 °C in flowing oxygenated steam. They showed that the considerable amount of the corrosion products from alloy 800 could be carried downstream from the core. This has significant implications for radiation fields around downstream components.

Burrill and Godin[63] exposed alloy 800 in a static autoclave containing neutral, deoxygenated water at 450 ºC and 25.3 MPa pressure. Visual examination after 389 h exposure revealed that the coupons were lustrous and appeared some blue coloration. The experiments were carried out in static one liter autoclaves at 450, 500, 550, and 600 °C in 25 MPa pressure for periods up to 1680 h. Pentilla and his colleagues reported a negligible weight gain for alloy 800H exposed to SCW for 600 h at 400 °C and 500 °C and a DO concentration of 0-150 ppb. A weight loss was also observed when the sample was exposed at the same temperatures under the hydrogenated water chemistry (30 cc/kg H_2).[39]

1.6.8 Oxide Dispersion Strengthened (ODS)

The high operating temperature of F/M steels is restricted to 550-600 °C,[64] and thus they are not capable of meeting the high temperature strength requirements for an SCWR fuel cladding. Since F/M steels were investigated comprehensively because of their good resistance to irradiation damage, the development of oxide dispersion strengthened (ODS) steels has recently been studied, using the knowledge based on F/M steels gathered over the years, to improve the creep and tensile characteristics of the material.[64] The method used to strengthen the materials, enabling them to perform acceptably in a stable manner at high-temperatures, is to incorporate a fine dispersion of oxide particles within the metal matrix. These particles act to obstruct (or pin down) the movement of dislocations, restricting the flow (deformation) of the material at the nano-scale level.[64]

Basically, in order to fabricate ODS steels, an ultrafine oxide particles is incorporated in the metal matrix. The raw materials which are in the form of powders having the desired chemical composition in order to approach a final product. In order to obtain the steel powders, an atomization process is employed to produce a fine-sized powder with the favorite chemical composition. The atomization is usually carried out under an inert environment. The atomized steel particles usually have a spherical shape with the dimension of 5-10 μm. The atomization process is an advanced technology which is employed to fabricate a wide variety range of powders for various metallurgical applications.[65]

Until now, the ODS steels appear to have improved creep resistance to much higher temperatures (>700 °C) in comparison with F/M steels. A disadvantage is that only small quantities of ODS material (<50 kg) can be made on a batch basis using powder metallurgy. In

addition, fabrication cost is prognosticated to be much more than producing conventional steel products using the melting processes on a large scale.[65] Another drawbacks is that the powder metallurgy process needs a long time to obtain well mixed powders for consolidation to fabricate a homogeneous production. Moreover, hot isostatic press technique is required to achieve a nonporous solid material.

The use of ODS alloys in an SCWR has been taken into consideration by vast number of researchers, but significant development work would be needed to qualify such materials.

1.7 Research Objectives

The following work aims at evaluating the corrosion resistance of the candidate austenitic alloys. Due to the moderate oxidation resistance of austenitic alloys in SCW relative to the F/M alloys, the austenitic alloys are promising candidates for SCWR applications where the alloy is in direct contact with SCW. As a matter of fact, the presence of some important shortages, such as limited data on corrosion and cracking susceptibility for austenitic SS Cr >20 wt.% alloy, limited corrosion test time exposure (max. about 1000h), and limited ultra-high temperature corrosion studies for austenitic alloys, motivated us to work on them in the current study. Besides, the response of candidate alloys in upside-down situation, the performance of austenitic steels in SCW for >1000h, and evaluation of austenitic steels in SCWR in case of further modification were considered in this work.

Moreover, this project focused on the study of metal corrosion and cracking initiation in SCW and provides an in-depth analysis of the degradation mechanisms for candidate alloys.

Furthermore, due to the fact that the mechanism of the crack initiation in austenitic alloys subjected to SCW is not entirely understood and experimental data for long term performance is not available yet, the oxidation and cracking initiation of austenitic stainless steel exposed to SCW for up to 20000 h exposure time.

1.8 Proposed Research

This study was planned to investigate the oxidation of several stainless, austenitic, and nickel-based alloys exposed to supercritical water (SCW) at 800 °C for 12 hours. Morphologies, microstructures, and chemical composition of oxide films formed on stainless steels (SS) 347H, 316L, and 310S, and alloys 625, 214, C2000, and 800H were investigated using weight measurement, X-ray diffraction patterns, scanning electron microscopy, and energy dispersive spectroscopy

Besides, the corrosion behavior of SS 316L capsules was investigated after 20,000 hours exposure to SCW (500°C). Also, the oxidation of SS 310S was investigated in capsules exposed to SCW for 20,000 h at 500 °C. In the complementary step, the effect of SCW exposure time on corrosion behavior of 304-ODS (oxide dispersion strengthened) steel in supercritical water (650 °C) was investigated. It should be mention that, all specimens were analyzed using SEM, EDS, TEM, XRD, and TOF-SIMS.

1.9 References

1 M.I. Hoffert, K. Caldeira, G. Benford, Advanced technology paths to global climate stability: energy for a greenhouse planet, Science, 298 (2002) 981-987.

2 U.S. DOE, Technology Roadmap Update for Generation IV Nuclear Energy Systems,Committee and the Generation IV International Forum, (2014).

3 U.S. DOE, A Technology Roadmap for Generation IV Nuclear Energy Systems, GIF-002-00, Committee and the Generation IV International Forum, (2002).

4 R.B. Duffey, I.L. Pioro, Supercritical water-cooled nuclear reactors: review and status, Encyclopedia of Life Support Systems EOLSS, Oxford, (2004).

5 R. Noyori, Homogeneous catalysis in supercritical fluids, Chemical reviews, 99 (1999) 353-354.

6 M.A. McHugh, V.J. Krukonis, Supercritical fluid extraction: principles and practice, Elsevier, (1994) 10.

7 E.U. Franck, Supercritical water and other fluids - A historical perspective, Supercritical Fluids - Fundamentals and Applications, Springer, (2000) 307-322.

8 R.B. Duffey, I.L. Pioro, Supercritical Water-Cooled Nuclear Reactors: Review and Status Oxford, (2005).

9 H. Weingärtner, E.U. Franck, Supercritical water as a solvent, Ange. Chemi. Int. Ed., 44 (2005) 2672-2692.

10 H. Peker, M. Srinivasan, J. Smith, B.J. McCoy, Caffeine extraction rates from coffee beans with supercritical carbon dioxide, AIChE , 38 (1992) 761-770.

11 G.M. Schneider, Physicochemical principles of extraction with supercritical gases, Ange. Chemi. Int.

Ed., 17 (1978) 716-727.

12 Y.P. Sun, Supercritical fluid technology in materials science and engineering: syntheses, properties, and applications, CRC, (2002).

13 F. Cansell, C. Aymonier, A. Loppinet-Serani, Review on materials science and supercritical fluids, Current Opinion in Solid State and Materials Science, 7 (2003) 331-340.

14 D. Broell, C. Kaul, A. Kraemer, P. Krammer, T. Richter, M. Jung, H. Vogel, P. Zehner, Chemistry in supercritical water, Ange. Chemi. Int. Ed., 38 (1999) 2998-3014.

15 E.U. Franck, Supercritical water and fluids - a historical perspective, NATO, 35 (2000) 307-322.

16 R.W. Shaw, T.B. Brill, A.A. Clifford, C.A. Eckert, E. Ulrich Franck, Supercritical water a medium for chemistry, Chem. and Eng. News., 69 (1991) 26-39.

17 P. Kritzer, Corrosion in high-temperature and supercritical water and aqueous solutions J. Supercrit. Fluids, 29 (2004) 1-29.

18 E.U. Franck, Physicochemical properties of supercritical solvents, Phys. Chemi, 88 (1984) 820-825.

19 H. Weingärtner, Supercritical water as a solvent, Ange. Chemi. Int. Ed., 44 (2005) 2672-2692.

20 A.E. Mather, E.U. Franck, Phase equilibria in the system carbon dioxide-water at elevated pressures, J. Phys. Chemi., 96 (1992) 6-8.

21 C.K. Chow, H.F. Khartabil, Conceptual fuel channel designs for CANDU - SCWR, Nuc. Eng. and Tech., 40 (2008) 139-146.

22 D. F. Wang, S. Wang, A preliminary cathena thermalhydraulic model of the Canadian SCWR for Safety analysis, AECL Nuc. Rev., 3 (2014) 9-16.

23 L.K.H. Leung, Update on the Canadian SCWR concept, The 3rd Canadian SCWR Info. Exch. Work. for the Phase II NSERC/NRCan/AECL Gen-IV Energy Tech., (2014).

24 X. Cheng, "Introduction to Thermal-Hydraulics", Proc. 5th Int. Symp. on SCWR, (2011) 13-17.

25 R. Viswanathan, J. Sarver, J.M. Tanzosh, Boiler materials for ultra-supercritical coal power plants-steamside oxidation, J. Mat. Eng. Perform., 15 (2006) 255-274.

26 Viswanathan, K. Coleman, U. Rao, Materials for ultra-supercritical coal-fired power plant boilers, J. Press. Vessel. Pip., 83 (2006) 778-783.

27 L. Heikenheimo, D. Guzonas, C. Fazio, GenIV materials and chemistry research - common issures with the SCWR concept, Proc. 4th Int. Symp. on SCWR, (2009).

28 P. Ampornrat, G.S. Was, Oxidation of ferritic–martensitic alloys T91, HCM12A and HT-9 in supercritical water, J. Nucl. Mater., 371 (2007) 1-17.

29 P. Ampornrat, G. Gupta, G.S. Was, Tensile and stress corrosion cracking behavior of ferritic–martensitic steels in supercritical water, J. Nucl. Mater., 395 (2009) 30-36.

30 S.S. Hwang, B.H. Lee, J.G. Kim, J. Jang, SCC and corrosion evaluations of the F/M steels for a supercritical water reactor, J. Nucl. Mater., 372 (2008) 177-181.

31 W.K. Boyd, H.A. Pray, Corrosion of stainless steels in supercritical water, Corros., 13 (1957) 375-385.

32 G.S. Was, S. Teysseyre, Z. Jiao, Corrosion of Austenitic Alloys in Supercritical Water, Corros, 62 (2006) 989-1005.

33 R. Novotny, P. Hähner, J. Siegl, P. Haušild, S. Ripplinger, S. Penttilä, A. Toivonen, Stress corrosion

cracking susceptibility of austenitic stainless steels in supercritical water conditions, J. Nucl. Mater., 409 (2011) 117-123.

34 X. Ren, K. Sridharan, T.R. Allen, Corrosion Behavior of Alloys 625 and 718 in Supercritical Water, Corros., 63 (2007) 603-612.

35 D.D. Cédric BOSCH, Stress corrosion cracking of Ni-based and Fe-based alloys in supercritical water, Corrosion. (2005) 45.

36 D.D. L. Fournier , C. Bosch and T. Magnin, Stress corrosion cracking of nickle-base superalloys in areated supercritical water, Corrosion. (2001).

37 S. Teysseyre, G.S. Was, Stress corrosion cracking of austenitic alloys in supercritical water, Corros., 62 (2006) 1100-1116.

38 Elaine Ann West, Influence of local stress and strain on intergranular cracking of 316l stainless steel in supercritical water, University of Michigan, (2010) 2-3.

39 Pentilla, S., Toivonen, A. Oxidation and SCC Behavior of Austenitic and ODS Steels in Supercritical Water, 6th Proc. 6th Int. Symp. on SCWR , Shenzhen, China (2013) 03-07.

40 Janik, P., Novotny, R., Nilsson, K. F., Siegl, J., Hausild, P. Pre-qualification of cladding materials for SCWR fuel qualification testing facility-stress corrosion cracking testing. Proc. 6th Int. Symp. on SCWR, Shenzhen, China, (2013) 03- 07.

41 Ulmer, R.C. Corrosion Study of Metals for Supercritical Pressure Power Plants, Corrosion (1960) 68.

42 K. Ehirlich, L. Heikinheimo, Materials for high performance reactors, J. Nucl. Mater., 327 (2004) 140-147.

43 G. S. Was, B. Alexandreanu, J. T. Busby, Proc. Adv. in frac. and fail. Preven. Trans tech publications,

(2004) 885.

44 C. Bailat, A. Almazouzi, N. Baluc, R. Schaublin, R. Groschel, M. Victoria, The effects of irradiation and testing temperature on tensile behavior of stainless steels, J. Nucl. Mater., 283-287 (2000) 446.

45 T. S. Byun, E. H. Lee, J. D. Hunn, Plastic deformation in 316LN stainless steel – characterization of deformation microstructures, J. Nucl. Mater. 321 (2003) 20.

46 G. Alexandreanu, G. S. Was, Grain Boundary Deformation-Induced Intergranular Stress Corrosion Cracking of Ni-16Cr-9Fe in 360°C Water, Corrosion. 59 (2003) 705.

47 E. M. Lehockey, A. M. Brennenstuhl, S. Pagan, M. A. Clark, V. Perovic, Proc. 13th Int. Conf. on Env. Deg. of Mat. in Nuc. Pow. Sys., (2007) 465.

48 S. Teysseyre, Q. Peng, G. Was, Stress Corrosion Cracking of Neutron- Irradiated Stainless Steels in Supercritical Water Material studies required for SCWR, J. Nucl. Mater., 371 (2007) 98–106.

49 R. Zhou, E.A. West, Z. Jiao, G. Was, Irradiation-assisted stress corrosion cracking of austenitic alloys in supercritical water, J. Nucl. Mater., 395 (2009) 11–22.

50 K. Sridharan, A. Zillmer, J. R. Licht, T. R. Allen, M. H. Anderson, L. Tan, Corrosion behavior of the candidate alloys for supercritical water reactors, Proc. ICAPP, (2004) 4136.

51 Y. Chen, K. Sridharan, T. Allen, Corrosion behavior of NF616 and D9 as Candidate Alloys for Supercritical Water Reactors Corrosion, (2005) 05391.

52 I. Betova, M. Bojinov, P. Kinnunen, V. Lehtovuori, S. Peltonen, S. Penttila, T. Saario, Proc. ICAPP, (2007).

53 J. Kaneda, S. Kasahara, J. Kuniya, K. Moriya, F. Kano, N. Saito, A. Shiori, T. Shibayama, H. Takahashi, Proc. 12th Int. Conf. on Env. Deg. of Mat. in Nuc. Pow. Sys., (2005)1342-1351.

54 T. Allen, D. Guzonas, G. S. Was, E. A. West, J. Nucl. Mater., (2010).

55 P. Ampornrat, G. Gupta, G. Was, Tensile and stress corrosion cracking behavior of ferritic–martensitic steels in supercritical water, J. Nucl. Mater., 395 (2009) 30–36.

56 G. S. Was, T. R. Allen, Proc. American Nuclear Society-ICAPP, 6 (2005) 3460.

57 R.G. Sanchez, Corrosion Performance of Candidate Materials for Canadian Gen IV Supercritical Water Cooled Reactor, (2014).

58 D. A. Guzonas, J. Wills, Do, T. Michel, Corrosion of candidate materials for use in a supercritical water CANDU reactor, Proc. 13th Int. Conf. on Env. Deg. of Mat. in Nuc. Pow. Sys., (2007) 1250-1261.

59 W.L. Pearl, E.G. Brush, G.G. Gaul, S. Leistikow, General Corrosion of Inconel Alloy 625 in Simulated Superheat Reactor Environment, J. Nuc. Applica., 3 (1967) 418- 432.

60 V.P. Deodeshmukh, Long-term performance of high-temperature foil alloys in water vapour containing environment. Part I: Oxidation behaviour, Oxid. of Metal., 79 (2013) 567-578.

61 X. Zhang, D. W. Shoesmith, Infuence of temperature on passive film properties on Ni-Cr-Mo alloy" Corros. Sci., 76 (2013) 424-431.

62 W.E. Ruther, R.R.Schlueter, R.H. Lee, R.K. Hart, Corrosion behavior of steels and nickel alloys in superheated steam. Corrosi., 22 (1966) 147-155.

63 K.A Burrill, Water Chemistries in Supercritical Water in Reactor Heat Transport Systems, Proc. 8th BNES Conf. on Wat. Chemi. of Nuc. Rea. Sys., (2000) 357-363.

64 R.L. Klueh, Elevated Temperature Ferritic and Martensitic Steels and their Application to Future

Nuclear Reactors, J. Int. Mat. Rev., 50 (2005) 287-310.

65 J. Bichoff, Oxidation Behavior of Ferritic-Martensitic and ODS Steels in Supercritical Water. Pennsylvania State University, (2011) 57-62.

Chapter 2: An Investigation of the Corrosion Resistance of Austenitic Stainless Steel and Nickel-base Alloys in Supercritical Water at 800 °C

2.1 Introduction

Canada's generation IV national program[1-4] involves the selection of materials and assessment of candidate alloys that can withstand the operating temperatures in the CANDU (Canadian deuterium uranium) supercritical water reactor (SCWR) which can reach 800 °C in upside down situation. Most commercial alloys such as austenitic steels (SS 304, SS 316) and nickel-base alloys suffer from nonuniform corrosion in SCW[5], therefore finding an appropriate candidate is a great challenge for SCWR application.

Researches on materials for reactors operating at temperatures above the thermodynamic critical point started in the early 1950s.[5] Some of the highest test temperatures reported for SCW corrosion tests were those reported by Boyd in 1956.[5] They studied the corrosion behavior of Ni-Cr-Fe alloys such as 410, 302, 347, 309, 310 stainless steels, and nickel-base alloys 625, 617, and 718 at different temperatures. It has been known that different alloying elements can change the oxidation and corrosion susceptibility of the base metal at high temperature. Iron and nickel participate in the formation of iron oxide and nickel oxide in the outer oxide layer. Indeed, outward diffusion of these two elements and reacting with oxygen lead to the formation of different oxides namely Fe_3O_4, Fe_2O_3, FeO, and NiO depending on the oxygen content and temperature. Chromium has an important role in the formation of various oxide layers on the

Material in this chapter has been submitted for publication in Corrosion Science.

exposed alloy to the SCW which can be in the form of chromium oxide. This layer plays a crucial role in protection of the surface against oxidation.[6,7]

Moreover, alloying elements including molybdenum, titanium, manganese, aluminum, and niobium affect oxide layer formation by promoting the formation of different phases in the oxide scale which cannot protect the surface against SCW.[8-14] Additionally, as there are differences in the potential values for different oxide compositions, it can accelerate the localized corrosion at high temperature leading to formation of pitting. Finally, diffusion rate differences at high temperature may result in the unwanted depletion or enrichment of alloying elements leading to the localized corrosion. It is worth noting that at high temperature SCW, it is possible for alloying elements and/or oxide structures to dissolve in the SCW resulting in formation of the pitting in the base metal or oxide layer.[15-18]

Recently, there have been numerous investigations on the oxidation of different alloys using SCW oxidation at high temperature.[19-25] A few studies have been conducted on the mechanism of oxide scales formation on metallic materials in SCW; proposing several mechanisms such as the solid-state growth mechanism and the metal dissolution/oxide precipitation mechanism.[26-29] However, limited studies have been done on evaluating the oxidation behavior of candidate alloys in SCW at the temperature of 800 °C. In this study, the corrosion resistance of several alloys exposed to SCW at 800 °C and 25 MPa for 12 h was investigated. The oxide scale and pittings formed during the exposure to SCW were subsequently characterized using weight gain/loss measurements, X-ray diffraction (XRD), and scanning electron microscopy (SEM) equipped with energy-dispersive X-ray spectroscopy (EDS). Oxidation and pitting mechanisms are proposed and discussed thoroughly.

Table 2-1: Chemical elemental analysis of the alloy (wt. %).

Alloys	Fe	Cr	Ni	Ti	Al	Nb	Si	Mo	Mn	Cu	C	S	P
SS 347H	B	17.9	10.5	-	-	0.79	1	-	2	-	0.08	0.03	0.04
SS 316L	B	17.2	11.7	-	-	-	0.84	2.14	1.97	-	.02	0.03	0.04
SS 310S	B	24.4	20.3	-	-	-	0.33	0.29	1.18	-	.04	0.001	0.02
Alloy 625	5	21.5	B	0.4	0.4	3.55	0.5	9	0.5	-	0.079	0.01	0.01
Alloy 214	3	16	B	-	4.5	-	0.17	-	0.37	-	0.05	0.01	0.01
Alloy C2000	2.9	23	B	1.6	-	-	0.04	16	0.38	1.6	0.05	0.01	0.01
Alloy 800H	B	20.49	31.49	0.57	0.5	-	0.13	-	0.76	-	0.075	0.01	0.01

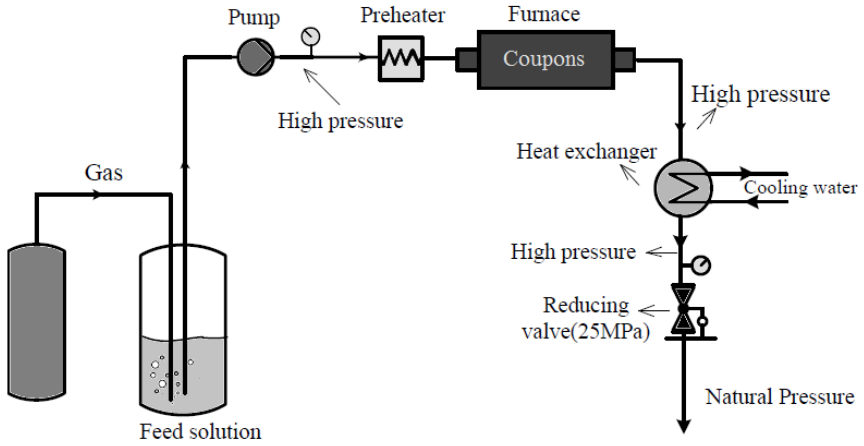

Figure 2-1: A general overview of the supercritical water loop used in this study.

2.2 Material and Methods

The materials used in this study were solution treated commercial sheets with a thickness of 2 mm. The elemental composition of the alloys is given in Table 2-1. The sheets were cut into rectangular shaped coupons measuring 20 mm in long and 10 mm wide. The coupon samples

were then polished with emery paper up to 600 grit and subsequently washed in an ultrasonic bath of pentane, isopropyl alcohol, and acetone to degrease the surfaces.

The corrosion tests were conducted using the SCW loop facility at university of Alberta at 800 °C and 25 MPa. The SCW loop is illustrated schematically in Figure 2-1. The oxygen level was maintained at a constant level which was balanced at 8 ppm by constant purging air. The inlet conductivity of water was measured 0.1 μS/cm and the flow rate was 2 - 2.5 L/h. After SCW exposure, the exposed coupons were dried in air. Weight changes of samples were measured with a Mettler Toledo™ Excellence plus XP Microbalance. A Bruker AXS diffractometer (Bruker D8 Discover) operating with Cu-K_α radiation with a wavelength of 1.5405 Å at 40 kV and 40 mA in the 2-theta range of 10° - 100°; a scan rate of 0.05° per second was used for X-ray diffraction (XRD) analysis. The surface morphology of the formed oxide layers on the coupons was examined with a scanning electron microscope (JEOL JSM-6301FXV field emission high-resolution SEM). A ZEISS EVO–MA15 SEM equipped with an energy dispersive x-ray spectroscope (EDS) was employed for the elemental analysis. A laminar flow of 1 cc/min of deionized water (DI) was applied to minimize the effect of flow on metal corrosion. The samples were placed in a tubular furnace and heated to 800 °C. The temperature of the furnace was calibrated using a Nextel ceramic insulated lead wire rated to 815 °C (Omega) as the reference thermocouple. The oxides were stripped from the metal samples by immersion in a solution of 100 kg/m^3 sodium hydroxide (NaOH) + 30 kg/m^3 potassium permanganate ($KMnO_4$) at 100 °C for about 5 min, followed by immersion in 100 kg/m^3 ammonium oxalate ($C_2H_8N_2O_4$) at 100 °C for about 5 min. The sequence was repeated three or more times depending on the oxide thickness. Samples were ultrasonically cleaned in deionized water.

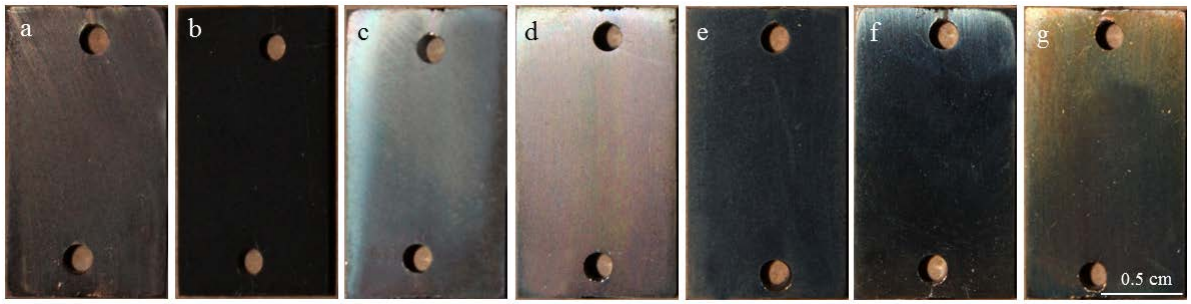

Figure 2-2: Surface color changes in samples exposed to SCW at 800 °C for 12 h. (a) SS 347H, (b) SS 316L, (c) SS 310S, (d) alloy 625, (e) alloy 214, (f) alloy C2000, and (g) alloy 800H.

2.3 Results and Discussion

2.3.1 Visual Observation of the Metal Surfaces Exposed to SCW at 800 °C

Figure 2-2 shows the surface color change in samples exposed to SCW for 12 h at 25 MPa and 800 °C. Figure 2-2a shows the surface of the SS 347H coupon after 12 h exposure to SCW. The brown color on the metal surface represents moderate oxidation. In the sample SS 316L, a uniform dark oxide scale formed on the surface exposed to SCW (Figure 2-2b). A thin oxide layer on the surfaces of SS 310S, alloy 625, and alloy 800H has a rainbow appearance in blueish green (Figure 2-2c), greenish red (Figure 2-2d), and greenish yellow (Figure 2-2g), respectively. Alloys 214 (Figure 2-2e) and C2000 (Figure 2-2f) present dark blueish rainbow surfaces. Less discoloration was observed in sample SS 347H, indicating that the oxide scale was more integrated.

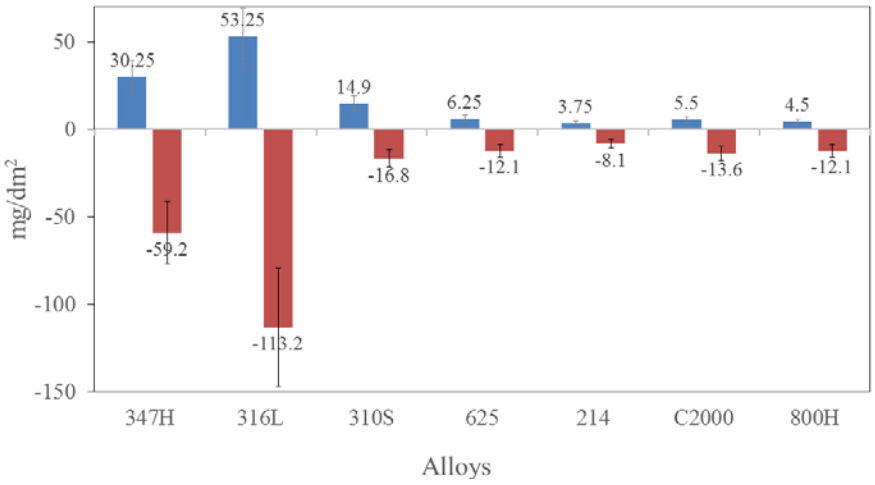

Figure 2-3: Weight gain and weight loss measurements of the samples after exposure to SCW at 800 ℃ for 12 h.

2.3.2 Weight Gain and Weight Loss Measurements

Weight changes for samples exposed to SCW at 25 MPa and 800 °C are shown in Figure 2-3. The weight gain is a direct measurement of the dried scales that formed on the metal surface after 12 h exposure to SCW. The weight loss measurement obtained after the sample was descaled. All the samples exposed to SCW exhibited a positive weight gain, suggesting oxide scale formation on the surface. The samples were divided into two groups: (1) iron-base alloys, namely SS 347H, SS 316L, SS 310S, and alloy 800H and (2) nickel-base alloys, namely alloy 625, alloy 214 and alloy C2000. The average weight gain of samples exposed to SCW was higher for the austenitic stainless steels than that of the nickel-base alloys.

The average weight gain of austenitic samples was 30.25 mg/dm^2 for SS 347H, 53.25 mg/dm^2 for SS 316L, 14.9 mg/dm^2 for SS 310S, and 4.5 mg/dm^2 for alloy 800H. The weight gain of alloy 800H was considerably lower than that of the other austenitic samples, indicating the higher resistivity of alloy 800H to SCW under the experimental conditions. The weight gain

of the nickel-base alloys was much lower than those of the iron-base alloys. The average weight gain of Ni-based samples was 6.25 mg/dm^2 for alloy 625, 3.75 mg/dm^2 for alloy 214, and 5.5 mg/dm^2 for alloy C2000. Among the nickel-based alloys, alloy 214 gained the lowest weight when exposed to SCW, indicating its higher corrosion resistance to SCW at 800 °C.

The samples were reweighed after removing the oxide scale to confirm the comparative results of the weight change. As the results in Figure 2-3 indicate, the average weight losses of the austenitic samples were 59.2 mg/dm^2 for SS 347H, 113.2 mg/dm^2 for SS 316L, 16.8 mg/dm^2 for SS 310S, and 12.1 mg/dm^2 for alloy 800H. The weight loss results showed that the amount of scale formed on alloy 800H and SS 310S was lower suggesting that alloy 800H and SS 310S had higher resistance to oxidation relative in comparison with austenitic samples when exposed to SCW at 800 °C for 12 h. The weight loss values of nickel-based alloys were generally lower than those of iron-based alloys. The average weight losses of nickel-based alloys were 12.1 mg/dm^2 for alloy 625, 8.1 mg/dm^2 for alloy 214, and 13.6 mg/dm^2 for alloy C2000. The lower average weight loss of the nickel-based alloys indicated that their corrosion resistance was superior relative to that of the iron-based alloys under these experimental conditions.

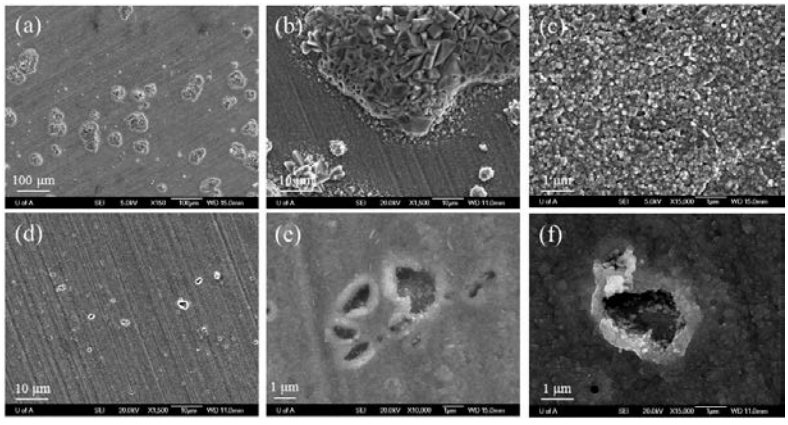

Figure 2-4: Surface morphologies of SS 347H after exposure to SCW at 800 °C for 12 h, with different magnifications of 150x (a), 1500x (b), 15000x (c), 150x (d), 10000x (e), 15000x (f) are presented.

2.3.3 Morphological observations of the oxide scales and elemental analyses by EDS

The surface morphology of the oxide layer formed on the surface of iron-based and nickel-based alloys was examined by SEM after exposure to supercritical water at 800 °C for 12 h. Elemental analysis of the scales and pitting were performed by EDS.

SS 347H

FESEM images of the SS 347H sample surface after exposure to SCW at 800 °C for 12 h are shown in Figure 2-4. Two different types of defect can be observed, oxide films and instances of pitting corrosion. Figure 2-4a shows the oxide layer formed on SS 347H. Herpes-shaped oxides (Figure 2-4b) are distributed on the compacted oxide layers with fine grains (Figure 2-4c). The herpes-shaped oxides are mainly composed of large grains with irregular shapes. Many holes are present among the loose grains. Pits with various sizes were also observed on the sample surface (Figure 2-4d). Examination at higher magnification indicates that the pits were a few μm wide. Their locations could be manifested by niobium carbide (NbC).[5,30,31]

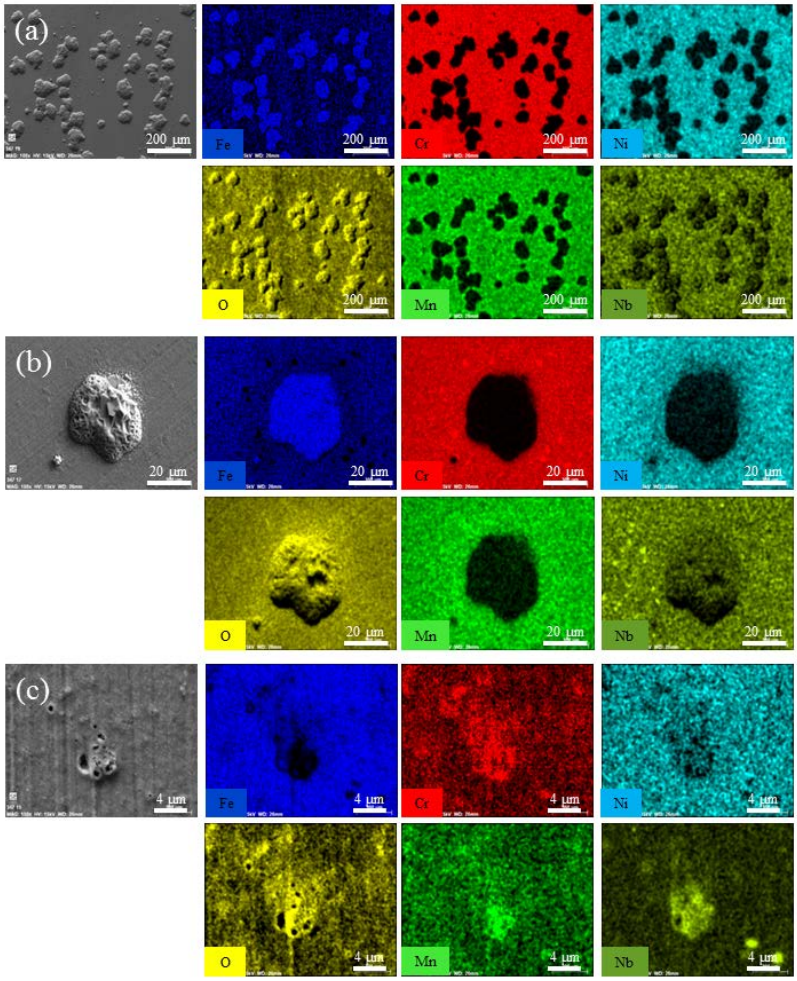

Figure 2-5: EDS elemental distribution on SS 347H after exposure to SCW at 800 °C for 12 h, at different magnification of 75x (a), 750x (b), 3000x (c).

Figure 2-5 illustrates the above features with their associated elemental EDS maps. Figure 2-5a shows elemental distribution on SS 347H surface after exposure to SCW at 800 °C for 12 h, indicating how elements vary around the herpes-shaped oxides. Figure 2-5b shows the oxide scale at higher magnification. Based on the EDS mapping analysis, it can be concluded that a thin layer of fine-grained oxide was rich in Cr-Ni-Fe, suggesting that the base oxidation layer probably consisted of a thin Cr_2O_3 layer or spinel structure $(Fe,Cr,Ni)_3O_4$. However, the herpes-

shaped oxides were free of Cr and were mainly composed of Fe and O. Therefore, the herpes-shaped oxides could be composed of an iron oxide such as magnetite. As pitting was a significant mode of corrosion observed in the tested samples, SEM-EDS performed inside and in the vicinity of pits revealed that oxygen, chromium, manganese, and/or niobium were concentrated, while nickel and iron were depleted inside the pits. The SCW condition at 800 °C most likely facilitate the formation of carbide, implying that pitting was initiated likely by galvanic corrosion due to the compositional differences between the metal and the oxide layer. Inclusions and oxides formed on the surface could lead to weak points in the oxide layer and become initiating sites for pitting corrosion. Since the potential values of the oxide scales were different, active sites for galvanic corrosion and pitting might appear beneath the scales.[30-33]

The SS 347 is an austenitic stainless steel derived from the prototype 18Cr-8Ni SS 302 with the addition of Nb to improve creep resistance. As Nb encourages carbide formation, the SS alloy is stabilized as the issue of grain boundary chromium depletion is avoided, reducing the propensity for the intergranular corrosion commonly seen in nonstabilized austenitic stainless steels. SS 347H is the higher carbon version of SS 347 with improved high temperature and creep properties. Consequently, the possibility of carbide formation in SCW at 800 °C could produce active sites for pitting and decrease corrosion resistance.

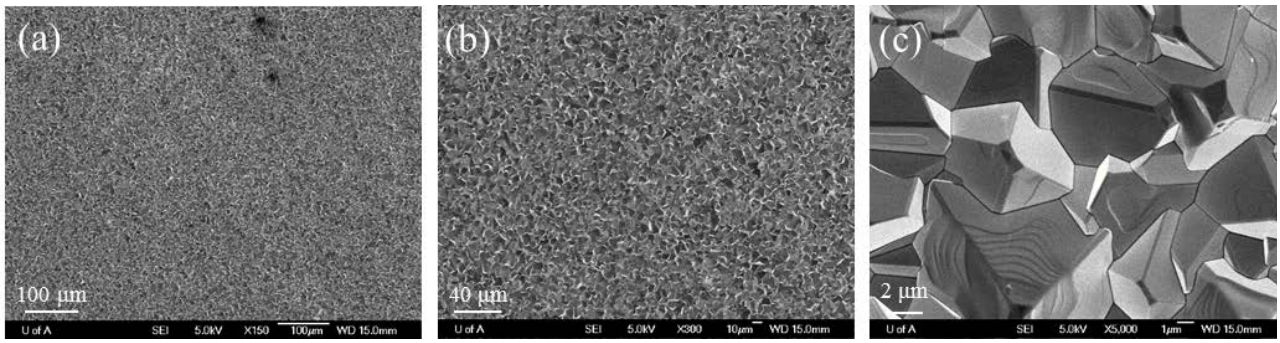

Figure 2-6: Surface morphologies of SS 316L after exposure to SCW at 800 °C for 12 h. Images with different magnifications of 150x (a), 300x (b), and 5000x (c) are presented.

SS 316L

Figure 2-6 shows SEM images of the oxide scales on SS 316L after exposure to SCW at 800 °C for 12 h. The SS 316L surface is covered with a uniform oxide layer consisting of octahedral particles of 1 to 6 µm in diameter. EDS elemental analysis of the oxide layer shows that the scales contained iron and oxygen, presumably in the form of magnetite (Figure 2-7).

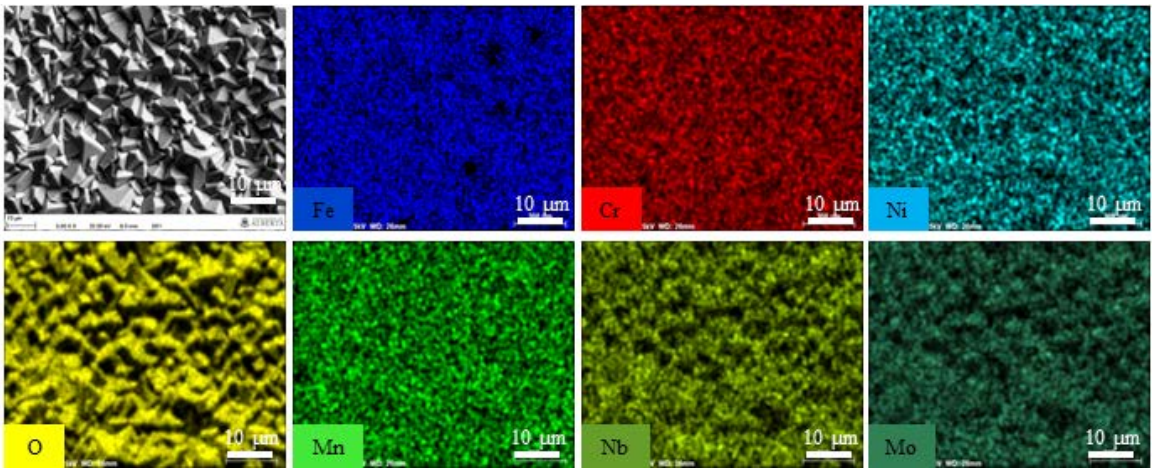

Figure 2-7: EDS elemental distribution on SS 316L after exposure to SCW at 800 °C for 12 h.

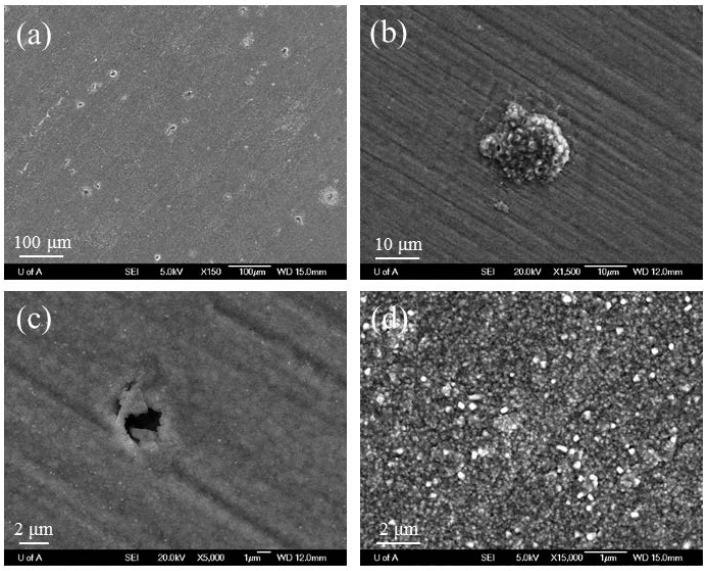

Figure 2-8: Surface morphologies of SS 310S after exposure to SCW at 800 °C for 12 h. Images at different magnifications of 150x (a), 1500x (b), 5000x (c), and 1500x (d) are presented.

In general, iron ions have a higher mobility than chromium ions in diffusing through the oxide layer due to the large number of catatonic vacancies[15]. This resulted in formation of iron oxide (Fe_3O_4) on the surface. Although diffusion of iron ions can occur through both grains and grain boundaries, grain boundaries have much higher diffusivity, which allowed a higher fraction to diffuse.[11] Oxygen diffuses mostly through the grain boundaries into the substrate, where iron concentration was low enough to form spinel phase. Since the magnetite layer is thick and uniform, no herpes-shaped oxide and/or pits appear on the surface exposed to the SCW. However, since the oxidation rate of SS 316L was high (Figure 2-2), and oxidation can lead to a high metal consumption, an increase in exposure time might cause spallation of the oxide.[9,10] Furthermore, the lower concentration of iron and higher concentration of oxygen at the grain boundaries resulted in the formation of chromium oxide at the spinel/substrate interface. Oxygen does not interact with nickel because chromium has higher affinity to oxygen relative to nickel;

therefore, in case of alloy SS 316L, nickel oxide never forms and a thin layer of chromium oxide can form at the grain boundaries.[11] This process is known as chromium depletion and enrichment in Ni in the grain boundaries close to the surface which leads to the susceptibility of the SS 316L to oxidation.

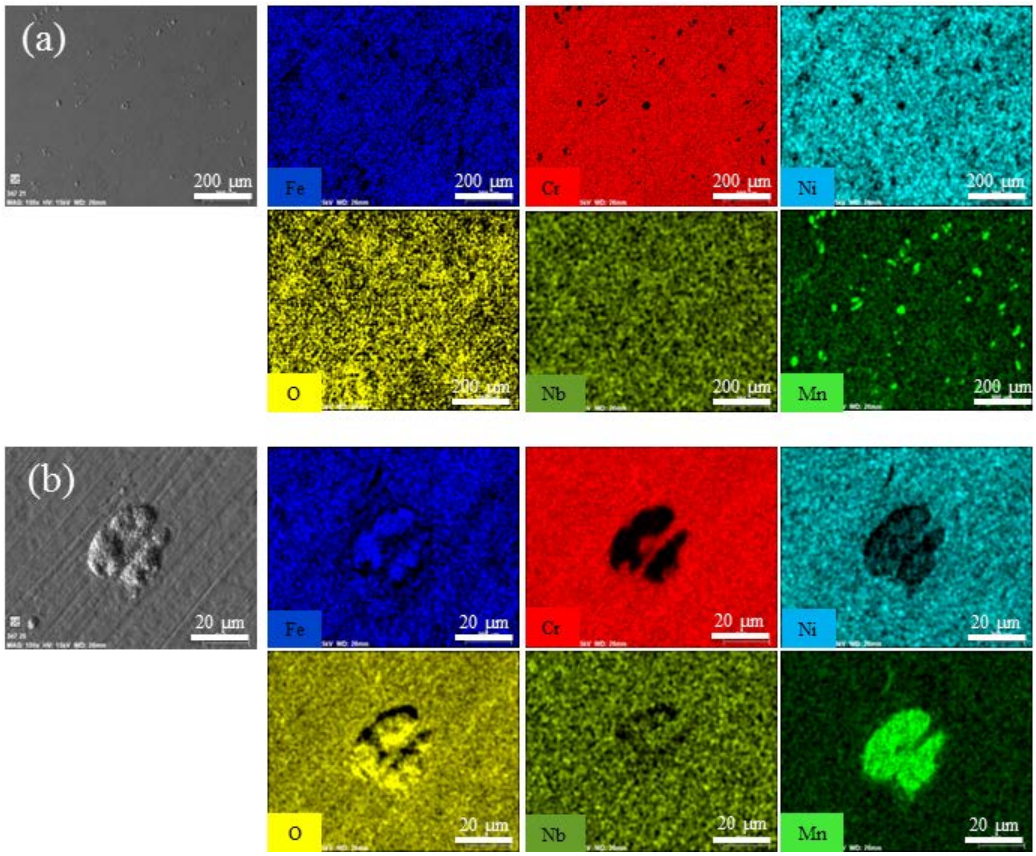

Figure 2-9: EDS elemental distribution on SS 310S after exposure to SCW at 800 °C for 12 h.

SS 310S

The surface morphology of the oxide layers on SS 310S was examined with SEM as shown in Figure 2-8. Figure 2-8a shows that a few islands formed on the SS 310S surface. At higher magnification, Figure 2-8b shows 12 µm herpes-shaped oxide particles on the SS 310S surface

and a 2 μm pit is observed in Figure 2-8c. At higher magnification (Figure 2-8d), the particle size of the oxide layer appeared to be in the range of 200 nm to 300 nm.

Figure 2-9 demonstrates an EDS map of the SS 310S sample after exposure to SCW at 800 °C for 12 h. A uniform oxide layer and a few small islands are apparent on the surface (Figure 2-9a). Higher magnification image shows herpes-shaped oxide particles made of iron, oxygen, and manganese in the form of $(Fe,Mn)_3O_4$ (Figure 2-9b). EDS mapping elemental analysis showed that the uniform oxide layer was made of chromium, oxygen, and iron, which could form chromium oxide (Cr_2O_3) and/or an Fe-Cr spinel structure ($FeCr_2O_4$). SS 310S contains 24–26 wt.% Cr and 19–22 wt.% Ni, and is alloyed with up to 2 wt.% Mn and 1.5 wt.% Si. Thus, a high concentration of chromium could lead to the formation of a uniform and protective chromium oxide/spinel oxide layer on the substrate and increase corrosion resistance to the SCW.[10,12,29] In other words, higher chromium content in the alloy SS 310S leads to the formation of chromium-rich oxide layer and consequently, reduces outward diffusion of iron ions to form iron oxide.

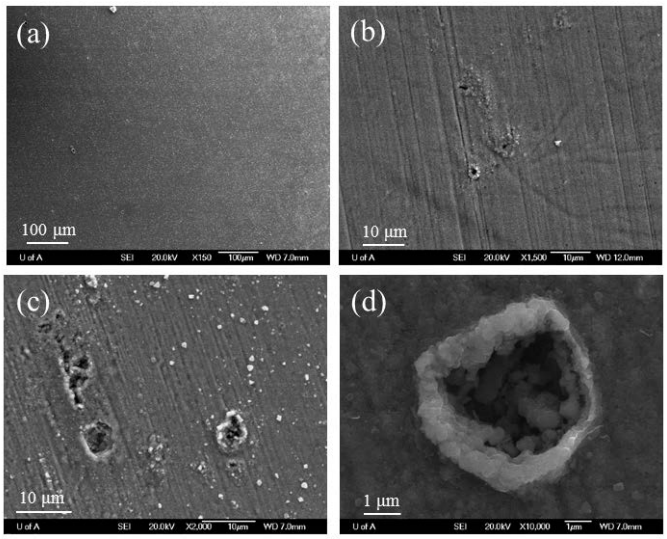

Figure 2-10: Surface morphologies of alloy 625 after exposure to SCW at 800 °C for 12 h. Images at different magnifications of 150x (a), 1500x (b), 2000x (c), and 10000x (d) are presented.

Alloy 625

SEM micrographs of alloy 625 after exposure to SCW at 800 °C for 12 h are shown in Figure 2-10. Figure 2-10a shows a fine oxide layer on the surface of the alloy. Higher magnification reveals a compact and uniform oxide scale on the surface with a few submicron to microns pits. Compared to the iron-based alloys, the amount of Fe element is much lower and therefore, iron oxide is not formed on the outer oxide layer. Additionally, the amount of oxygen content is low and it can be one reason why there is no rod-like NiO oxide on the outer surface of the formed scale.

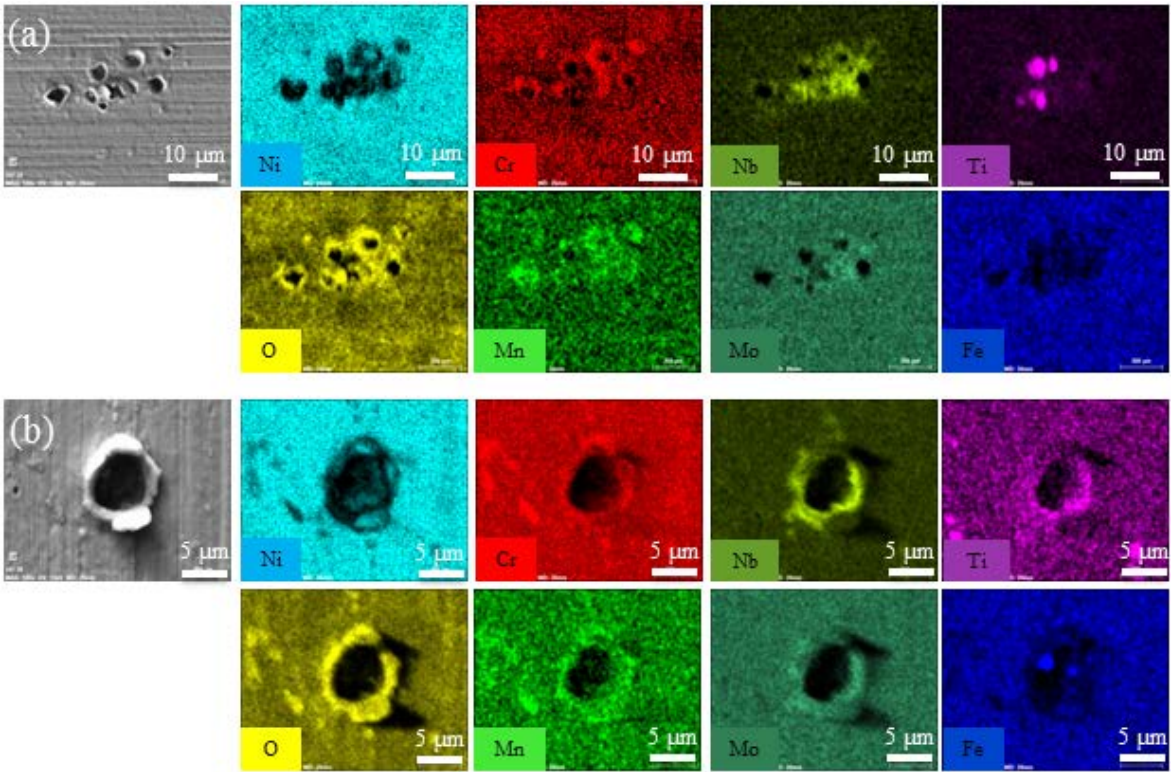

Figure 2-11: EDS elemental distribution on alloy 625 after exposure to SCW at 800 °C for 12 h.

EDS elemental mapping analysis was carried out on the pits and the results are illustrated in Figure 2-11 with two different magnifications. The pits appear to be free of nickel, iron, and

molybdenum, while the concentration of oxygen and chromium is higher around the pits. EDS results indicate that the pits were filled by niobium, titanium, and manganese, and oxygen. Thus, the pitting may be associated with Nb- and/or Ti-rich precipitates (likely γ'-phase), which can be initiated by galvanic corrosion due to compositional differences between the matrix and the γ-phase oxide.[34]

EDS elemental analysis demonstrated that the compact uniform oxide layer formed on alloy 625 contained nickel, chromium, iron, and oxygen. A reaction between Fe, NiO, and Cr_2O_3 at high temperature would likely produce a $Ni[Cr,Fe]_2O_4$ spinel oxide.[14,35,36] The $NiCr_2O_4$ spinel oxide was more probably to form at a higher temperature by solid solution reaction of NiO and Cr_2O_3. In fact, it was proposed that NiO and Cr_2O_3 both formed at the early stage of the corrosion test, and NiO then reacted with either individual Cr_2O_3 particles or later formed Cr_2O_3 oxide layer to form stable spinel oxide at high temperature operation in SCW.[14]

Alloy 625 is a typical nickel–chromium–molybdenum–iron alloy as well as a solid-solution hardenable alloy. At high temperature, a chromium-depleted zone could be formed at the metal/oxide interface and grain boundaries then become the most viable pathway to supply chromium for the growth of an inner oxide layer, subsequently leading to elevated oxide topography along the grain boundaries. Surface oxidation and pitting corrosion were reported to be the principal corrosion mechanisms of this alloy under SCW conditions.[15,-17] Many studies have demonstrated considerably higher corrosion resistance for this alloy comparing to austenitic steels. The weight changes are typically quite small even at the highest temperatures, making them difficult to measure, and leading to significant scatter in the data. Various studies have shown that the surface oxide formed by corrosion in SCW has a double layer structure consisting

of a nickel/iron-rich outer layer and a chromium-rich inner layer. A diffusion layer is also formed between the oxide layer and the base alloy, where the element compositions gradually change from that of the oxide to that of the bulk alloy concentration. Pits of varying sizes are typically observed on the sample surface,[15-17] possibly initiated at metal carbide inclusions. Pitting was found to be suppressed when the samples were exposed to relatively higher oxygen content or higher temperature SCW.

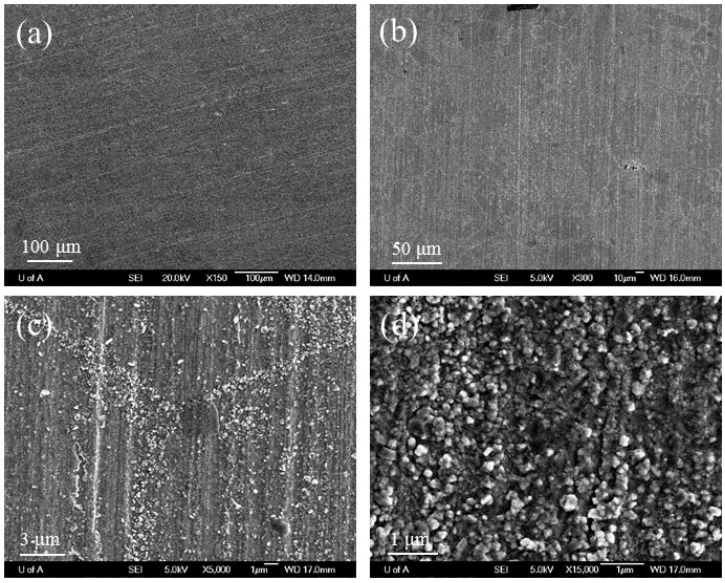

Figure 2-12: Surface morphologies of alloy 214 after exposure to SCW at 800 °C for 12 h, at different magnifications of 150x (a), 300x (b), 5000x (c), and 15000x (d) are presented.

Alloy 214

The surface morphology of alloy 214 after exposure to SCW at 800 °C for 12 h is shown in Figure 2-12. SEM images at lower magnification (Figure 2-12a and Figure 2-12b) show a uniform oxide layer on the alloy 214 surface without localized oxidation leading to the formation of large grain size oxide islands and/or pitting corrosion. SEM observations at higher magnifications (Figure 2-12c and Figure 2-12d) confirmed that a uniform compact oxide scale

had formed on alloy 214 which could increase the corrosion resistance of the surface to SCW. A thin layer of fine oxide with nanoscale/submicron grain size appears on the alloy surface.

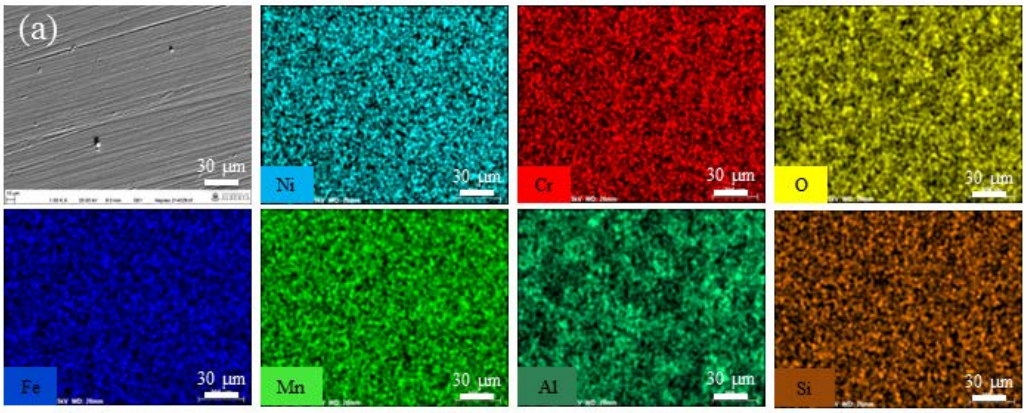

Figure 2-13: EDS elemental distribution on alloy 214 after exposure to SCW at 800 °C for 12 h.

EDS mapping analysis was conducted on the oxide layer to evaluate the chemical composition of the scale. Figure 2-13a indicates a uniform distribution of elements in the oxide scale, including Ni, Cr, O, and Al, which could be identified as NiO and $Ni(Cr, Al)_2O_4$ spinels as the outer oxide layer and Cr_2O_3 and Al_2O_3 as the inner oxide layer.[34-36] Since the oxide is compact and the metal surface is uniformly covered, it would be difficult to observe oxide scales different from those containing $Ni(Cr, Al)_2O_4$ spinels.[13]

At only 16 wt.% Cr, alloy 214 is one of the most corrosion resistive alloys available for high temperature service. Moreover, alloy 214 contains 4.4 wt.% Al and owes its oxidation resistance to a tightly adherent alumina scale. Most alloys owe their corrosion resistance to a chromia (Cr_2O_3) scale, but chromia can oxidize and evaporate in SCW.[2] For the Ni–Cr–Al alloy, various alloy constituents can be oxidized to form NiO and $Ni(Cr, Al)_2O_4$ spinels, together with Cr_2O_3 and Al_2O_3 during oxidation.[13,37,38] For alloy 214, Al and Cr have a higher affinity towards

oxygen relative to Ni and Fe, i.e. Al and Cr oxides are more thermodynamically stable than Ni and Fe oxides. This investigation demonstrated that the oxides on the surfaces of the oxidized alloy 214 are Cr_2O_3, Al_2O_3 and $NiCr_2O_4$. It is known that the driving force for the growth of oxides is the Gibbs free energy associated with the reaction between oxygen and the respective metals.[38]

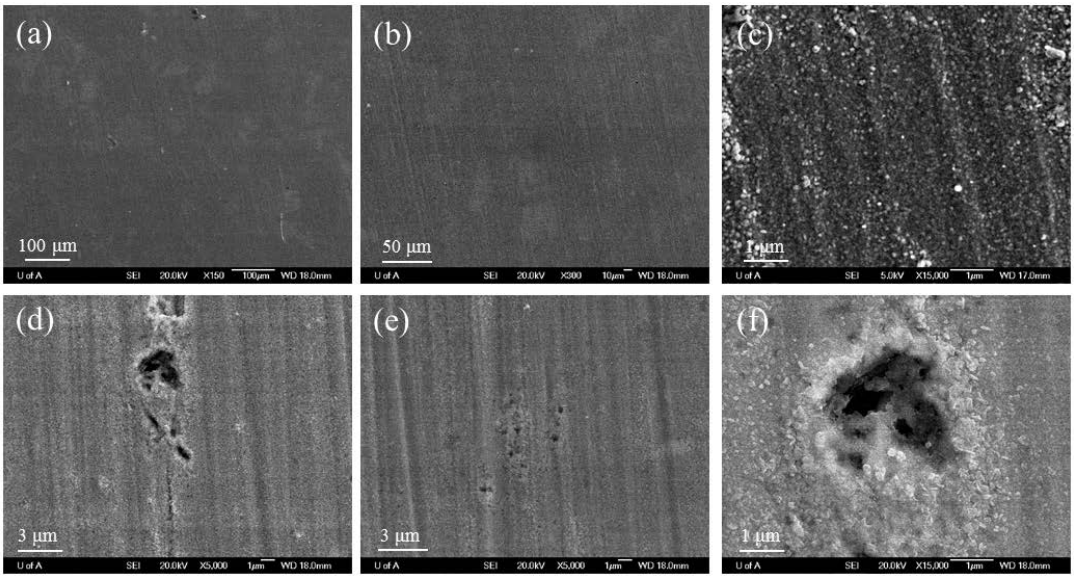

Figure 2-14: Surface morphologies of alloy C2000 after exposure to SCW at 800 °C for 12 h, at different magnifications of 150x (a), 300x (b), 15000x (c), 5000x (d), 5000x (e), and 15000x (f) are presented.

Alloy C2000

The top-view morphology of alloy C2000 after exposure to SCW at 800 °C for 12 h is shown in Figure 2-14. The metal surface appears to be covered uniformly with oxide scales (Figure 2-14a and Figure 2-14b). At high resolution, the SEM image in Figure 2-14c shows a fine, submicron grain size oxide layer on the metal surface. The oxides show a dual-layer structure, consisting of a loose outer layer of coarse polyhedral grains and a compact inner layer of tiny grains. A few defects in the form of localized pitting corrosion can be detected in higher

resolution SEM images (Figure 2-14d-f). The pits are small, in the range of 0.5 µm to 2 µm. In fact, alloy C2000 shows a proper corrosion resistance to SCW.

Figure 2-15 shows EDS analysis of alloy C2000 after exposure to SCW at 800 °C for 12 h. The main oxide layer contains Ni, Cr, and O representing a $NiCr_2O_4$ spinel structure[9] which covers the sample's surface. EDS analysis of the pits revealed that they were free of Ni and Mo; however, elements such as O and Cr were present around the pits.

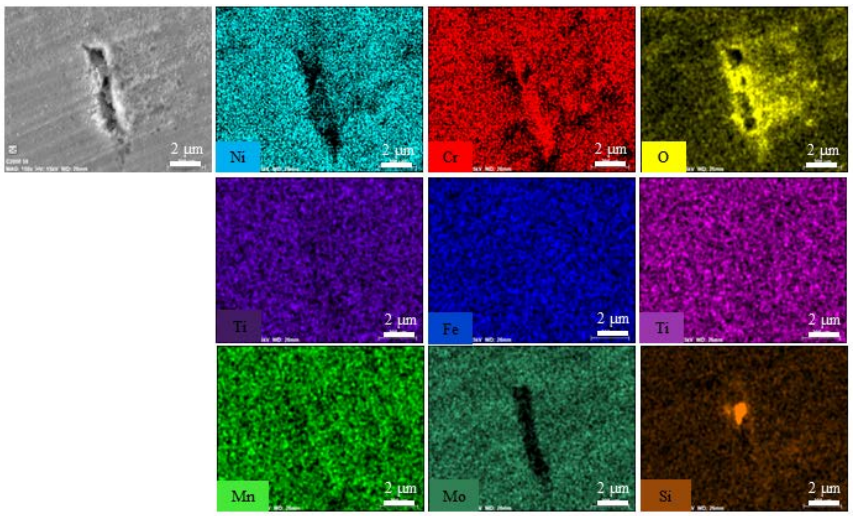

Figure 2-15: EDS elemental distribution on alloy C2000 after exposure to SCW at 800 °C for 12 h.

It was proposed that these pits could form due to silicon inclusions resulting in galvanic corrosion. As silicon oxide is not stable in SCW at 800 °C, the silicon inclusions would evaporate leaving pits on the metal surface.

Initially, Ni and Cr oxidized by reacting with dissolved oxygen in the SCW to form a mixed layer of NiO and Cr_2O_3 on the alloy C2000 exposed to the SCW at 800 °C. Simultaneously, the formation of this layer would lower the oxygen potential at oxide/metal interface, making NiO less stable. Oxidation can continue by outward cation (Ni^{2+}) diffusion to the oxide/water

interface and reaction with oxygen, and inward anion (O^{2-}) diffusion to the oxide/substrate interface and reaction with enriched Cr, resulting in an outer NiO layer. This occurs because Ni has a higher diffusivity than Cr.[8,9] As the oxidation proceeds, a part of NiO reacts with Cr_2O_3 to form $NiCr_2O_4$ spinel phase. Since Mo has a low diffusivity in the inner layer, it is retained and enriched in the inner layer. At higher oxygen content, it is probable for the Mo oxide to form. However, since the oxygen content is low in this the current experiment condition, Mo oxide was not detected in the scale.

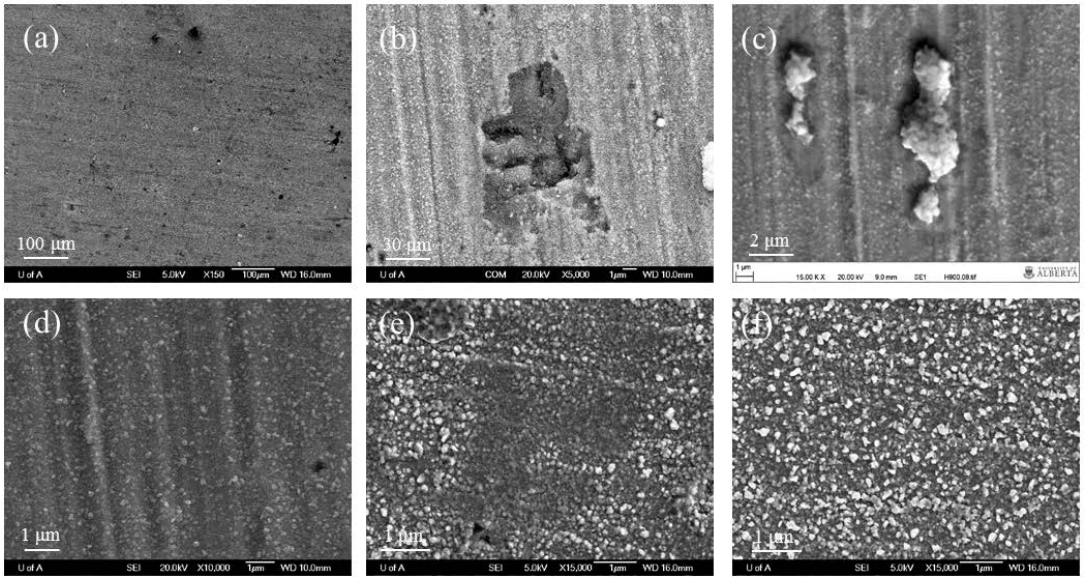

Figure 2-16: Surface morphologies of alloy 800H samples after exposure to SCW at 800 °C for 12 h, at different magnifications of 150x (b), 5000x (b), 15000x (c), 10000x (d), 15000 (e), and 15000x (f) are presented.

Alloy 800H

SEM micrographs of the outer oxide layer formed on alloy 800H after exposure to SCW at 800 °C for 12 h are presented in Figure 2-16. A low magnification SEM micrograph shows a thin oxide layer on the metal surface (Figure 2-16a). Higher magnification micrograph of different

location indicates that this layer is made of very fine crystals 150 nm - 250 nm in size. A few defects in the form of localized pitting corrosion (Figure 2-16b) and small oxide islands are apparent on the metal surface (Figure 2-16c).

These islands along with a spinel matrix are frequently observed on oxide surfaces on alloy 800H after exposure to SCW. The morphological differences indicate that these oxides might potentially have different compositions/structures.

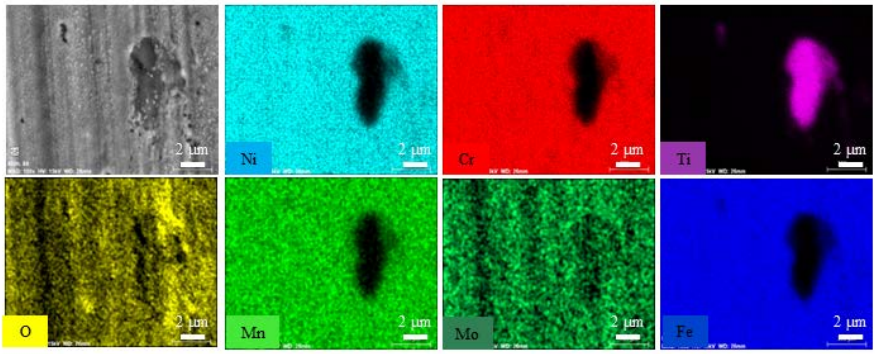

Figure 2-17: EDS elemental distribution on alloy 800H exposed to SCW at 800 °C for 12 h.

EDS mapping analysis of alloy 800H after exposure to SCW at 800 °C for 12 h is shown in Figure 2-17. The presence of Ti beneath the iron oxide island implies that titanium carbides might be involved in the formation of these islands. Figure 2-17a and Figure 2-17b illustrate the elemental distribution in the main oxide layer and in the pits and Figure 2-17c shows an oxide island formed on the oxide matrix. Elemental analysis revealed that the oxide island contained oxygen and iron, indicative of a magnetite phase presence. EDS mapping micrographs of the pits suggest that the main matrix was composed of Fe, Ni, Cr, and O elements in the form of a spinel structure. At high resolution, these spinel oxide layers had submicron sized grains. More

importantly, the EDS map results revealed that the pits were filled with Ti, indicating that titanium carbide could form during high temperature exposure to SCW.[33,39-42]

Alloy 800H is an iron-nickel-chromium alloy having the same basic composition as alloy 800 but with significantly higher creep rupture resistance. Alloy 800H contains a higher concentration of carbon (0.05 to 0.1 wt.%) which contribute to its resistance to stress rupture. Alloy 800 is normally used at temperatures up to 593 °C; above this temperature alloy 800H is used when resistance to creep and rupture is required. Other regions of the alloy 800H sample surface contain titanium carbides surrounded by chromium oxide as shown in Figure 2-17.

2.4 Phase identification by XRD

XRD patterns of the surface of alloys exposed to SCW at 800 °C were obtained. Some reflections of austenite appear in the XRD patterns because the oxide layer is thin and the incident X-ray penetrates through the oxide layers and reach to the metal substrate, the diffracted beam then contains information about both the metallic substrate and the oxide layer. Thus, based on the integrity and size of the oxide scales formed on the surface of the metal exposed to SCW, different phases can be detected in the XRD pattern.

Figure 2-18a shows a typical XRD profile from the surface of SS 347H alloy after exposure to SCW at 800 °C for 12 h. All the peaks agree that spinel oxides are the dominant phases on the metal surface and that spinel oxides are dominated by Fe_3O_4 and $FeCr_2O_4$. In addition, peaks related to gamma austenite and chromium oxide were observed in the XRD pattern representing the outer oxide layer but not uniformly covering the surface. In other words, there were

magnetite islands on the compacted Fe-Cr spinel structure. Since the spinel structure is a few μm thick, XRD patterns showed peaks for chromium oxide as well as austenite in the substrate.

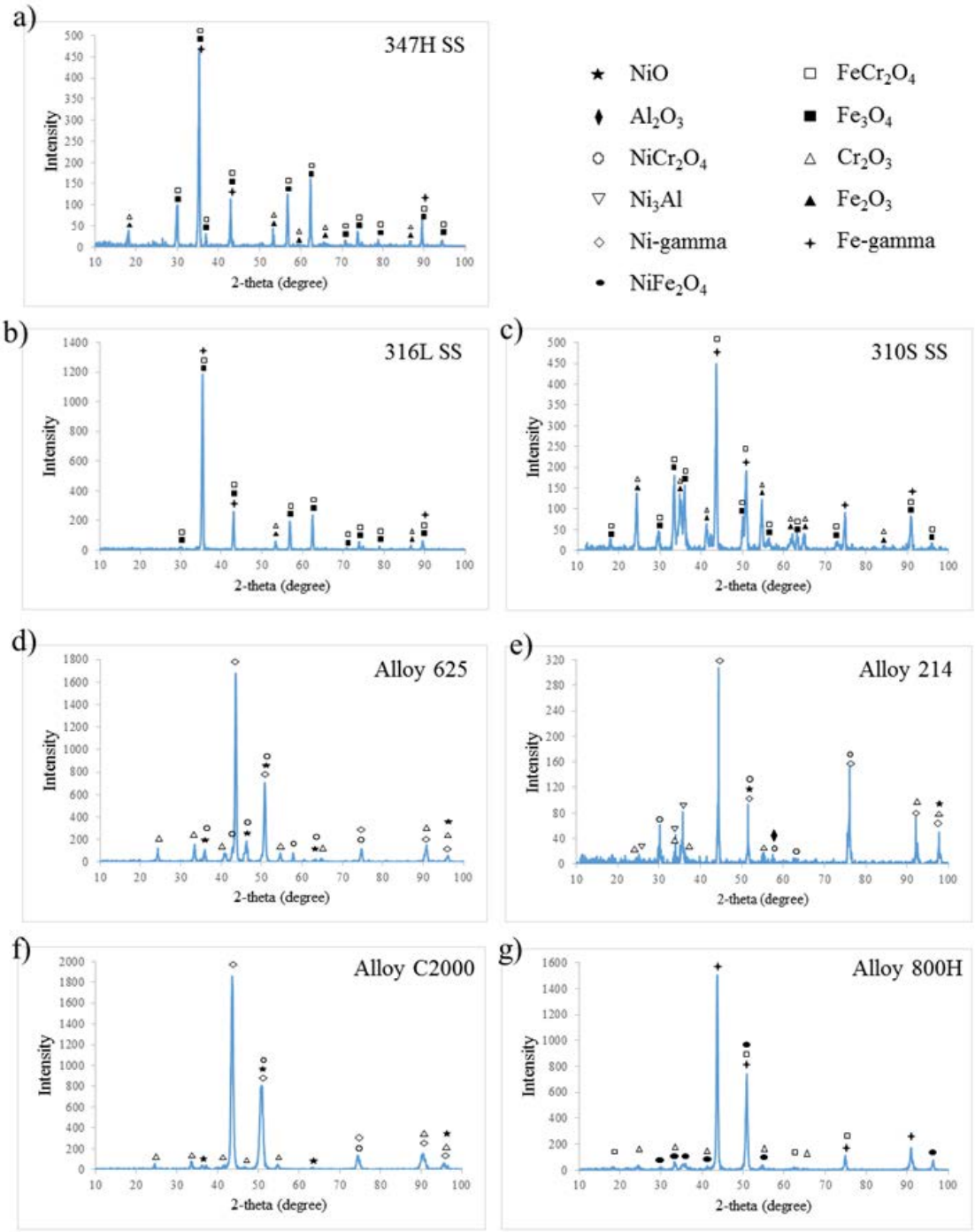

Figure 2-18: XRD patterns of the outer surface of alloys exposed to SCW at 800 °C for 12 h: (a) SS 347H, (b) SS 316L, (c) SS 310S, (d) alloy 625, (e) alloy 214, (f) alloy C2000, and (g) alloy 800H.

An XRD pattern of the SS 316L sample after exposure to SCW at 800 °C for 12 h is shown in Figure 2-18b. The XRD pattern exhibits three peaks associated with austenite, magnetite (Fe_3O_4), and spinel ($FeCr_2O_4$) phases. Since the outer oxide layer is thick and uniformly covers surface of the SS 316L sample, the probability of detecting chromium oxides was low. As there is an overlap between some reflections of chromium oxide and hematite (Fe_2O_3), hematite might be present in a negligible amount on the outer oxide layer.

Figure 2-18c is an XRD pattern of the SS 310S sample after exposure to SCW at 800 °C for 12 h. The highest peak intensity is characterized for the austenite phase which is identified as the gamma phase in the SS 310S sample. The dominant oxides in the scales are identified as a Fe-Cr spinel structure and chromium oxide.

Figure 2-18d shows the XRD pattern taken from alloy 625 after exposure to the SCW at 800 °C for 12 h. Since the amount of Ni and Cr is high compared to the stainless steel alloys, oxidation resistance is higher and consequently the oxide layer formed on the surface is thin. As the XRD results indicates, the main oxide layer on the surface of alloy 625 is nickel oxide (NiO) and nickel-chromium or a nickel-iron spinel ($Ni[Cr,Fe]_2O_4$).

Figure 2-18e demonstrates an XRD pattern of alloy 214 after exposure to SCW at 800 °C for 12 h. There are different phases formed on the exposed surface to the corrosive media, including Ni-gamma matrix, Ni-Cr spinel ($NiCr_2O_4$), and chromium oxide as the main constituents. Additionally, two weak peaks including nickel aluminide (Ni_3Al) and aluminum oxide (Al_2O_3) were detected in the XRD pattern. It is known that this alloy has 4.5 wt.% Al that participates in the formation of Ni_3Al and Al_2O_3.

Figure 2-18f presents the XRD patterns of alloy C2000 when exposed to the SCW at 800 °C for 12 h. It is noteworthy that no XRD peaks were found to indicate presence of iron oxides in the corrosion layer. Moreover, few weak peaks of Mo oxide (namely MoO_2) and a higher $NiO/NiCr_2O_4$ peak ratio were found for the sample exposed to the SCW. XRD and SEM/EDS analyses indicate that the outer Ni-rich oxide layer is mainly NiO. However, since the oxide scale is thin and Ni-Cr spinel and chromium oxide phases were detected in the XRD peaks, the inner Cr/Ni-rich oxide layer is mainly a mixture of Cr_2O_3 and $NiCr_2O_4$.

Figure 2-18g shows XRD spectra obtained from the alloy 800H exposed to the SCW at 800 °C for 12 h. It is interesting to note that no iron oxide peak was detected in the XRD pattern of alloy 800H. Three dominant phases are present in the XRD pattern of the alloy 800H exposed to the SCW, including Fe-gamma matrix, Ni-Fe spinel structure ($NiFe_2O_4$), and chromium oxide (Cr_2O_3). The formed oxide layer is composed of two layers namely the outer oxide layer of the Ni-Fe spinel structure and the inner thin oxide layer of Cr_2O_3. A very weak peak of the Fe-Cr spinel phase was detected in the XRD pattern, indicating possibility of the $FeCr_2O_4$ spinel formation at high temperature in the inner oxide layer.

The following list summarizes the findings from SEM, EDS, and XRD analyses which were used to examine the surfaces of metals subjected to SCW at 800 °C for 12 h.

(i) Oxidation of the metal samples produced an oxide layer such as iron oxide in the form of magnetite (Fe_3O_4) and nickel oxide (NiO). This oxide layer formed with a thick and uniform scale with large (few μm) crystallites or islands on the surface.

(ii) Spinel phases formed in a fine (submicron) grain sized inner oxide layer with a composition based on the chemical composition of the alloy with the general formula MCr_2O_4 (M=Fe, Ni, and Al).

(iii) A thin layer of chromium oxide (Cr_2O_3) was observed at the spinel/metal substrate interface. This layer is known as a diffusion layer because it can control outward diffusion of Fe and Ni as well as inward diffusion of O throughout the scales. The thickness of the chromium oxide varies between 50 nm and 300 nm depending on the SCW condition.

(iv) If alloying elements such as Al, Nb and Ti are present in the alloy candidate examined in the SCW, it is possible to detect other oxides in the oxide layer such as Ni_3Al, NbC, TiC, Al_2O_3 and $(Ni,Cr,Al)_3O_4$ as the spinel structure.

2.5 Conclusions

Iron-based and nickel-based alloy samples were subjected to supercritical water for 12 h at 800 °C and 25 MPa, and the samples were examined by weight measurement, SEM, EDS, and XRD. The main conclusions of the current study are:

1. Nickel-based alloys, alloy 214, alloy C2000, and alloy 625 showed lower weight loss and lower weight gain compared to iron-based alloys such as stainless steels 347H and 316L. Weight loss and weight gain results were similar for the high chromium iron-based alloys such as alloy 800H and SS 310S, indicating that the inner oxide layer could prevent/postpone outward diffusion of iron to form thick outer oxide scale. In case of nickel-based alloy, the formation of protective inner oxide layer can control formation of outer oxide layer. In fact, Cr and Ni play

important roles in the formation of protective layer on the candidate alloys exposed to the SCW at 800 °C for 12 h.

2. SEM investigations revealed that the formation of oxide layers on the alloys' surface with different morphologies and grain sizes. EDS mapping analysis conducted on the oxide layers indicated presence of various elements on the outer surface. Higher levels of Cr and Ni in the alloy indicated formation of a thin protective oxide layer as observed in the nickel-based alloys, while lower amounts of Cr and Ni resulted in formation of herpes-shaped oxide crystals as the outer oxide layer on the iron-based alloys which may not provide protection against SCW conditions. Alloys containing Mo, Nb and Ti, regardless of being nickel-based or iron-based alloys, were susceptible to pitting. EDS micrographs revealed the role of alloying elements in the pitting corrosion.

3. XRD patterns showed that the main oxide structures on the iron-based alloys were iron oxide (magnetite) as the outer oxide layer and chromium oxide (Cr_2O_3) and chromium-iron spinel as the inner oxide layer. The main oxide phases on the nickel-based alloys were nickel oxide (NiO) in the outer oxide scale and chromium oxide (Cr_2O_3) and nickel-chromium spinel in the inner oxide layer. Additionally, other phases such as Al_2O_3 and $NiFe_2O_4$ can form in the oxide films depending on the composition of the alloy.

4. Based on the oxidation and pitting observations, the following order would be suggested (the best performance to the worst):

Oxidation resistance: alloy 214 > alloy 800H > alloy 625 > C2000 > SS 310S > SS 347H > SS 316L

Pitting resistance: alloy 214 > SS 310S > SS 316L > alloy 800H > C2000 > SS 347H > alloy 625

Thus, the best alloy candidates among the austenitic stainless steels and nickel-based alloy can be SS 310S and alloy 214, respectively.

Acknowledgments

The authors gratefully acknowledge the financial support from the NSERC/NRCAN/AECL CRD program.

2.6 References

1 D. Guzonas, R. Novotny, Supercritical water-cooled reactor materials - Summary of research and open issues, Prog. Nucl. Energy. 77 (2014) 361–372.

2 D. a. Guzonas, W.G. Cook, Cycle chemistry and its effect on materials in a supercritical water-cooled reactor: A synthesis of current understanding, Corros. Sci. 65 (2012) 48–66.

3 D. Guzonas, Materials Requirements for the Canadian SCWR Concept, IAEA TM Mater. Chem. SCWRs, CNNC NPIC, (2013).

4 J. Li, W. Zheng, S. Penttilä, P. Liu, O.T. Woo, D. Guzonas, Microstructure stability of candidate stainless steels for Gen-IV SCWR fuel cladding application, J. Nucl. Mater., 454 (2014) 7–11.

5 W.K. Boyd, H.A. Pray, Corrosion of Stainless Steels In Supercritical Water, Corros., 13 (1957) 33–42.

6 R. Novotný, P. Janík, S. Penttilä, P. Hähner, J. Macák, J. Siegl, High Cr ODS steels performance under supercritical water environment, J. Supercrit. Fluids., 81 (2013) 147–156.

7 J. Perrow, W. Smeltzer, The Oxidation of an Iron-5 Per Cent Chromium Alloy in the Temperature Range 600°–850° C, J. Electrochem. Soc., 109 (1962) 1023–1026.

8 X. Zhang, D.W. Shoesmith, Influence of temperature on passive film properties on Ni–Cr–Mo Alloy C-2000, Corros. Sci., 76 (2013) 424–431.

9 Q. Zhang, R. Tang, K. Yin, X. Luo, L. Zhang, Corrosion behavior of Hastelloy C-276 in supercritical water, Corros. Sci., 51 (2009) 2092–2097.

10 T. Mohammadi, X. Huang, Effect of Al and Ti addition on performance of stainless steel 310 in supercritical water, Corros. Eng. Sci. Technol., (2014).

11 M. Nezakat, H. Akhiani, S. Penttilä, S.M. Sabet, J. Szpunar, Effect of thermo-mechanical processing on oxidation of austenitic stainless steel 316L in supercritical water, Corros. Sci. (2015).

12 N. Otsuka, Y. Shida, H. Fujikawa, Internal-external transition for the oxidation of Fe-Cr-Ni austenitic stainless steels in steam, Oxid. Met., 32 (1989) 13–45.

13 A. Chyrkin, N. Mortazavi, M. Halvarsson, D. Grüner, W.J. Quadakkers, Effect of thermal cycling on protective properties of alumina scale grown on thin Haynes 214 foil, Corros. Sci., 98 (2015) 688–698.

14 K.H. Chang, S.M. Chen, T.K. Yeh, J.J. Kai, Effect of dissolved oxygen content on the oxide structure of Alloy 625 in supercritical water environments at 700°C, Corros. Sci., 81 (2014) 21–26.

15 W.J. Quadakkers, J. Zurek, M. Hänsel, Effect of water vapor on high-temperature oxidation of FeCr alloys, JOM., 61 (2009) 44–50.

16 L. Qiu, D. Guzonas, D.G. Webb, Zirconium Dioxide Solubility in High Temperature Aqueous Solutions, J. Solution Chem., 38 (2009) 857–867.

17 S.R.J. Saunders, M. Monteiro, The oxidation behaviour of metals and alloys at high temperatures in atmospheres containing water vapour: A review, Prog. Mater. Sci., 53 (2008) 775–837.

18 J. Young, J. Zurek, L. Singheiser, W.J. Quadakkers, Temperature dependence of oxide scale formation on high-Cr ferritic steels in Ar–H_2–H_2O, Corros. Sci., 53 (2011) 2131–2141.

19 B. Alexandreanu, G. Was, Grain boundary deformation-induced intergranular stress corrosion cracking of Ni-16Cr-9Fe in 360 C water, Corros., (2003).

20 P. Ampornrat, G. Was, Oxidation of ferritic–martensitic alloys T91, HCM12A and HT-9 in supercritical water, J. Nucl. Mater., 371 (2007) 1–17.

21 P.L. Andresen, Effects of Temperature on Crack Growth Rate in Sensitized Type 304 Stainless Steel and Alloy 600, Corrosion., 49 (1993) 714–725.

22 K. Arioka, T. Yamada, T. Miyamoto, T. Terachi, Dependence of stress corrosion cracking of alloy 690 on temperature, cold work, and carbide precipitation—role of diffusion of vacancies at crack tips, Corrosion., 67 (2011) 1-18.

23 H. Asteman, J. Svensson, L. Johansson, Indication of chromium oxide hydroxide evaporation during oxidation of 304l at 873 k in the presence of 10 % water vapor, Oxid. Met. 52 (1999) 95–111.

24 H. Asteman, J. Svensson, L. Johansson, Oxidation of 310 steel in H_2O/O_2 mixtures at 600 °C: the effect of water-vapour-enhanced chromium evaporation, Corros. Sci. 44 (2002) 2635–2649.

25 N. Boukis, W. Habicht, G. Franz, E. Dinjus, Behavior of Ni-base alloy 625 in methanol-supercritical water systems, Mater. Corros. 54 (2003) 326–330.

26 X. Gao, X. Wu, Z. Zhang, H. Guan, E. Han, Characterization of oxide films grown on 316L stainless steel exposed to H2O2-containing supercritical water, J. Supercrit. Fluids., 42 (2007) 157–163.

27 M. Sun, X. Wu, Z. Zhang, E.-H. Han, Analyses of oxide films grown on Alloy 625 in oxidizing supercritical water, J. Supercrit. Fluids., 47 (2008) 309–317.

28 M. Sun, X. Wu, Z. Zhang, E.-H. Han, Oxidation of 316 stainless steel in supercritical water, Corros. Sci., 51 (2009) 1069–1072.

29 M. Sun, X. Wu, E.-H. Han, J. Rao, Microstructural characteristics of oxide scales grown on stainless steel exposed to supercritical water, Scr. Mater., 61 (2009) 996–999.

30 a. N. Hansson, L. Korcakova, J. Hald, M. Montgomery, Long term steam oxidation of TP 347H FG in power plants, Mater. High Temp., 22 (2005) 263–2670.

31 N.Q. Zhang, B.R. Li, Y. Bai, H. Xu, Oxidation of austenitic steel tp347hfg exposed to supercritical water with different dissolved oxygen concentration, Appl. Mech. Mater., 148-149 (2011) 1179–1183.

32 R. Fujisawa, M. Sakaihara, Y. Kurata, Y. Watanabe, Corrosion behaviour of nickel base alloys and 316 stainless steel in supercritical water under alkaline conditions, Corros. Eng. Sci. Technol., 40 (2005) 244–248.

33 B.S. Amirkhiz, J. Li, Y. Zeng, W. Zheng, TEM study of supercritical water corrosion in 310s and 800h alloys, Microsc. Microanal., 20 (2014) 1866–1867.

34 L. Tan, X. Ren, K. Sridharan, T.R. Allen, Corrosion behavior of Ni-base alloys for advanced high temperature water-cooled nuclear plants, Corros. Sci., 50 (2008) 3056–3062.

35 X. Ren, K. Sridharan, T.R. Allen, Corrosion behavior of alloys 625 and 718 in supercritical water, Corrosion., 63 (2007) 603–612.

36 B. Somerday, R. Bradshaw, K. Wiggans, Stress corrosion cracking of Ni-based alloys in batch supercritical water oxidation environments, Corros., (2004) 1–22.

37 G. Was, S. Teysseyre, Z. Jiao, Corrosion of austenitic alloys in supercritical water, Corrosion., 62 (2006) 989–1005.

38 Y. Wang, Y. Liu, H. Tang, W. Li, Oxidation behaviors of porous Haynes 214 alloy at high temperatures, Mater. Charact., 107 (2015) 283–292.

39 M.L. Hattali, S. Valette, F. Ropital, N. Mesrati, D. Tréheux, Interfacial behavior on Al2O3/HAYNES® 214TM joints fabricated by solid state bonding technique with Ni or Cu–Ni–Cu interlayers, J. Eur. Ceram. Soc., 32 (2012) 2253–2265.

40 B.A. Pint, K.L. More, P.F. Tortorelli, The Effect of Water Vapor on Oxidation Performance of Alloys Used in Recuperators, ORNL (2002).

41 L. Tan, T.R. Allen, Y. Yang, Corrosion behavior of alloy 800H (Fe–21Cr–32Ni) in supercritical water, Corros. Sci., 53 (2011) 703–711.

42 L. Tan, K. Sridharan, T.R. Allen, The effect of grain boundary engineering on the oxidation behavior of INCOLOY alloy 800H in supercritical water, J. Nucl. Mater., 348 (2006) 263–271.

Chapter 3: Oxidation and Cracking Susceptibility of 316L Stainless Steel in Supercritical Water

3.1 Introduction

Supercritical water (SCW) is a nonpolar solvent that can dissolve gases like oxygen to complete miscibility.[1] Water above the temperature of 374.15 °C and the pressure of 22.1 MPa will be in a supercritical state. In this state, water acts as a dense gas and exhibits properties significantly different from those of water below the critical point.[1,2] At the critical point, the specific enthalpy of water increases about 20% and water behaves as a single phase when it reaches the critical point.[1-3] A supercritical water reactor (SCWR) that uses SCW as the coolant has high thermal efficiency and a simplified single phase coolant design compared to current light water reactors.[2]

To choose an appropriate alloying system for application in SCWR, the chemical behavior of the alloy under the conditions of the application should be considered. Oxide films that grow on metal substrates upon exposing to SCW are known to affect the properties of the metal and thus the operation of the SCWR.[3] The mechanisms of processes affecting the lifetime of the candidate materials in relevant conditions must be properly identified through extensive experimental tests. Knowledge of general corrosion resistance of metals in SCW has been considered to be a basic step because it is a critical issue in itself and plays an important role in

other detrimental processes linked to joint interaction of environment and stress, such as stress corrosion cracking (SCC) or corrosion fatigue.[4]

Several investigations have been conducted to evaluate the high temperature oxidation of steel in air or oxygen.[5-9] Austenitic stainless steels (SS) have been found to have high corrosion resistance in high temperature SCW, and several researchers have studied the oxidation and SCC of austenitic alloys exposed to SCW conditions.[5-15] Different parameters in the operational conditions can affect the SCC behavior of austenitic SS including water chemistry, temperature, chemical composition, and loading.[16,17] On steel with a low amount of chromium content, a complex oxide layer composed of hematite (Fe_2O_3), magnetite (Fe_3O_4), Cr_2O_3, and $FeCr_2O_4$ spinel may form. Was et al. [18-23] proposed that the outer oxide layer is composed of non-uniform large grains of magnetite, and the inner oxide layer is a fine-grained oxide, compact and very adherent to the substrate metal. The inner oxide layer is generally nonporous, very protective, and chromium rich. Most of high temperature oxidation studies on steels are based on the assumption that oxides on low-alloy steels grow by the outward diffusion of iron, since the lattice diffusion coefficient of oxygen anions in iron oxides is very small.[15-21] The level of an SCW oxidizing environment depends on the metal species and the amount of the oxygen in the solution. Thus, the oxidation behavior of an alloy in SCW can vary significantly. Corrosion in the form of oxidation and SCC of the structural materials in an SCWR is a serious concern.[22-33]

Here, the oxidation behaviour and crack susceptibility of SS 316L capsule samples are investigated in SCW at 500 °C and 25 MPa at various exposure times. Oxide layers formed during exposure to SCW were characterized using X-ray diffraction (XRD), scanning electron microscopy (SEM), Auger electron spectroscopy (AES), and transmission electron microscopy

(TEM) equipped with energy-dispersive X-ray spectroscopy (EDS), selected area electron diffraction (SAED), high resolution TEM images with the corresponding fast Fourier transform (FFT) patterns, and electron energy loss spectroscopy (EELS). Analyses of the formation of oxide layers on SS 316L are presented here and possible oxidation mechanisms are provided and discussed in chapter 4.

3.2 Material and Methods

3.2.1 Materials

316L stainless steel (UNS 31603) tubes with an outer diameter of 9.525 mm and a wall thickness of 1.65 mm were purchased from Swagelok, The tubes were manufactured according to the specification defined in ASTM-A213 for stainless steels and were supplied in a solution annealed state. Table 3-1 lists chemical composition in weight percent (wt.%) of the alloy employed in this research.

Table 3-1: Chemical elemental analysis of the alloy.

Alloy	**Chemical Composition (wt.%)**								
316L Stainless Steel	Fe	C	Cr	Ni	P	Si	Mo	Mn	S
	Balance	0.029	17.2	11.7	0.022	0.84	2.14	1.97	0.027

Tube samples were cut into 10 cm long sections to make capsule specimens for SCW exposure. In order to degrease the tube sections, they were washed with pentane, isopropyl alcohol, and acetone in an ultrasonic bath before being filled with neutral pH deionized water

(DI) containing 8 ppm dissolved oxygen (DO). The two high pressure caps were used to make static capsules from tube sections. The static capsules were placed in a tubular furnace and heated to 500 °C. The temperature of the furnace was calibrated using Nextel ceramic insulated lead wire rated to 815 °C (Omega) as the reference thermocouple. The pressure of the water inside the tube depends on its volume and storage temperature. According to the NIST steam chart,[34] the pressure of a tube filled to 9.5% volume with DI water is 25 MPa at 500 °C. Stress on the tube wall due to internal pressure was calculated. Separate static capsules were heated to 500 °C for pressure calibration and monitoring.

3.2.2 Characterizations

After SCW exposure, the tubes were cut into smaller segments. The inner surfaces of the tubes were plated with a thin layer of Ni coating to avoid spallation of the oxide film during sample preparation. Samples were mounted with epoxy resin and polished down to 0.5 μm in alumina solution before metallurgical examination. Surface morphologies of the oxide layers on the inner wall of the tubes were examined with a scanning electron microscope (ZEISS EVO-MA15) equipped with an energy dispersive x-ray spectroscope (EDS) with secondary electron (SE) detector. Cross-section morphologies were captured with backscattered electrons. A Bruker AXS diffractometer (Bruker Discover 8) detector operating with Cu-K_α radiation with a wavelength of 1.5405 Å at 40 kV and 40 mA in the 2-theta range 20°–80° at a scan rate of 0.05° per second was used for X-ray diffraction (XRD) analysis. Samples were prepared for transmission electron microscopy (TEM) using the focused-ion-beam (FIB) lift-out technique. Electron transparent samples were prepared using an ion beam voltage of 40 keV with the

current dropping from 7 nA to 35 pA. The TEM study was done using an FEI Tecnai Osiris Transmission Electron Microscope equipped with an X-FEG gun at 200 keV. EELS/EDS line profile measurements were performed on at least 100 points per line profile. Spectra at 0.3 eV/channel (1340 channels) were obtained in the range of 500 to 900 eV. This range covers O, Cr, Fe, Mn, and Ni edges. After recording spectra, in order to get profiles for each element as a function of distance, the background was first subtracted in the EELS spectra and profiles were extracted from spectra by placing an energy window of appropriate size over the element's edge. EELS spectra from a few points throughout the line profile represent the overall features of each series. Identification of phases was performed by selected area electron diffraction (SAED) and EELS spectra with the help of the Gatan Microscopy Suite® software (GMS), version 3.11 package.

Scanning transmission electron microscopy (STEM) imaging using high-angle annular-dark-field (HAADF) contrast and EDS mapping was utilized for characterization of the cross-section samples exposed to SCW. To characterize the oxidized region and identify phases, conventional bright field/dark field imaging and electron diffraction techniques were applied.

In samples exposed to SCW at 500 ^{o}C for 20000 h at 25 MPa, Auger electron spectroscopy (AES) was utilized to attain element mappings in a formed crack. AES measurements were performed using a JAMP-9500F Auger microprobe (JEOL) with a single-pass cylindrical mirror analyzer manufactured by Perkin-Elmer: Physical Electronics Division. The instrument is equipped with a Shottky field emitter that produces an electron probe diameter of about 3 to 8 nm at the sample. Accelerating voltage and emission currents for SEM and Auger imaging were 15 kV and 8 nA, respectively. The working distance was 24 mm. The sample was rotated 30

degrees away from the primary electron beam to face the electron energy analyzer. One M5 lens with 0.6% energy resolution was used for Auger spectroscopy and imaging. Auger peaks of Si KLL (1600 eV), Ag MNN (350 eV), and Au MNN (2015 eV) were selected for the mapping. Auger peaks of Si KLL (1600 eV), Ag MNN (350 eV), and Au MNN (2015 eV) were selected for the mapping. The intensity of each pixel in the Auger image was calculated by (P–B)/B, where P and B are the peak and background intensities, respectively. The intensity definition helps to reduce the edge effect of islands and dots. An auto probe tracking technique was used to compensate for possible drifting of the image during the analysis as a result of power instabilities. Phase stability of the Ni-Fe-Cr-O_2 system was considered for SS 316L in the SCW at 500 ^{o}C and 25 MPa using FactSage 6.1 software from Thermfact Ltd. and GTT Technology.

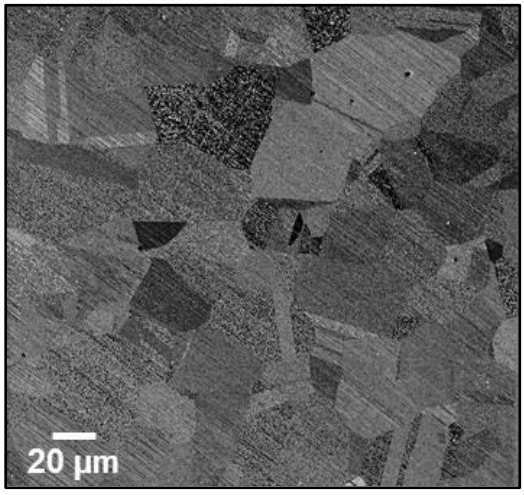

Figure 3-1: SEM micrograph of the used alloy SS 316L tube sample.

3.3 Results

3.3.1 Microstructure of the As-Received Material

Figure 3-1 shows the scanning ion micrograph of the SS 316L alloy. It shows an annealed microstructure which has equiaxed grains. Pattern in the micrograph illustrates that cold drawing and annealing can produce considerable amount of twining microstructural features.

3.3.2 Morphological Investigations and Cross-Sectional Elemental Analyses on the Formed Oxide Layers

Figure 3-2a-d show SEM micrographs of the ID surface of SS 316L tube samples exposed to SCW at 500 ^{o}C and 25 MPa for 500 h, 5000 h, 10000 h, and 20000 h. The oxide layers formed on the inner surface of the tubes at different SCW exposure times show scales consisting of crystallite particles at various densities and crystallite sizes. After 500 h of SCW exposure, the ID surface of a SS 316L tube sample was covered with fairly small crystallites while oxide crystallite size was significantly larger after 5000 h SCW exposure. The crystallite grain size was about 2 μm for a sample exposed to SCW for 500 h. polyhedral shape grains were distributed uniformly on the inner surface. At an exposure time of 5000 h, the crystallite grain size was measured 9 μm, indicating that coarsening of the oxide grains on the outer surface of the scale occurred with SCW exposure time. After 10000 h of SCW exposure, the crystallite grain size was measured approximately 12 μm. This suggests that grain growth between 5000 h and 10000 h (3 μm) was slower than grain growth between 500 h and 5000 h (7 μm) which could be due to diffusion through the oxide layer. Morphological investigations of samples exposed to SCW for

20000 h indicated that although the grains were polyhedral shape, they were inclined to be flat. After 20000 h of SCW exposure, the crystallite grain size was about 14 μm, consequently the oxide layer was much rougher at 20000 h than at 500 h SCW exposure.

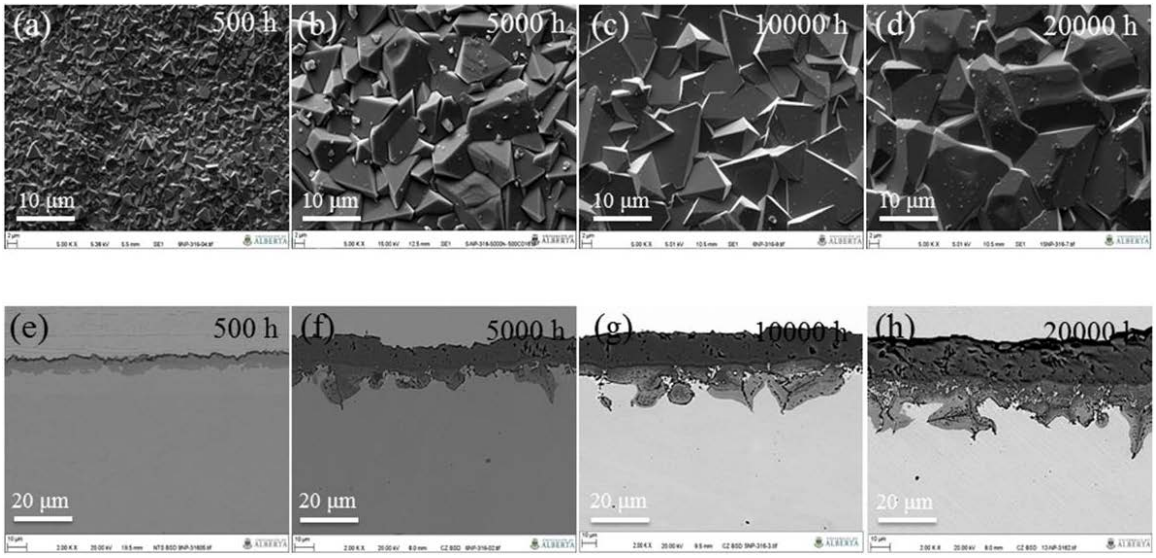

Figure 3-2: (a-d) Outer surface and (e-h) cross-sectional images of the SS 316L tubes exposed to the SCW after various exposure times.

Figure 3-2e-h illustrate cross-sectional images of tube samples taken from SS 316L capsules exposed to SCW at 500 ^{o}C and 25 MPa for different exposure times. After 500 h of SCW exposure, a thin layer of oxide with an average thickness of 7 μm had formed on the surface of the sample tubes (Figure 3-2e). In general, the oxide layer formed on the SS 316L alloy was fairly uniform and covered the original bulk alloy (Figure 3-2e). Some localized discontinuity in the oxide layer existed in the early stages of corrosion, however, this discontinuity was not observed in the alloy after 500 h of SCW exposure. Increasing the SCW exposure did not change the stability of the oxide layer significantly, but the oxide grain size increased after 5000 h SCW exposure (Figure 3-2f). These observations were consistent with the surface morphology in

Figure 3-2a, i.e. an even oxidation occurred on the alloy surface which induced formation of a uniform thin oxide layer on the ID surface of the tube sample which grew to an average thickness of 17 µm. When the exposure time was increased to 10000 h, the thickness of the scales increased on the both inner and outer oxide layers.

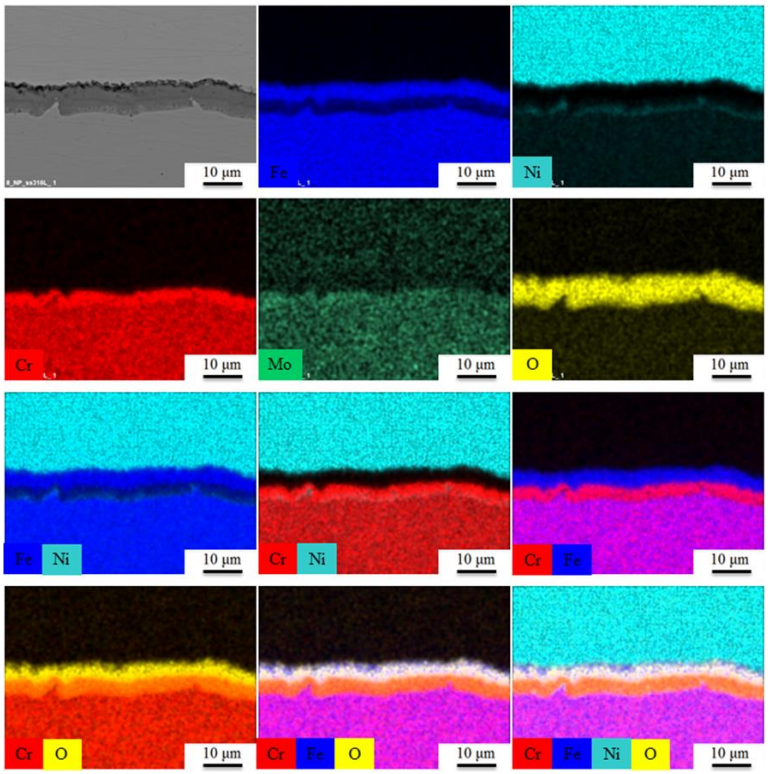

Figure 3-3: EDS elemental distribution taken from cross-section of the oxide layer formed on the SS 316L after exposure to the SCW for 500 h of the exposure time.

The outer oxide layer shows a porous continuous morphology after 10000 h of SCW exposure. When SCW exposure time was increased from 5000 h to 10000 h, the average thickness of the two oxide layers increased from 17 µm to 24 µm (Figure 3-2g). To investigate the long term performance of the alloy, SS 316L capsules were exposed to SCW for 20000 h. Cross-sectional SEM observations indicated that the average thickness of the oxide layer increased to 36 µm after 20000 h SCW exposure. A few microcracks were detected on the inner

oxide layer, possibly due to oxidation and increased stress intensity on the inner surface of the capsule during SCW exposure. Preferential oxidation at the grain boundaries can create active sites for microcracks formation. Cross-sectional observations indicated that there were two oxide layers, a porous outer scale and a fairly dense inner oxide layer containing microcracks. A few bright spots were observed in the upper inner oxide layer, indicating a possible segregation of noble alloying elements.

To study elemental composition and distribution in the oxide layer at the austenite/oxide phase boundaries and in the bulk region close to austenitic grain boundaries, EDS elemental analyses were performed on tube samples taken from capsules exposed to SCW at 500 ^{o}C and 25 MPa for different exposure times. Figure 3-3 shows the elemental distribution in the internal oxidation layer for the SS 316L alloy after SCW exposure for 500 h at 500 ^{o}C and 25 MPa. It was apparent that the oxide formed as a dual-layer structure. As shown in the individual and overlay maps, the outer layer was mainly composed of iron and oxygen which could represent magnetite and the inner layer was Fe-Cr spinel, indicating that the inner oxide layer comprised lower oxygen and iron and higher chromium relative to the outer oxide layer. It was difficult to observe the inner oxide layer since it was thin at areas adjacent to surface.

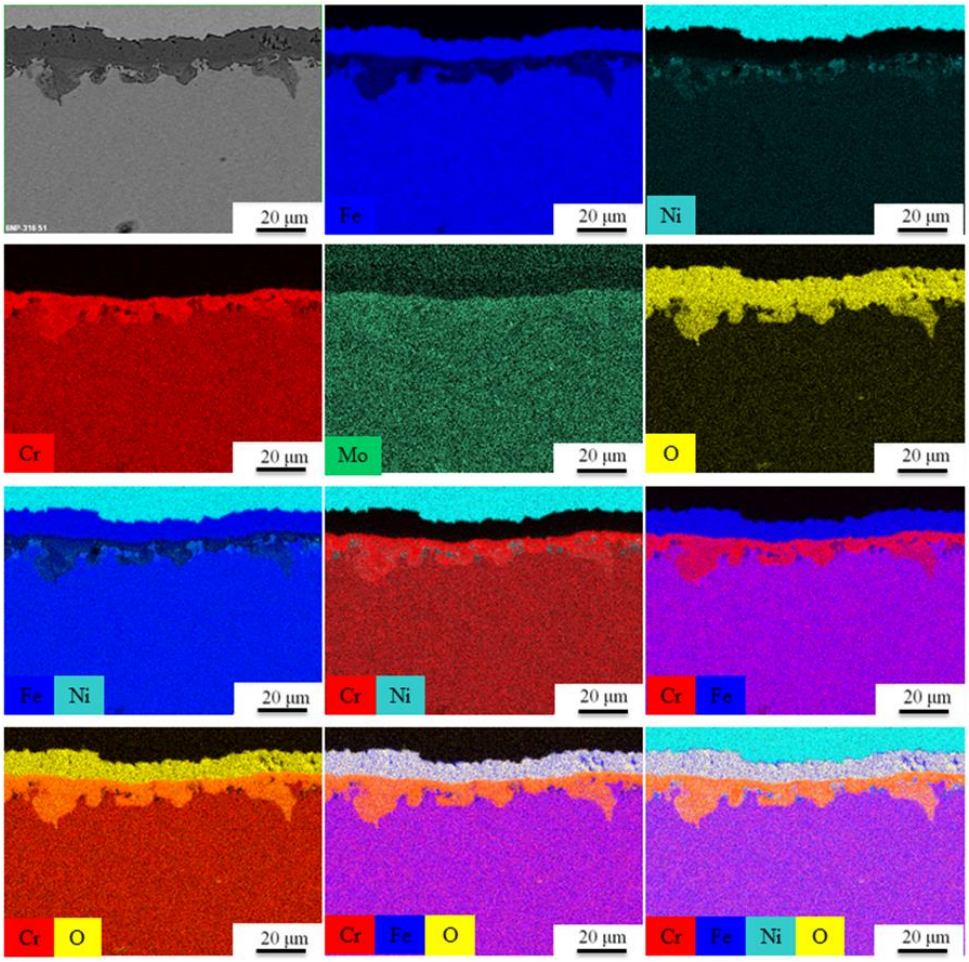

Figure 3-4: EDS elemental distribution taken from cross-section of the oxide layer formed on the SS 316L after exposure to the SCW for 5000 h of the exposure time.

Figure 3-4 depicts elemental maps of a tube sample from a SS 316L capsule exposed to SCW for 5000 h at 500 ^{o}C and 25 MPa. The thickness of the oxide layer varied between 500 h and 5000 h SCW exposure but the structure and composition of the two oxide layers were similar, consistent with Was et al.[35] findings; Fe_3O_4 + spinel/Cr_2O_3/SS 316L from the outer to inner layer. Furthermore, few micro-cracks were appeared in the inner oxide layer/SS 316L tube sample. In the other words, oxidation occurred within grains and micro-cracks initiated from the grain boundaries of the oxidized grains, for the sake of high energy of grain boundaries.

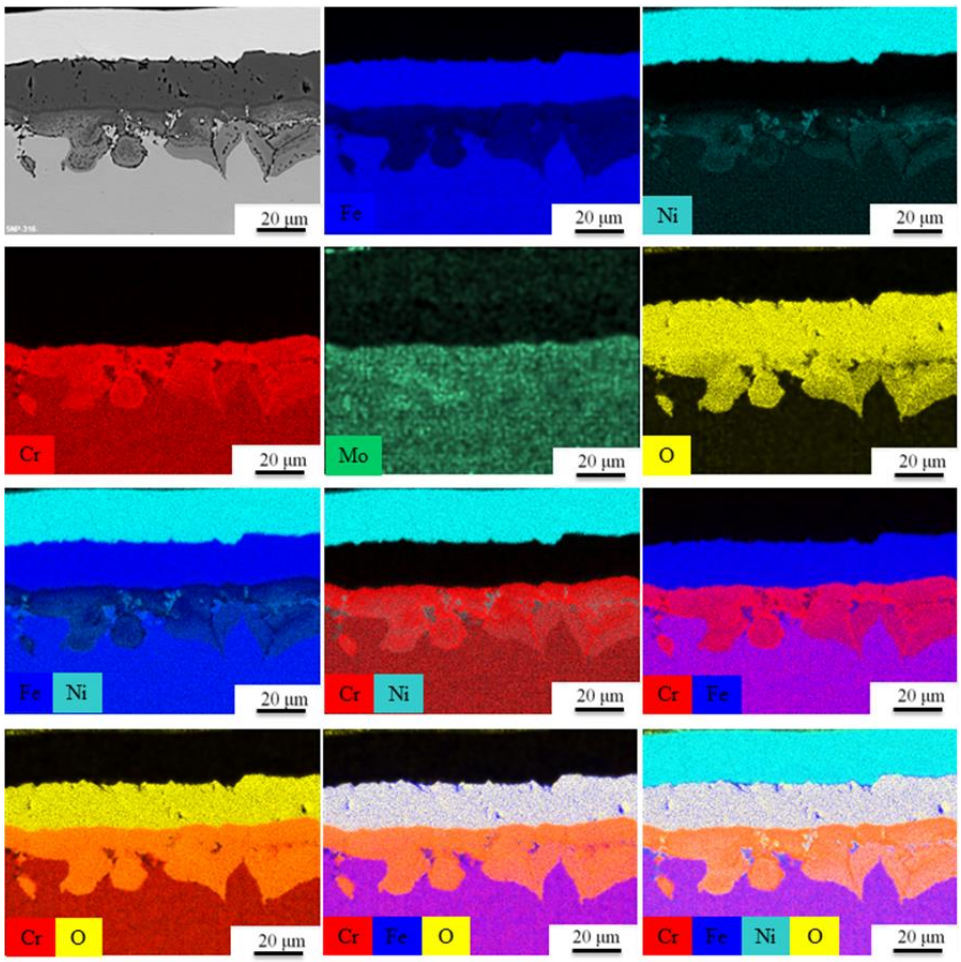

Figure 3-5: EDS elemental distribution taken from cross-section of the oxide layer formed on the SS 316L after exposure to the SCW for 10000 h of the exposure time.

Figure 3-5 shows the elemental composition in a tube sample taken from a capsule exposed to SCW for 10000 h at 500 ^{o}C and 25 MPa. It was evident that the thickness of the outer oxide layer had increased compared to that in samples from shorter SCW exposures. Additionally, some cracks were observed to have formed along the phase boundary of magnetite and spinel. Localized variations in thickness were apparent in the oxide layers, in particular the oxide layers

were thinner in the vicinity of austenitic grain boundaries. In case of the long-time exposure to the SCW, Ni was enriched at the oxide/metal interface.

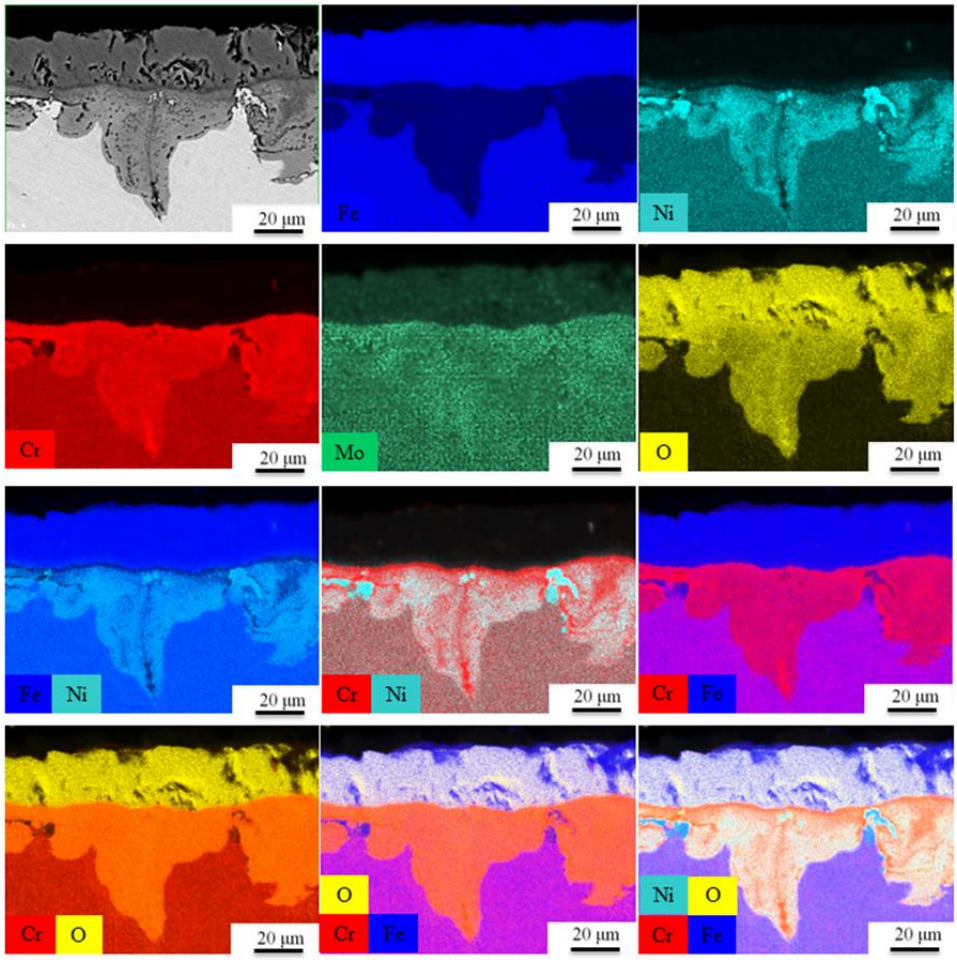

Figure 3-6: EDS elemental distribution taken from cross-section of the oxide layer formed on the SS 316L after exposure to the SCW for 20000 h of the exposure time.

Figure 3-6 shows EDS elemental analysis results for the tube sample taken from a capsule exposed to SCW for 20000 h at 500 ^{o}C and 25 MPa. The outer oxide layer was porous with higher pore density relative to that of previous samples exposed for shorter times. Similar to what was observed in tube samples from capsules exposed to SCW for 10000 h, Ni elemental

segregation was observed in the inner oxide layer close to inner/outer oxide layer interface. However, the inner oxide layer was thicker for samples with 10000 h SCW exposure time. As expected, microcracks were aligned perpendicular to the direction of circumferential stress. EDS elemental mapping of chromium and nickel indicated that most of the cracks were chromium enriched and nickel depleted.

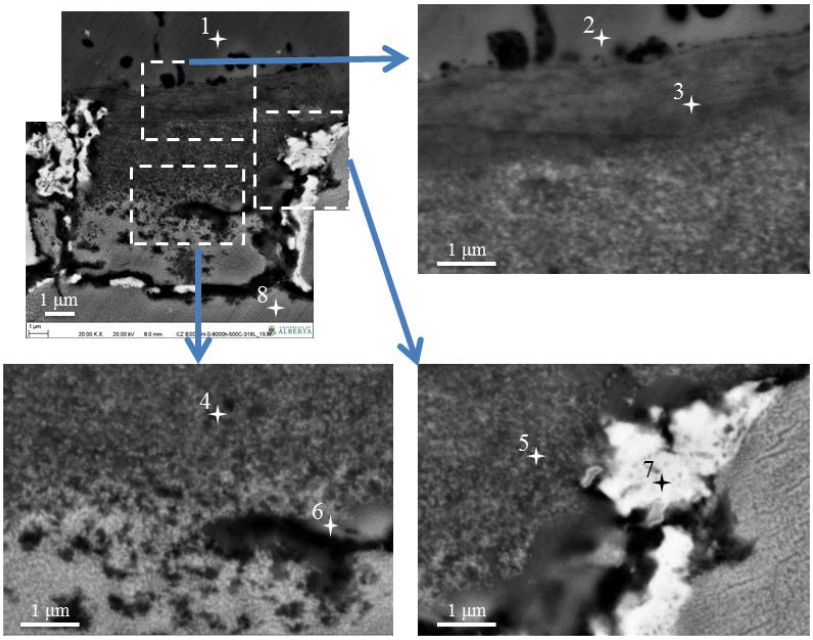

Figure 3-7: SEM images with the corresponding point EDS elemental analyses taken from the tube sample exposed to the SCW for 20000 h.

Figure 3-7 displays SEM images with corresponding EDS elemental analyses points on a tube sample taken from a capsule exposed to SCW for 20000 h at 500 ^{o}C and 25 MPa. A summary of EDS elemental analysis values is given in Table 3-2. Points 1 and 2 were located at the outer oxide layer which was known to be magnetite which was supported by the EDS analysis. Points 3, 4, 5, and 6 indicate a mixture of Fe, Cr, O, and Ni elements. These points were

located in the inner oxide layer area and suggest presence of a Fe-Cr spinel ($FeCr_2O_4$) phase. The presence of Ni showed that Ni segregation could take place in those regions. Point 7 was taken from the white area located on the inner oxide layer at the SS 316L interface. As the EDS analysis demonstrated, Ni was enriched at the oxide/metal interface. Point 8 is the point for EDS elemental analysis taken from the base metal SS 316L (see Table 3-2).

Table 3-2: EDS Chemical concentration of areas on the oxide layer of the tube sample exposed to the SCW for 20000 h.

Spectrum #	O	Cr	Fe	Ni	Mn	Mo
1	21.31	0.29	75.47	0.20	0.64	0
2	21.72	1.04	72.74	1.99	0.51	0
3	18.06	26.75	35.08	9.73	1.63	3.08
4	14.84	22.59	32.00	18.77	2.17	2.67
5	13.75	22.15	32.98	20.50	1.99	2.49
6	11.97	20.79	40.58	14.75	1.97	2.12
7	0.41	4.22	53.40	35.75	0.34	0.58
8	0.33	15.19	64.25	11.03	1.33	1.46

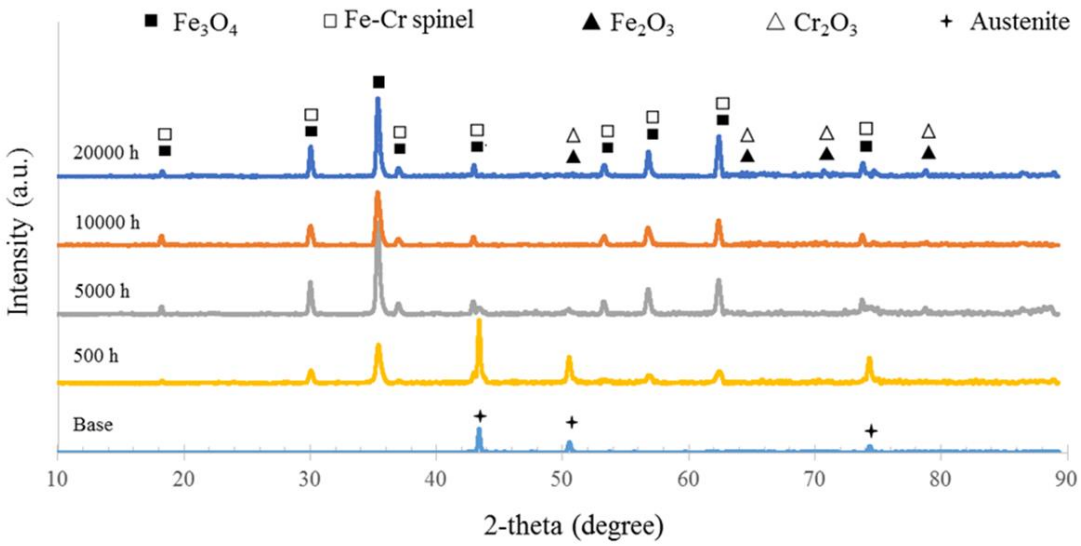

Figure 3-8: XRD patterns taken from the oxide layer formed on surface the SS 316L tube sample exposed to the SCW for various exposure times.

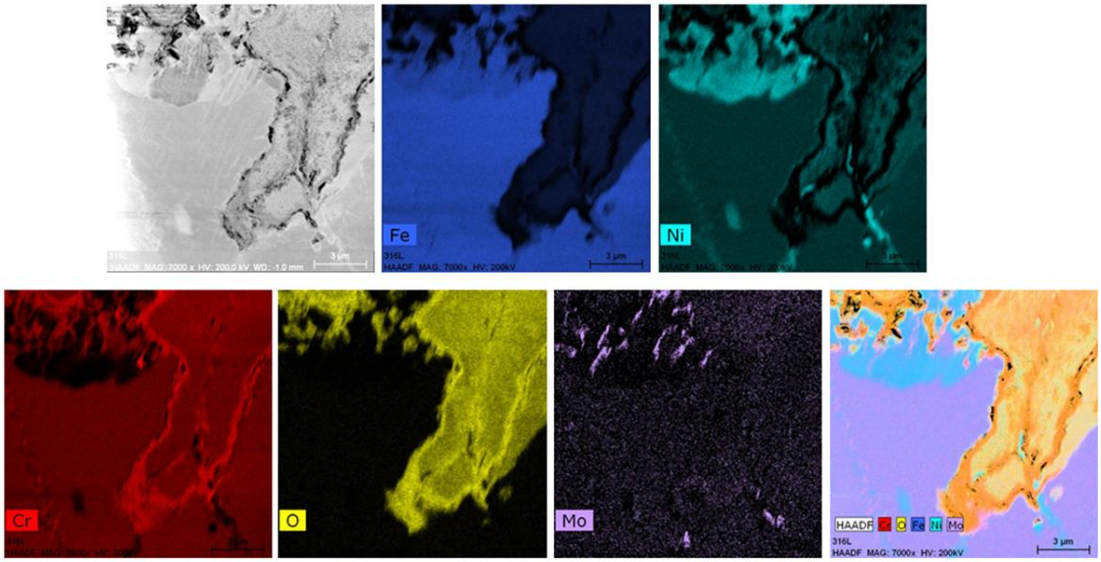

Figure 3-9: STEM-HAADF image with EDS elemental mapping of Cr, O, Fe, Ni, and Mo taken from the inner layer of the formed oxide inside the capsule after 20000 h exposure to SCW at 500 °C and 25 MPa.

3.3.3 X-Ray Diffraction Patterns

Figure 3-8 illustrates XRD patterns for tube samples taken from SS 316L capsules exposed to SCW at 500 ^{o}C and 25 MPa for different exposure times. Peaks of FCC austenite, magnetite (Fe_3O_4), spinel ($FeCr_2O_4$), and hematite/chromium oxide (Fe_2O_3/Cr_2O_3) were observed in the XRD spectra. The XRD pattern of the pristine sample indicated that austenite was the main phase in the SS 316L. An oxide layer that formed on the ID surface of tube samples during 500 h exposure to SCW at 500 ^{o}C and 25 MPa was mainly composed of Fe_3O_4 with smaller quantities of Fe_2O_3/Cr_2O_3. Similar phases were still present when the exposure time was increased to 5000 h. The intensity of magnetite reflection increased while the intensity of austenite phase decreased. XRD patterns of SS 316L tube samples taken from capsules exposed to SCW for 5000 h at 500 ^{o}C and 25 MPa indicated that coarse Fe_3O_4 crystallites formed on the tube surface. Chromium oxide and hematite on the ID surface of the SS 316L tube samples were not detected

in significant quantities by XRD after longer exposure times. As the SCW exposure time was increased to 20000 h, the same compounds were observed in all samples, with magnetite being the primary phase.

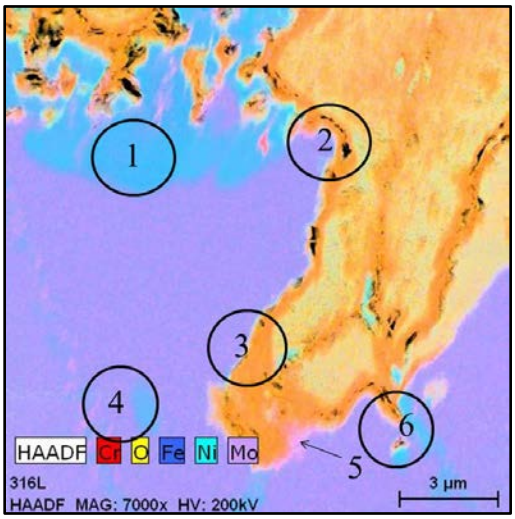

Figure 3-10: TEM image with corresponding point for the SAED pattern analysis.

3.3.4 Transmission Electron Microscopy Observations (TEM) and EELS Analyses

Figure 3-9 shows an STEM-HAADF image with an EDS overlay and a separate elemental maps for Fe, Ni, Cr, O, and Mo in the inner oxide layer that formed inside SS 316L capsules after 20000 h exposure to SCW at 500 ^{o}C and 25 MPa. Elemental maps indicated that chromium enrichment took place at the frontier of the oxide layer and that Ni and Mo were segregated at the tip and upper part of the inner oxide layer, respectively.

TEM analysis was conducted on the highlighted points shown in Figure 3-10. Figure 3-11 show bright and dark filed TEM micrographs as well as corresponding selected area electron diffraction (SAED) pattern of a point 1 of Figure 3-10. Figure 3-11b presents dark field

micrograph obtained from the 111 reflection of Ni. The SAED pattern in Figure 3-11c indicates that segregation of Ni took place in the inner oxide/metal substrate interface.

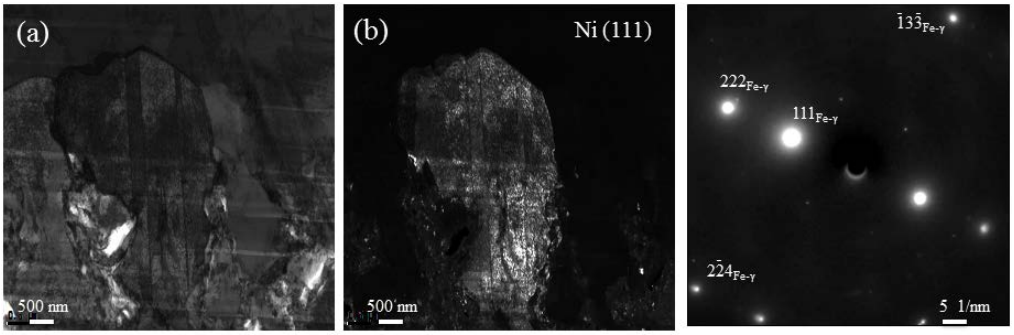

Figure 3-11: TEM micrographs of point 1 of Figure 3-10; (a) Bright field micrograph, (b) dark filed image obtained using g = 111_{Ni} reflection, and (c) corresponding indexed SAED pattern of the grain oriented near the -312 zone axis.

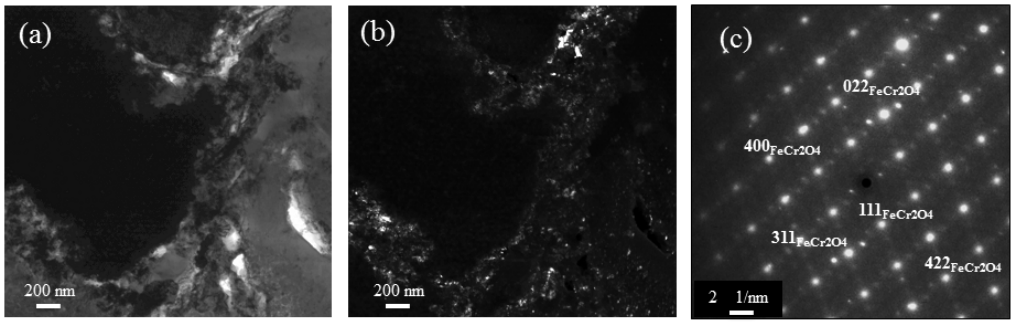

Figure 3-12: TEM micrographs of point 2 of Figure 3-10; (a) Bright field micrograph, (b) dark filed image obtained using g = 220_{Fe-Cr} reflection, and (c) corresponding indexed SAED pattern of a grain in the inner oxide layer oriented near the 1-10 zone axis.

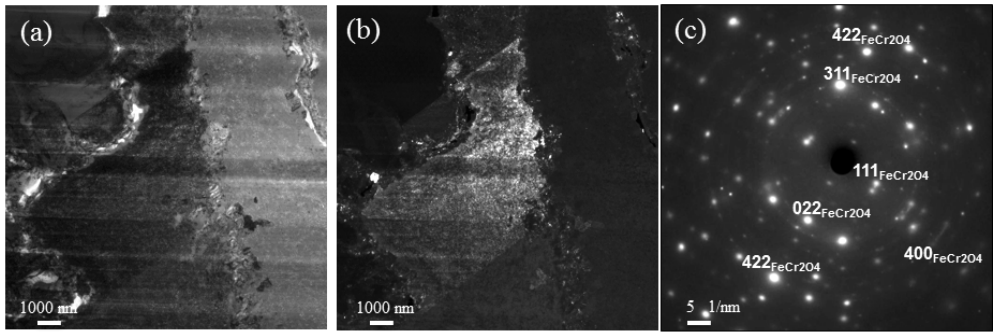

Figure 3-13: TEM micrographs of point 3 of Figure 3-10; (a) Bright field micrograph, (b) dark filed image obtained using g = $400_{FeCr2O4}$ reflection, and (c) corresponding SAED pattern of a grain in the inner oxide layer adjacent to the metal substrate oriented near the 2-11 zone axis.

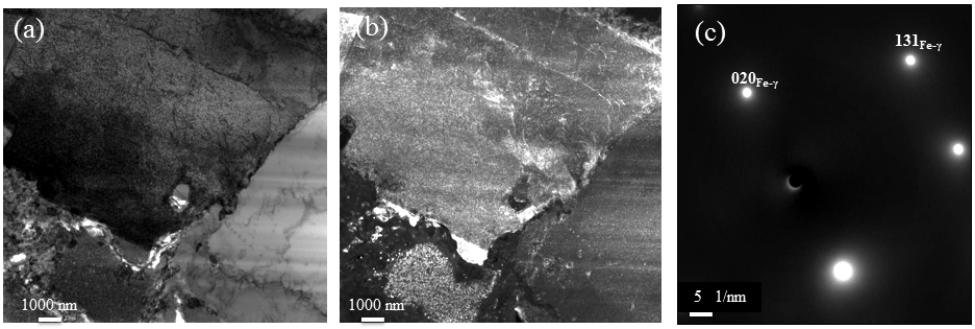

Figure 3-14: TEM micrographs of point 4 of Figure 3-10; (a) Bright field micrograph, (b) dark filed image obtained using g = $020_{Fe\text{-}\gamma}$ reflection, and (c) corresponding SAED pattern of a grain oriented near the -103 zone axis.

Figure 3-12a shows a bright field TEM micrograph from point 2 and Figure 3-12b depicts a dark field image using the 220 reflection of Fe-Cr spinel. The corresponding SAED pattern is shown in Figure 3-12c along 1-10 zone axis from inner oxide layer in a SS 316L tube sample. Figure 3-13a demonstrated bright field TEM micrograph taken from point 3 of Figure 3-10 and Figure 3-13b shows a dark field image obtained using the 044 reflection of $FeCr_2O_4$. Figure 3-13c is a SAED pattern of the inner oxide layer adjacent to the metal substrate. This pattern was identified as Fe-Cr spinel, namely the $FeCr_2O_4$. Figure 3-14a shows a bright field TEM micrograph taken at point 4 and Figure 3-14b illustrated the dark filed image using the 0-20 reflection. Figure 3-14c is a SAED pattern of the Fe-gamma phase along zone axis of -103. Figure 3-15a shows a bright field TEM micrograph taken from point 5. As shown in Figure 3-9, the area around point 5 was enriched with chromium, oxygen, and iron. The SAED results presented in Figure 3-15b show that the inner oxide layer was composed of Fe-Cr spinel, which was the predominant phase, and that Cr_2O_3 oxide was present as a thin layer at the interface of the $FeCr_2O_4$/SS 316L substrate, consistent with findings of [36].

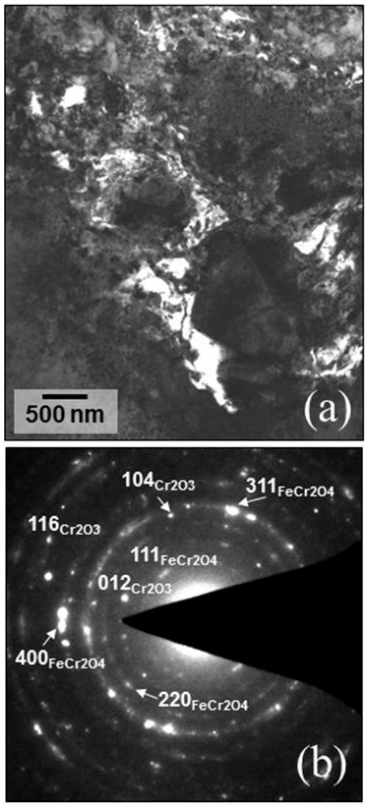

Figure 3-15: (a) Bright field TEM micrograph taken from the point 5, (b) corresponding SAED pattern, the inner oxide layer was made of Fe-Cr spinel which was the dominant phase and Cr_2O_3 was present as a thin layer at the interface of $FeCr_2O_4$/SS 316L substrate.

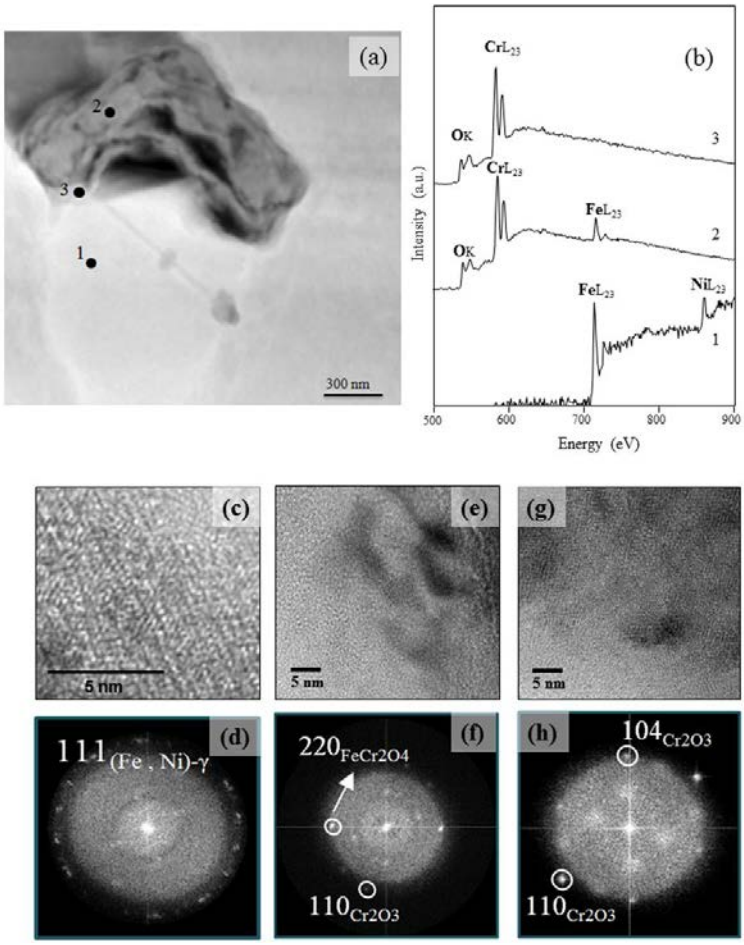

Figure 3-16: (a) Bright field TEM micrograph taken from the micro-crack tip in the sample exposed to the SCW for 20000 h, (b) EELS spectra results of the points 1, 2, and 3 of the image presented in panel (a), and HRTEM images with corresponding FFT patterns taken from (c,d) point 1, (e,f) point 2, and (g,h) point 3 of panel (a).

Figure 3-16a is a bright field TEM image of a crack initiated in the SS 316L capsule exposed to SCW for 20000 h at 500 ^{o}C and 25 MPa. EELS edge energies for Fe, Cr, O, Ni, and Mn can be summarized as follows: edges at 525 - 570 eV, 575 - 605 eV, 700 - 725 eV, 835 - 870 eV, and 620 - 655 eV energy loss range correspond to oxygen, chromium, iron, nickel, and manganese, respectively.[36] EELS results for three points are shown in Figure 3-16b. Point 1 contains Fe and Ni edges with characteristics corresponding to the SS 316L tube sample and Ni

segregation. The spectrum at point 2 contains O, Cr, and Fe, indicating that this point represents a $FeCr_2O_4$ phase. Point 3 contains chromium and oxygen which can be correlated with a chromium oxide phase.

FFT patterns of high resolution TEM (HRTEM) images of these three points are displayed in Figure 3-16c-h. The FFT pattern of point 1 is shown in Figure 3-16c-d. The spotted discontinuous ring in FFT pattern of region 1 can be attributed to the gamma phase of the Fe/Ni at the crack tip. The HRTEM illustrated in Figure 3-16e displayed a mixture of Fe-Cr spinel and chromium oxide.

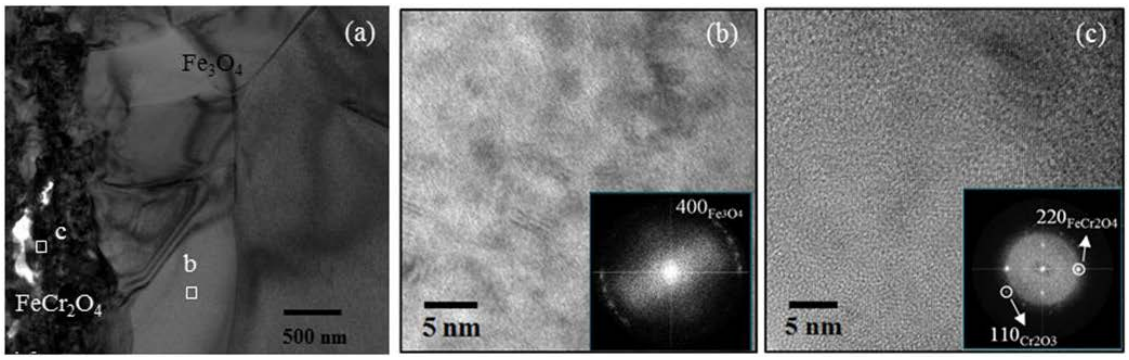

Figure 3-17: (a) Bright field TEM image taken from the point 6 of Figure 3-10, (b) HRTEM image with the corresponding fast Fourier transform (FFT) pattern taken from the (b) point b and (c) point c of the micrograph shown in panel (a).

The HRTEM and corresponding FFT pattern associated with point 2 suggests that the dominant phase at point 2 was Fe-Cr spinel. The point 3 HRTEM and FFT pattern are displayed in Figure 3-16g-h, revealing presence of chromium oxide at the interface of the inner oxide layer of the SS 316L tube sample. Figure 3-17a shows TEM bright field image taken from a cross-section of the scale on a tube sample from the SS 316L capsule exposed to SCW for 20000 h at 500 ^{o}C and 25 MPa. In the same micrograph, gray area with large grain size consists of

magnetite and the fine grain sized dark region composed of Fe-Cr spinel. HRTEM images and FFT patterns of these two areas indicated that magnetite, Fe-Cr spinel, and chromium oxide were present in the scale.

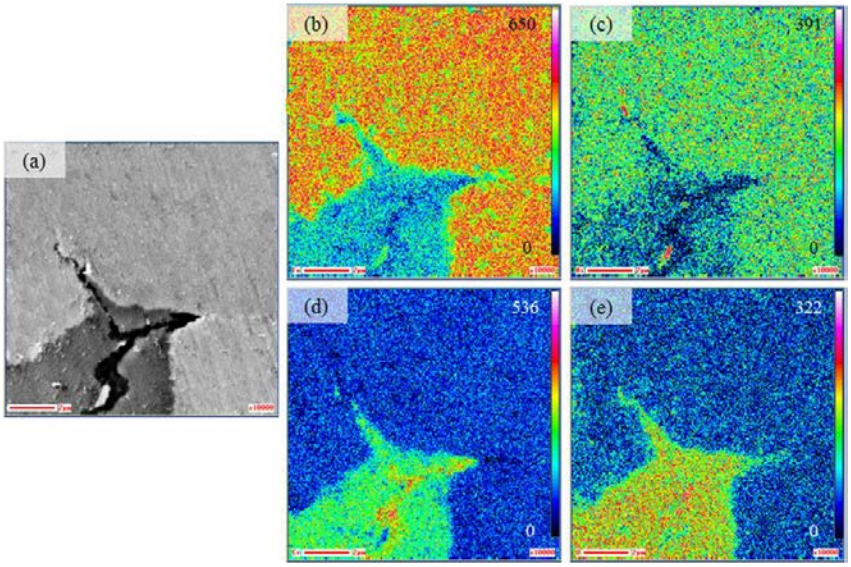

Figure 3-18: (a) SEM image from the selected area and (b-e) are the Fe, Ni, Cr, and O distribution at the tip of a micro-crack taken from the wall of tube capsule sample.

3.3.5 Auger Electron Spectroscopy

In an AES mapping analysis of the microcrack tip in the wall of a tube sample from a capsule exposed to SCW for 20000 h at 500 ^{o}C and 25 MPa. Figure 3-18(a) is the area of interest and (b–e) show the distribution of Fe, Ni, Cr, and O at the tip of the microcrack. The chromium concentration is high at the tip of the crack and low far away from the crack tip, indicating that chromium is depleted remote from the crack tip. The concentration of Fe is low at the crack tip and in the open mouth part of the microcrack. Ni enrichment is also noticed at the crack tip which indicates that Ni segregated to the crack tip.

3.4 Discussions

The above results demonstrate the development of oxide layers having formed on the inner surface of SS 316L capsules exposed to SCW at 500 ^{o}C and 25 MPa. The outer oxide layer was composed of a Fe-rich oxide with a spinel structure according to cross-sectional SEM and TEM elemental analyses (EDS), which was confirmed by XRD analysis. The results suggest that the outer layer was mainly composed of Fe_3O_4 due to the redeposition of iron. Selective depletion of chromium and iron from the alloy was observed in the EDS maps, indicating that these two elements migrated outward from the SS 316L tube surface to the water inside the tube and redeposited, forming an oxide layer on the inner wall of the alloy.

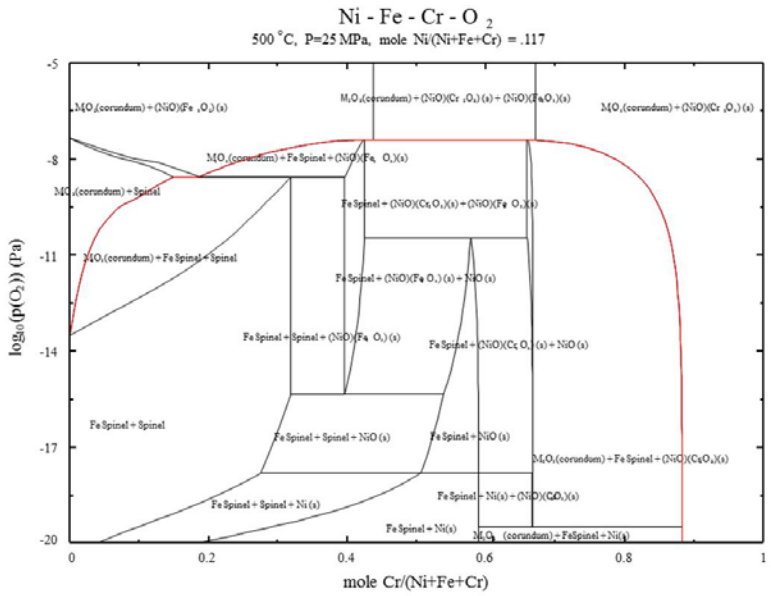

Figure 3-19: Calculated phase diagram as a function of oxygen partial pressure for the Fe-Cr-O_2-Ni system at 500 °C.

EDS maps revealed that oxygen migrated from the outer surface of the alloy to the inner oxide layer. The inner oxide layer was likely composed of a chromium-rich oxide with a spinel structure. EELS and SAED pattern observations suggested that the inner layer was composed of

Fe-Cr spinel with fine grains. Our results agree with Was et. al.[1] who have shown that magnetite was the dominant phase in the outer oxide layer of stainless steel alloys such as SS 316L and SS 304 after exposure to SCW at 550 °C and 25 MPa. In similar experiments, the inner oxide layer was dominated by $FeCr_2O_4$.[15,19,27]

The type of oxide layer formed on the inner surface of a SS 316L capsule exposed to SCW at 500 ^oC and 25 MPa depends on the partial pressure of oxygen. Thus, the sequence of oxide formation can be predicted. Figure 3-19 is a phase diagram of the Ni-Fe-Cr-O_2 system at 500 ^oC and 25 MPa. In this phase diagram, the *x*-axis is the alloy composition of $\frac{X_{Cr}}{X_{Cr}+X_{Fe}+X_{Ni}}$ and the *y*-axis represents oxygen partial pressure. Different structures, including face-centered cubic (FCC), magnetite (Fe_3O_4), spinel ($FeCr_2O_4$), and corundum ($[Fe,Cr]_2O_3$ and Cr_2O_3), with different chemical compositions, exist in the oxide layers formed on an alloy exposed to SCW at 500 ^oC and 25 MPa. One available phase with FCC structure is Ni. Tan et al.[37] reported that the oxygen partial pressure was about 2×10^{-16} atm on the outer surface of oxides exposed to SCW containing 25 ppb dissolved oxygen.

This calculation can be extracted by correlating the fitted parabolic rate constant with diffusion equation of Wagner's relation. In this study, water with the primary 25 ppb dissolved oxygen was used as the main feed. Based on these parameters and the stability diagram, a stable phase formation depends on the molar fraction of chromium in each layer which can be Fe_3O_4 + $FeCr_2O_4$, Fe + Fe_2O_3, or Cr_2O_3. Because there was no chromium in the outer oxide layer, the outer layer was assumed to be Fe_3O_4. The partial pressure of oxygen in the inner oxide layer was lower than that of the outer oxide layer and chromium was detected in the inner oxide layer. These conditions suggest that $FeCr_2O_4$ was present in the inner oxide layer in accordance with

XRD patterns, TEM-SAED patterns, EELS spectra, AES, and the SEM-EDS results. The FFT patterns taken from a microcrack tip suggest that Ni was segregated to the crack tip from a thin layer of chromium oxide at the inner oxide layer of the SS 316L tube sample. The diffusion layer (which is the interface between oxide layers and metallic substrate known as chromium oxide layer in this study) and inner layer contained iron and chromium. However, iron and chromium contents in the diffusion layer were different from those of the inner layer. Based on the EDS mapping results, the structural difference between inner and diffusion layers was the $FeCr_2O_4$ content. Accordingly, the main phase of the outer oxide layer was magnetite.

Oxidation of SS 316L capsules exposed to SCW at 500 ^oC and 25 MPa is described here according to the findings. Series of simplified schemas of the oxide layers formed on tube surfaces are displayed in Figure 3-20. The oxidation of steel in a supercritical liquid is similar to that in a gaseous environment. Oxidation in gaseous environments is dominated by molecular processes, and the diffusion rates of anions and cations in the oxide are the rate determining steps.[7]

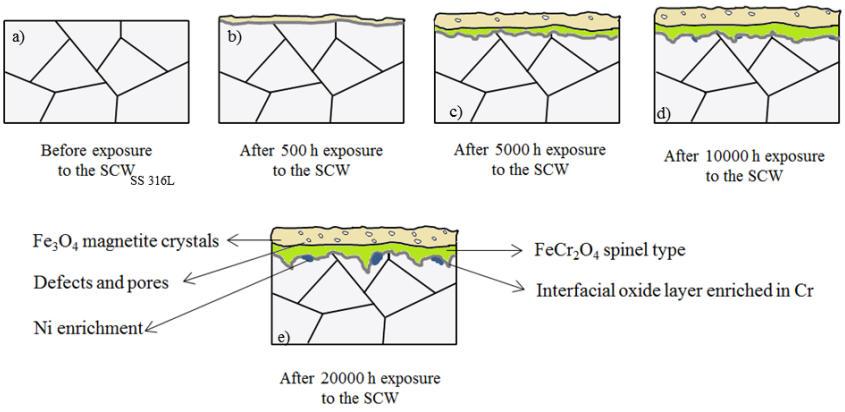

Figure 3-20: Schematic representation of the oxide formed on an alloy SS 316L tube sample, (a) before exposure, and after (b) 500 h, (c) 5000 h, (d) 10000 h, and (e) 20000 h exposure to the SCW.

SS 316L oxidation in an aqueous environment results in formation of two oxide layers, an outer layer composed of magnetite crystallites (Fe_3O_4) and a compact inner layer, interfacial between the steel tube and the outer oxide layer. Spinel enriched in iron and chromium, depending on the Fe-Cr spinel stoichiometry, may be deposited in different compositions and crystallite structures in the inner and outer layers. Diffusion phenomena play an important role in the formation of oxide layers. Based on the higher oxygen affinity of Cr relative to Fe, chromium oxide can be formed at the initial stage of oxidation however due to hydrothermal assisted evaporation of chromium oxide and different rates of chromium diffusion in grains and grain boundaries, some areas will be chromium depleted.

This phenomenon leads to a lack of chromium oxide regions and consequently a lack of protection of the base metal. Fe diffuses outward along grain boundaries and causes short-circuit paths to form Fe_3O_4.[38-40] Following this mechanism, iron cations diffuse from the inner oxide layer to the outer oxide layer and react with oxygen to form the iron-rich outer oxide layer. At the same time, oxygen anions diffuse to the inner oxide layer to form the chromium-rich inner oxide layer.[41] The reaction between Cr_2O_3 and Fe results in the formation of Fe-Cr spinel ($FeCr_2O_4$). SAED patterns obtained from TEM observations of tube samples exposed to SCW for 20000 h at 500 ^oC and 25 MPa suggested that the inner oxide layer consisted mainly of Fe-Cr spinel. In addition, a thin layer of Cr_2O_3 was detected at the inner oxide/metal substrate interface. With prolonged exposure time, Fe can travel through the spinel layer and further reacs with water, resulting in formation of a thicker Fe_3O_4 layer. The same oxide layer structure was observed in the cross section of SS 316L tube samples taken from capsules exposed to SCW at 500 ^oC and 25 MPa for different times. With the oxygen initial partial pressure in this study,

oxidation of iron and chromium was thermodynamically favorable.[8] However, based on the static nature of the tubing capsule with no oxygen supply and long test duration, the initial oxygen would rapidly be consumed and the sample would reach a deaerated condition.

Was et al.[9,10] proposed that since chromium diffusion in the austenitic alloy structure is fairly low at 500 °C, outward diffusion of iron and inward diffusion of oxygen favored the formation of a double layer film structure consisting of an iron-rich oxide on the top and a chromium enriched phase in the inner oxide layer. Our SEM images consistently illustrated that a double layer structure of oxide film was formed homogenously on SS 316L samples after 500 h exposure to SCW at 500 °C and 25 MPa. XRD patterns suggested that magnetite and chromium-iron spinel were the main phases in the oxide scales. Prolonging the exposure time to the corrosive media led to the formation of a thick porous oxide layer on alloy tube surfaces. SEM images in Figure 3-2 show many pores in the outer oxide layer which would allow diffusion of ions through the oxide film. The porosity can be attributed to the formation of an Fe_3O_4 phase, with a structure of $(Fe^{3+}, Fe^{2+})(Fe^{2+}, Fe^{3+}, Va)_2(Fe^{2+}, Va)(O^{2-})_4$. (Fe^{3+}, Fe^{2+}) and (Fe^{2+}, Fe^{3+}, Va) represent tetrahedral and octahedral sublattices of the iron cations, (Fe^{2+}, Va) represents an interstitial sublattice between cation and anion sublattices to account for deviations from stoichiometry, and (O^{2-}) represents oxygen anions.[42,43] The vacancies collapse into pores when the vacancy concentration of Fe_3O_4 is high enough.[44]

After tube samples were exposed to SCW for 20000 h at 500 ^{o}C and 25 MPa, the lower concentration of iron and higher concentration of oxygen at the grain boundaries of the oxide layers relative to that in grains led to chromium oxide formation. Because chromium has a higher affinity towards oxygen than nickel does,[29] Ni segregated to the inner oxide layer/SS 316L tube

sample interface. TEM-SAED and EELS results indicated that Fe_3O_4 formed on the outer oxide layer, $FeCr_2O_4$ was the main phase in the inner oxide layer, Cr_2O_3 uniformly formed as a thin layer, and Ni segregation appeared at the inner oxide layer/SS 316L tube sample interface. Cation diffusion in such a Cr-rich oxide layer has been known to be smaller than in Fe- and/or Ni-rich oxides. The presence of such a Cr-rich layer will thus be inclined to decrease the growth rate of the oxide scale, acting as a barrier against the diffusion of metal and oxygen ions.[7] The following sequence was observed in a cross-section image from the outer to inner layers of a tube sample exposed to SCW at 500 ^oC and 25 MPa: Fe_3O_4 + Fe-Cr spinel/Cr_2O_3/Ni-enrichment SS 316L tube sample.

Scott et al.[16] proposed that intergranular SCC can be explained by selective internal oxidation. Based on this model, selective oxidation of chromium oxide in grain boundaries leads to embrittlement followed by a crack initiation. Oxide formation is dependent on oxygen diffusion, which can be hindered by surface film formation. Thus, the nature of this oxide layer plays an important role in prevention of selective internal oxidation (SIO)[17] and crack propagation. Failure analysis in constant extension rate test (CERT) stainless steel alloys in a pressurized water environment shows the presence of a thin oxide layer around intergranular cracks.[17] An increase in chromium content was shown to improve resistance to SIO and IGSCC through the formation of a protective oxide layer that limited the diffusion of oxygen.[45]

CERT experiments on SCC of metals in SCW under accelerated conditions suggested that SCC might be initiated from surface-environmental interactions.[4,5,18] For SS 316L, it was proposed that tarnish-rupture was the cracking mechanism at the primary development stage and that crack tip stress was elevated and crack initiation was facilitated.[4] In this study, due to a low

magnitude of applied stress, only the primary stage of the tarnish-rupture mechanism was observed in the tube samples. A combination of hoop stress and the formation of heterogeneous oxidation pits on the inner tube wall facilitated SCC crack initiation and intergranular cracking under the outer oxide layer.[45]

SEM-EDS analysis showed metallic nickel enrichment ahead of the crack tip. One explanation for nickel enrichment is a difference in thermodynamic stability among the component elements. It is reasonable to suppose that chromium and iron are selectively dissolved and nickel remained at the reaction front. Nickel enrichment could be also due to different diffusion rates of elements present in the system although the differences are not severely high to cause the observed phenomena. Nonetheless, it has been reported that the diffusion rate of nickel is slower than that of chromium and iron.[45,46] although the mechanism of nickel enrichment is not clear, this result revealed that selective dealloying of iron and chromium occurred at the crack tip.

3.5 Conclusions

This work was aimed to investigate the oxidation and cracking susceptibility of SS 316L exposed to supercritical water at 500 °C and 25 MPa. Diffusion phenomena played an important role in the formation of two oxide layers having developed on the SS 316L substrate. The results showed that iron diffused outward and oxygen diffused inward. SEM observations of the outer layer scales showed that they were continuously formed on the surface of the metal. The crystallite size of the oxide increased as the exposure to SCW increased to 20000 h. High resolution TEM observations, EDS, EELS, and SAED analyses, and FFT patterns taken from

cross-sections of the oxide layers confirmed that the outer oxide layer was composed mainly of granular Fe_3O_4 and the inner layer consisted of fine grains of chromium-rich spinel oxide, $FeCr_2O_4$, with a thin layer of chromium oxide at the $FeCr_2O_4$/SS 316L sample interface. EDS of tube samples exposed to SCW for 20000 h at 500 °C and 25 MPa showed nickel enrichment at the metal/oxide interface. XRD results showed different phases on the outer surface of the oxide layer, including Fe_3O_4, $FeCr_2O_4$, and Fe_2O_3/Cr_2O_3. Thicker oxide scales and rougher surfaces on SS 316L samples resulted from extended exposure to SCW. Microcracks in the inner oxide layer were observed in samples exposed to SCW for 20000 h at 500 °C and 25 MPa. Microcrack initiation may have occurred due to the stresses induced by chromium and nickel migration, as microcrack tips were filled with corrosion products composed of chromium-rich oxides and were enriched with nickel.

Acknowledgments

The authors gratefully acknowledge financial support from the NSERC/NRCAN/AECL CRD program.

3.6 References

1 G. Was, S. Teysseyre, S. Mckinley, Z. Jiao, Corrosion of austenitic alloys in supercritica water, Corros., (2005) 1–20.

2 P. Kritzer, Corrosion in high-temperature and supercritical water and aqueous solutions: a review, J.

Supercrit. Fluids., 29 (2004) 1–29.

3 H.L. Hu, Z.J. Zhou, L. Liao, L. Zhang, M. Wang, S.F. Li, Corrosion behavior of a 14Cr-ODS steel in supercritical water, J. Nucl. Mater., 437 (2013) 196–200.

4 R. Novotný, P. Janík, S. Penttilä, P. Hähner, J. Macák, J. Siegl, High Cr ODS steels performance under supercritical water environment, J. Supercrit. Fluids., 81 (2013) 147–156.

5 R. Zhou, E.A. West, Z. Jiao, G. Was, Irradiation-assisted stress corrosion cracking of austenitic alloys in supercritical water, J. Nucl. Mater., 395 (2009) 11–22.

6 Y. Zeng, J. Li, B.S. Amirkhiz, W. Zheng, M. Matchim, M. Podlesny, Corrosion and stress corrosion cracking of UNS S31008 and UNS N08810 alloys in supercritical water, Corros., (2015).

7 M. Sun, X. Wu, Z. Zhang, E.-H. Han, Oxidation of 316 stainless steel in supercritical water, Corros. Sci., 51 (2009) 1069–1072.

8 S. Cissé, L. Laffont, B. Tanguy, M.-C. Lafont, E. Andrieu, Effect of surface preparation on the corrosion of austenitic stainless steel 304L in high temperature steam and simulated PWR primary water, Corros. Sci., 56 (2012) 209–216.

9 J. Bischoff, A.T. Motta, EFTEM and EELS analysis of the oxide layer formed on HCM12A exposed to SCW, J. Nucl. Mater., 430 (2012) 171–180.

10 M. Le Calvar, P.M. Scott, T. Magnin, P. Rieux, Strain Oxidation Cracking of Austenitic Stainless Steels at 610°C, Corrosion., 54 (1998) 101–105

11 R. Nishimura, Characterization and perspective of stress corrosion cracking of austenitic stainless steels in acid solutions using constant load method, Corros. Sci., 49 (2007) 81–91.

12 S. Penttilä, A. Toivonen, J. Li, W. Zheng, R. Novotny, Effect of surface modification on the corrosion

resistance of austenitic stainless steel 316L in supercritical water conditions, J. Supercrit. Fluids., 81 (2013) 157–163.

13 K. Arioka, T. Yamada, T. Terachi, G. Chiba, Cold work and temperature dependence of stress corrosion crack growth of austenitic stainless steels in hydrogenated and oxygenated high-temperature water, Corrosion., (2007) 1114–1123.

14 S.N. Lvov, Advanced techniques for high temperature electrochemical and corrosion studies, Corros., (2004) 1–16.

15 W. Zieliński, K. Kurzydłowski, TEM studies of the oxide scales formed on type 316 stainless steel during annealing at 600 °c in a vacuum and air, Scr. Mater., 43 (2000) 33–37.

16 Z. Shen, L. Zhang, R. Tang, Q. Zhang, SCC susceptibility of type 316Ti stainless steel in supercritical water, J. Nucl. Mater., 458 (2015) 206–215.

17 Z. Shen, L. Zhang, R. Tang, Q. Zhang, The effect of temperature on the SSRT behavior of austenitic stainless steels in SCW, J. Nucl. Mater., 454 (2014) 274–282.

18 P. Ampornrat, G. Gupta, G. Was, Tensile and stress corrosion cracking behavior of ferritic–martensitic steels in supercritical water, J. Nucl. Mater., 395 (2009) 30–36.

19 E.A. West, G. Was, IGSCC of grain boundary engineered 316L and 690 in supercritical water, J. Nucl. Mater., 392 (2009) 264–271.

20 G. Gupta, P. Ampornrat, X. Ren, K. Sridharan, T.R. Allen, G. Was, Role of grain boundary engineering in the SCC behavior of ferritic–martensitic alloy HT-9, J. Nucl. Mater., 361 (2007) 160–173.

21 S. Teysseyre, Q. Peng, G. Was, Stress Corrosion Cracking of Neutron- Irradiated Stainless Steels in

Supercritical Water Material studies required for SCWR, J. Nucl. Mater., 371 (2007) 98–106.

22 J. Konys, S. Fodi, J. Hausselt, H. Schmidt, V. Casal, Corrosion of High-Temperature Alloys in Chloride-Containing Supercritical Water Oxidation Systems, Corrosion., 55 (1999) 45–51.

23 S. Teysseyre, Q. Peng, C. Becker, G. Was, Facility for stress corrosion cracking of irradiated specimens in supercritical water, J. Nucl. Mater., 371 (2007) 98–106.

24 X. Zhong, X. Wu, E.-H. Han, Effects of exposure temperature and time on corrosion behavior of a ferritic–martensitic steel P92 in aerated supercritical water, Corros. Sci., 90 (2015) 511–521.

25 O. Yeliseyeva, V. Tsisar, Z. Zhou, Corrosion behavior of Fe–14Cr–2W and Fe–9Cr–2W ODS steels in stagnant liquid Pb with different oxygen concentration at 550 and 650°C, J. Nucl. Mater. 442 (2013) 434–443.

26 I. Wright, B. Pint, An Assessment of the High Temperature Oxidation Behavior of Fe-Cr Steels in Water Vapor and Steam, Corros., (2002).

27 E.A. West, Influence of local stress and strain on intergranular cracking of 316L stainless steel in supercritical water, Michigan, (2010).

28 D. Rodriguez, A. Merwin, D. Chidambaram, On the oxidation of stainless steel alloy 304 in subcritical and supercritical water, J. Nucl. Mater., 452 (2014) 440–445.

29 M. Nezakat, H. Akhiani, S. Penttilä, S.M. Sabet, J. Szpunar, Effect of thermo-mechanical processing on oxidation of austenitic stainless steel 316L in supercritical water, Corros. Sci., (2015).

30 J. Weiss, A. Pineau, Fatigue and creep-fatigue damage of austenitic stainless steels under multiaxial loading, Metall. Trans. A., 24 (1993) 2247–2261.

31 D.S. Morton, S.A. Attanasio, G.A. Young, P.L. Andersen, T.M. Angeliu, P.L. Andresen, The

influence of dissolved hydrogen on nickel alloy SCC: A window to fundamental insight, (2000).

32 D. Guzonas, J.S. Wills, G.A. McRae, S. Sullivan, K. Chu, K. Heaslip, et al., Corrosion- resistant coating for use in a supercritical water CANDU reactor, in: 12th Int. Conf. Environ. Degrad. Mater. Nucl. Power Syst. React., (2005) 1379–1386.

33 E.-H. Han, L. Zhang, W. Ke, H. Guan, Corrosion behvavior of meterials in supercritical water oxidation system, Corros., (2001).

34 A.H. Harvey, E.W. Lemmon, NIST / ASME Steam Properties — STEAM-Version 3.0, U.S. Dep. Commer. Natl. Inst. Stand. Technol. Stand. Ref. Data Progr. Gaithersburg, Maryl., 20899 (2013).

35 G. Was, S. Teysseyre, Z. Jiao, Corrosion of Austenitic Alloys in Supercritical Water, Corrosion., 62 (2006) 989–1005.

36 J. Bischoff, A.T. Motta, EFTEM and EELS analysis of the oxide layer formed on HCM12A exposed to SCW, J. Nucl. Mater., 430 (2012) 171–180.

37 L. Tan, Y. Yang, T.R. Allen, Oxidation behavior of iron-based alloy HCM12A exposed in supercritical water, Corros. Sci., 48 (2006) 3123–3138.

38 A. D. Siwy, T.E. Clark, a. T. Motta, Transmission electron microscopy of oxide development on 9Cr ODS steel in supercritical water, J. Nucl. Mater., 392 (2009) 280–285.

39 X. Zhong, X. Wu, E.-H. Han, Effects of exposure temperature and time on corrosion behavior of a ferritic–martensitic steel P92 in aerated supercritical water, Corros. Sci., 90 (2015) 511–521.

40 J. Bischoff, A.T. Motta, Oxidation behavior of ferritic-martensitic and ODS steels in supercritical water, J. Nucl. Mater., 424 (2012) 261–276.

41 J. Bischoff, A.T. Motta, R.J. Comstock, Evolution of the oxide structure of 9CrODS steel exposed to

supercritical water, J. Nucl. Mater., 392 (2009) 272–279.

42 J. Bischoff, A.T. Motta, Oxidation behavior of ferritic-martensitic and ODS steels in supercritical water, J. Nucl. Mater., 424 (2012) 261–276.

43 J. Bischoff, A.T. Motta, R.J. Comstock, Evolution of the oxide structure of 9CrODS steel exposed to supercritical water, J. Nucl. Mater., 392 (2009) 272–279.

44 H. Hu, Z. Zhou, M. Li, L. Zhang, M. Wang, S. Li, et al., Study of the corrosion behavior of a 18Cr-oxide dispersion strengthened steel in supercritical water, Corros. Sci., 65 (2012) 209–213.

45 Z. Suo, D.V. Kubair, A.G. Evans, D. Clarke, V.K. Tolpygo, Stresses induced in alloys by selective oxidation, Acta Mater., 51 (2003) 959–974.

46 Z. Suo, A Continuum Theory That Couples Creep and Self-Diffusion, J. Appl. Mech., 71 (2004) 646.

Chapter 4: Oxidation and Cracking Susceptibility of 310S Stainless Steel in Supercritical Water: Part I - Investigation by SEM, AES, and XRD

4.1 Introduction

Supercritical water reactors (SCWRs) are promising generation IV nuclear reactors that provide a much higher thermal efficiency and are simpler to construct compared with the current light water reactors.[1] Based on the working conditions, the operating temperature and pressure of an SCWR are designed to exceed the thermodynamic critical point of water. SCW is known as a non-polar solvent which can dissolve gases like oxygen up to complete miscibility. Water above a temperature of 374.15 °C and a pressure of 22.1 MPa is in a supercritical state and acts as a dense gas, exhibiting properties significantly different from the regular water.[2,3] At the critical point, the specific enthalpy of water increases about 20%, and water behaves as a single phase.[2-4] A SCWR which uses SCW as a coolant has high thermal efficiency and a simplified single phase coolant design compared to the current light water reactors.[3]

To choose an appropriate alloying system for application in SCWR, all the important parameters should be considered. Oxide scales on metal substrates are known to affect the properties of engineering materials. It is necessary that the mechanisms of processes affecting lifetime of the candidate materials in relevant conditions are properly identified through the extensive experimental tests.[3] Knowledge of general corrosion resistance in SCW has been considered as a basic step as it is a critical issue in itself and plays an important role in other

detrimental processes such as stress corrosion cracking (SCC) and corrosion fatigue (CF).[5] Various investigations have been conducted to evaluate the high temperature oxidation of steel in air or oxygen.[6-10] Austenitic stainless steels (SS) have been used for the sake of their high corrosion resistance in high temperature SCW environments, also several researchers have studied the oxidation and SCC of austenitic alloys exposed to SCW under different conditions.[5-16] Parameters that affect SCC of austenitic SS include water chemistry, temperature, chemical composition, loading conditions, and etc.[17,18] For steels with a low chromium content, a complex oxide layer composed of hematite, magnetite, Cr_2O_3, and $FeCr_2O_4$ spinel may form on the metal surface. Was et al.[19-24] proposed that the outer oxide layer is composed of nonuniform large grains comprising magnetite, and the inner oxide layer is made of fine grained oxides, which is compact and very adherent to the base metal. The inner layer is generally dens, protective and rich in chromium. Most of the studies on high-temperature oxidation of steels have been based on the assumption that oxides on low-alloy steels grow by the outward Fe diffusion because of sluggish oxygen anions diffusion through the lattice of iron oxides.[15-21]

Cr as one of the major alloying elements of stainless steels can promote the formation of a protective surface oxide and Ni can enhance the stability of the protective oxide. Therefore, a higher amount of Cr and Ni in the composition of the stainless steel can simply result in a superior high temperature performance of stainless steel in SCW. In ferritic stainless steel with high chromium content, Cr_2O_3 forms in the first stage of oxidation and $(Cr, Mn)_3O_4$ spinel oxide forms in a later stage.[25] Based on the amount of oxygen in the solution, SCW can be a very aggressive oxidizing environment. Thus, the oxidation behaviour of the alloy in SCW can vary

significantly. Consequently, oxidation and SCC of structural materials in SCWR are of importance.[22-34]

In the present work, the oxidation of SS 310S was investigated in SCW at 500 °C and 25 MPa during various exposure times. The oxide layers, formed on the alloy during exposure to SCW, were characterized using X-ray diffraction (XRD), scanning electron microscopy (SEM) equipped with energy-dispersive X-ray spectroscopy (EDS), and Auger electron spectroscopy (AES), and their phase stability was mapped. The development of the oxide layers was studied and an appropriate oxidation mechanism is proposed.

4.2 Experimental Procedure

4.2.1 Materials

310S stainless steel (SS) tubes with an outer diameter of 9.525 mm and a wall thickness of 1.65 mm were purchased from Swagelok. The tubes were manufactured according to specifications defined in ASTM-A213 for stainless steels and were supplied in a solution annealed state. The chemical composition (wt. %) of the alloy is given in Table 4-1.

Table 4-1: Elemental chemical composition of alloy 310S SS used in this study.

Alloy	**Chemical Composition (wt. %)**								
310S Stainless Steel	Fe	C	Cr	Ni	P	Si	Mo	Mn	S
	Balance	0.048	24.4	20.36	0.024	0.33	0.29	1.18	0.001

Tube samples were cut into 10 cm long sections to make capsule specimens for SCW exposure. Tube sections were washed with pentane, isopropyl alcohol, and acetone in an ultrasonic bath prior to filling with neutral pH deionised water (DI) containing 8 ppm dissolved oxygen (DO). Two high pressure caps were used to make static capsules from tube sections. The static capsules were placed in a tubular furnace and heated to 500 °C. The temperature of the furnace was calibrated using Nextel ceramic insulated lead wire rated to 815 °C (Omega) as the reference thermocouple. The pressure of the water inside the tube depends on volume and temperature of the water. According to the NIST steam chart,[35] the pressure of a tube filled with a 9.5% volume of DI water is 25 MPa at 500 °C. Stress on the tube wall due to the internal pressure was calculated by heating separate static capsules to 500 °C.

4.2.2 Characterizations

After SCW exposure, the capsules were cut into smaller segments. The inner surfaces of the tubes were plated with a thin layer of Ni coating to avoid spallation of the oxide film during sample preparation. Samples were mounted with epoxy resin and polished down to 0.5 μm in alumina solution before microscopic examination. The surface morphology of the oxide layers on the ID of the tubes were evaluated by a scanning electron microscope (SEM, ZEISS EVO-MA15) equipped with energy dispersive X-ray capability and secondary electron (SE) detector. Cross-section morphologies were captured with backscattered electrons. A Bruker AXS diffractometer (Bruker Discover 8) operating with Cu-K_α radiation with a wavelength of 1.5405 Å at 40 kV and 40 mA in the 2-theta range 20°-80° with a scan rate of 0.05° per second was used for X-ray diffraction (XRD) analysis. Samples were prepared using the focused-ion-beam (FIB)

lift-out technique to be examined by field emission scanning electron microscopy (FESEM). Electron transparent samples were prepared using an ion beam voltage of 40 keV with the current dropping from 7 nA to 35 pA.

Auger electron spectroscopy (AES) was utilized to attain element mappings of a formed crack for samples exposed to SCW at 500 °C for 20000 h. The AES measurements were performed using a JAMP-9500F Auger microprobe (JEOL) with a single-pass cylindrical mirror analyzer manufactured by Perkin-Elmer: Physical Electronics Division. The instrument is equipped with a Shottky field emitter that produces an electron probe diameter of about 3 to 8 nm. Accelerating voltage and emission currents for SEM and Auger imaging were 15 kV and 8 nA, respectively. The working distance was 24 mm. The sample was rotated 30 degrees away from the primary electron beam to face the electron energy analyzer. One M5 lens with 0.6% energy resolution was used for the Auger spectroscopy and imaging. Auger peaks of Si KLL (1600 eV), Ag MNN (350 eV), and Au MNN (2015 eV) were selected for the mapping. The intensity of each pixel in the Auger image was calculated by (P–B)/B, where P and B are the peak and background intensities, respectively. The intensity definition helps to reduce the edge effect of islands and dots. An auto probe tracking technique was used to compensate for possible drifting of the image during the analysis as a result of power instabilities.

Phase stability of the Ni-Fe-Cr-O_2 system in SS 310S samples was considered using the software FactSage 6.1 from Thermfact Ltd. and GTT Technology.

4.3 Results

4.3.1 Microstructure of the As-Received Material

Figure 4-1 shows a scanning ion micrograph of SS 310S exhibiting an annealed microstructure with equiaxed grains. Cold drawing and twinning features are evident in the micrograph.

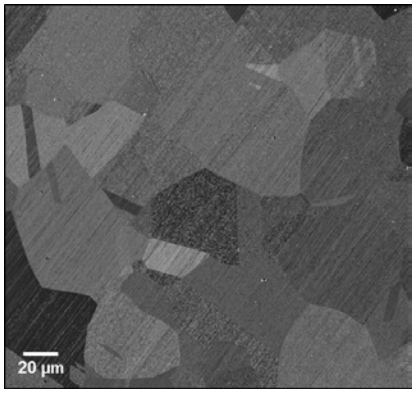

Figure 4-1: SEM micrograph of the used SS 310S sample.

4.3.2 Morphological Investigations of the Oxide Layers

SEM images (Figure 4-2a-c) of SS 310S samples exposed to SCW at 500 °C and 25 MPa for 500 h show that a thin oxide layer of polyhedral crystallite particles of ~ 800 nm formed on the ID surface of the tubing. When the SCW exposure time was prolonged to 5000 h (Figure 4-3), the oxide layer grew and the crystallites coarsened (Figure 4-3a-b), and localized crystalline islands appeared with sizes up to 2.9 µm (Figure 4-3c). The remaining surface area was covered with a continuous fine oxide layer with an average crystal size of 850 nm.

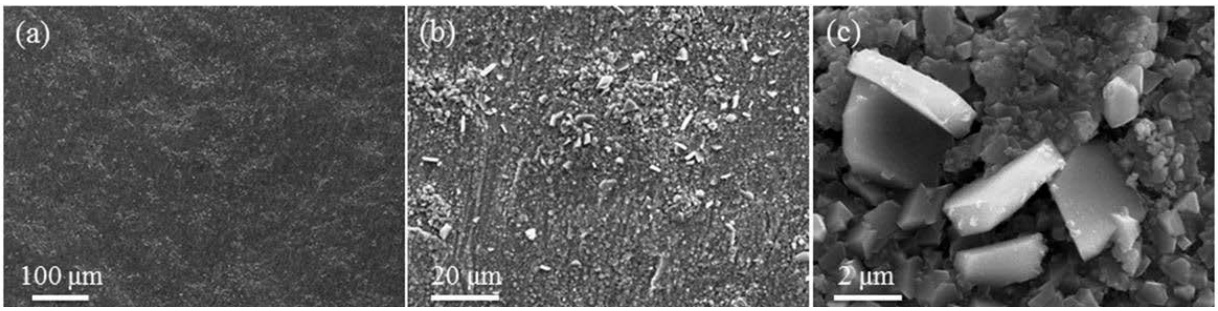

Figure 4-2: Outer surface images of the SS 310S sample exposed to the SCW after 500 h exposure time 150x (a), 1000x (b), 10000x (c).

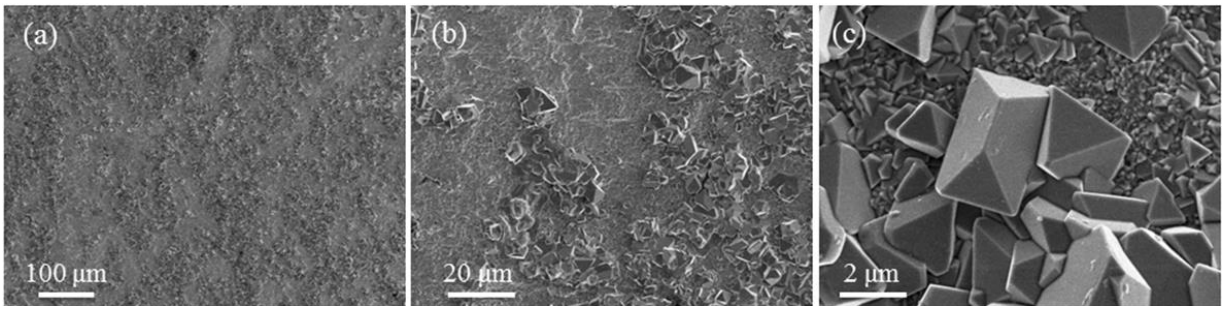

Figure 4-3: Outer surface images of the SS 310S sample exposed to the SCW after 5000 h exposure time 150x (a), 1000x (b), 10000x (c).

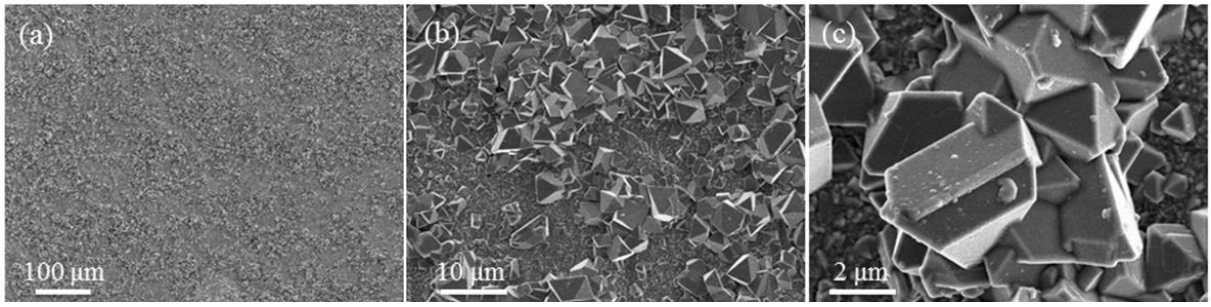

Figure 4-4: Outer surface images of the SS 310S sample exposed to the SCW after 10000 h exposure time 150x (a), 1900x (b), 10000x (c).

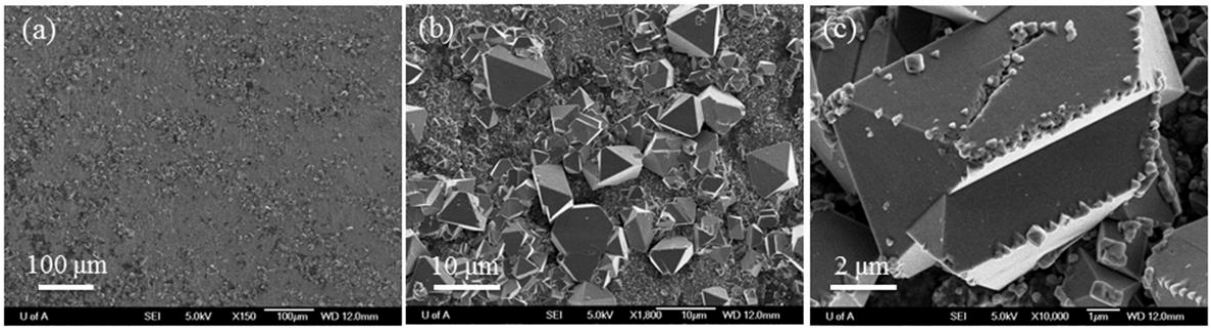

Figure 4-5: Outer surface images of the SS 310S sample exposed to the SCW after 20000 h exposure time 150x (a), 1900x (b), 10000x (c).

SEM images of samples exposed to SCW for 10000 h (Figure 4-4) show islands with crystallite sizes of 4.2 μm (Figure 4-4c) surrounded with a fine uniform oxide. The reduction in growth rate between 5000 h and 10000 h SCW exposure time was likely due to ion diffusion limitation through the oxide layer. Morphological examinations on the sample exposed to SCW for 20000 h (Figure 4-5a-b) indicated that the polyhedral grains had a tendency to be faceted and flat. SEM images of samples exposed to SCW for 20000 h showed a grain size of about 5.6 μm (Figure 4-5c), much rougher than grains produced at 500 h and 5000 h of SCW exposure.

4.3.3 Cross-Sectional Studies of the Oxide Layer

Figure 4-6 illustrate cross-sectional images of SS 310S samples exposed to SCW at 500 °C and 25 MPa for different exposure times. A thin (~ 1.2 μm) fairly uniform oxide layer covered the inner surface of the bulk alloy after 500 h SCW exposure (Figure 4-6a). Some localized discontinuities present in the oxide layer in the later stages of corrosion, while these discontinuities were not observed after 500 h of SCW exposure.

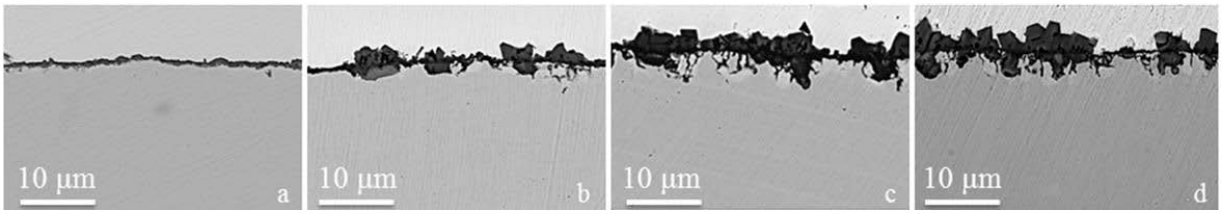

Figure 4-6: Cross-section micrographs taken from the alloy 310S SS exposed the SCW for (a) 500 h, (b) 5000 h, (c) 10000 h, and (d) 20000 h of SCW exposure time.

A thin oxide layer with an average thickness of around 1.2 μm was observed on the ID surface of the sample tubing from the capsule exposed to SCW. The longer test time had no

significant effect on the stability of the oxide layers but the oxide grain coarsened after 5000 h SCW exposure (Figure 4-6b). In fact, localized grain growth was observed on the alloy surface exposed to SCW. These observations were consistent with the surface morphology in Figure 4-3, i.e. oxidation occurred on the inner and outer surfaces of the capsule exposed to SCW. The oxide layer grew to an approximate average thickness of 4.1 μm. There was no change in thickness of the oxide layer while the oxide growth occurred locally. When the exposure time was increased to 10000 h, a continuous grain growth in the oxide islands took place on the both inner and outer oxide layers. After 10000 h SCW exposure, the outer oxide layer exhibited a porous morphology. As the exposure time increased from 5000 h to 10000 h, the average thickness in the islands increased to 6.2 μm (Figure 4-6c). A few microcracks were initiated beneath the inner oxide layer (Figure 4-6c), which could be attributed to stresses produced by scale formation on the surface.

The SS 310S samples were exposed to the corrosive media for 20000 h. Corresponding cross-sectional SEM observations indicated that the average thickness of the oxide layer increased to 9.7 μm. Compared to the shorter exposure times, branching of the microcracks took place as a result of probable dealloying of the chromium element and stress concentration beneath the pits and oxide layers. Preferential oxidation in the grain boundaries can provide active sites for the initiation of microcracks. Based on the cross-sectional observations, there were two oxide layers on the ID surface of the SS 310S tubing, a porous outer oxide and a fairly dense inner oxide film containing microcracks that extended to the SS 310S substrate.

4.3.4 EDS Elemental Analyses

EDS elemental analyses were performed on capsules exposed to SCW at 500 °C and 25 MPa for different times to investigate the elemental composition and distribution in the oxide layer at the austenite/oxide phase interfaces and in the bulk region adjacent to austenitic grain boundaries. Figure 4-7 displays elemental maps for Fe, Cr, Ni, and O in the oxide layer formed on the SS 310S inner surface after exposure to SCW for 500 h. Individual and overlay elemental maps showed that the thin oxide layer was mainly composed of chromium and oxygen and a small amount of iron which could represent the formation of chromium oxide and Fe-Cr spinel. It was difficult to observe magnetite on the top oxide layer. Figure 4-8 is an elemental map of a SS 310S sample exposed to SCW for 5000 h at 500 °C and 25 MPa. The thickness of the oxide layer had increased relative to that at 500 h SCW exposure and two distinct oxide layers were detected: (1) a discontinuous oxide layer on the outer surface composed of iron and oxygen (most probably magnetite) and (2) a uniform and continuous inner oxide layer mainly composed of chromium and oxygen and small amount of iron (was most likely due to presence of chromium oxide and Fe-Cr spinel).

Thus, the oxide layer on the exposed surface could be defined as Fe_3O_4 + Fe-Cr spinel/Cr_2O_3/SS 310S, from the outer to inner oxide layer. Furthermore, a few microcracks were apparent on the inner oxide layer at the interface with the SS 310S metal. Oxidation occurred within the grain and microcracks were initiated from the grain boundary of the oxidized grain. Selective depletion of chromium and iron was observed in the EDS elemental maps, indicating that these two elements migrated outward to form the oxide layer. EDS map of oxygen revealed that O migrated from the outer surface of the scale to the inner oxide layer.

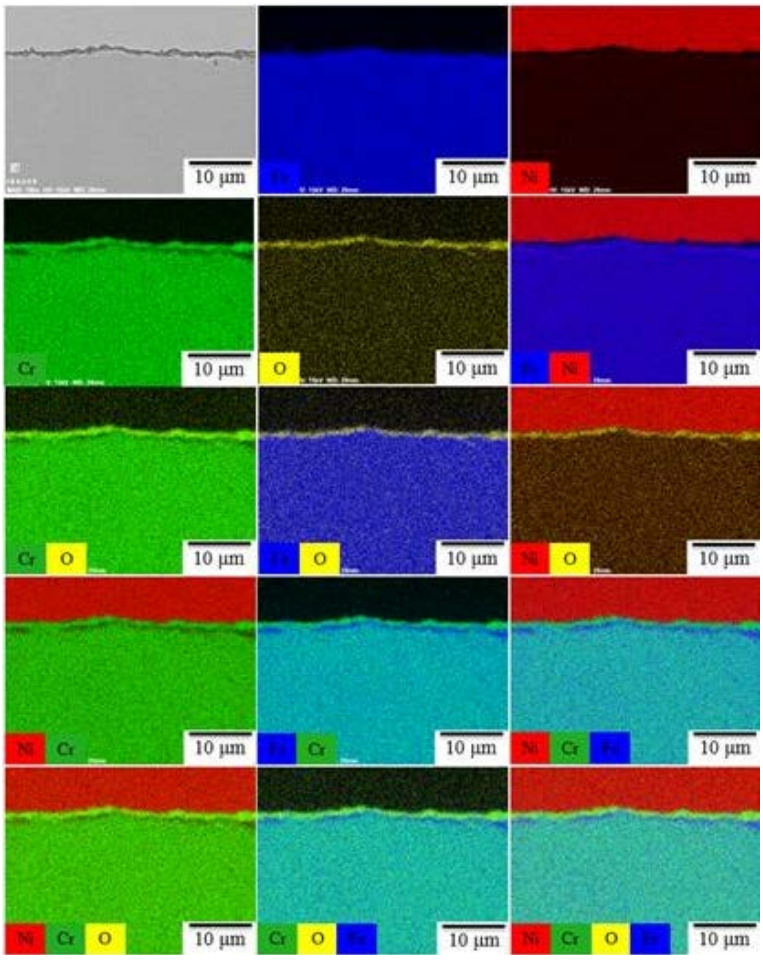

Figure 4-7: EDS elemental maps taken from cross-section of the oxide layer formed on the SS 310S alloy after exposure to the SCW for 500 h exposure time.

To investigate oxidation of the SS 310S sample after exposure for a protracted time, samples were exposed to SCW for 10000 h and 20000 h at 500 °C and 25 MPa. Figure 4-9 illustrates elemental distribution in a tube sample from a SS 310S capsule exposed to SCW for 10000 h. The thickness of the outer and inner oxide layers increased in comparison with samples exposed to SCW for 5000 h. A number of microcracks were observed in the inner oxide layer along the phase boundary of Fe-Cr spinel/Cr_2O_3 and the metal substrate. Localized variations in the

thickness of the outer oxide layer were detected and Ni was enriched at the inner oxide/metal substrate interface.

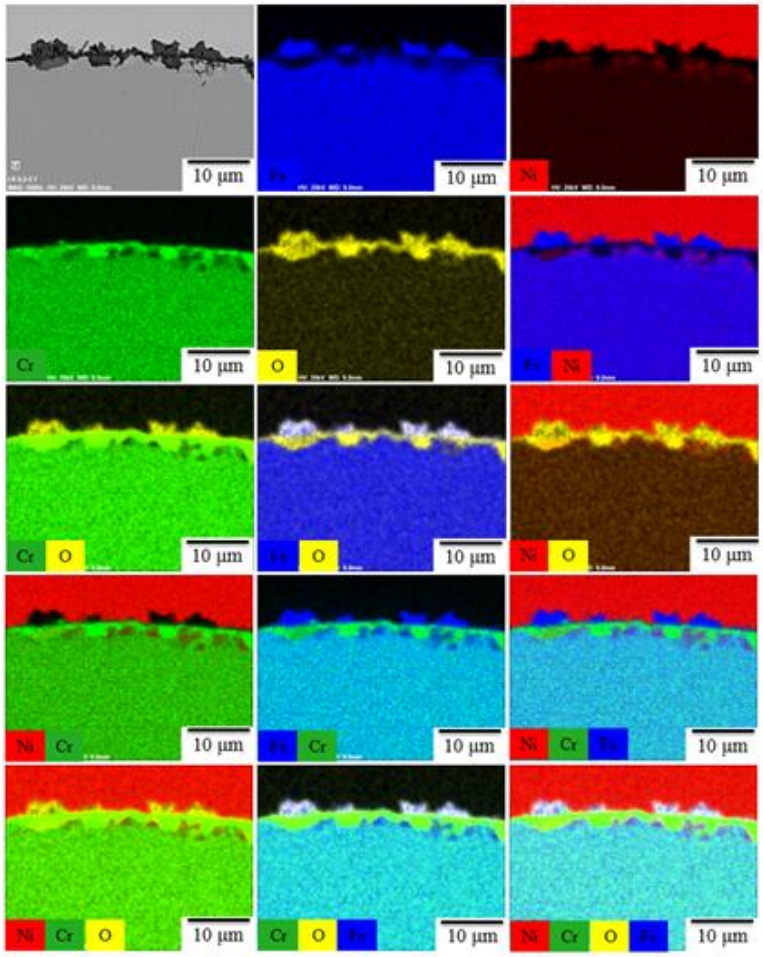

Figure 4-8: EDS elemental map from cross-section of the oxide layer formed on the SS 310S alloy after exposure for 5000 h.

Figure 4-10 depicts EDS analysis results for a capsule exposed to SCW for 20000 h. The outer oxide layer was porous and the pore density was higher than that of samples exposed for shorter times. Similar to the capsule exposed to SCW for 10000 h, elemental nickel segregation was observed in the inner oxide layer close to the SS 310S. Additionally, microcracks appeared perpendicular to the direction of circumferential stress (hoop stress) with most of the cracks were

chromium and oxygen enriched and nickel and iron depleted. SEM-EDS maps showed metallic nickel enrichment ahead of the crack tip. Nickel enrichment could be due to the selective dissolution of chromium and iron leaving nickel at the reaction front. Another explanation for nickel enrichment is the difference in element diffusion rates, although the difference is not large enough to account for the observed behaviour. Nonetheless, it has been reported that Ni diffusion rate is more sluggish compared to that of chromium and iron.[36,37] Although the mechanism of nickel enrichment is not clear, this reveals that selective dissolution of iron and chromium occurred at the crack tip.

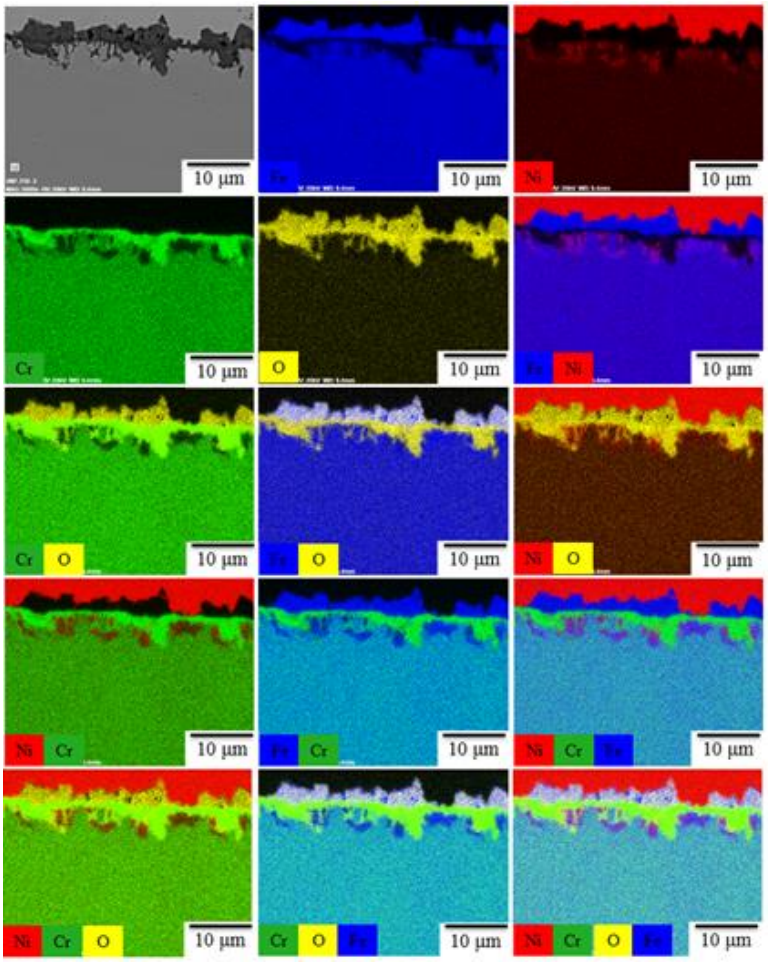

Figure 4-9: EDS elemental distribution from cross-section of the oxide layer formed on the SS 310S after exposure to the SCW for 10000 h.

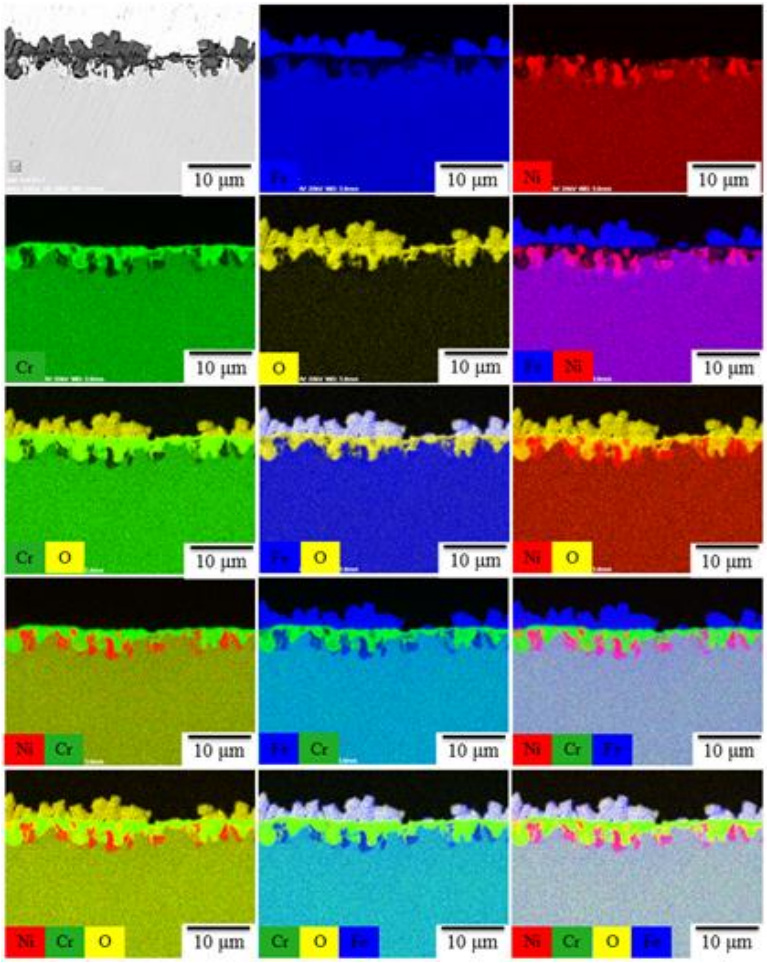

Figure 4-10: EDS elemental maps from a cross-section of the oxide layer formed on the SS 310S alloy after 20000 h SCW exposure time.

4.3.5 X-Ray Diffraction Patterns

Figure 4-11 shows XRD spectra for tubing samples of SS 310S capsules exposed to SCW at 500 °C and 25 MPa for different exposure times. Austenite, magnetite (Fe_3O_4), spinel $FeCr_2O_4$, and Fe_2O_3/Cr_2O_3 (hematite/chromium oxide) were detected in the XRD patterns, with FCC austenite as the primary phase. After 500 h of exposure to SCW at the same temperature and pressure, XRD results revealed that $FeCr_2O_4$ was the major component of the oxide layer that formed on the ID surface of the tube sample, with smaller quantities of Fe_3O_4 and Cr_2O_3. All

phases were still present when the SCW exposure time was increased to 5000 h. However, with prolonged exposure time, the intensity of Fe-Cr spinel rose while the intensity of austenite reduced. XRD patterns for SS 310S tube samples of capsules that had been exposed to SCW for 5000 h indicated that the coarse crystallite formed on the surface was Fe_3O_4. Quantity of chromium oxide/Fe-Cr spinel phases detected by XRD on the inner surface of the SS 310S samples were significant after longer SCW exposure times. The same compounds were observed in all samples when the SCW exposure time was increased to 20000 h.

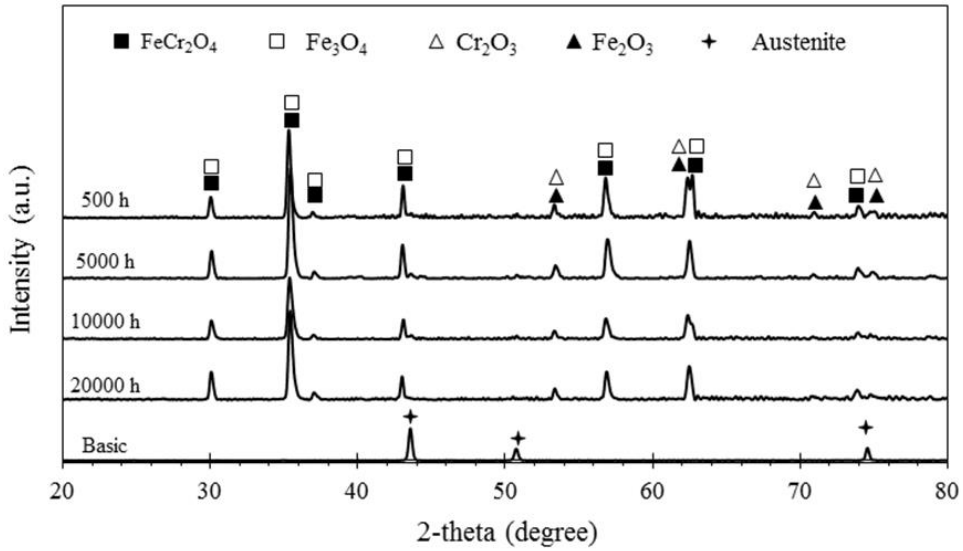

Figure 4-11: XRD spectra from the oxide layer formed on surface the SS 310S tube sample exposed to the SCW for various exposure times.

4.3.6 SEM Images and Auger Electron Spectroscopy Analysis

High resolution FESEM images taken from samples which were exposed to SCW for 20000 h at 500 °C and 25 MPa are shown in Figure 4-12. A cross-section image of the scale formed on the ID surface of the SS 310S tubing exhibits a porous morphology (Figure 4-12b). Additionally, microcrack apparently initiated at the inner oxide/SS 310S interface (Figure 4-12b-c).

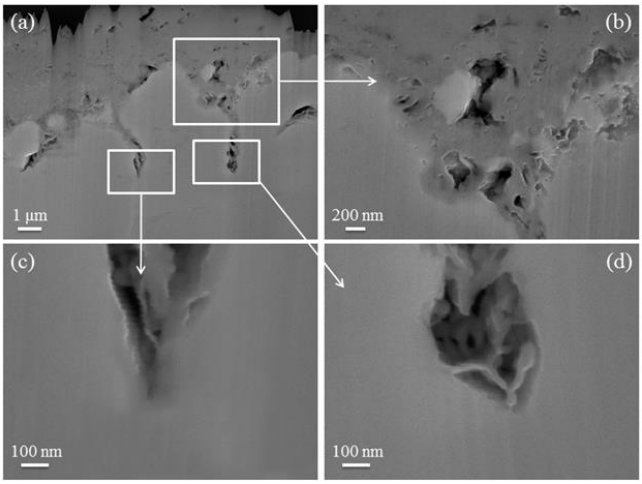

Figure 4-12: FESEM images from the cross-section of the SS 310S sample exposed to the SCW for 20000 h, 10000x (a), 30000x (b), 100000x (c), 100000x (d).

AES mapping was conducted on a tubing sample of a SS 310S capsule exposed to SCW for 20000 h at 500 °C and 25 MPa. Figure 4-13 illustrates AES mapping micrographs recorded from the cross-section of the oxide layer and Figure 4-14 shows a selected microcrack tip area where (a) is the interest area and (b–e) show the Fe, Ni, Cr, and O distribution at the microcrack tip in the wall of the capsule sample.

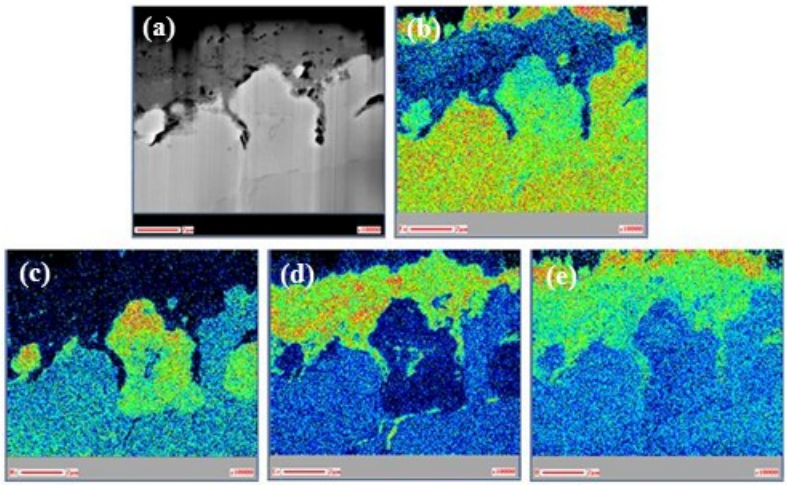

Figure 4-13: (a) SEM image from the selected area and (b-e) AES maps of Fe, Ni, Cr, and O for the cross section of the SS 310S sample exposed to the SCW for 20000 h.

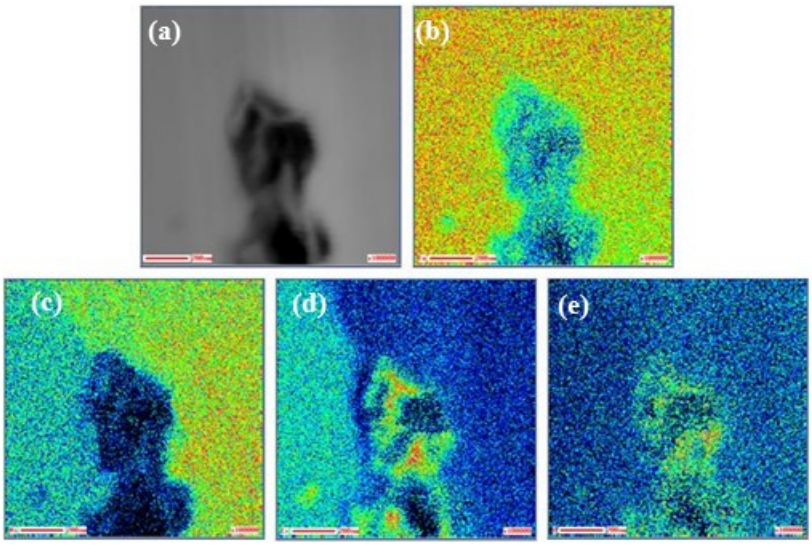

Figure 4-14: (a) SEM image from the selected area and (b-e) AES analysis results with corresponding Fe, Ni, Cr, and O maps at the tip of a micro-crack taken from the wall of tube capsule sample.

The elemental distribution on the cross-section of the exposed capsule show two discrete oxide layers: an outer oxide layer composed of a higher concentration of Fe and O, identified as magnetite and an oxide layer with a lower concentration of Fe and higher concentration of chromium and O which could be identified as Fe-Cr spinel and chromium oxide. The elemental map for nickel indicates that Ni-enrichment took place beneath the formed scales. As seen in Figure 4-14, the chromium concentration at the microcrack tip is high although chromium concentration remote from the crack tip is low, showing chromium depletion. It is interesting to note Fe depletion at the crack tip. Iron depletion was only observed in the open mouth of the microcrack. The Ni enrichment at the crack tip reveals that segregation of this element took place on the crack tip. AES results further confirmed the SEM and EDS findings.

4.4 Discussions

4.4.1 Phase Stability Diagram Studies

The type of oxide layer formed on the inner surface of the SS 310S sample exposed to SCW depended on the partial pressure of oxygen, thus the oxide sequences can be predicted. Figure 4-15 is a phase diagram of the Ni-Fe-Cr-O_2 system for a SS 310S sample exposed to SCW at 500 °C and 25 MPa. In the phase diagram, the *x*-axis represents the alloy composition $\frac{X_{Cr}}{X_{Cr}+X_{Fe}+X_{Ni}}$ and the *y*-axis represents the partial pressure of oxygen. This type of phase diagram would determine the stable phase region of different alloy compositions at various oxygen partial pressures. Different structures, including FCC, Fe-spinel, spinel, and corundum, with different chemical compositions, exist in the oxide layer formed at 500 °C.

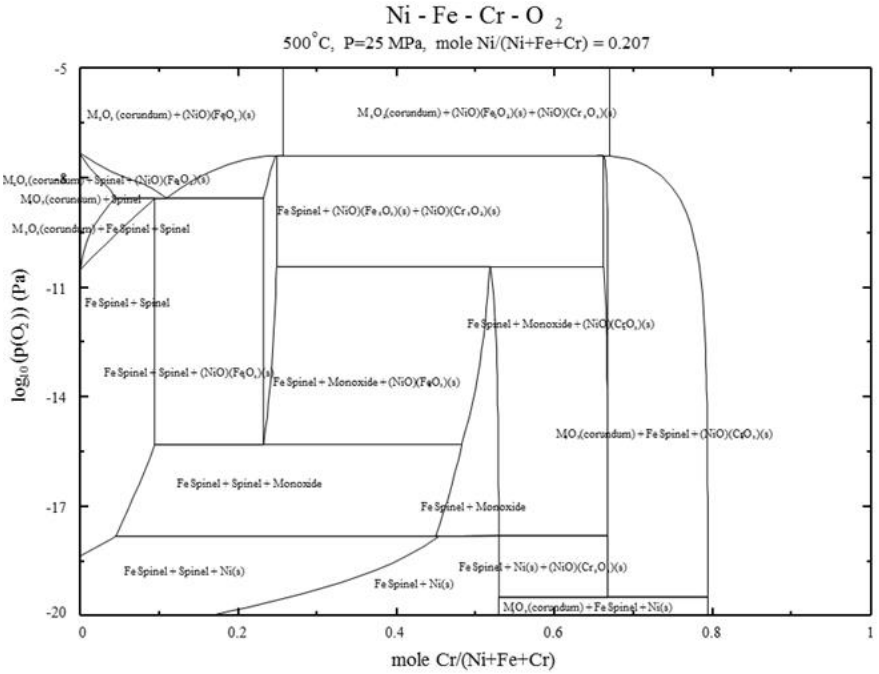

Figure 4-15: Calculated diagram of phases versus oxygen partial pressure for the Fe-Cr-O_2-Ni system.

The phase with FCC structure is Ni, the phases with spinel structure are Fe_3O_4 and $FeCr_2O_4$, and the phases with the corundum structure are $(Fe,Cr)_2O_3$ and Cr_2O_3. Tan et al.[38] reported that the partial pressure of oxygen was about 2×10^{-16} atm on the outer surface of oxides formed in metal tubing exposed to SCW containing 25 ppb dissolved oxygen. This calculation was performed by correlating the fitted parabolic rate constant with diffusion equation using Wagner's relation. In this study, water with 25 ppb dissolved oxygen was used as the main feed. Based on these premises and the stability diagram, a stable phase formation depends on the molar fraction of chromium in each layer which can be Fe_3O_4, $FeCr_2O_4$, Fe and Fe_2O_3 or Cr_2O_3. However, there is no chromium in the outer layer, which suggests that the outer layer may possibly be Fe_3O_4. The oxygen partial pressure of the inner oxide layer was lower than that of the outer layer. It is possible to detect chromium in the inner layer, therefore $FeCr_2O_4$ can be detected in the inner layer. This deduction is in accordance with XRD patterns, SEM micrographs, and EDS analysis results.

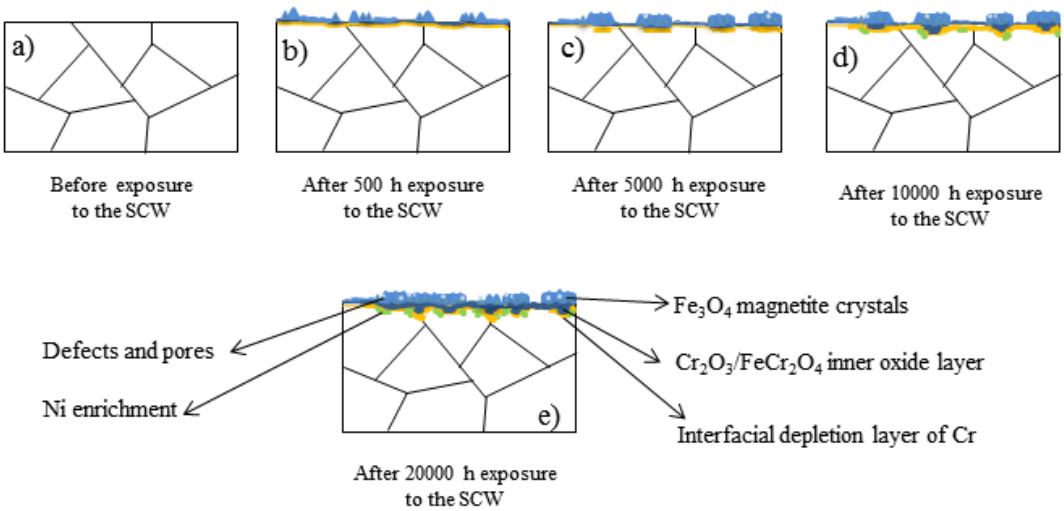

Figure 4-16: Schematic representation of the oxide formed on an SS 310S tube sample, (a) before exposure, and after (b) 500 h, (c) 5000 h, (d) 10000 h, and (e) 20000 h SCW exposure.

4.4.2 Oxidation and Cracking Susceptibility Mechanism of the SS 310S in the SCW

Oxidation of the SS 310S sample is described below according to the experimental results. The oxidation behaviour of steel in a supercritical condition is similar to that in a gaseous environment. Oxidation in gaseous environments is dominated by molecular processes and the diffusion rates of anions and cations in the oxide are rate determining steps.[8] Figure 4-16 summarizes the oxidation mechanism in the SS 310S exposed for different times at 500 °C and 25 MPa. Oxidation of SS 310S in an aqueous environment results in the formation of two distinct oxide layers, an outer layer composed of magnetite crystallites (Fe_3O_4) and a compact inner layer interfacial with the alloy surface. Iron and chromium enriched spinel phase, depending on the stoichiometry (Fe-Cr spinel type), may be disposed on the inner and outer oxide layers. Inner and outer layer characteristics are quite different in terms of chemical composition and crystallinity.

Generally, diffusion phenomena play an important role in the formation of an oxide layer. Based on the higher oxygen affinity of chromium than iron, chromium oxide can be formed at the initial stage of oxidation where oxygen partial pressure is high, however, due to hydrothermal assisted evaporation of chromium oxide and different rates of chromium diffusion in grains and grain boundaries, some areas will be chromium depleted. This phenomenon leads to a lack of protection of the substrate metal in the chromium depleted oxide regions. Fe diffuses outward along grain boundaries and causes short-circuit paths to form Fe_3O_4.[39-41] Following this mechanism, iron cations diffuse from the inner oxide layer to the outer oxide layer and react with oxygen to form the iron-rich outer oxide layer. At the same time, oxygen anions diffuse to the

inner oxide layer to form the chromium-rich inner oxide layer.[42] Furthermore, the reaction between Cr_2O_3 and Fe results in formation of a Fe-Cr spinel ($FeCr_2O_4$).

EDS analysis of the cross-section specimens exposed to SCW for different exposure times confirmed that the inner oxide layer mainly consisted of Fe-Cr spinel. In addition, a thin layer of Cr_2O_3 was detected at the inner oxide/metal substrate interface. With prolonged exposure up to 20000 h, Fe can migrate through the spinel layer and reacts with water, resulting in the formation of a thick Fe_3O_4 layer. The same oxide layer structure was observed in cross sections of tube samples taken from SS 310S capsules exposed to SCW for different times. Oxidation of iron and chromium is thermodynamically favorable at the initial partial pressure of oxygen in this study.[8] However, based on the static nature of the SS 310S capsule, with no continuous oxygen supply and a long test duration, the initial oxygen would be rapidly consumed and a deaerated condition would be reached.

Was et al.[9,10] proposed that since chromium diffusion in the austenitic alloy structure is fairly low at 500 °C, outward diffusion of iron and inward diffusion of oxygen, favored formation of a double layer structure consisting of an iron-rich oxide on top and a chromium enriched phase in the inner oxide layer. However, as the alloy SS 310S has higher bulk chromium content, it promotes formation of a corundum-type $[Cr,Mn]_2O_3$ external layer. Small amount of magnetite crystals can form after 500 h exposure to the SCW. Cross-sectional SEM micrographs consistently illustrated a double layer structure of homogenous oxide film on the SS 310S samples exposed to SCW for 500 h at 500 °C. According to the XRD patterns, the main phases in the scales were chromium-iron spinel. Prolonging the SCW exposure time led to the

formation of a thick porous magnetite scale with an inner oxide layer (adjacent to the metal substrate) consisting mainly of a spinel structure.

The critical chromium concentration for transforming less-protective internal oxidation ($FeCr_2O_4$) into more-protective external oxidation (e.g. Cr_2O_3), causing a decrease in oxygen inward diffusion in austenitic Fe-Cr-Ni alloys, reported to be approximately 20 wt.%.[43,44] It has been proposed that a spinel $FeCr_2O_4$ layer is less protective than a chromium -rich $[Mn,Cr]_2O_3$ layer because Fe diffusion in a spinel $FeCr_2O_4$ layer is three times faster than chromium, whereas Fe and Cr diffusion coefficients in a Cr_2O_3 layer are similar.[45] The formation of a $[Fe,Cr]_3O_4$ layer on top of a protective corundum-type $[Cr,Mn]_2O_3$ external layer has been rationalized by the solubility of Fe in Cr_2O_3, which allows its outward diffusion to the oxide surface. The critical chromium concentration to prevent this formation from happening is reported to be 25 wt.%.[45] It has been reported that an increase in the bulk chromium content reduces the Fe activity in the near-surface regions, correspondingly reducing the Fe solubility in Cr_2O_3.[45]

The formation of a corundum-type $[Cr,Mn]_2O_3$ external layer on SS 310S (24.4 wt.% Cr) as well as the absence of an outer $[Fe,Cr]_3O_4$ layer is consistent with these reported tendencies. Thus, the formation of the corundum-type $[Cr,Mn]_2O_3$ external layer was likely responsible for the superior corrosion resistance of SS 310S relative to SS 316L since SS 316L has a lower chromium content (about 17.2 wt.% Cr).[46,47] An increase in the SCW exposure time, inward diffusion of oxygen and outward diffusion of Fe could possibly have led to the formation of porous magnetite islands on the outer surface of the scale and Fe-Cr spinel structures in the inner oxide layer. The sustained growth of the protective Cr_2O_3 external layer is well known to be dependent on the chromium diffusion, not only from grains and grain boundaries in the near-

surface region but also from grains and grain boundaries deeper in the alloy.[48] Such a condition tends to form a chromium-depleted zone in the alloy. The higher the chromium alloying content, the shallower the depleted zone.

SEM images of the sample exposed to SCW for 20000 h (Figure 4-5) showed many pores in the outer oxide layer; pores play an important role in the diffusion of ions through the oxide film. The porosity can be attributed to the formation of a Fe_3O_4 phase, with a structure of $(Fe^{3+}, Fe^{2+})(Fe^{2+}, Fe^{3+}, Va)_2(Fe^{2+}, Va)(O^{2-})_4$. (Fe^{3+}, Fe^{2+}) and (Fe^{2+}, Fe^{3+}, Va) represent tetrahedral and octahedral sublattices respectively, for the iron cations, (Fe^{2+}, Va) represents an interstitial sublattice between the cation and anion sublattices to account for deviations from stoichiometry, and (O^{2-}) represents oxygen anions.[49,50] The vacancies combined and formed pores when the vacancy concentration in Fe_3O_4 is sufficiently high.[51] After SS 310S capsules were exposed to SCW for 20000 h at 500 °C and 25 MPa, the oxide layers presented a lower concentration of iron and higher concentration of oxygen at the grain boundaries, compared with the bulk grains. This shift in ion concentrations resulted in chromium oxide formation. Oxygen-nickel interactions were minimal because chromium has a higher affinity toward oxygen than nickel[31] therefore Ni segregates at the inner oxide/SS 310S tube sample interface. Cation diffusion in a chromium - rich oxide layer has been known to be smaller than that in Fe- or Ni-rich oxides. The presence of a Cr-rich layer thus decreases the growth rate of the oxide scale, acting as a barrier against the diffusion of metal and oxygen ions.[8] In summary, the following sequence was observed in the cross-section image of a tube sample taken from a SS 310S capsule exposed to SCW: Fe_3O_4 + Fe-Cr spinel/Cr_2O_3/Ni-enrichment/SS 310S metal substrate, from the inside to the outside of the SS 310S tubing.

Scott et al.[16] proposed that intergranular SCC can be explained by selective internal oxidation. Based on this model, selective oxidation of chromium oxide in grain boundaries leads to embrittlement followed by crack initiation. Oxide formation is dependent on oxygen diffusion, which can be hindered by surface film formation. Thus, the oxide layer plays an important role to prevent selective internal oxidation[17] (SIO and crack propagation). In constant extension rate tests (CERTs), stainless steel alloys in a pressurized water environment showed presence of a thin oxide layer around intergranular cracks.[17] An increase in chromium content can improve the resistance to SIO and intergranular stress corrosion cracking (IGSCC) by promoting formation of a protective oxide layer which limits the diffusion of oxygen.[36] CERT experiments on SCC of metals in SCW under accelerated conditions suggested that SCC might be initiated from surface-environmental interactions.[4,5,18] For SS 310S, it was proposed that tarnish-rupture was the cracking mechanism at the primary development stage and as the crack tip stress elevated, crack initiation was facilitated.[4] In this study, due to a low magnitude of applied stress, only the primary stage of the tarnish-rupture mechanism was observed in the tube samples. A combination of hoop stress and the formation of heterogeneous oxidation pits on the inner tube wall facilitated SCC crack initiation and intergranular cracking beneath the oxide layer.[36]

4.5 Conclusions

The oxidation and cracking susceptibility of SS 310S alloy was investigated in supercritical water at 500 °C and 25 MPa for different exposure times. The presence of alloying elements played an important role in ion diffusion phenomenon and also in the formation of an oxide layer on the inner wall of capsules exposed to SCW. After 20000 h exposure to SCW, iron diffused

outward and oxygen diffused inward in the SS 310S. SEM observations of the oxide scales and cross-sectional EDS elemental analysis indicated that the oxide layer was composed of two distinct layers: an outer layer composed mainly of granular magnetite (Fe_3O_4) and an inner layer (adjacent to the metal substrate) composed of fine grains of chromium-rich spinel oxide ($FeCr_2O_4$). The crystallite size of the oxide increased with SCW exposure to 20000 h. Nickel enrichment was observed at the metal/oxide interface of samples exposed to SCW for 20000 h. XRD results were consistent with Fe_3O_4, $FeCr_2O_4$, and Fe_2O_3/Cr_2O_3 phases on the outer surface of the oxide layer. Microcracks were observed beneath the inner oxide layer, interfacial with the metal substrate. Microcrack tips were filled with a chromium-rich oxide and enriched with nickel. Oxidation and crack susceptibility mechanisms were proposed for the SS 310S upon exposure to SCW corrosive environment.

Acknowledgments

The authors gratefully acknowledge financial support from the NSERC/NRCAN/AECL CRD program.

4.6 References

1 K.H. Chang, S.M. Chen, T.K. Yeh, J.J. Kai, Effect of dissolved oxygen content on the oxide structure of Alloy 625 in supercritical water environments at 700°C, Corros. Sci., 81 (2014) 21–26.

2 G. Was, S. Teysseyre, Z. Jiao, Corrosion of austenitic alloys in supercritica water, Corros., (2005) 1–20.

3 P. Kritzer, Corrosion in high-temperature and supercritical water and aqueous solutions: a review, J. Supercrit. Fluids., 29 (2004) 1–29.

4 H.L. Hu, Z.J. Zhou, L. Liao, L. Zhang, M. Wang, S.F. Li, et al., Corrosion behavior of a 14Cr-ODS steel in supercritical water, J. Nucl. Mater., 437 (2013) 196–200.

5 R. Novotný, P. Janík, S. Penttilä, P. Hähner, J. Macák, J. Siegl, et al., High Cr ODS steels performance under supercritical water environment, J. Supercrit. Fluids., 81 (2013) 147–156.

6 R. Zhou, E.A. West, Z. Jiao, G. Was, Irradiation-assisted stress corrosion cracking of austenitic alloys in supercritical water, J. Nucl. Mater., 395 (2009) 11–22.

7 Y. Zeng, J. Li, B.S. Amirkhiz, W. Zheng, M. Matchim, M. Podlesny, Corrosion and stress corrosion cracking of UNS S31008 and UNS N08810 alloys in supercritical water, in: Corros., (2015).

8 M. Sun, X. Wu, Z. Zhang, E.-H. Han, Oxidation of 316 stainless steel in supercritical water, Corros. Sci., 51 (2009) 1069–1072.

9 S. Cissé, L. Laffont, B. Tanguy, M.-C. Lafont, E. Andrieu, Effect of surface preparation on the corrosion of austenitic stainless steel 304L in high temperature steam and simulated PWR primary water, Corros. Sci., 56 (2012) 209–216.

10 J. Bischoff, A.T. Motta, EFTEM and EELS analysis of the oxide layer formed on HCM12A exposed to SCW, J. Nucl. Mater., 430 (2012) 171–180.

11 M. Le Calvar, P.M. Scott, T. Magnin, P. Rieux, Strain Oxidation Cracking of Austenitic Stainless Steels at 610°C, Corrosion., 54 (1998) 101–105.

12 R. Nishimura, Characterization and perspective of stress corrosion cracking of austenitic stainless steels in acid solutions using constant load method, Corros. Sci., 49 (2007) 81–91.

13 S. Penttilä, A. Toivonen, J. Li, W. Zheng, R. Novotny, Effect of surface modification on the corrosion resistance of austenitic stainless steel 316L in supercritical water conditions, J. Supercrit. Fluids., 81 (2013) 157–163.

14 K. Arioka, T. Yamada, T. Terachi, G. Chiba, Cold work and temperature dependence of stress corrosion crack growth of austenitic stainless steels in hydrogenated and oxygenated high-temperature water, Corros., (2007) 1114–1123.

15 S.N. Lvov, Advanced techniques for high temperature electrochemical and corrosion studies, Corros., (2004) 1–16.

16 W. Zieliński, K. Kurzydłowski, TEM studies of the oxide scales formed on type 316 stainless steel during annealing at 600 °c in a vacuum and air, Scr. Mater., 43 (2000) 33–37.

17 Z. Shen, L. Zhang, R. Tang, Q. Zhang, SCC susceptibility of type 316Ti stainless steel in supercritical water, J. Nucl. Mater., 458 (2015) 206–215.

18 Z. Shen, L. Zhang, R. Tang, Q. Zhang, The effect of temperature on the SSRT behavior of austenitic stainless steels in SCW, J. Nucl. Mater., 454 (2014) 274–282.

19 P. Ampornrat, G. Gupta, G. Was, Tensile and stress corrosion cracking behavior of ferritic–martensitic steels in supercritical water, J. Nucl. Mater., 395 (2009) 30–36.

20 E.A. West, G. Was, IGSCC of grain boundary engineered 316L and 690 in supercritical water, J. Nucl. Mater., 392 (2009) 264–271.

21 G. Gupta, P. Ampornrat, X. Ren, K. Sridharan, T.R. Allen, G. Was, Role of grain boundary engineering in the SCC behavior of ferritic–martensitic alloy HT-9, J. Nucl. Mater., 361 (2007) 160–173.

22 S. Teysseyre, Q. Peng, G. Was, Stress corrosion cracking of neutron- irradiated stainless steels in supercritical water material studies required for SCWR, J. Nucl. Mater., 371 (2007) 98–106.

23 J. Konys, S. Fodi, J. Hausselt, H. Schmidt, V. Casal, Corrosion of High-Temperature Alloys in Chloride-Containing Supercritical Water Oxidation Systems, Corrosion., 55 (1999) 45–51.

24 S. Teysseyre, Q. Peng, C. Becker, G. Was, Facility for stress corrosion cracking of irradiated specimens in supercritical water, J. Nucl. Mater., 371 (2007) 98–106.

25 A. D. Siwy, T.E. Clark, a. T. Motta, Transmission electron microscopy of oxide development on 9Cr ODS steel in supercritical water, J. Nucl. Mater., 392 (2009) 280–285.

26 X. Zhong, X. Wu, E.-H. Han, Effects of exposure temperature and time on corrosion behavior of a ferritic–martensitic steel P92 in aerated supercritical water, Corros. Sci., 90 (2015) 511–521.

27 O. Yeliseyeva, V. Tsisar, Z. Zhou, Corrosion behavior of Fe–14Cr–2W and Fe–9Cr–2W ODS steels in stagnant liquid Pb with different oxygen concentration at 550 and 650°C, J. Nucl. Mater., 442 (2013) 434–443.

28 I. Wright, B. Pint, An assessment of the high temperature oxidation behavior of fe-cr steels in water vapor and steam, Corros., (2002).

29 E.A. West, Influence of local stress and strain on intergranular cracking of 316L stainless steel in supercritical water, Michigan, (2010).

30 D. Rodriguez, A. Merwin, D. Chidambaram, On the oxidation of stainless steel alloy 304 in subcritical and supercritical water, J. Nucl. Mater., 452 (2014) 440–445.

31 M. Nezakat, H. Akhiani, S. Penttilä, S.M. Sabet, J. Szpunar, Effect of thermo-mechanical processing on oxidation of austenitic stainless steel 316L in supercritical water, Corros. Sci., (2015).

32 J. Weiss, A. Pineau, Fatigue and creep-fatigue damage of austenitic stainless steels under multiaxial loading, Metall. Trans. A., 24 (1993) 2247–2261.

33 D.S. Morton, S.A. Attanasio, G.A. Young, P.L. Andersen, T.M. Angeliu, P.L. Andresen, The influence of dissolved hydrogen on nickel alloy SCC: A window to fundamental insight, (2000).

34 D. Guzonas, J.S. Wills, G.A. McRae, S. Sullivan, K. Chu, K. Heaslip, Corrosion- resistant coating for use in a supercritical water CANDU reactor, in: 12th Int. Conf. Environ. Degrad. Mater. Nucl. Power Syst. React., (2005). 1379–1386.

35 A.H. Harvey, E.W. Lemmon, NIST / ASME Steam Properties-STEAM-Version 3.0, U.S. Dep. Commer. Natl., 20899. (2013).

36 Z. Suo, D.V. Kubair, A.G. Evans, D. Clarke, V.K. Tolpygo, Stresses induced in alloys by selective oxidation, Acta Mater., 51 (2003) 959–974.

37 Z. Suo, A continuum theory that couples creep and self-diffusion, J. Appl. Mech., 71 (2004) 646.

38 L. Tan, Y. Yang, T.R. Allen, Oxidation behavior of iron-based alloy HCM12A exposed in supercritical water, Corros. Sci., 48 (2006) 3123–3138.

39 A. D. Siwy, T.E. Clark, a. T. Motta, Transmission electron microscopy of oxide development on 9Cr ODS steel in supercritical water, J. Nucl. Mater., 392 (2009) 280–285.

40 X. Zhong, X. Wu, E.-H. Han, Effects of exposure temperature and time on corrosion behavior of a ferritic–martensitic steel P92 in aerated supercritical water, Corros. Sci., 90 (2015) 511–521.

41 J. Bischoff, A.T. Motta, Oxidation behavior of ferritic-martensitic and ODS steels in supercritical water, J. Nucl. Mater., 424 (2012) 261–276.

42 J. Bischoff, A.T. Motta, R.J. Comstock, Evolution of the oxide structure of 9CrODS steel exposed to supercritical water, J. Nucl. Mater., 392 (2009) 272–279.

43 I. Wright, R. Dooley, A review of the oxidation behaviour of structural alloys in steam, Int. Mater. Rev., 55 (2010) 129–167.

44 B. Pint, Effect of water vapor on the oxidation resistance of stainless steel, Corros, 259 (2000).

45 S. Mahboubi, Effect of Cr content on corrosion resistance of Fe-Cr-Ni alloys exposed in supercritical water, MacMaster, (2014).

46 T. Terachi, T. Yamada, T. Miyamoto, K. Arioka, K. Fukuya, Corrosion Behavior of Stainless Steels in Simulated PWR Primary Water—Effect of Chromium Content in Alloys and Dissolved Hydrogen—, J. Nucl. Sci. Technol., 45 (2008) 975–984.

47 T. Terachi, K. FUJII, K. ARIOKA, Microstructural characterization of SCC crack tip and oxide film for SUS 316 stainless steel in simulated PWR primary water at 320 C, J. Nucl. Sci., 42 (2005) 225–232.

48 S.C. Tsai, A.M. Huntz, C. Dolin, Diffusion of O^{18} in massive Cr_2O_3 and in Cr_2O_3 scales at 900 °C and its relation to the oxidation kinetics of chromia forming alloys, Oxid. Met., 43 (1995) 581–596.

49 J. Bischoff, A.T. Motta, Oxidation behavior of ferritic-martensitic and ODS steels in supercritical water, J. Nucl. Mater., 424 (2012) 261–276.

50 J. Bischoff, A.T. Motta, R.J. Comstock, Evolution of the oxide structure of 9CrODS steel exposed to supercritical water, J. Nucl. Mater., 392 (2009) 272–279.

51 H. Hu, Z. Zhou, M. Li, L. Zhang, M. Wang, S. Li, et al., Study of the corrosion behavior of a 18Cr-oxide dispersion strengthened steel in supercritical water, Corros. Sci., 65 (2012) 209–213.

Chapter 5: Oxidation and Cracking Susceptibility of 310S Stainless Steel in Supercritical Water: Part II - Transmission Electron Microscopy Observations

5.1 Introduction

The supercritical water reactor (SCWR) is one of the Generation IV nuclear reactor concepts currently being studied to meet future demands for efficient and safe energy production.[1] A SCWR that uses SCW as the coolant has high thermal efficiency and a simplified single phase coolant design compared to current light water reactors.[2] Supercritical water (SCW) resembles a nonpolar solvent that can dissolve gases like oxygen to complete miscibility.[3] Water above a temperature of 374.15 °C and a pressure of 22.1 MPa is in a supercritical state and acts as a dense gas exhibiting properties significantly different from that of water below the critical point.[2-3] At the critical point, the specific enthalpy of water increases by 20% and water behaves as a single phase.[2-4]

Processes that affect the lifetime of candidate SCWR materials in relevant conditions need to be identified and their mechanisms studied through extensive experimental tests. For example, oxide scales that form on metal substrates are very well known to affect the properties of engineering materials. Austenitic stainless steels (SS) have been found to have high corrosion resistance in high temperature SCW, and several researchers have studied oxidation and SCC of

Material in this chapter has been submitted for publication in Corrosion Science.

austenitic alloys exposed to SCW corrosive environments.[5-11] Parameters affecting austenitic SS's response to a SCC media in the usual operational conditions include water temperature, chemical composition, and pressure.[12,13]

Various investigations have been conducted to study high temperature oxidation of steel in air or oxygen.[9,14-17] The oxide layers that form on austenitic SS during SCW exposure have been analyzed using scanning electron microscopy (SEM), X-ray diffraction (XRD), electron backscatter diffraction (EBSD), and transmission electron microscopy (TEM).[17-22] These investigations have shown that a complex oxide layer composed of hematite, magnetite, Cr_2O_3, and $FeCr_2O_4$ spinel may form on steel with low chromium content. Was et al.[23-28] proposed that two oxide layers formed on SS samples upon exposure to SCW: an outer oxide layer mainly composed of large nonuniform grains of magnetite and an inner compact fine-grained oxide layer which firmly adhered to the substrate. The inner oxide layer was reported to be generally nonporous, chromium rich, and very protective for the substrate metal. It is assumed that at high temperatures, oxides on low-alloy steels grow by an outward diffusion of Fe due to the sluggish oxygen anions diffusion through the iron oxides lattice.[15-21] Although oxidation is variable based on the SS composition and solution oxygen level, SCW can be a very aggressive oxidizing environment. Consequently, understanding the oxidation mechanism and cracking susceptibility of SS in SCWR environments is of vital importance for their industrial applications.[22-37]

The objective of this research is to study SCC susceptibility of SS 310S in SCW at 500 °C and 25 MPa after protract exposure. The purpose of the TEM analysis was firstly to determine nanometer scale morphology of the film and secondly to analyze chemical composition of the oxide film at high magnifications. The formed oxide layers were characterized using

transmission electron microscopy (TEM) equipped with energy-dispersive X-ray spectroscopy (EDS), selected area electron diffraction (SAED), high resolution TEM images with corresponding fast Fourier transform (FFT) patterns, and electron energy loss spectroscopy (EELS).

5.2 Experimental and Instrumentations

5.2.1 Materials

310S stainless steel tubes with an outer diameter of 9.525 mm and a wall thickness of 1.65 mm were purchased from Swagelok. The tubes were manufactured according to the specification defined in ASTM-A213 for stainless steels and were supplied in a solution annealed state. Table 5-1 shows the chemical composition of the alloy used in the present research in weight percent (wt. %).

Table 5-1: Chemical elemental analysis of the SS 310S.

Alloy	**Chemical Composition (wt. %)**								
310S Stainless Steel	Fe	C	Cr	Ni	P	Si	Mo	Mn	S
	Balance	0.029	17.2	11.7	0.022	0.84	2.14	1.97	0.027

Tube samples were cut in segments of 10 cm long to make capsule specimens for SCW exposure. Tube sections were cleaned ultrasonically with pentane, isopropyl alcohol, and acetone to be degreased thoroughly prior to exposure to neutral pH deionised (DI) water containing 8 ppm dissolved oxygen (DO). Two high pressure caps were used to make static capsules from

tube sections. The static capsules were placed in a tubular furnace and heated to 500 °C for 20000 h. The temperature of the furnace was calibrated using Nextel ceramic insulated lead wire rated to 815 °C (Omega) as the reference thermocouple. Upon heating the water in a closed system, water vapor pressure builds up and pressurizes the tube. This pressure is directly related to the water volume and temperature. According to the NIST steam chart,[38] the pressure of a tube filled with a 9.5% volume by DI water is 25 MPa at 500 °C. As such, the tube is under axial and hoop stresses, which can be readily calculated.

5.2.2 Characterization

After SCW exposure, the tubes were cut into small segments. A thin layer of nickel were plated onto the ID surface of the tube samples to avoid spallation of the oxide film during sample preparation. For microscopic examinations, samples were mounted with epoxy resin and polished down to 0.5 μm in alumina solution. Tube samples were prepared for transmission electron microscopy (TEM) using the focused-ion-beam (FIB) lift-out technique. Electron transparent samples were prepared using an ion beam voltage of 40 keV with the current dropping from 7 nA to 35 pA. Scanning transmission electron microscopy (STEM) imaging using high-angle annular-dark-field (HAADF) contrast and EDS mapping was utilized for characterization of the cross-sections of samples exposed to SCW. To characterize the oxidized region ahead of the microcrack tip and for phase identification, conventional bright field imaging and electron diffraction techniques were applied. TEM was performed using FEI's Tecnai Osiris TEM equipped with an X-FEG gun at 200 keV. EELS/EDS line profile measurements were performed on at least 100 points per line profile. Spectra at 0.3 eV/channel (1340 channels) were

obtained in the range of 500 to 900 eV. After obtaining a spectrum series, in order to get profiles for each element (counts as a function of distance), the background was first subtracted in the EELS spectra series, and profiles were extracted from spectra by placing an energy window of appropriate width over each element's edge. EELS spectra from a few points throughout the line profile were assumed to represent the overall features of each series. Characterization of phases was performed by selected area electron diffraction (SAED) and EELS spectra with the help of Gatan Microscopy Suite® software (GMS), version 3.11.

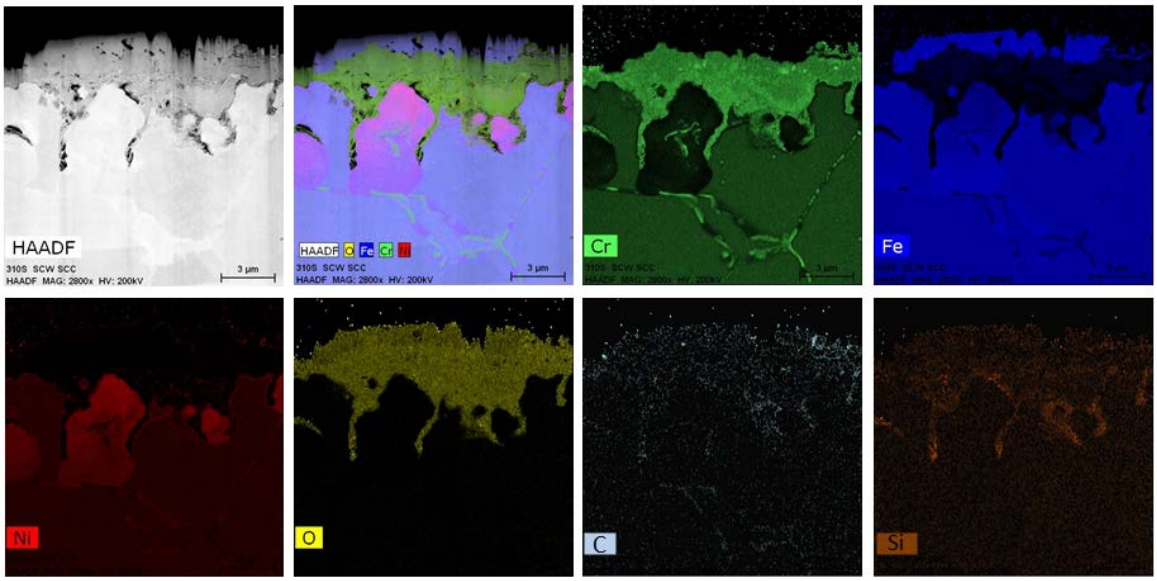

Figure 5-1: High angle annular dark field (HAADF) image with EDS elemental maps for Cr, O, Fe, Ni, Si and C from the substrate and the oxide layer after 20000 h SCW exposure at 500 °C and 25 MPa.

5.3 Results and Discussions

Figure 5-1 shows high angle annular dark filed (HAADF) micrograph with EDS overlay of Cr, O, Fe, and Ni and individual elemental maps for Fe, Ni, Cr, O, C, and Si from the oxide layer inside the capsule after 20000 h SCW exposure at 500 °C and 25 MPa. The qualitative chemical

analysis indicated that chromium enrichment took place at the frontier of oxide and segregation of Ni happened at the tip and upper part of the inner oxide layer, respectively. As seen, Fe elemental map demonstrates that iron was present on the outer surface of the substrate and indicates that the outer oxide layer inside the tubing was mainly composed of Fe. Oxygen was present both in the outer and inner oxide layers. The carbon EDS map suggested that carbide might be formed at the grain boundaries due to high temperature corrosion. Based on the elemental distribution on the EDS overlay of Cr, O, Fe, and Ni elements, it was possible to identify the phases in the oxide layers formed on the SS 310S tubing ID surface.

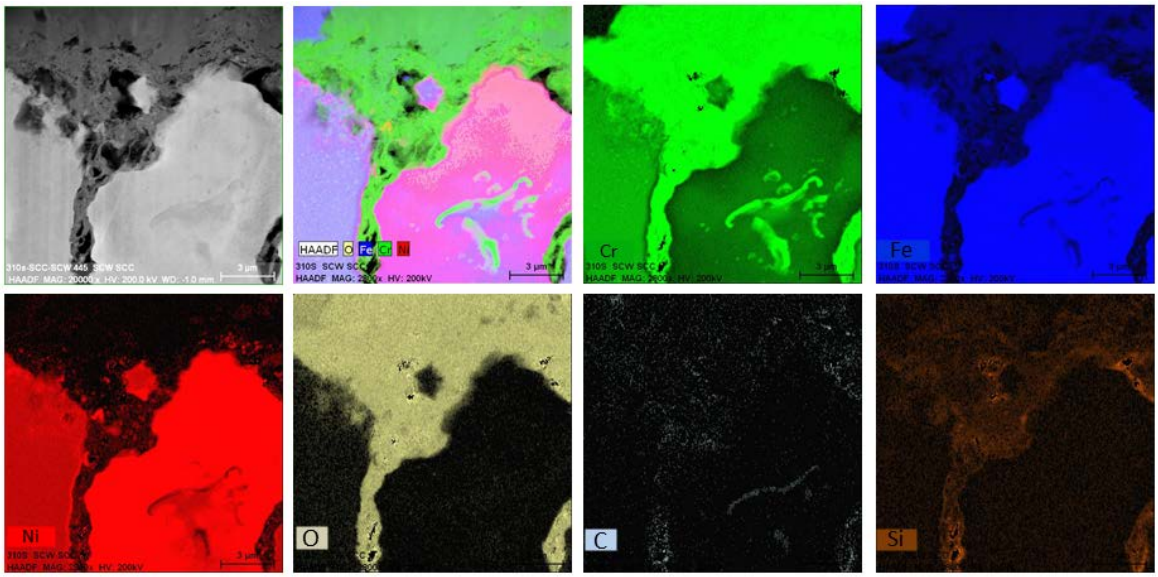

Figure 5-2: STEM-HAADF micrograph with corresponding EDS elemental maps for Cr, O, Fe, Ni, Si and C obtained from a micro-crack close to the substrate/oxide layer interface after 20000 h SCW exposure at 500 °C and 25 MPa.

In order to study the phase formation and elemental distribution in microcracks and their surroundings, EDS mapping was conducted at a higher magnification compared to that in STEM-HAADF image in Figure 5-1. Figure 5-2 demonstrates STEM-HAADF micrograph with corresponding EDS Fe, Cr, Ni, O, C, and Si maps. The oxide layer was predominantly composed

of chromium and oxygen, indicative of chromium oxide and a few spinel structures presence. Ni enrichment was observed adjacent to a microcrack, showing that the depletion of elements such as nickle and chromium has occurred. Furthermore, EDS maps revealed that the microcrack was filled with chromium oxide. HAADF image and associated EDS results displaying maps for Fe, Cr, Ni, O, C, and Si at an area close to a microcrack are shown in Figure 5-3. The chromium and O EDS maps indicated that chromium oxide formed on the surface in a region in which there was no magnetite above it.

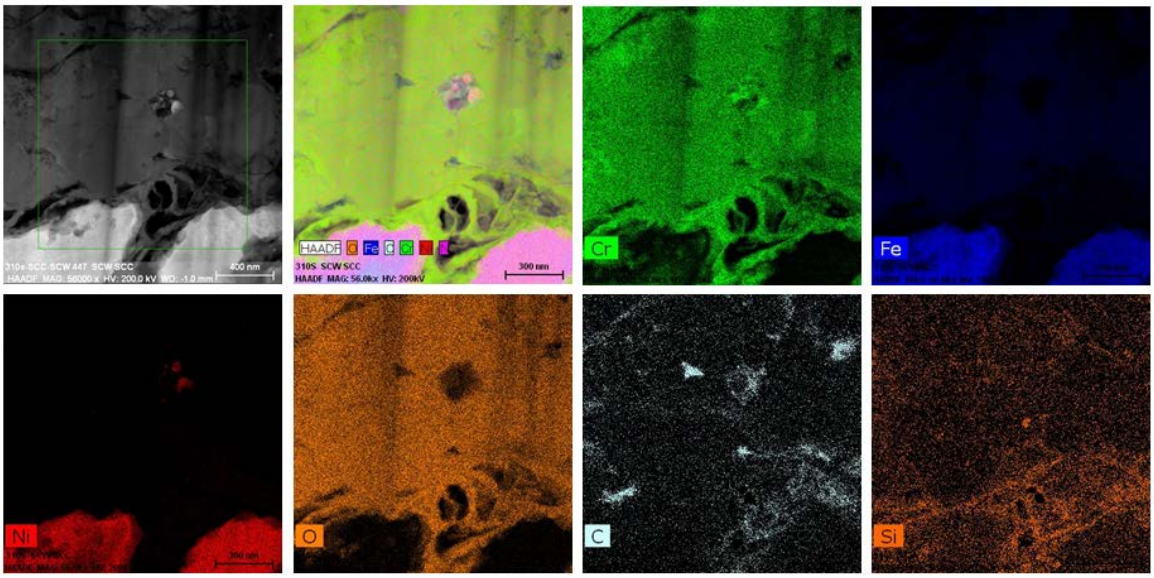

Figure 5-3: STEM-HAADF image and EDS elemental maps for Cr, O, Fe, Ni, Si and C from the substrate/oxide layer interface after 20000 h SCW exposure at 500 °C and 25 MPa.

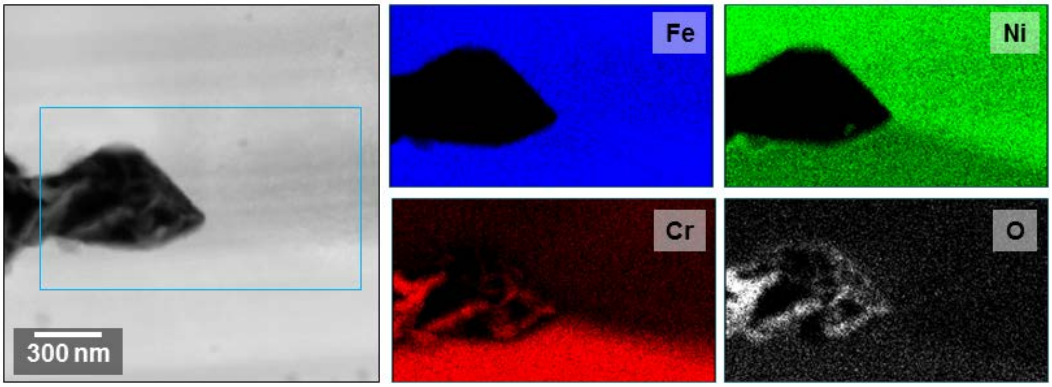

Figure 5-4: HAADF TEM image of a crack tip and corresponding elemental maps for Fe, Cr, Ni, and O.

A Cr_2O_3 thin layer covered the substrate and acted as a protective layer against the corrosive medium. Finally, the C elemental map indicates that carbide may have formed due to high temperature corrosion. High magnification TEM micrographs of microcracks and EDS maps confirmed that microcracks were free of Ni and Fe, and were filled with chromium and oxgen (Figure 5-4).

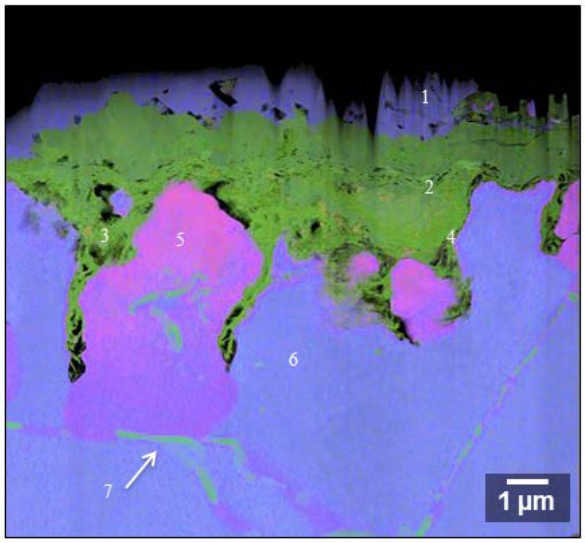

Figure 5-5: Overlay TEM-EDS elemental map of selected areas.

To extract crystallographic information of the oxide layer formed on the ID surface of the SS 310S tube, bright field micrographs and SAED patterns were collected from different points shown in Figure 5-5. Figure 5-6a shows a bright field TEM micrograph at point 1. It was expected that this area was composed of magnetite. The corresponding SAED pattern is presented in Figure 5-6b. The electron diffraction pattern obtained from point 1 indicated that the outer oxide layer was made of magnetite which was consistent with the oxidation behavior of austenitic stainless steels.

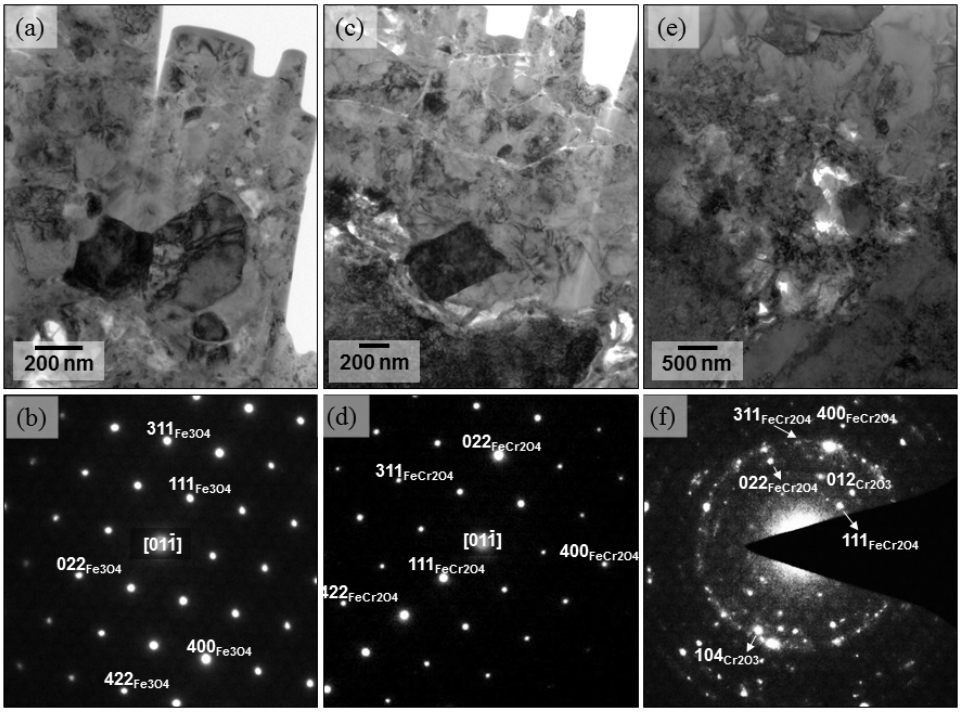

Figure 5-6: (a,b) Bright field TEM micrographs and SAED patterns from point 1, (c,d) bright field TEM micrograph and SAED patterns taken from point 2, and (e,f) bright field TEM micrograph and SAED patterns obtained from point 3.

Figure 5-6c shows a bright field image of the inner oxide layer. It is known that spinel can form in the inner oxide layer, and in case of SS 310S it is $FeCr_2O_4$.[14] The electron diffraction pattern at point 2 confirmed that the inner oxide layer consisted mainly of Fe-Cr spinel (Figure 5-6d). Figure 5-6e shows a bright field image of point 3 with a related SAED pattern from the inner oxide layer adjacent to the metal substrate (Figure 5-6f). This pattern was identified as a mixture of chromium oxide and Fe-Cr spinel, namely $Cr_2O_3/FeCr_2O_4$.

Figure 5-7a demonstrates a bright field image from point 4, representing an area with a thin chromium oxide film. In the inner oxide layer, near the oxide/metal interface, a thin layer enriched in chromium and oxygen can be identified. Because there are no other elements except for chromium and oxygen in this area, it would be assumed that chromium oxide and spinel

structures may have formed. The related SAED pattern at point 4 indicated that pure chromium oxide was formed at the oxide/substrate interface (Figure 5-7b).

Figure 5-7c and Figure 5-7d depict the bright field image from point 5 of Figure 5-5 and the corresponding SAED pattern. EDS analysis revealed segregation or enrichment of Ni at the inner oxide/metal substrate interface. Electron diffraction patterns showed that the gamma-Ni phase was present at point 5. Figure 5-7e shows a bright field TEM micrograph at point 6. The SAED pattern confirmed that the EDS results, indicating that a gamma-Fe phase was present at point 6 (Figure 5-7f).

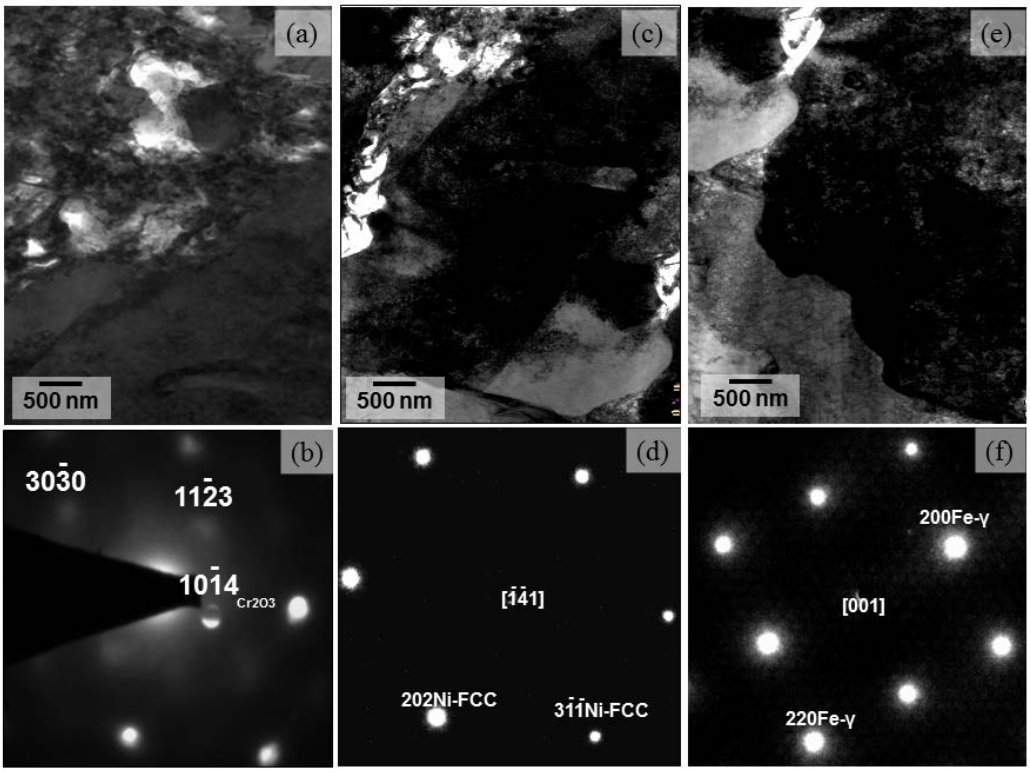

Figure 5-7: (a,b) Bright field TEM micrograph and corresponding SAED pattern from point 4, (c,d) bright field TEM micrograph and associated SAED pattern obtained from point 5, and (e,f) bright field TEM micrograph and corresponding SAED pattern from point 6.

HRTEM micrographs with corresponding fast Fourier transform (FFT) patterns from different points on sample are shown in Figure 5-8 and Figure 5-9. HRTEM image and corresponding FFT pattern of point 1 are shown in Figure 5-8a and Figure 5-8b, respectively. HRTEM micrograph and FFT pattern of a mixture of Fe-Cr spinel and chromium oxide are shown in Figure 5-8c and Figure 5-8d, respectively, suggesting that at point 3 the dominant phase was Fe-Cr spinel with a small amount of chromium oxide. HRTEM image and FFT pattern from point 4 (Figure 5-8e and Figure 5-8f, respectively) reveals presence of chromium oxide at the interface between the inner oxide layer and the SS 310S substrate.

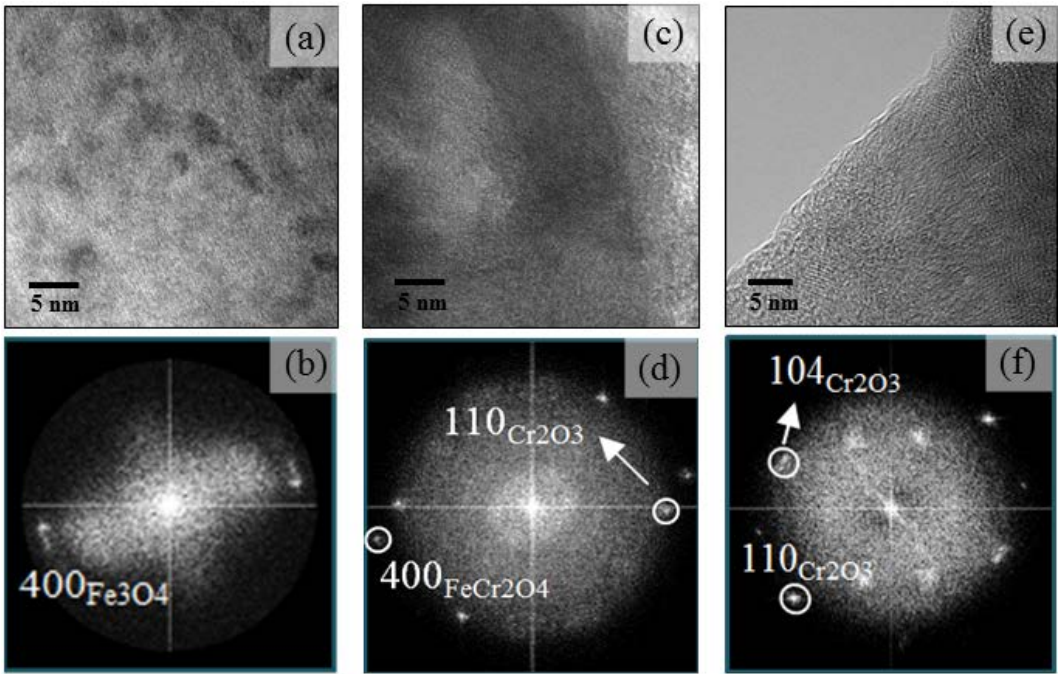

Figure 5-8: (a,b) HRTEM and corresponding FFT pattern taken from point 1, (c,d) HRTEM and FFT pattern from point 3, and (e,f) HRTEM and corresponding FFT pattern obtained from the point 4 of the Figure 5-5.

Figure 5-9a and Figure 5-9d show STEM images obtained from point 7 on the cross-section of the oxide scale. Figure 5-9b and Figure 5-9c are HRTEM micrograph and corresponding FFT

pattern of the area as labeled in Figure 5-9a. The FFT pattern in Figure 5-9c shows that Cr_7C_3 has formed at the grain boundary. Figure 5-9b shows that the carbide had small grain size. Additionally, Figure 5-9b and Figure 5-9c show HRTEM images and FFT patterns, respectively for the area indicated in Figure 5-9d. As seen in the HRTEM image, carbide with a large grain size was present at the grain boundary. The FFT pattern was utilized to determine composition of the carbide, which was $Cr_{23}C_6$.

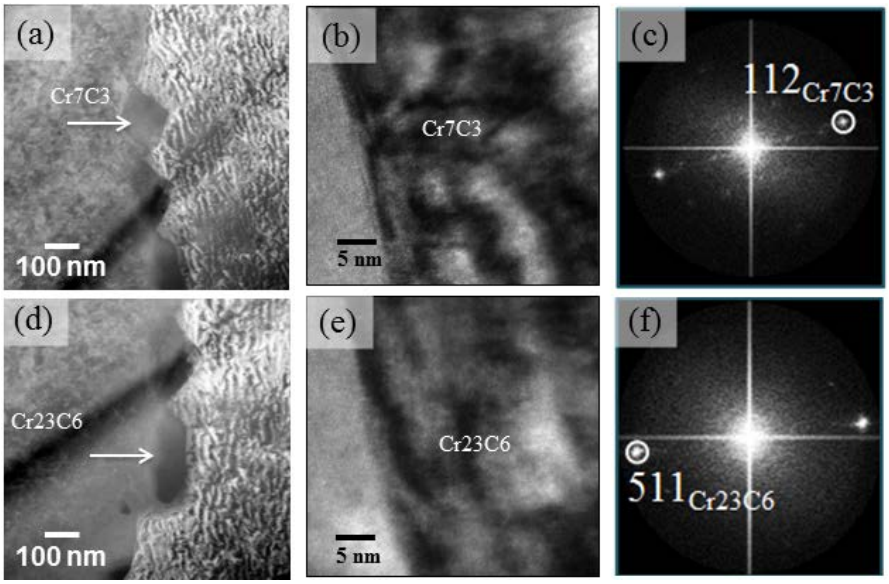

Figure 5-9: Bright field TEM micrograph, high resolution TEM, and corresponding FFT patterns taken from the grain boundaries of the area 7 on Figure 5-5, showing two different kinds of carbide including (a,b,c) Cr_7C_3 and (d,e,f) $Cr_{23}C_6$.

EELS was performed to determine chemical composition of oxide layers on SS 310S samples exposed to SCW for 20000 h at 500 °C and 25 MPa. This technique offers not only high resolution information in nanometer scale but also chemical and bonding data. According to a study by Bischoff et al.,[39] EELS analysis is a practical method to detect formation of a thin oxide layer on a metallic substrate and to study its chemical composition at various locations and depths.[40,41]

Figure 5-10a shows a TEM image taken from a cross-section of a sample exposed to SCW for 20000 h at 500 °C and 25 MPa. EELS analysis was conducted on five different locations. Point "b" was selected from the substrate metal SS 310S, and the EELS spectrum is shown in Figure 5-10b with energy ranges relevant to the elements. The Cr $L_{2,3}$ edges at ~ 582 eV, the Mn $L_{2,3}$ edges at ~ 629 eV, Fe $L_{2,3}$ edges at ~ 729 eV, and Ni $L_{2,3}$ edges at ~ 882 eV were detected. These peaks indicated that point "b" was not affected by the SCW corrosive media.

The EELS spectrum for the outer oxide layer, point "c", is illustrated in Figure 5-10c. Two distinctive group of peaks are observed in Figure 5-10c, the area between 545 eV to 573 eV which could be related to oxygen and the range between 729 eV to 751 eV known as the Fe edge. Based on energy of the edges, the outer oxide layer was identified as a defective magnetite scale. Point "d" was selected from the inner oxide layer and the EELS spectrum is shown in Figure 5-10d. The three edges shown in Figure 5-10d reveal that Fe-Cr spinel structure, $FeCr_2O_4$ may have formed. To characterize the scales in the microcrack, an EELS spectrum was collected at point "e" and the result is shown in Figure 5-10e. Similar to point "d", three apparent edges in the spectrum are characterized as spinel structures. Additionally, a small yet noticeable Mn peak is shown in the spectrum, suggesting that the scale present in the microcrack could be $[Fe,Mn]Cr_2O_4$. Finally, EELS spectrum of the crack tip, point "f", is shown in Figure 5-10f. Based on the position of the edges, two main edges correspond to oxygen and chromium and a weak edge is associated to Mn, most likely represents $[Cr,Mn]_2O_3$.

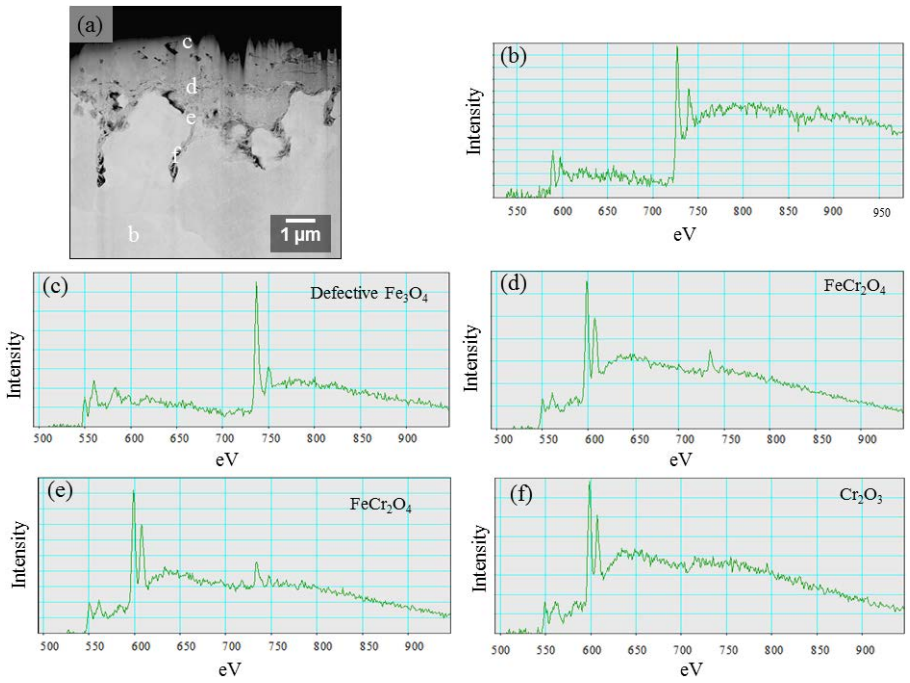

Figure 5-10: (a) HAADF micrograph taken from the cross-section of the exposed sample to the SCW for 20000 h with five selected points and corresponding EELS spectrum from (b) point "b" which is base metal, (c) point "c", the outer oxide layer, (d) point "d", the inner oxide layer, (e) point "e", the scales in the micro-crack, and (f) point "f", the crack tip.

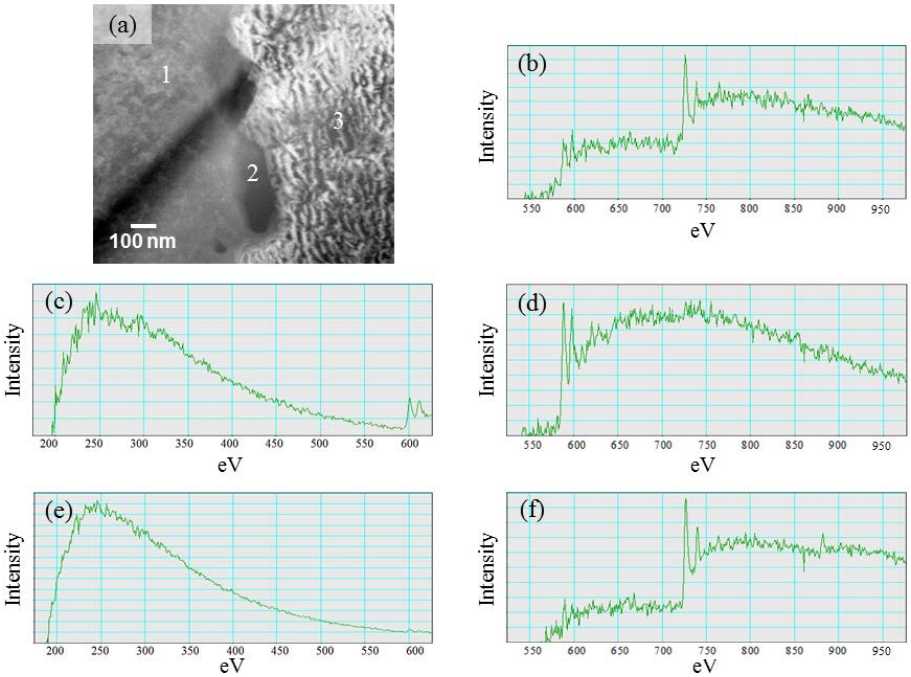

Figure 5-11: (a) HAADF TEM image from the grain boundary of the substrate near to the formed scale (as shown in Figure 5-5 as point "7"), (b) EELS spectrum for Point "1", (c,d) EELS spectrum for the Point "2", (e,f) EELS spectrum for Point "3".

Figure 5-11a shows a TEM image taken from the grain boundary of the base metal close to the formed scale (point "7" of Figure 5-5). Three locations on this micrograph were chosen for EELS analysis. EELS spectrum of point "1" is illustrated in Figure 5-11b. There are two areas with significant energy loss edges, one in the range of 586 eV to 598 eV, identified as chromium edges and the other in the range of 726 eV to 743 eV, characterized as Fe edges. These two sharp edges revealed that point "1" was from the SS 310S. Point "2" was selected from the dark oval shape area and the EELS spectra are shown in Figure 5-11c for 200 eV to 600 eV, and Figure 5-11d for 550 eV to 950 eV range of energy loss. These two spectra reveal that at point "2" chromium and C can be identified as chromium carbide. Point "3" was selected for the chemical analysis and the EELS spectra are shown in Figure 5-11e and Figure 5-11f. Fe and Ni were significant in that area while no Cr and C were detected in this region. In the other words, point "3" identified as an area in which chromium depletion and Ni enrichment took place.

The chemical compositions and microstructures of oxides/corrosion products along microcracks were examined using SEM-EDX and XRD. Results of these studies have indicated that the oxides formed at high temperatures along cracks have double layer structure, i.e. an inner layer composed of chromium rich spinel structures and an outer layer composed of iron rich magnetite phase. Although sample preparation for TEM using focused ion beam (FIB) milling is relatively slow, it is the only method that provides the means to prepare electron transparent foils from locations that can be preselected in submicrometer scale. The results show that FIB is a proper method for preparation of electron transparent lamella from specific locations within cracked specimens.[42]

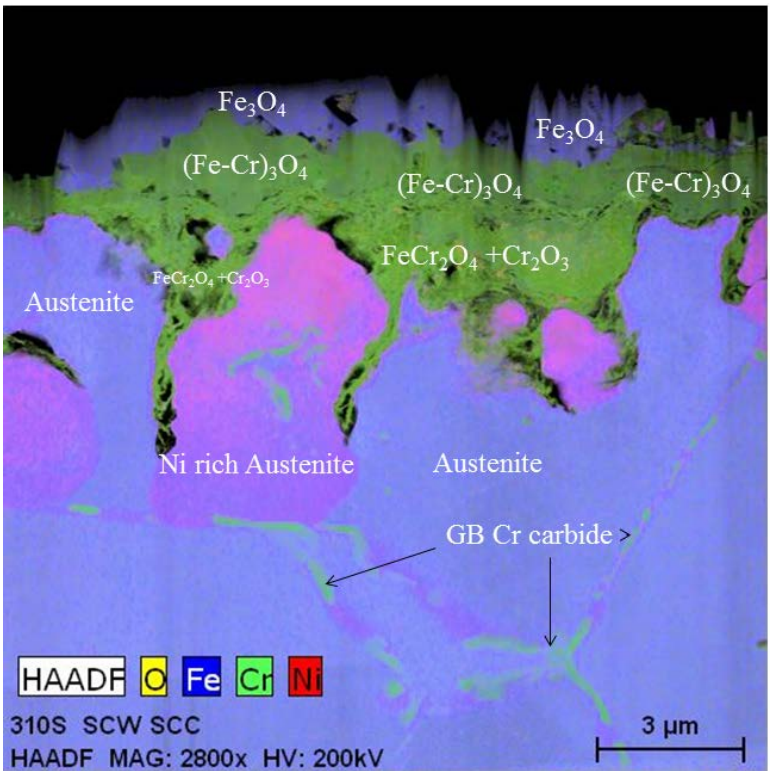

Figure 5-12: TEM-EDS overlay map with the corresponding identified phases in each area.

In this study, water with 25 ppb dissolved oxygen was used as the main feed. Based on these premises and the stability diagram, stable phase formation depends on the chromium molar fraction in each layer which can be Fe_3O_4, $FeCr_2O_4$, pure Fe, and Fe_2O_3 or Cr_2O_3. However, there is no chromium in the outer layer. Thus, the outer layer was Fe_3O_4. Chromium was detected in the inner oxide layer which implies that the layer most probably contains $FeCr_2O_4$ phase, consistent with SAED patterns, EELS spectra, and EDS elemental analyses. HRTEM and corresponding FFT patterns from the oxide layer and crack tip confirmed that there was Ni segregation as well as a thin layer of chromium oxide at the inner oxide adjacent to the SS310S metal substrate. The diffusion layer and the inner layer mainly composed of iron and chromium. However, the contents of iron and chromium in the diffusion layer were different from the inner

layer. Based on the EDS results, the difference between the inner layer and the diffusion layer would be $FeCr_2O_4$ content. Accordingly, the main phase in the outer oxide layer is magnetite. A summary of the composition and phase formation in samples exposed to SCW for 20000 h is shown in Figure 5-12.

Cross-sectional TEM and elemental analyses (EDS) indicated that the outer oxide was composed of an iron-rich oxide with a spinel structure. This was supported by FFT, SAED, and EELS analyses. Therefore, it is concluded that the outer layer is composed mainly of Fe_3O_4 which may have occurred through diffusion of iron from the metal to the oxide layer. TEM, EELS, and SAED patterns suggested that the inner layer was made of fine grained chromium-rich oxide such as Fe-Cr spinel. These results agree with those reported by Was et al.[2] who indicated that magnetite was the dominant phase in the outer oxide layer formed on stainless steel alloys such as 316L and 304 after SCW exposure 550 °C and 25 MPa. $FeCr_2O_4$ has been reported to be the dominant phase in the inner oxide layer under similar conditions.[11,24,32] SAED patterns obtained from TEM observations of tube samples of SS 310S capsules exposed to SCW for 20000 h confirmed that the inner oxide layer consisted mainly of Fe-Cr spinel. In addition, a thin Cr_2O_3 layer was detected at the oxide/metal substrate interface. TEM and EELS analyses of cross-sections of SS 310S tube sample exposed to SCW showed that with prolonged exposure Fe diffuses from the metal to the spinel layer in the outer oxide layer and upon a reaction with water a thicker Fe_3O_4 layer will form. In first stages of the experiment with initial oxygen partial pressure, iron and chromium oxidation are thermodynamically favorable.[8] However, static nature of the capsule and no oxygen supply along the protracted test result in rapid consumption of available oxygen and establishment of a deaerated condition. Was et al.[9,10] proposed that since

chromium diffusion in the austenitic structures is fairly low at 500 °C, outward diffusion of iron and inward diffusion of oxygen favored formation of a double layer film structure, consisting of an iron-rich oxide on top (outer layer) and a chromium enriched phase in the inner oxide layer.

TEM analysis also implied chromium carbide formation in the grain boundary of the SS 310S exposed to SCW. Since the carbide formed had a nanometer scale grain size, it would be difficult to detect it by conventional methods such as SEM. Moreover, the accuracy of EDS elemental analysis might be poor to detect carbides formed at the grain boundaries. High resolution TEM equipped with FFT, EDS, EELS, and SAED definitely facilitate characterization of the phases formed in samples exposed to SCW.

5.4 Conclusion

This research was aimed to study oxidation and stress corrosion cracking susceptibility of stainless steel exposed to supercritical water at high temperature for extensive periods. EDS elemental analyses, high resolution TEM observations, EELS, SAED, and FFT patterns were employed to characterize oxide films formed on the inner surface of SS 310S samples exposed to SCW at 500 °C and 25 MPa for 20000 h. The oxide film consisted of two layers; an outer layer composed mainly of granular Fe_3O_4 (magnetite) and an inner layer of fine grained chromium-rich spinel oxide, $FeCr_2O_4$. A thin chromium oxide layer was observed at the inner oxide layer/metal substrate interface. Moreover, formation of chromium carbides at grain boundaries was observed through HRTEM imaging and EELS analyses. Microcracks were observed beneath the inner oxide film. Qualitative chemical analysis of a crack tip suggested that the main

corrosion product could be chromium oxide with Ni segregation at the crack tip. Microcracks may have been initiated by the stresses induced as a result of oxide buildup and ion diffusion.

Acknowledgment

The authors gratefully acknowledge financial support from the NSERC/NRCAN/AECL CRD program.

5.5 References

1 A. D. Siwy, T.E. Clark, a. T. Motta, Transmission electron microscopy of oxide development on 9Cr ODS steel in supercritical water, J. Nucl. Mater., 392 (2009) 280–285.

2 G. Was, S. Teysseyre, S. Mckinley, Z. Jiao, Corrosion of austenitic alloys in supercritical water, Corros., (2005) 1–20.

3 P. Kritzer, Corrosion in high-temperature and supercritical water and aqueous solutions, a review, J. Supercrit. Fluids., 29 (2004) 1–29.

4 H.L. Hu, Z.J. Zhou, L. Liao, L. Zhang, M. Wang, S.F, Corrosion behavior of a 14Cr-ODS steel in supercritical water, J. Nucl. Mater., 437 (2013) 196–200.

5 M. Le Calvar, P.M. Scott, T. Magnin, P. Rieux, Strain Oxidation Cracking of Austenitic Stainless Steels at 610°C, Corrosion., 54 (1998) 101–105.

6 R. Nishimura, Characterization and perspective of stress corrosion cracking of austenitic stainless steels (type 304 and type 316) in acid solutions using constant load method, Corros. Sci., 49 (2007) 81–91.

7 S. Penttilä, A. Toivonen, J. Li, W. Zheng, R. Novotny, Effect of surface modification on the corrosion resistance of austenitic stainless steel 316L in supercritical water conditions, J. Supercrit. Fluids. 81 (2013) 157–163.

8 K. Arioka, T. Yamada, T. Terachi, G. Chiba, Cold work and temperature dependence of stress corrosion crack growth of austenitic stainless steels in hydrogenated and oxygenated high-temperature water, Corrosion., (2007) 1114–1123.

9 Y. Zeng, J. Li, B.S. Amirkhiz, W. Zheng, M. Matchim, M. Podlesny, Corrosion and stress corrosion cracking of UNS S31008 and UNS N08810 alloys in supercritical water, Corros., 25 (2015) 36-45.

10 S.N. Lvov, Advanced techniques for high temperature electrochemical and corrosion studies, Corros., 45 (2004) 1–16.

11 W. Zieliński, K. Kurzydłowski, TEM studies of the oxide scales formed on type 316 stainless steel during annealing at 600 °c in a vacuum and air, Scr. Mater., 43 (2000) 33–37.

12 Z. Shen, L. Zhang, R. Tang, Q. Zhang, SCC susceptibility of type 316Ti stainless steel in supercritical water, J. Nucl. Mater. 458 (2015) 206–215.

13 Z. Shen, L. Zhang, R. Tang, Q. Zhang, The effect of temperature on the SSRT behavior of austenitic stainless steels in SCW, J. Nucl. Mater., 454 (2014) 274–282.

14 R. Zhou, E.A. West, Z. Jiao, G. Was, Irradiation-assisted stress corrosion cracking of austenitic alloys in supercritical water, J. Nucl. Mater., 395 (2009) 11–22.

15 M. Sun, X. Wu, Z. Zhang, Oxidation of 316 stainless steel in supercritical water, Corros. Sci., 51 (2009) 1069–1072.

16 S. Cissé, L. Laffont, B. Tanguy, M.-C. Lafont, E. Andrieu, Effect of surface preparation on the

corrosion of austenitic stainless steel 304L in high temperature steam and simulated PWR primary water, Corros. Sci., 56 (2012) 209–216.

17 J. Bischoff, A.T. Motta, EFTEM and EELS analysis of the oxide layer formed on HCM12A exposed to SCW, J. Nucl. Mater., 430 (2012) 171–180.

18 L. Tan, Y. Yang, T.R. Allen, Porosity prediction in supercritical water exposed ferritic/martensitic steel HCM12A, Corros., Sci. 48 (2006) 4234–4242.

19 L. Tan, Y. Yang, T.R. Allen, Oxidation behavior of iron-based alloy HCM12A exposed in supercritical water, Corros. Sci., 48 (2006) 3123–3138.

20 T. Terachi, T. Yamada, T. Miyamoto, K. Arioka, K. Fukuya, "Corrosion behavior of stainless steels in simulated pwr primary water-effect of chromium content in alloys and dissolved hydrogenJ. Nucl. Sci. Technol., 45 (2008) 975–984.

21 G. Was, P. Ampornrat, G. Gupta, S. Teysseyre, E. West, T.R. Allen, Corrosion and stress corrosion cracking in supercritical water, J. Nucl. Mater., 371 (2007) 176–201.

22 M. Sun, X. Wu, E.-H. Han, J. Rao, Microstructural characteristics of oxide scales grown on stainless steel exposed to supercritical water, Scr. Mater., 61 (2009) 996–999.

23 P. Ampornrat, G. Gupta, G. Was, Tensile and stress corrosion cracking behavior of ferritic–martensitic steels in supercritical water, J. Nucl. Mater., 395 (2009) 30–36.

24 E.A. West, G. Was, IGSCC of grain boundary engineered 316L and 690 in supercritical water, J. Nucl. Mater., 392 (2009) 264–271.

25 G. Gupta, P. Ampornrat, X. Ren, T.R. Allen, G. Was, Role of grain boundary engineering in the SCC behavior of ferritic–martensitic alloy HT-9, J. Nucl. Mater., 361 (2007) 160–173.

26 S. Teysseyre, Q. Peng, G. Was, Stress Corrosion Cracking of Neutron- Irradiated Stainless Steels in Supercritical Water Material studies required for SCWR, J. Nucl. Mater., 371 (2007) 98–106.

27 J. Konys, S. Fodi, J. Hausselt, H. Schmidt, V. Casal, Corrosion of High-Temperature Alloys in Chloride-Containing Supercritical Water Oxidation Systems, Corrosion., 55 (1999) 45–51.

28 S. Teysseyre, Q. Peng, C. Becker, G. Was, Facility for stress corrosion cracking of irradiated specimens in supercritical water, J. Nucl. Mater., 371 (2007) 98–106.

29 X. Zhong, X. Wu, E.-H. Han, Effects of exposure temperature and time on corrosion behavior of a ferritic–martensitic steel P92 in aerated supercritical water, Corros. Sci., 90 (2015) 511–521.

30 O. Yeliseyeva, V. Tsisar, Z. Zhou, Corrosion behavior of Fe–14Cr–2W and Fe–9Cr–2W ODS steels in stagnant liquid Pb with different oxygen concentration at 550 and 650°C, J. Nucl. Mater., 442 (2013) 434–443.

31 I. Wright, B. Pint, An assessment of the high temperature oxidation behavior of Fe-Cr steels in water vapor and steam, Corros., (2002).

32 E.A. West, Influence of local stress and strain on intergranular cracking of 316L stainless steel in supercritical water, Michigan, (2010).

33 D. Rodriguez, A. Merwin, D. Chidambaram, On the oxidation of stainless steel alloy 304 in subcritical and supercritical water", J. Nucl. Mater., 452 (2014) 440–445.

34 M. Nezakat, H. Akhiani, S. Penttilä, S.M. Sabet, J. Szpunar, Effect of thermo-mechanical processing on oxidation of austenitic stainless steel 316L in supercritical water, Corros. Sci., 12 (2015) 125-436.

35 J. Weiss, A. Pineau, Fatigue and creep-fatigue damage of austenitic stainless steels under multiaxial loading, Metall. Trans. A., 24 (1993) 2247–2261.

36 D.S. Morton, S.A. Attanasio, G.A. Young, P.L. Andersen, T.M. Angeliu, P.L. Andresen, The influence of dissolved hydrogen on nickel alloy SCC" A window to fundamental insight, (2000) 13.

37 D. Guzonas, J.S. Wills, G.A. McRae, S. Sullivan, K. Chu, K. Heaslip, "Corrosion- resistant coating for use in a supercritical water CANDU reactor", 12th Int. Conf. Environ. Degrad. Mater. Nucl. Power Syst. React., (2005)1379–1386.

38 A.H. Harvey, E.W. Lemmon, NIST / ASME Steam Properties-STEAM-Version 3.0, U.S. Dep. Commer., 208 (2013).

39 J. Bischoff, A.T. Motta, EFTEM and EELS analysis of the oxide layer formed on HCM12A exposed to SCW, J. Nucl. Mater., 430 (2012) 171–180.

40 R. F. Egerton, Electron energy-loss spectroscopy in the electron microscope, 3rd edition, 3 (2011).

41 I. Tallo, T. Thomberg, K. Kontturi, A. Jänes, E. Lust, Nanostructured carbide-derived carbon synthesized by chlorination of tungsten carbide, Carbon., 49 (2011) 4427–4433.

42 Y.Z. Huang, S. Lozano-Perez, R.M. Langford, J.M. Titchmarsh, M.L. Jenkins, Preparation of transmission electron microscopy cross-section specimens of crack tips using focused ion beam milling, . Microsc., 207 (2002) 129–36.

Chapter 6: Investigation of Oxidation Behavior of an Austenitic 304 - Oxide Dispersion Strengthened Steel in Supercritical Water at 650 °C

6.1 Introduction

Water above a temperature of 374.15 °C and a pressure of 22.1 MPa is in a supercritical state. Supercritical water (SCW) acts as a dense gas and exhibits properties significantly different from that of water below the critical point (normal water).[1,2] At the critical point, the specific enthalpy of water increases by about 20% and water behaves as a single phase.[1-3] A supercritical water reactor (SCWR) which uses SCW as a coolant has a high thermal efficiency and a simplified single phase coolant design compared to current light water reactors.

To find a suitable alloy system for application in a SCWR, different parameters and mechanisms of processes affecting the lifetime of the candidate materials in relevant conditions are identified through extensive experimental tests. Knowledge of general corrosion resistance in SCW is a critical concern and plays an important role in detrimental processes such as environmental effects and mechanical stress, which can cause stress corrosion cracking (SCC) and corrosion fatigue (CF).[4] Due to the widespread application of SCW, many studies have been focused on the corrosion/oxidation of structural materials in SCW corrosive environments.[5-7] Oxide dispersion strengthened (ODS) iron-base alloys are potential alloys for use in the development of SCWRs due to their high creep resistance and radiation damage resistance.

Material in this chapter has been submitted for publication in Corrosion Science.

Novotny et al. investigated oxidation of the ODS ferritic alloys MA956 and PM2000 in SCW containing < 200 ppb dissolved oxygen (DO) at 650 °C and 25 MPa. They found that hematite and magnetite formed on the surface of all samples after 1800 h exposure.[4] The corrosion of 18Cr-ODS and 14Cr-ODS ferritic alloys in SCW containing 300 ppb DO at 600 °C and 25 MPa up to 1000 h has also been studied.[3,8] Magnetite and hematite were detected on the outer oxide layer of 18Cr-ODS. Bischoff et al. investigated responses of 9Cr-ODS and 14Cr-ODS ferritic alloys to SCW containing < 20 ppb DO at 500 °C, 600 °C, and 25 MPa for exposure times of up to 2000 h.[5] Through microbeam synchrotron radiation diffraction and fluorescence analyses of the oxide film, the presence of magnetite on the outer oxide layers and nonuniform iron-chromium spinel in the inner oxide layers were confirmed.[5] Isselin et al. studied corrosion properties of 16Cr-ODS + 4% Al and 16Cr-ODS ferritic alloys in SCW containing 8 ppm DO at 550 °C and 25 MPa up to 250 h.[6] They found that the oxide monolayer on 16Cr-ODS was composed of hematite and chromium oxide; however, the outer oxide layer on the 16CrODS + 4% Al alloy was composed of magnetite and hematite, and the inner layer was mainly made of aluminum oxide. Was et al. [9] found that ferritic steels undergo higher weight gain compared to austenitic stainless steels. Moreover, a series of austenitic stainless steels, namely 304 and 316, were exposed to deaerated supercritical water to observe how alloying elements can affect oxide layer formation on the substrate.[1,10] Penttila et al. suggested that modified austenitic steel and high chromium ODS steel would be suitable candidates for in core applications.[11] Austenitic stainless steels have been widely utilized as the main structural materials for use in SCW systems due to their excellent combination of microstructural stability, mechanical properties, and corrosion resistance in high temperature and high-pressure conditions compared to

ferritic/martensitic steels.[12] However, the oxidation data of modified austenitic stainless steels such ODS austenitic stainless steel alloys in SCW is still limited.

In the present work, the oxidation of a 304-ODS alloy in SCW at 650 °C and 25 MPa were investigated. The oxide layers formed during exposure to SCW were characterized using X-ray diffraction (XRD), time-of-flight secondary ion mass spectrometry (TOF-SIMS), scanning electron microscopy (SEM), and transmission electron microscopy (TEM) equipped with energy-dispersive X-ray spectroscopy (EDS) and electron energy loss spectroscopy (EELS). The formation of these oxide layers was analyzed based on the above measurements, and a most probable corrosion mechanism is discussed and proposed.

6.2 Experimental and Instrumentations

6.2.1 Materials

Chemical composition of 304-ODS alloy used in the present study is listed in Table 6-1. The fabrication process[3] comprised the following steps: the prealloyed powders and yttria (Y_2O_3) powders were mechanically alloyed by high energy ball milling in a pure argon atmosphere for 30 h, then the powders were HIPed at 1150 °C for 3 h under a pressure of 120 MPa, followed by annealing at 1000 °C. The corrosion coupons were fabricated from the bulk alloy with dimensions of 2 cm × 2 cm × 0.2 cm. The coupons were polished down to 1200 grit using sand papers. After polishing specimens, the coupons were cleaned in sequence with pentane, isopropyl alcohol, and acetone in an ultrasonic bath. Corrosion tests at 650 °C and 25 MPa were conducted using the SCW loop facility at University of Alberta. The SCW loop is described in

detail in Figure 6-1. Oxygen was maintained at a constant level of < 500 ppb by constantly purging the SCW loop with argon. The conductivity of inlet water was 0.1 μS/cm and the flow rate was 3.3 - 3.5 L/h. After SCW exposure, test coupons were dried immediately.

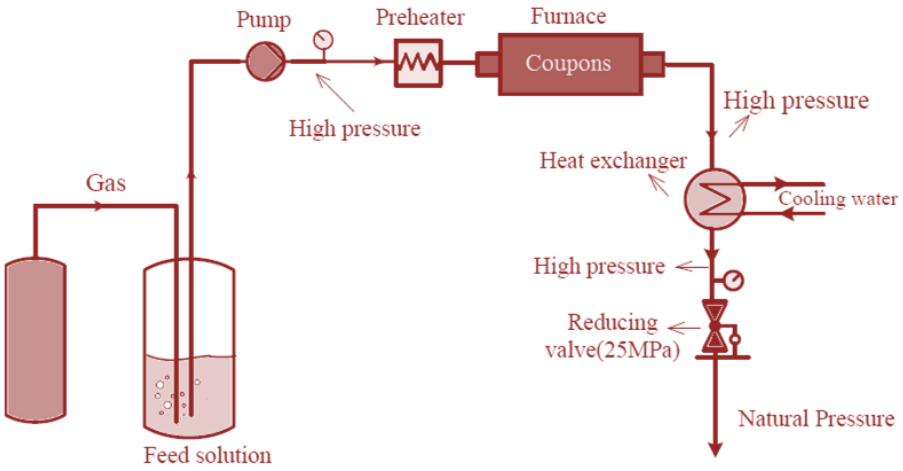

Figure 6-1: The supercritical water loop used in this study.

Table 6-1: Chemical composition of 304-ODS alloy.

Alloy	**Chemical Composition (wt.%)**									
304 ODS steel	Fe	C	Cr	Ni	P	Si	Mo	Mn	Y_2O_3	Ti
	Balance	0.035	18.12	8.02	0.023	0.85	1.08	1.91	0.35	0.5

6.2.2 Characterizations

The following characterization methods were used in this research:

a. To minimize the error in measurements, every weight measurement was conducted five times. All samples were measured using a METTLER-TOLEDO XPE105 analytical balance with an accuracy of ± 0.01 mg to record the weight change before and after exposure to SCW at 650 °C.

b. X-ray diffraction (XRD) analysis was performed using a Rigaku-X-ray diffractometer with a Cu-K_α radiation source (λ = 1.5406 Å) operated at 40 kV and 40 mA in the 2-theta range 10° - 70° at the scan rate of 0.05° per second.

c. Surface morphology of samples was examined with a ZEISS (EVO-MA15) scanning electron microscope equipped with an energy-dispersive X-ray spectroscope at 20 kV. To investigate the cross-section of the oxide films formed on the test coupons, the coupons were electroplated with nickel to protect the oxide layers. The samples were mounted with epoxy resin and then polished using sand paper to 2400 grit by a standard polishing technique before SEM/EDS investigation.

d. Prior to analyze the oxide formed on the specimens with transmission electron microscopy (TEM), samples were prepared using a Hitachi NB-5000 Dual Focused Ion/Electron Beam (FIB). TEM samples were prepared using an FIB lift-out technique. Electron transparent lamellas were prepared using an ion beam voltage of 40 KeV with a current drop of 7nA to 35 pA. TEM analysis was performed with a JEOL 2200FS transmission electron microscope operated at 200 kV in a scanning mode (STEM) with a nominal analytical beam size of 0.7 nm. EELS/EDS line profile measurements were performed on at least 100 points per line profile. Spectra were obtained in a range of 500 - 900 eV, covering O, Ti, Cr, Fe, Mn, and Ni core loss edges. After obtaining spectra, in order to obtain profiles for each element (as a function of distance), the background was first subtracted in the EELS spectra series, and profiles were extracted from spectra by placing an energy window of appropriate width over the element's edge. Elemental profiles were extracted from the EELS spectrum series; a few points throughout the line profile represented the overall features of each series.

e. Time-of-flight secondary ion mass spectrometry (TOF-SIMS) analysis was carried out using a TOF-SIMS IV instrument (ION-ToF Gmbh). The information depth of TOF-SIMS analysis was limited to the top 1 to 20 monolayers. Ions from mass 1 (hydrogen) to ~ 9000 amu (for cluster ions) were detected with resolutions ranging from concentrations of 1 ppb to 1 ppm, depending on the element. In the current work, the analysis source used was Ga^+, operating at 15 kV and the sputtering source was Cs^+, operating at 2 kV. To minimize atmospheric exposure, the samples were stored under argon until the SIMS test.

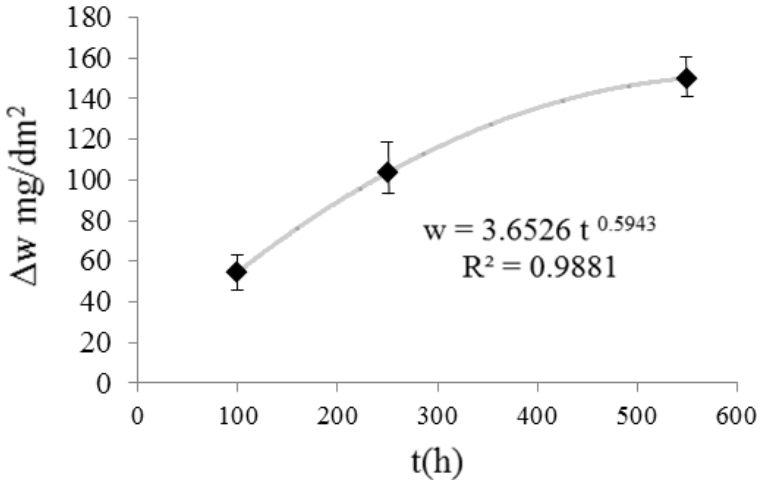

Figure 6-2: Weight gain of 304-ODS coupons as a function of exposure time in SCW at 650 °C and 25 MPa.

6.3 Results and Discussions

6.3.1 Weight Gain

Weight changes of the 304-ODS alloy coupons after exposure to SCW for 100, 250, and 550 h are plotted in Figure 6-2. Weight change data showed that the weight of coupons increased with SCW exposure time. After initial exposure, the weight gain was low although it increased

significantly after the exposure time was extended to 550 h. Curve fitting of the weight change results revealed that the oxidation of 304-ODS alloy at 650 °C and 25 MPa in an atmosphere containing ~ 500 ppb DO followed a parabolic law. This phenomenon can be attributed to an oxide formation on the outer surface of the coupons leading to lower ions and atoms diffusion rate and larger diffusion length. Weight gain data can be represented by Equation 1:

$$\Delta W = kt^n \quad (1)$$

Where ΔW represents weight gain, k is a constant, t is the exposure time, and n is the time exponent. The data produced a good fitting result with n = 0.594 and k = 3.653. About 400 mg/dm^2 weight gain has been reported for SS 316L coupons after 600 h exposure in SCW at 600 °C and 25 MPa in an atmosphere containing about 25 ppb DO.[9] For 18Cr-ODS ferritic steel, a weight increase of about 300 mg/dm^2 after about 600 h in similar SCW conditions was observed.[8] In this study, the 304-ODS alloy exhibited much less weight gain relative to that of SS 316L in similar experimental conditions. The higher corrosion resistance of the 304-ODS alloy compared to commercial SS 316L could be due to a significant difference in the microstructure of the alloys. A smaller grain size in ODS alloys promotes short-circuit diffusion and consequently reduces corrosion rate at higher temperatures.[5,13] Dispersed oxide along grain boundaries of ODS alloys can also reduce cation diffusion during oxidation.[8]

In comparison with previous studies,[3,8,9] experimental parameters such as temperature and DO in the present study were slightly higher, and the weight gain data might reflect the higher parameters. Additionally, the 304-ODS alloy showed less weight gain than that of the 18Cr-ODS alloy under similar experimental conditions. However the mechanism(s) involved in SCW corrosion of 304-ODS alloys is still unknown.[9]

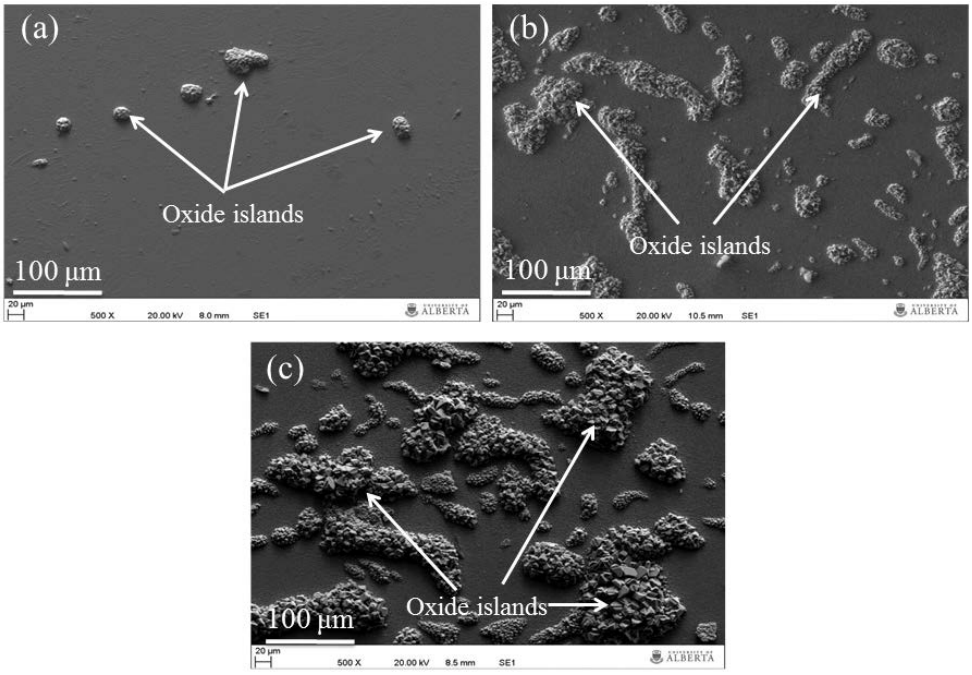

Figure 6-3: SEM micrographs of the oxide formed on the surface of 304-ODS coupons after (a) 100 h, (b) 250 h, and (c) 550 h SCW exposure.

6.3.2 Morphological Investigation of Oxide Layers Formed on the 304-ODS Coupons

Figure 6-3 and Figure 6-4 show topography and cross-section of the oxide formed on the surface of 304-ODS alloy coupons after SCW exposure at 650 °C and 25 MPa for (a) 100 h, (b) 250 h, and (c) 550 h. The surface oxide film consisted of different oxide crystal size. After the first 100 h exposure, localized crystalline islands formed and distributed discreetly. A continuous layer of the large crystalline oxide did not form in this stage (Figure 6-3a).

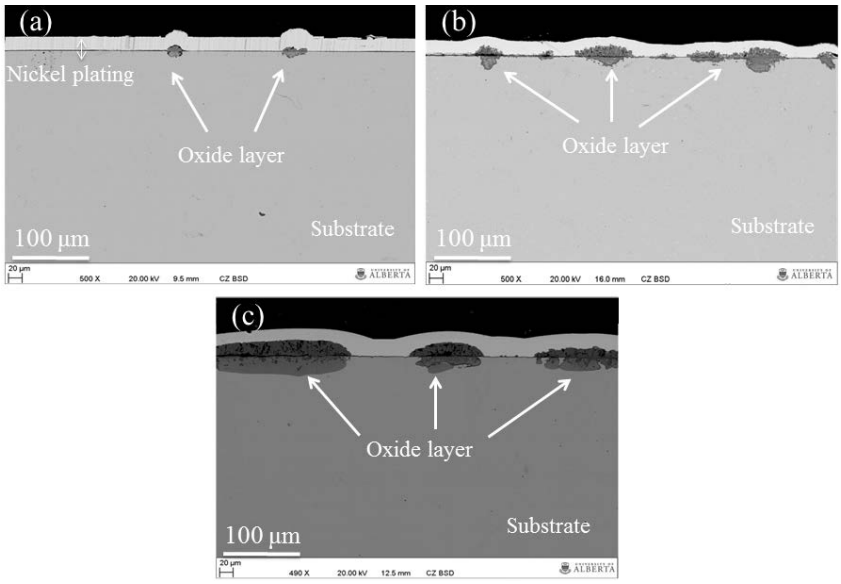

Figure 6-4: SEM micrographs of a cross-section of the oxide islands formed on the surface of 304-ODS coupons after (a) 100 h, (b) 250 h, and (c) 550 h SCW exposure at 650 °C and 25 MPa.

The remaining surface area was covered with a continuous fine oxide layer. The cross-section morphology showed that the depth of discretely localized islands was less than a few µm and the continuous fine oxide layer on the remaining surface area was less than 1µm thick (Figure 6-4a). When the exposure time was increased to 250 h, surface morphology analysis (Figure 6-3b) indicated that the quantity and size of discretely distributed localized islands had increased, which was consistent with the weight gain measurements. The cross-section morphology of the same coupon (Figure 6-4b) revealed that the depth of discretely distributed localized crystalline islands had increased significantly. Increasing exposure time to 550 h resulted in the growth and coarsening of discretely distributed localized islands on coupon surfaces (Figure 6-3c). The cross-section morphology of the same coupon (Figure 6-4c) revealed that only area of discretely localized islands enlarged, and there was no significant change in the oxide thickness for the sample exposed for 550 h compared to the sample exposed for 250 h.

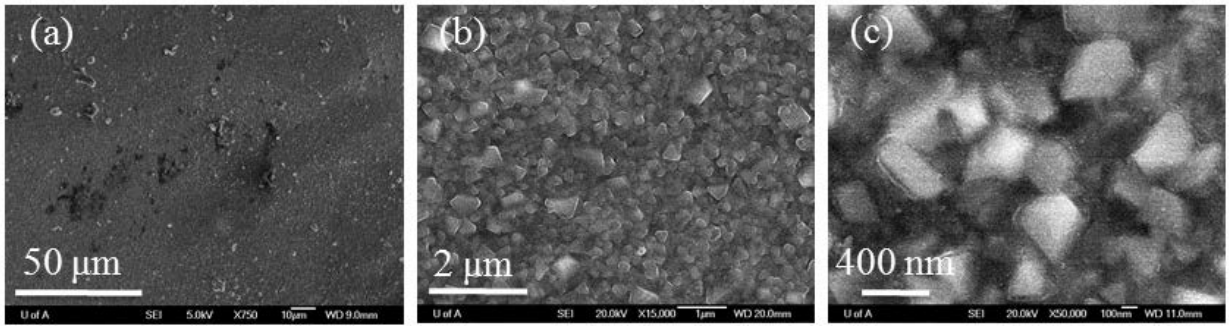

Figure 6-5: SEM micrographs of the outer surface area of 304-ODS coupons after exposure to SCW at 650 °C for 100 h at different magnifications, 750x (a), 15000x (b), 25000x (c).

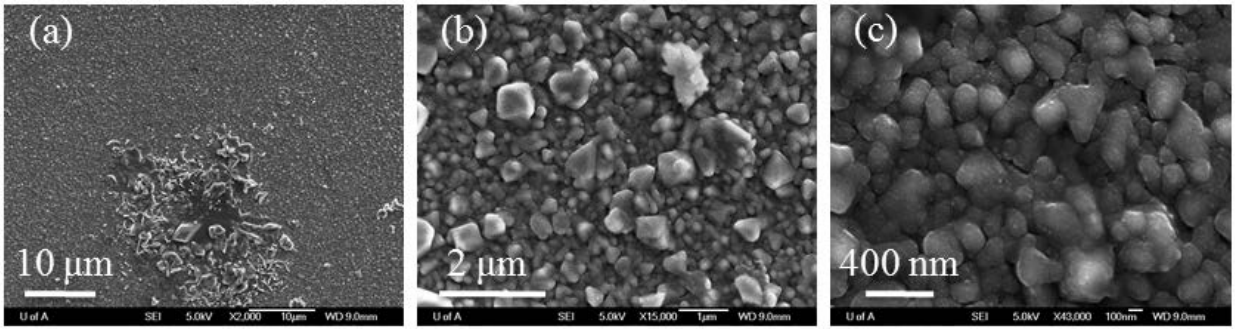

Figure 6-6: SEM micrographs of the outer surface area of 304-ODS coupon specimens after exposure to SCW at 650 °C for 250 h at different magnifications, 2000x (a), 15000x (b), 43000x (c).

SEM micrographs of the outer surface area of the coupons after exposure to SCW at 650 °C for 100 h is shown in Figure 6-5. This demonstrates that the oxide layer consists mainly of dense oxide islands with an average crystal size of 200 nm - 300 nm. SEM images from the outer surface of the coupons after extending the exposure time to 250 h are shown in Figure 6-6. The oxide layer is made of coarse crystals surrounded by coarse and fine oxide layers. The coarse oxide crystals (~ 20 µm), the fine oxide crystals (~ 1 µm), and the very fine oxide crystals (~ 200 - 500 nm) are shown in Figure 6-6a, Figure 6-6b, and Figure 6-6c, respectively.

Top-view SEM micrographs (Figure 6-7a-c) illustrate that the coupons outer surface after 550 h exposure at 650 °C consisted of very large oxide islands surrounded by fine oxide layers.

The outer surface between the large oxide islands consists of small crystalline oxides, as shown in Figure 6-7d. The average size of the islands was 100 to 300 μm and the size of small oxide crystals was about 400 to 700 nm (Figure 6-7e-f).

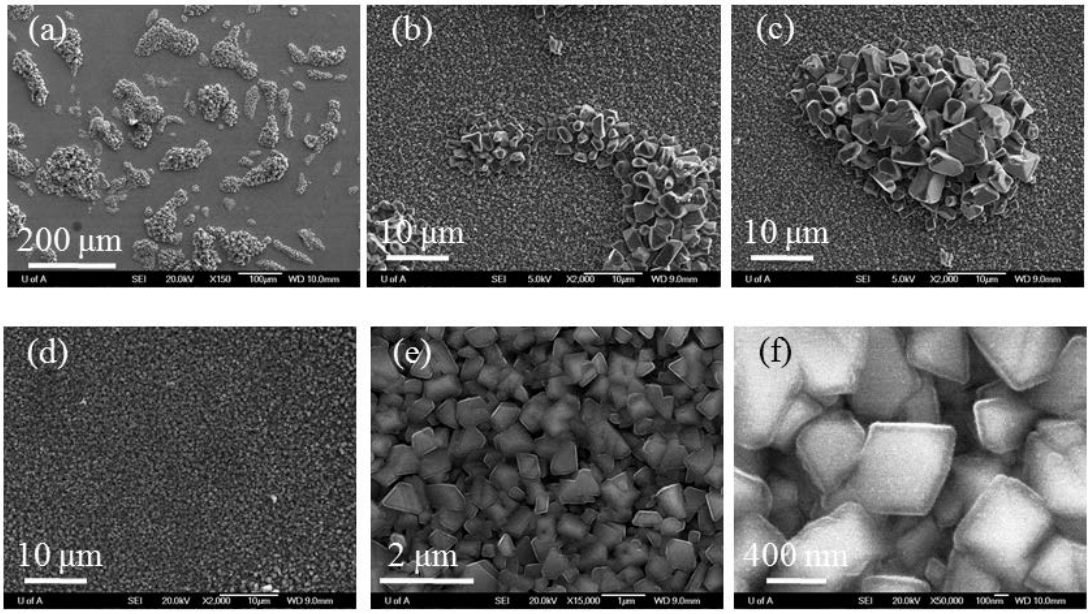

Figure 6-7: SEM micrographs of the outer surface area of the 304-ODS coupons after SCW exposure at 650 °C for 550 h at different magnifications, 150x (a), 2000x (b), 2000x (c). 2000x (d), 15000x (e), 50000x (f).

6.3.3 X-Ray Diffraction Analysis

XRD analysis was conducted on the 304-ODS alloy coupons exposed to SCW for different exposure times at 650 °C and 25 MPa to identify oxide phases formed on coupon surfaces. As shown in Figure 6-8, XRD analysis revealed that magnetite and chromium-iron spinel were present in the oxide layers of coupon samples after 100 h, 250 h, and 550 h SCW exposure. Although hematite and chromium oxide were detected, their peak intensities suggested that they were not dominant phases in the oxide layer. Austenite was identified as the major phase in XRD patterns of the substrate after 100 h, 250 h, and 550 h of SCW exposure at 650 °C and 25 MPa.

The same results were reported by Was et al. who found that magnetite was the dominant phase on the outer layer of oxides formed on top of stainless steel alloys such as 316L and 304 upon exposure to SCW at a temperature of 550 °C and a pressure of 25 MPa [1].

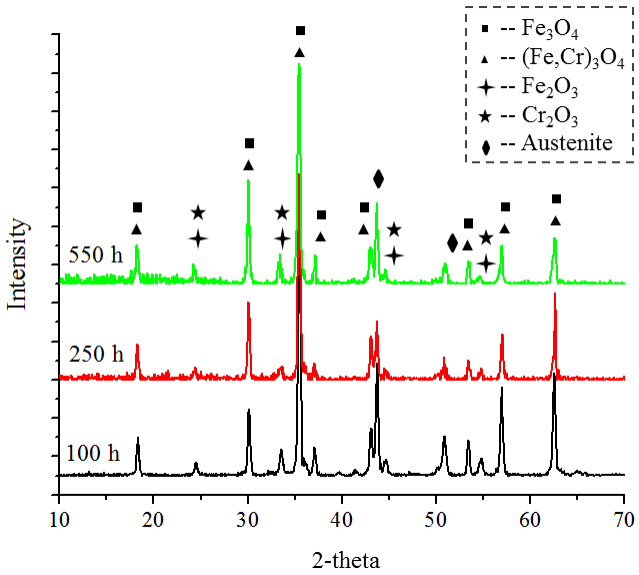

Figure 6-8: XRD spectra scanned from top surface of 304-ODS coupons after 100, 250 and 550 h SCW exposure at 650 °C and 25 MPa.

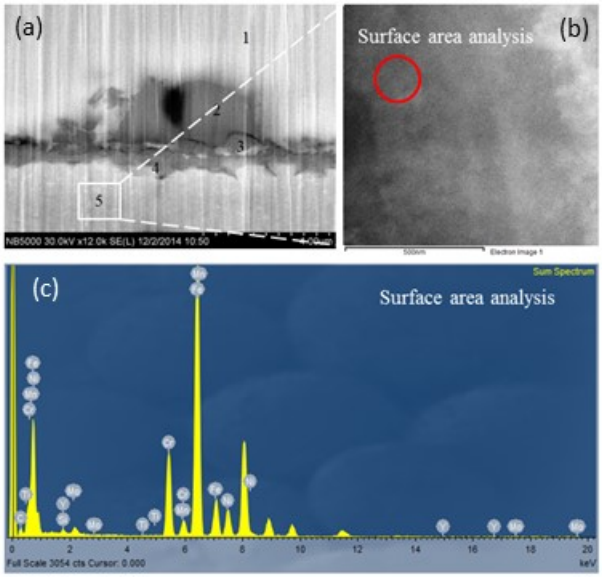

Figure 6-9: (a) SEM micrograph taken from the cross-section of the oxide layer on 304-ODS coupons after 100 h SCW exposure at 650 °C prepared using FIB milling, (b) TEM micrograph of area 5, and (c) EDS analysis from area 5.

6.3.4 Energy-Dispersive X-Ray Spectroscopy (EDS) Qualitative Chemical Analysis

Figure 6-9a shows SEM image from the cross-section of the oxide layer after 100 h exposure of 304-ODS coupons to SCW at 650 °C. The oxide scale was characterized by EDS to determine chemistry of the oxide layer. Point 1 is the Ni plating layer. Point 2 is the outer oxide layer consisting of large oxide gains. The EDS results taken from point 2 (Figure 6-9c) show that the large oxide grains are mainly composed of Fe and O with an atomic ratio close to that of Fe_3O_4. Lower content of Fe and higher level of chromium were evident at point 3, consistent with the inner oxide layer. This most probably represents a Fe- Cr-mixed oxide phase. Pure elemental Ni or Ni oxide might also be present in this region because Ni was detected by EDS. The elemental composition at point 4 was very analogous to that of point 3. However, significantly higher Ni content was observed at this point, indicating a Ni enrichment. The chromium content detected at point 4 was slightly less than that at point 3. A TEM micrograph obtained from point 4 is shown in Figure 6-9b. the EDS results revealed that Yttrium was available in the substrate. It can be seen that the chemical composition was close to that of the pristine coupons. A summary of the elemental analyses is given in Table 6-2.

Table 6-2: EDS chemical analysis taken from different points of Figure 6-9.

Element	Point 1	Point 2	Point 3	Point 4
O	-	21.34	21.95	12.68
Cr	-	0.48	29.37	23.18
Ni	99.3	-	4.69	17.98
Mn	-	0.29	0.66	1.34
Mo	-	-	2.69	1.06
Fe	0.7	77.97	40.02	34.68
Si	-	-	0.54	0.46

Figure 6-10 and Figure 6-11 show SEM micrographs and elemental maps of the oxide layer on the outer surfaces of the samples after 550 h SCW exposure at 650 °C. The surface oxide film consisted of crystals with different sizes. Coarse crystalline oxides were discretely distributed on the substrate and did not form a continuous oxide layer. However, the balance area around the large oxide crystals was covered with very fine crystalline oxide layers.

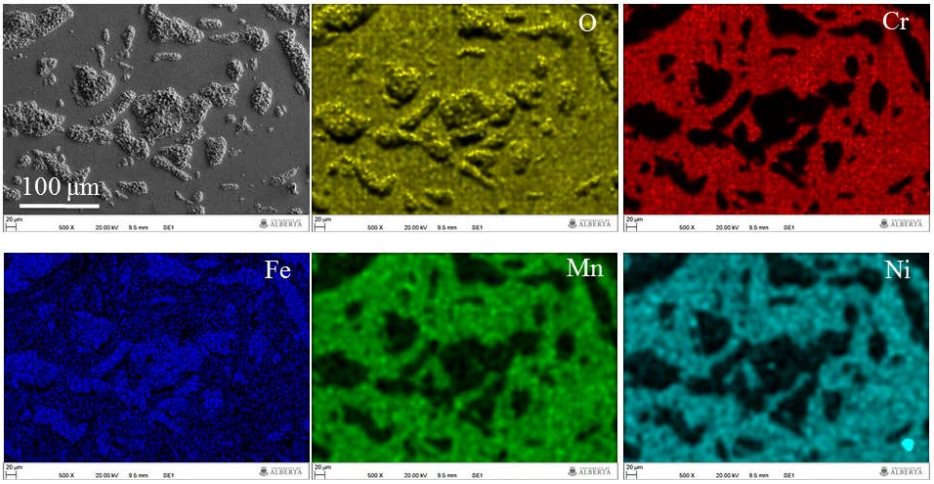

Figure 6-10: SEM micrographs and EDS elemental maps of the oxide layer formed on outer surface of 304-ODS samples after 550 h SCW exposure at 650 °C.

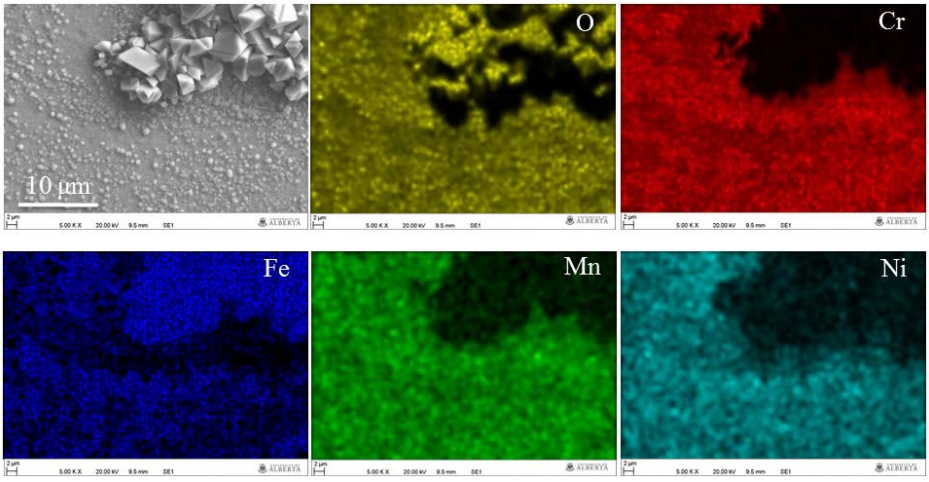

Figure 6-11: SEM micrographs and corresponding EDS elemental maps for O, Cr, Fe, Mn, and Ni of the oxide layer formed on outer surface of 304-ODS sample after 550 h SCW exposure at 650 °C (higher magnification of Figure 6-10).

The EDS elemental maps of the oxide layer revealed that the coarse crystalline oxide layer contained a higher amount of Fe and lower concentrations of Cr, Mn, and Ni. However, surfaces covered with fine crystalline oxides contained higher concentrations of Cr, Mn, and Ni. The fact that the fine crystalline oxides were very thin indicates that they contained high amounts of Ni and Mn.

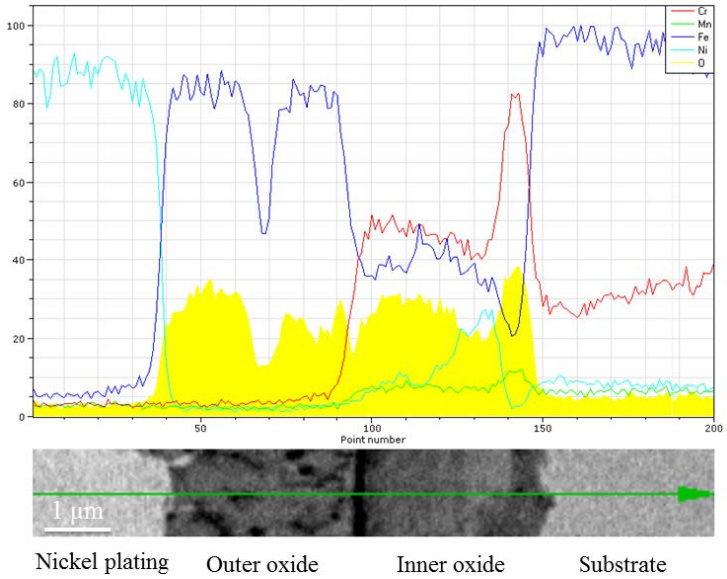

Figure 6-12: Cross-sectional TEM micrograph and corresponding EDS line scan through the oxide on the 304-ODS coupons after SCW exposure for 550 h at 650 °C and 25 MPa (yellow, blue, red, and turquoise lines indicate the concentration profile (at. %) of oxygen, iron, chromium, and nickel, respectively.)

Figure 6-12 illustrates a magnified cross-section micrograph of the crystalline islands on a 304-ODS sample and a corresponding EDS line scan for chromium, iron, nickel, manganese, and oxygen after 550 h exposure to SCW at 560 °C and 25 MPa. The EDS line scan showed that the outer part of the oxide layer was enriched with iron and oxygen with low concentrations of chromium and nickel. The outer regions of the oxide layer appeared to be magnetite, as suggested by XRD results. The inner oxide layer was chromium-rich and partially iron depleted. Although the accuracy of EDS analysis of light elements such as oxygen is low, the EDS line

scan indicates that the oxygen concentration is lower in the inner oxide layer relative to that in the outer oxide layer. Was et al. characterized the iron and oxygen in the outer oxide layer of SS 316L and SS 304 as magnetite on the alloy samples exposed to SCW at 550 °C and 25 MPa.[1]

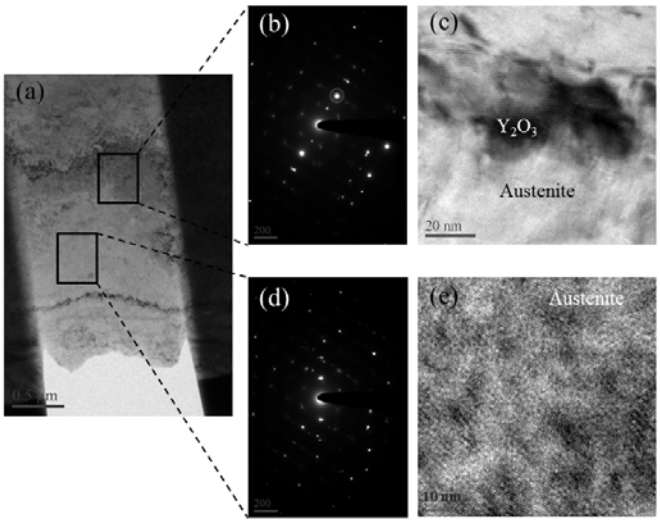

Figure 6-13: TEM micrographs of the 304-ODS samples exposed to SCW for 550 h, (a) STEM image of the intact sample prepared using FIB milling technique, (b) the corresponding selected area electron diffraction (SAED) pattern, (c) high resolution TEM (HRTEM) micrograph, (d) SAED pattern taken from the matrix, and (e) HRTEM image from the matrix.

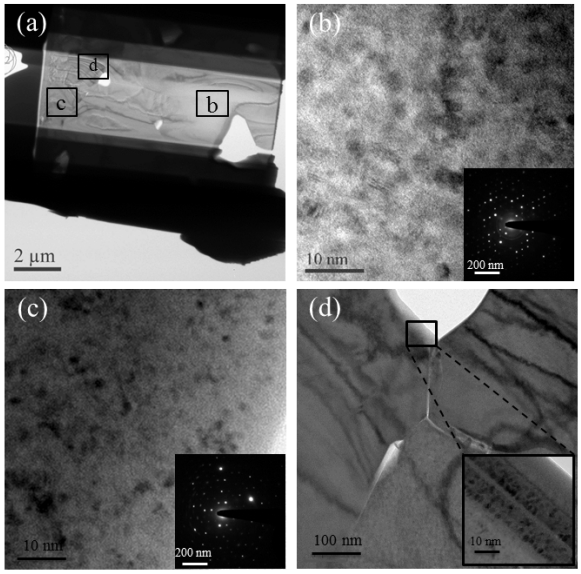

Figure 6-14: (a) STEM image from the outer layer oxide islands on the 304-ODS sample, (b and c) HRTEM micrographs and corresponding SAED patterns from the middle part of the outer oxide layer, (d) higher magnification image of grain adjacent to a large pore.

6.3.5 Transmission Electron Microscopy Observations (TEM) and EELS Analyses

The TEM samples in this study include the substrate metal before exposure to corrosive medium (Figure 6-13) and the outer oxide layer formed upon 550 h SCW exposure at 650 °C (Figure 6-14). Figure 6-13a is a STEM micrograph obtained from the intact sample lamella. Figure 6-13b demonstrates selected area electron diffraction (SAED) pattern from the same specimen. The small *d*-spacing of the substrate metal corresponds to the fine grain size of the sample.

An image of higher resolution is shown in Figure 6-13c, demonstrating apparent strain fields in the matrix. Investigations revealed that the matrix was strained due to the Y_2O_3 nanoparticles presence. Figure 6-13d shows a SAED pattern from a FCC austenite matrix. Figure 6-13e shows a high resolution TEM (HRTEM) micrograph of this area. Figure 6-14a is a STEM image of a sample from the outer oxide layer on a sample exposed to SCW for 550 h. Large pores were observed in the TEM image of samples taken from the oxide layer. Figure 6-14b and Figure 6-14c show HRTEM images and corresponding SAED patterns taken from center part of the outer oxide layer. The indexed SAED patterns are consistent with the Fe_3O_4 structure which is an inverse spinel structure. The overall pore distribution and grain structure in the oxide layer do not appear to be uniform. Figure 6-14d shows a higher magnification image of the grain adjacent to a large pore. The grain boundaries of oxides appear to have elongated pores in it. EELS analysss has been conducted to elucidate the compositional characteristics of oxide layers as shown in Figure 6-15a. As reported by Bischoff et al., EELS analysis is an advanced and valuable method to investigate chemical composition at different locations and depths of oxide on the substrate.[14] Figure 6-15b illustrates a general plot of three different areas, including an oxygen edge at an

energy loss range of 525 eV- 570 eV, a chromium edge at 575 eV- 605 eV, and an iron edge at 700 eV- 725 eV.[14]

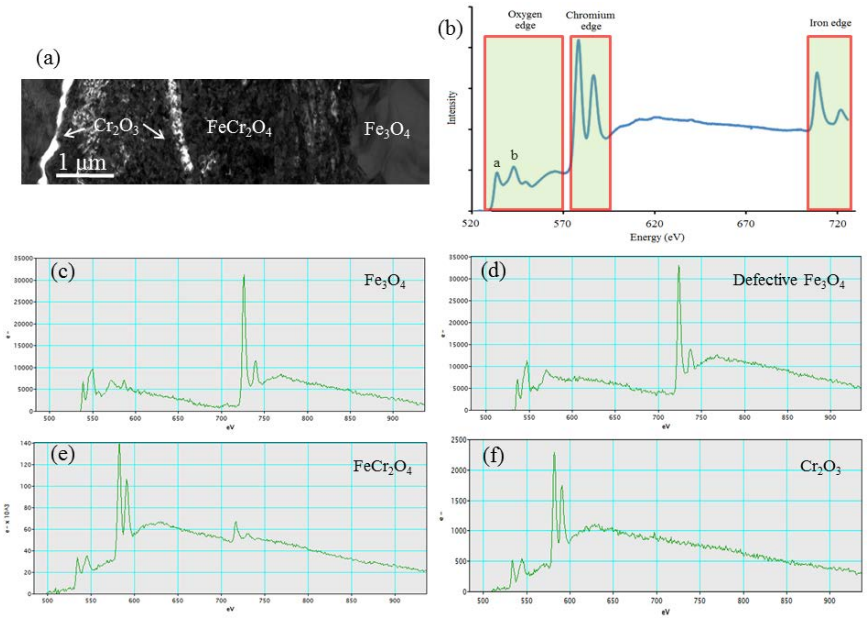

Figure 6-15: (a) TEM image from the scale of a 304-ODS sample exposed to the SCW for 550 h, (b) typical core-loss EELS spectrum, with the oxygen edge background removed, showing the oxygen, chromium, and iron edges (reproduced from [14]), and (c-f) corresponding EELS spectra for Cr, Fe, and O.

The relative height and position of each peak give information on the electronic structure and coordination chemistry of the absorbing O atoms and can facilitate an estimation of the valance state of iron, the average interatomic distance between the absorbing O atom and its nearest neighbors, the relative covalency of the Fe-O bond, and the coordination number. According to the EELS results presented in Figure 6-15c and Figure 6-15d, the regions containing no chromium resemble a spectrum of Fe_3O_4. The results indicated that the average amplitude of peak (a) relative to peak (b) had a value of 0.667, similar to the stoichiometric Fe_3O_4 spectrum, which is in agreement with values reported by Bischoff et al.[14].

Moreover, the average peak (b) to peak (a) energy difference was 9.82 eV. The defective Fe_3O_4 spectrum, shown in Figure 6-15d, has an amplitude ratio of 0.637 and a peak energy difference of 9.64 eV. The defective Fe_3O_4 spectrum, shown in Figure 6-15d, has an amplitude ratio of 0.637 and a peak energy difference of 9.64 eV. Figure 6-15e is a spectrum containing both iron and chromium with a chromium to iron ratio near 2.9 which is quite different from the Fe_3O_4 spectrum showing a relatively high amplitude ratio between peaks (a) and (b). This ratio is equal to 0.878 and the measured peak energy difference is around 9.43 eV, suggesting that this spectrum represents $FeCr_2O_4$ phase. Figure 6-15f is an EELS spectrum corresponding to Cr_2O_3, showing only chromium edge with a chromium to iron ratio close to 5.98. This can be associated with a chromium oxide phase containing a very small amount of iron. This spectrum shows a large energy difference of 10.405 eV between edge (b) and edge (a) and an amplitude ratio of about 0.97, which is much higher than the energy difference and amplitude of other spectra. These results are in an agreement with those of Bischoff et al.[14]

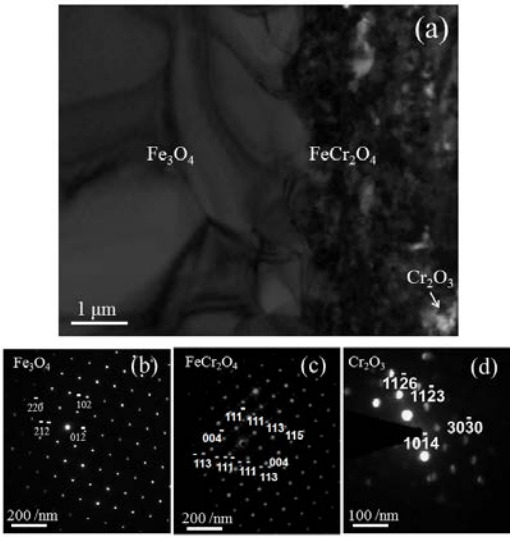

Figure 6-16: (a) TEM bright field micrograph obtained from the inner and outer layers of the coarse crystal oxide islands, (b) SAED analysis of the outset part of crystalline oxides, (c) SAED pattern of inner layer of the coarse crystalline oxide islands, and (d) SAED pattern of the fine crystalline oxide located between the coarse crystalline oxide islands. Results were obtained from the sample exposed to SCW for 550 h.

The TEM image taken from the cross-section of the scale from the sample exposed to SCW for 550 h is shown in Figure 6-16a. SAED analysis of the inner and outer layers of the coarse crystal oxide islands revealed that the outset part of the oxide crystals is made of Fe_3O_4. Also, the SAED analysis of the inner layer of the coarse crystal oxide islands demonstrated that $FeCr_2O_4$ is the major phase in that region (Figure 6-16c). The SAED analysis of the fine crystalline oxide located between the coarse crystal oxide islands showed that the areas are mainly composed of Cr_2O_3, as shown in Figure 6-16d. Therefore, the TEM analysis supports thermodynamic data in the phase diagram.

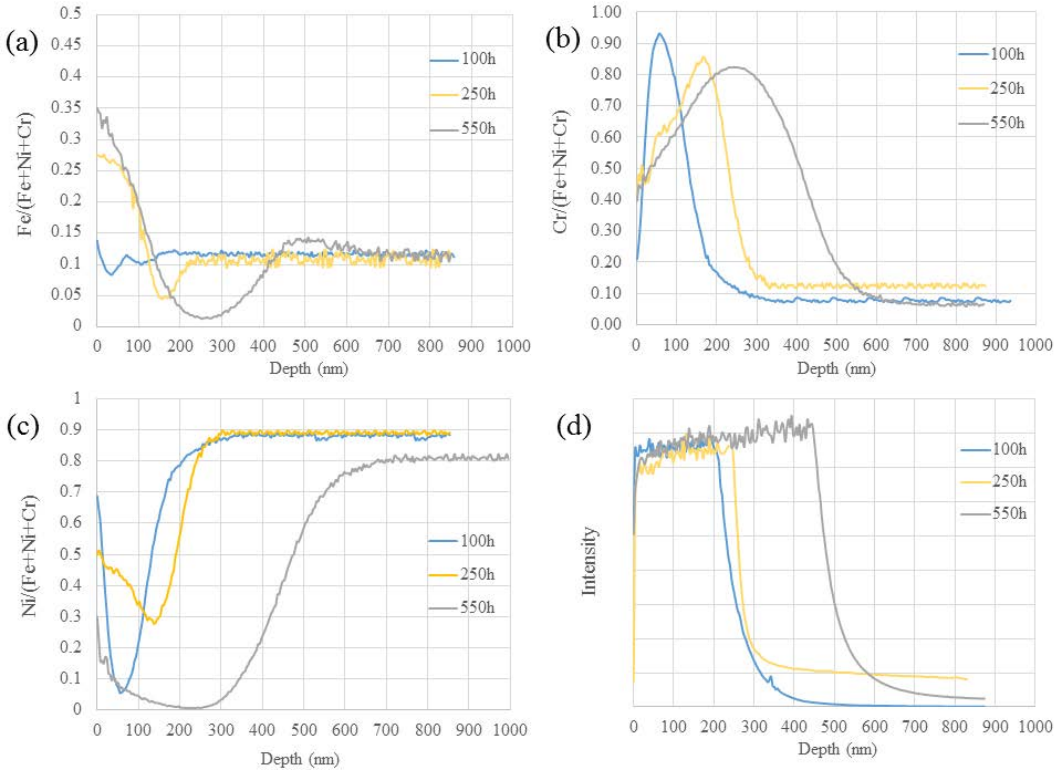

Figure 6-17: TOF-SIMS results showing the effect of 304-ODS SCW exposure time on the elemental profile for (a) Fe, (b) Cr, (c) Ni, and (d) O.

6.3.6 Secondary Ion Mass Spectrometry Analysis (SIMS)

The elemental SMIS results of samples exposed to SCW are shown in Figure 6-17. It can be seen that exposure time had a remarkable influence on the elemental profile for Fe, Cr, and Ni and had a trivial effect for the O profile. The chromium peak profile shifted to the right which can be attributed to the fact that chromium was depleted in the outer oxide surface when the exposure time was increased to 550 h (Figure 6-17b).

On the other hand, the iron peak profile shifted to the left in similar exposure times as the outer layer was enriched with iron oxide (Figure 6-17a). The nickel peak profile shifted to the left in similar exposure times as the inner layer was enriched with nickel (Figure 6-17c). It is worth noting that the approximate thickness of the oxide layer in the thin section did not change significantly when the exposure time was increased from 100 h to 550 h. SIMS profile data suggested that the chemistry in this layer can change significantly. It is critical to determine whether certain elements are preferentially dissolved from the anodic film due to increasing SCW exposure time. Since secondary ion yields depend on the chemical environment of the target, it is difficult to relate the strength of the SIMS signals to the concentration of different elements. Therefore, the ratios of the intensities of $\frac{Fe}{Fe+Ni+Cr}$, $\frac{Ni}{Fe+Ni+Cr}$, and $\frac{Cr}{Fe+Ni+Cr}$ are depicted for comparison (Figure 6-17a).

6.3.7 Oxide Formation on the SS-304-ODS Alloy in SCW

Figure 6-18 is a stability diagram illustrating the stable regions for phases of different alloy compositions at various oxygen partial pressures. Different structures including FCC, BCC, spinel, and corundum with different chemistries exist in the oxide layer formed at 650 °C.

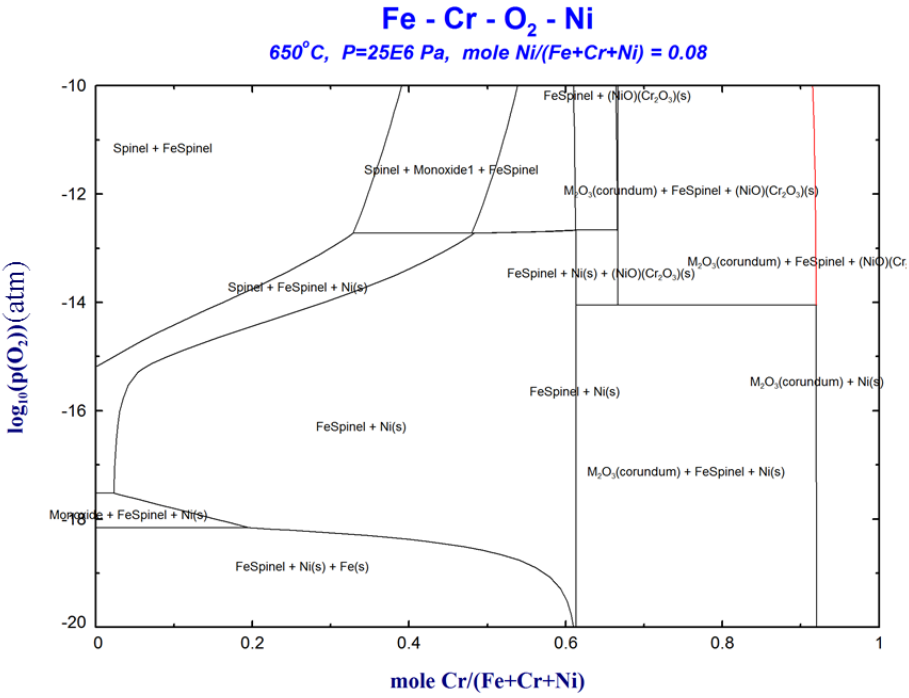

Spinel = $FeCr_2O_4$, Fe Spinel= Fe_3O_4 , Monoxide = NiO , Corundrundum= $(Fe, Cr)_2O_3$

Figure 6-18: Calculated diagram of phases as a function of oxygen partial pressure for the Fe-Cr-O_2-Ni system of 304-ODS alloy in SCW at 650 °C.

Phases with BCC and FCC structures contain Fe and Ni, respectively, phases with the spinel structure contain Fe_3O_4 and $FeCr_2O_4$, and phases with the corundum structure contain $(Fe,Cr)_2O_3$ and Cr_2O_3. Tan et al. reported that the partial pressure of oxygen was about 2×10^{-16} atm on the outer surface of oxides exposed to SCW containing 25 ppb dissolved oxygen.[15] This calculation can be extracted by correlating the fitted parabolic rate constant with the diffusion equation of Wagner's relation. Water with 25 ppb dissolved oxygen was fed top the system. Based on these

premises and the stability diagram, stable phase formation depends on the molar fraction of chromium in each layer, which can be Fe_3O_4, $FeCr_2O_4$, Fe, and Fe_2O_3 or Cr_2O_3. However, there is no chromium in the outer layer. Thus, the outer layer was known as Fe_3O_4. The oxygen partial pressure of the inner oxide layer was lower than that of the outer layer. On the other hand, it was possible to detect chromium in the inner layer. Therefore, $FeCr_2O_4$ was identified in the inner layer. This phenomenon is in accordance with the XRD patterns. The diffusion layer and inner layer contained iron and chromium simultaneously. However, the iron and chromium content in the diffusion layer was different from that in the inner layer. Based on the EDS elemental maps and line scans, the structural difference between inner and diffusion layers was $FeCr_2O_4$ content. Accordingly, the main phase of the oxide layer was magnetite.

According to the experimental results observed in this study, the oxidation of the SS304-ODS alloy can be described as follows. Diffusion plays an important role in the formation of the oxide layer. Since the oxygen affinity of chromium is higher than that of iron, chromium oxide formed at the first stages of oxidation. However, some areas were chromium depleted due to hydrothermal assisted evaporation of chromium oxide and the different rates of chromium diffusion in bulk grains and grain boundaries. This phenomenon led to a lack of protection on the substrate metal and the lack of chromium oxide, causing Fe to diffuse outward along grain boundaries and short-circuit paths to form Fe_3O_4.[5,13,16] Iron cations diffused from the inner oxide layer to the outer oxide layer and reacted with oxygen to form the iron-rich outer oxide layer. At the same time, oxygen anions migrated to the inner oxide layer to form the chromium-rich inner oxide layer.[17] Furthermore, the reaction between Cr_2O_3 and Fe resulted in the formation of Fe-Cr spinel ($FeCr_2O_4$). With prolonged SCW exposure time, Fe traveled through the spinel layer and

further reacted with water forming a thicker layer of Fe_3O_4. Fe_3O_4 oxide layer structure was observed in the cross sections of SS304-ODS samples after a 550 h SCW exposure at 650 °C and 25 MPa (Figure 6-12).

The chemical composition of the inner oxide layer depends on the oxygen partial pressure.[18] As the oxides grow continuously on both surfaces and deep toward the substrate core, the oxygen concentration in the inner oxide layers decreases. Therefore, chromium oxide and chromium-iron spinel preferably formed on the verge of the inner oxide layer where there is a partially iron depleted region with lower oxygen partial pressure.[9] Finally, because of the decreasing oxygen concentration in the inner oxide layer, oxide growth can be controlled with the cations diffusion through the oxide film.[19,20] In our experiments, at the interface between the inner layer and the substrate, a Cr_2O_3 layer was found that appeared to drastically reduce diffusion of oxygen and thus prevent any more oxidation.[6] The mechanism can be explained by an outward diffusion of iron ions which produces the outer layer, and an inward diffusion of oxygen forming the inner oxide. The TEM-EDS elemental analysis of the sample exposed to SCW for 550 h revealed theoretical pattern of the formation of various oxide layers. The EDS line scan in Figure 6-12 showed that the oxygen concentration dropped in the inner oxide layer and the iron concentration amplified in the outer oxide layer. Additionally, there is an area in the inner oxide layer in which the chromium concentration was higher, which may possibly be attributed to the formation of Cr_2O_3 and/or $(Fe,Cr)_2O_3$ at the substrate/$FeCr_2O_4$ interface.

The 304-ODS steel showed better corrosion resistance in comparison with the 304 alloy. The ODS steel typically had smaller grain size than conventional steels. The short circuit diffusion paths will increase the diffusion length, which may slow down the corrosion rate.[9]

Additionally, the formation of Y–Ti-rich oxides along the grain boundaries in the steel might act to block cation diffusion.[9] Furthermore, it is proposed that Y-Ti-O particles at the grain boundaries may facilitate formation of chromium oxide leading to slower corrosion rates.[5]

6.4 Conclusions

Oxidation of austenitic stainless steel 304-ODS was investigated upon exposure to SCW (650 °C/25 MPa) for different time periods using gravimetric measurements, SEM and TEM analysis, phase formation, and chemical analysis by XRD, EDS, EELS, and SIMS. Diffusion phenomena played a significantly important role in formation of the oxide layer on the substrate. The results showed that iron diffused outward and oxygen diffused inward. Prolonging the SCW exposure time resulted in thicker oxide scales and rougher surfaces. The sample weight gain was higher for samples with longer exposure times. However, the change rates lowered following a parabolic law. The microstructure of the oxide formed on the 304-ODS alloy was investigated by electron microscopy. XRD spectra indicated that different phases including Fe_3O_4, $FeCr_2O_4$, and Cr_2O_3, formed in the oxide layer. To investigate the sequence of oxides formed on the substrate, SEM/TEM observations equipped with EDS detector were conducted on sample cross-sections. It is proposed that the oxide film was predominantly composed of an outer magnetite layer and an inner Fe–Cr spinel phase layer. SIMS and EELS results illustrated that the outer oxide consisted of Fe_3O_4 and that inner oxides were composed of $FeCr_2O_4$ and a nanometer thick layer of Cr_2O_3. As a result, both $FeCr_2O_4$ and Cr_2O_3 phases in the inner oxide layer exhibited a complex structure with a non-uniform distribution of elements. Based on the results reported in

this chapter, a mechanism was proposed for the oxidation of a SS304-ODS alloy exposed to supercritical water.

Acknowledgments

The authors gratefully acknowledge the financial support from the NSERC/NRCAN/AECL CRD program.

6.5 References

1 G. Was, S. Teysseyre, S. Mckinley, Z. Jiao, Corrosion of austenitic alloys in supercritica water, Corros., (2005) 1–20.

2 P. Kritzer, Corrosion in high-temperature and supercritical water and aqueous solutions: a review, J. Supercrit. Fluids., 29 (2004) 1–29.

3 H.L. Hu, Z.J. Zhou, L. Liao, L. Zhang, M. Wang, S.F. Li, Corrosion behavior of a 14Cr-ODS steel in supercritical water, J. Nucl. Mater., 437 (2013) 196–200.

4 R. Novotný, P. Janík, S. Penttilä, P. Hähner, J. Macák, J. Siegl, High Cr ODS steels performance under supercritical water environment, J. Supercrit. Fluids., 81 (2013) 147–156.

5 J. Bischoff, A.T. Motta, Oxidation behavior of ferritic-martensitic and ODS steels in supercritical water, J. Nucl. Mater., 424 (2012) 261–276.

6 J. Isselin, R. Kasada, a. Kimura, Corrosion behaviour of 16%Cr-4%Al and 16%Cr ODS ferritic steels under different metallurgical conditions in a supercritical water environment, Corros. Sci., 52 (2010)

3266–3270.

7 Z. Dong, W. Chen, W. Zheng, D. Guzonas, Corrosion behavior of chromium oxide based ceramics in supercritical water (SCW) environments, Corros. Sci., 65 (2012) 461–471.

8 H. Hu, Z. Zhou, M. Li, L. Zhang, M. Wang, S. Li, Study of the corrosion behavior of a 18Cr-oxide dispersion strengthened steel in supercritical water, Corros. Sci., 65 (2012) 209–213.

9 G. Was, P. Ampornrat, G. Gupta, S. Teysseyre, E. West, T.R. Allen, et al., Corrosion and stress corrosion cracking in supercritical water, J. Nucl. Mater., 371 (2007) 176–201.

10 I. Wright, B. Pint, An Assessment of the High Temperature Oxidation Behavior of Fe-Cr Steels in Water Vapor and Steam, Corros., (2002).

11 S. Penttilä, I. Betova, M. Bojinov, P. Kinnunen, A. Toivonen, Estimation of kinetic parameters of the corrosion layer constituents on steels in supercritical water coolant conditions, Corros. Sci., 53 (2011) 4193–4203.

12 Z. Shen, L. Zhang, R. Tang, Q. Zhang, SCC susceptibility of type 316Ti stainless steel in supercritical water, J. Nucl. Mater., 458 (2015) 206–215.

13 A. D. Siwy, T.E. Clark, a. T. Motta, Transmission electron microscopy of oxide development on 9Cr ODS steel in supercritical water, J. Nucl. Mater., 392 (2009) 280–285.

14 J. Bischoff, A.T. Motta, EFTEM and EELS analysis of the oxide layer formed on HCM12A exposed to SCW, J. Nucl. Mater., 430 (2012) 171–180.

15 L. Tan, Y. Yang, T.R. Allen, Oxidation behavior of iron-based alloy HCM12A exposed in supercritical water, Corros. Sci., 48 (2006) 3123–3138.

16 X. Zhong, X. Wu, E.-H. Han, Effects of exposure temperature and time on corrosion behavior of a

ferritic–martensitic steel P92 in aerated supercritical water, Corros. Sci., 90 (2015) 511–521.

17 J. Bischoff, A.T. Motta, R.J. Comstock, Evolution of the oxide structure of 9CrODS steel exposed to supercritical water, J. Nucl. Mater., 392 (2009) 272–279.

18 X. Ren, K. Sridharan, T.R. Allen, Corrosion of ferritic-martensitic steel HT9 in supercritical water, J. Nucl. Mater., 358 (2006) 227–234.

19 G.S. Was, T.R. Allen, Time, temperature, and dissolved oxygen dependence of oxidation of austenitic and ferritic-martensitic alloys in supercritical water, ICAPP, 05 (2005) 3460–3483.

20 I. Wright, R. Dooley, A review of the oxidation behavior of structural alloys in steam, Int. Mater. Rev. ,55 (2010) 129–167.

Chapter 7: Concluding Remarks

7.1 Conclusions

The objective of this research was investigation of the corrosion and oxidation of different candidate alloys from nickel based ones such as alloy 625, 214, and C2000 and iron based alloys such as stainless steel 347H, 316L, 310S and 800H in ultra-high temperature SCW at 800 °C. Additionally, it was also focused on complimentary long term experiments and analysis to evaluate the long-term performance of two of them (SS 316L and SS 310S) and their susceptibility to crack initiation at 500 °C. Furthermore, corrosion behavior of an oxide dispersion strengthen (ODS) alloy 304 was investigated at 650 °C. The main characterization techniques used in this research were electron microscopy, namely scanning/transmission electron microscopy equipped with energy dispersive spectroscopy, selected area electron diffraction (SAED), high resolution TEM images with the corresponding fast Fourier transform (FFT) patterns, electron energy loss spectroscopy (EELS), Auger electron microscopy (AES), and X-ray diffraction (XRD). The alloys corroded upon exposure to the supercritical water loop at university of Alberta for different exposure times up to 20000 h. This enabled us to evaluate the oxide microstructure by changing the exposure time, and thus to suggest an oxidation mechanism. The main conclusions of this study can be presented as following.

1. In case of short term SCW exposure at the ultra-high temperature of 800 °C, it was mainly focused on the short term corrosion behavior of nickel based alloy 625, 800H, 214, and C2000, and stainless steels candidates such as 347H, 316L, 310S stainless steel.

1.1. Gravimetric measurements in the form of weight gain/loss indicated the amount of scales formed on the surface which was exposed to the SCW at 800 °C. In fact, higher Cr and Ni content resulted in formation of a protective oxide layer on the surface.

1.2. Electron microscopy and compositional analysis on the outer surface oxide layer in which oxide scales formed, showed how the alloying elements can influence the oxide formation as a result of SCW exposure time. It was observed that the magnetite and Fe-Cr spinel structure were primarily formed on the outer oxide layer of iron based alloys and in the case of nickel-base alloys, nickel oxide, and Ni-Cr spinel were the main phases. In addition, scanning electron microscopy (SEM) observations from the top layer of the scales showed that except SS 310S, SS 316L, and alloy 214, other candidates suffer from pitting corrosion. The source of pitting corrosion was associated with phases enriched with Ti, Nb, and Si.

2. Corrosion behavior of SS 316L in SCW at 500 °C for different exposure time has been investigated.

2.1. Elemental analysis results showed that iron diffused outwards and oxygen diffused inwards through the surface oxide layer. SEM observations from the top scale layers demonstrated that oxides continuously formed on the surface. Additionally, oxide crystallite size coarsened with prolonging the exposure time up to 20000 h in the SCW.

2.2. Energy dispersive spectroscopy (EDS) elemental analysis obtained from the cross sections of the exposed samples to the SCW indicated that the oxide film consisted of two distinct layers, the outer layer composed of Fe_3O_4 and the inner layer consisting of fine grains of chromium-rich spinel oxide, $FeCr_2O_4$. Regarding the samples which were exposed to SCW for 20000 h, EDS results confirmed the formation of an enriched nickel phase at the metal/oxide

interface. Prolonging SCW exposure time resulted in the formation of a thicker oxide scale and rougher surface. It was observed that, regarding the samples which were exposed to SCW for 20000 h microcracks were detected beneath the inner oxide layer. The XRD results confirmed the presence of different phases such as Fe_3O_4, $FeCr_2O_4$, and Fe_2O_3/Cr_2O_3 on the outer surface of the oxide layer.

2.3. High resolution TEM (HRTEM) observations, EDS, EELS, and SAED analysis taken from cross section of the oxide layer confirmed that the outer oxide layer mainly consisted of the magnetite; furthermore, the inner oxide layer composed of the chromium spinel and a thin layer of chromium oxide at the of $FeCr_2O_4$/SS 316L interface.

3. Oxidation and cracking susceptibility of SS 310S in SCW at 500 °C for different exposure time indicated that the presence of the alloying elements played an important role in the diffusion phenomenon and also in the formation of oxide layer on the substrate.

3.1. It was observed that after protracted SCW exposure, two types of diffusion took place including outward diffusion of iron and inward diffusion of oxygen. Moreover, AES and SEM observations from the top layer of the scales and cross-sectional EDS elemental analysis indicated that the oxide layer was composed of two separate layers, outer layer was mainly coarsen magnetite and inner oxide layer consisted of $FeCr_2O_4$. It was also observed that, the crystallite size of the oxide coarsened by prolonging the exposure time up to 20000 h. According to the EDS results, for the 20000 h SCW exposure, nickel enrichment was observed at the metal/oxide interfaces. The XRD results revealed that different phases such as Fe_3O_4, $FeCr_2O_4$, and Fe_2O_3/Cr_2O_3 formed on the outer surface of the oxide layer.

3.2. TEM-EDS elemental analysis of the cross section from samples exposed to the SCW supported the SEM observations that the oxide film consisted of two layers including the outer layer of granular Fe_3O_4 and the inner layer consisted of fine-grained of chromium-rich spinel oxide. Furthermore, HRTEM, EELS, and SAED confirmed that the outer oxide layer consisted of magnetite and the inner oxide layer composed of chromium spinel and a thin layer of chromium oxide at the interface of the oxide and SS 310S substrate. It appeared that the inner oxide layer played an active role in impeding the outward diffusion of iron ions and therefore influenced the corrosion rates of the SS 310S.

3.3. The formation of chromium carbides, such as $Cr_{23}C_6$ and Cr_7C_3 at the grain boundaries was confirmed using HRTEM micrographs and EELS analysis.

4. Concerning the SS 310S and SS 316L samples exposed to the SCW for 20000 h, microcracks were appeared beneath the inner oxide layer. Elemental analysis at the crack tip revealed that the main corrosion product was the chromium oxide. Moreover, Ni enrichment at the crack tip was observed. It was proposed that microcracks initiation can be resulted from the stress concentration ahead of the microcracks tip which was filled with corrosion products such as a chromium-rich oxide and enriched nickel phase.

5. Regarding the oxidation behavior of austenitic stainless steel 304-ODS, it was observed that diffusion phenomenon played a significant role in the formation of the oxide layer on the substrate. Results exhibited that iron diffused outwards and oxygen diffused inwards.

5.1. The weight gain increased by escalating the SCW exposure time, and the weight gain rate decreased following parabolic law.

5.2. The microstructure of the oxide formed on 304-ODS alloy was investigated by electron microscopy. It was proposed that the oxide film is composed of an outer magnetite layer and an inner Fe-Cr spinel oxide layer.

5.3. XRD spectra confirmed tha presence of different phases including Fe_3O_4, $FeCr_2O_4$, and Cr_2O_3 in the oxide layer.

5.4. SIMS and EELS results showed that the outer oxide consisted of magnetite (Fe_3O_4) and inner oxides were made of $FeCr_2O_4$. Nanometer thick layer of Cr_2O_3 exhibited a complex structure with a non-uniform distribution of elements.

7.2 Recommendations for further work

In the core of SCWR, the concentration of oxygen may increase due to the irradiation. It can be considered as a good idea to evaluate the effects of the direct injection of oxygen agent such as H_2O_2 to the SCW oxidation chamber. Proposed experiments will help to understand the performance of candidate alloys in real operating conditions. However, direct injection of liquids to SCW chamber may destabilize the SCW atmosphere. Due to facility limitation, only indirect injection of H_2O_2 is possible, although partial decomposition of H_2O_2 in preheaters may reduce the effectiveness of the tests.

An electron back scattered diffraction (EBSD) study regarding the formed oxide layers would give an insight on the grain size and the proportion of phases in certain regions of the oxide scale, and would help in identification of the unknown phases. In fact, it would be of

interest to investigate the orientation relationships between the oxide film and the metal substrate since precipitation of the oxides may follow the substrate metal microstructure.

The cracking susceptibility data were obtained under the static SCW condition. However, dynamic SCW will be the main concern in SCWR. Capsule samples can be connected to dynamic SCW in order to be compared with the obtained results from the static SCW tests. Dynamic SCW can increase the mobility of corrosion products in SCWR. Maintaining the stream of SCW over the course of a long exposure test can be considered the major challenge. Also the temperature in SCWR can fluctuate. In order to reduce the temperature fluctuation in dynamic SCW, feed water supply to preheaters should be limited to a low amount.

Bibliography

1. Roadmap for Generation IV Nuclear Systems, (2002) 30-49.
2. R. Duffey, I. Pioro, Encyclopedia of EOLSS, Oxford, UK, (2004).
3. E. Franck, NATO, (2000), 307-322.
4. R. Shaw, E. Franck, Chemical and Engineering News, 69 (1991) 26-39.
5. P. Kritzer, J. Supercrit. Fluids, 29 (2004) 1-29.
6. E. Franck, Physic Chem, 88 (1984) 820-825.
7. H. Weingärtner, Chemie, 44 (2005) 2672-2692.
8. A. Mather, E. Franck, J. Physic. Chemis, 96 (1992) 6-8.
9. P. Saha, N, Aksan, J. Anderso, J. Nucl. Eng, 264 (2013) 3-23.
10. R. Viswanathan, J of Mat. Eng and Perform, 15 (2006) 255-274.
11. R. Viswanathan, Int J. Press. Ves. And Pip, 83 (2006) 778-783.
12. P. Ampornrat, G. Was, J. Nucl. Mater, 371 (2007) 1-17.
13. P. Ampornrat, G. Gupta, G.S. Was, J. Nucl. Mater, 395 (2009) 30-36.
14. S. Hwang, B. Lee, J. Kim, J. Nucl. Mater, 372 (2008) 177-181.
15. W. Boyd, H Pray, Corrosion, 13(1957) 375-385.
16. R. Novotny, P. Hähner, J. Siegl, J. Nucl. Mater, 409 (2011) 117-123.
17. D. Guzonas, R. Novotny, Prog. Nucl. Energy. 77 (2014) 361–372.

18. D. Guzonas, W. Cook, Corros. Sci. 65 (2012) 48–66.

19. J. Li, W. Zheng, S. Penttilä, P. Liu, D. Guzonas, J. Nucl. Mater. 454 (2014) 7–11.

20. R. Novotný, P. Janík, S. Penttilä, J. Siegl, J. Supercrit. Fluids. 81 (2013) 147–156.

21. J. Perrow, W. Smeltzer, J. Electrochem. Soc. 109 (1962) 1023–1026.

22. X. Zhang, D.W. Shoesmith, Corros. Sci. 76 (2013) 424–431.

23. Q. Zhang, R. Tang, K. Yin, X. Luo, L. Zhang, Corros. Sci. 51 (2009) 2092–2097.

24. T. Mohammadi, X. Huang, Corros. Eng. Sci. Technol. 1 (2014).

25. N. Otsuka, Y. Shida, H. Fujikawa, Oxid. Met. 32 (1989) 13–45.

26. A. Chyrkin, N. Mortazavi, M. Halvarsson, Corros. Sci. 98 (2015) 688–698.

27. K. Chang, S. Chen, T. Yeh, J. Kai, Corros. Sci. 81 (2014) 21–26.

28. W. Quadakkers, J. Zurek, M. Hänsel, JOM. 61 (2009) 44–50.

29. L. Qiu, D. Guzonas, D. Webb, J. Solution Chem. 38 (2009) 857–867.

30. S. Saunders, M. Monteiro, F. Rizzo, Prog. Mater. Sci. 53 (2008) 775–837.

31. J. Young, J. Zurek, W. Quadakkers, Corros. Sci. 53 (2011) 2131–2141.

32. B. Alexandreanu, G. Was, Corros., (2003).

33. P. Ampornrat, G. Was, J. Nucl. Mater. 371 (2007) 1–17.

34. P. Andresen, Corros. 49 (1993) 714–725.

35. K. Arioka, T. Yamada, T. Terachi, Corros. 67 (2011) 1-18.

36. H. Asteman, J. Svensson, L. Johansson, Oxid. Met. 52 (1999) 95–111.

37. H. Asteman, J. Svensson, L. Johansson, Corros. Sci. 44 (2002) 2635–2649.

38. N. Boukis, W. Habicht, G. Franz, E. Dinjus, Mater. Corros. 54 (2003) 326–330.

39. X. Gao, X. Wu, Z. Zhang, E. Han, J. Supercrit. Fluids. 42 (2007) 157–163.

40. M. Sun, X. Wu, Z. Zhang, E.-H. Han, J. Supercrit. Fluids., 47 (2008) 309–317.

41. M. Sun, X. Wu, E.-H. Han, J. Rao Scr. Mater. 61 (2009) 996–999.

42. A. Hansson, J. Hald, M. Montgomery, Mater. High Temp. 22 (2005) 263–2670.

43. N. Zhang, B.R. Li, Y. Bai, H. Xu, Appl. Mech. Mater.,149 (2011) 1179–1183.

44. R. Fujisawa, M. Sakaihara, Corros. Eng. Sci. Technol. 40 (2005) 244–248.

45. B. Amirkhiz, J. Li, Y. Zeng, W. Zheng, Microanal. 20 (2014) 1866–1867.

46. L. Tan, X. Ren, K. Sridharan, T. Allen, Corros. Sci. 50 (2008) 3056–3062.

47. X. Ren, K. Sridharan, T. Allen, Corros. 63 (2007) 603–612.

48. B. Somerday, R. Bradshaw, K. Wiggans, Corros 2004 (2004) 1–22.

49. G. Was, S. Teysseyre, Z. Jiao, Corros. 62 (2006) 989–1005.

50. Y. Wang, Y. Liu, H. Tang, W. Li, Mater. Charact. 107 (2015) 283–292.

51. M.L. Hattali, S. Valette, D. Tréheux, J. Eur. Ceram. Soc. 32 (2012) 2253–2265.

52. L. Tan, T. Allen, Y. Yang, Corros. Sci. 53 (2011) 703–711.

53. L. Tan, K. Sridharan, T. Allen, J. Nucl. Mater. 348 (2006) 263–271.

54. P. Kritzer, J. Supercrit. Fluids. 29 (2004) 1–29.

55. R. Zhou, E.A. West, Z. Jiao, G. Was, J. Nucl. Mater. 395 (2009) 11–22.

56. Y. Zeng, J. Li, B.S. Amirkhiz, W. Zheng, M. Podlesny, Corros 2015 (2015)

57. S. Cissé, L. Laffont, B. Tanguy, E. Andrieu, Corros. Sci. 56 (2012) 209–216.

58. M. Le Calvar, P Scott, T. Magnin, P. Rieux, Corros., 54 (1998) 101–105.

59. R. Nishimura, Corros. Sci., 49 (2007) 81–91.

60. S. Lvov, Corros., 2004 (2004) 1–16.

61. W. Zieliński, K. Kurzydłowski, Scr. Mater., 43 (2000) 33–37.

62. G. Gupta, P. Ampornrat, T. Allen, G. Was Nucl. Mater., 361 (2007) 160–173.

63. J. Konys, S. Fodi, J. Hausselt, H. Schmidt, V. Casal, Corros., 55 (1999) 45–51.

64. S. Teysseyre, Q. Peng, C. Becker, G. Was, J. Nucl. Mater., 371 (2007) 98–106.

65. X. Zhong, X. Wu, E. Han, Corros. Sci., 90 (2015) 511–521.

66. O. Yeliseyeva, V. Tsisar, Z. Zhou, J. Nucl. Mater., 442 (2013) 434–443.

67. I. Wright, B. Pint, Corros., (2002) 02.

68. E. West, Univeristy of Michigan, (2010).

69. D. Rodriguez, A. Merwin, D. Chidambaram, J. Nucl. Mater., 452 (2014) 440-445.

70. M. Nezakat, H. Akhiani, S. Penttilä, S.M. Sabet, J. Szpunar, Corros. Sci., (2015).

71. J. Weiss, A. Pineau, Metall. Trans. A., 24 (1993) 2247–2261.

72. E. Han, L. Zhang, W. Ke, H. Guan, Corros., (2001) 256-270.

73. A. Harvey, E. Lemmon, NIST, (2013) 99-208.

74. L. Tan, Y. Yang, T. Allen, Corros. Sci., 48 (2006) 3123–3138.

75. A. Zhong, X. Wu, E. Han, Corros. Sci., 90 (2015) 511–521.

76. J. Bischoff, A. Motta, R. Comstock, J. Nucl. Mater., 392 (2009) 272–279.

77. H. Hu, Z. Zhou, M. Li, L. Zhang, S. Li, Corros. Sci., 65 (2012) 209–213.

78. Z. Suo, D. Kubair, A. Evans, V. Tolpygo, Acta Mater., 51 (2003) 959–974.

79. K. Chang, S. Chen, T. Yeh, J. Kai, Corros Sci., 81 (2014) 21–26.

80. P. Kritzer, J. Supercrit. Fluids., 29 (2004) 1–29.

81. Y. Zeng, J. Li, B.S. Amirkhiz, M. Podlesny, Corros., 2015 (2015) 5469.

82. M. Sun, X. Wu, Z. Zhang, E. Han, Corros. Sci., 51 (2009) 1069–1072.

83. S. Cissé, L. Laffont, B. Tanguy, E. Andrieu, Corros. Sci. 56 (2012) 209–216.

84. J. Bischoff, A. Motta, J. Nucl. Mater. 430 (2012) 171–180.

85. R. Nishimura, Corros. Sci. 49 (2007) 81–91.

86. K. Arioka, T. Yamada, T. Terachi, G. Chiba, Corros, 2007 (2007) 1114–1123.

87. W. Zieliński, K. Kurzydłowski, Scr. Mater., 43 (2000) 33–37.

88. Z. Shen, L. Zhang, R. Tang, Q. Zhang, J. Nucl. Mater., 458 (2015) 206–215.

89. Z. Shen, L. Zhang, R. Tang, Q. Zhang, J. Nucl. Mater., 454 (2014) 274–282.

90. P. Ampornrat, G. Gupta, G. Was, J. Nucl. Mater., 395 (2009) 30–36.

91. E. West, G. Was, J. Nucl. Mater., 392 (2009) 264–271.

92. S. Teysseyre, Z. Jiao, E. West, G. Was, J. Nucl. Mater., 371 (2007) 107-117.

93. J. Konys, S. Fodi, J. Hausselt, H. Schmidt, V. Casal, Corros., 55 (1999) 45–51.

94. D. Siwy, T. Clark, A. Motta, J. Nucl. Mater., 392 (2009) 280–285.

95. X. Zhong, X. Wu, E. Han, Corros. Sci., 90 (2015) 511–521.

96. O. Yeliseyeva, V. Tsisar, Z. Zhou, J. Nucl. Mater., 442 (2013) 434–443.

97. D. Rodriguez, A. Merwin, J. Nucl. Mater., 452 (2014) 440–445.

98. J. Weiss, A. Pineau, Metall. Trans. A., 24 (1993) 2247–2261.

99. D. Guzonas, J. Wills, S. Sullivan, K. Heaslip, (2005) 1379–1386.

100. Z. Suo, J. Appl. Mech., 71 (2004) 646.

101. L. Tan, Y. Yang, T. Allen, Corros. Sci., 48 (2006) 3123–3138.

102. X. Zhong, X. Wu, E. Han, Corros. Sci., 90 (2015) 511–521.

103. J. Bischoff, A. Motta, J. Nucl. Mater. 424 (2012) 261–276.

104. J. Bischoff, A. Motta, R. Comstock, J. Nucl. Mater. 392 (2009) 272–279.

105. B. Pint, J. Rakowski, Corros., 56 (2000) 259.

106. S. Mahboubi, MacMaster,, 14 (2014) 36-45.

107. T. Terachi, T. Yamada, K. Arioka, J. Nucl. Sci. Technol., 45 (2008) 975–984.

108. T. Terachi, K. Fujii, K. Arioka, J. Nucl. Sci., 42 (2005) 225–232.

109. S. Tsai, A. Huntz, C. Dolin, Oxid. Met., 43 (1995) 581–596.

110. P. Kritzer, J. Supercrit. Fluids., 29 (2004) 1–29.

111. H. Hu, Z. Zhou, L. Liao, L. Zhang, S. Li, J. Nucl. Mater., 437 (2013) 196–200.

112. R. Nishimura, Corros. Sci., 49 (2007) 81–91.

113. S. Penttilä, A. Toivonen, R. Novotny, J. Supercrit. Fluids., 81 (2013) 157–163.

116. W. Zieliński, K. Kurzydłowski, Scr. Mater., 43 (2000) 33–37.

117. S. Cissé, L. Laffont, B. Tanguy, E. Andrieu, Corros. Sci., 56 (2012) 209–216.

118. T. Terachi, T. Yamada, K. Fukuya, J. Nucl. Sci. Technol., 45 (2008) 975–984.

119. G. Was, P. Ampornrat, G. Gupta, T. Allen, J. Nucl. Mater., 371 (2007) 176–201.

120. P. Ampornrat, G. Gupta, G. Was, J. Nucl. Mater., 395 (2009) 30–36.

121. G. Gupta, P. Ampornrat, , T. Allen, G. Was, J. Nucl. Mater., 361 (2007) 160–173.

122. X. Zhong, X. Wu, E. Han, Corros. Sci., 90 (2015) 511–521.

123. O. Yeliseyeva, V. Tsisar, Z. Zhou, J. Nucl. Mater., 442 (2013) 434–443.

124. D. Rodriguez, A. Merwin, J. Nucl. Mater., 452 (2014) 440–445.

125. J. Weiss, A. Pineau, Metall. Trans. A., 24 (1993) 2247–2261.

126. D. Morton, S. Attanasio, G. Young, P. Andersen, Envdeg 11th, 2 (2000).

127. T. Thomberg, K. Kontturi, A. Jänes, E. Lust, Carbon., 49 (2011) 4427–4433.

128. Y. Huang, S. Lozano-Perez, R. Langford, J. Microsc., 207 (2002) 129–36.

129. G. Was, S. Teysseyre, S. Mckinley, Z. Jiao, Corros., (2005) 1–20.

130. P. Kritzer, J. Supercrit. Fluids., 29 (2004) 1–29.

131. J. Isselin, R. Kasada, A. Kimura, Corros. Sci., 52 (2010) 3266–3270.

132. Z. Dong, W. Chen, W. Zheng, D. Guzonas, Corros. Sci., 65 (2012) 461–471.

133. H. Hu, Z. Zhou, M. Li, , M. Wang, S. Li, Corros. Sci. 65 (2012) 209–213.

134. G. Was, P. Ampornrat, G. Gupta, T. Allen, J. Nucl. Mater., 371 (2007) 176–201.

135. S. Penttilä, I. Betova, A. Toivonen, Corros. Sci., 53 (2011) 4193–4203.

136. L. Tan, Y. Yang, T. Allen, Corros. Sci., 48 (2006) 3123–3138.

137. X. Zhong, X. Wu, E. Han, Corros. Sci., 90 (2015) 511–521.

138. X. Ren, K. Sridharan, T. Allen, J. Nucl. Mater., 358 (2006) 227–234.

139. G. Was, T. Allen, ICAPP'05, 6 (2005) 3460–3483.

140. I. Wright, R. Dooley, Int. Mater. Rev., 55 (2010) 129–167.

141. Pentilla, S., 6th Proc. 6th Int. Symp. on SCWR , Shenzhen, China (2013) 03-07.

142. Janik, P., Novotny, Proc. 6th Int. Symp. on SCWR, China, (2013) 03- 07.

143. Ulmer, R.C., Corrosion (1960) 68.

144. K. Ehirlich, L. Heikinheimo, J. Nucl. Mater., 327 (2004) 140-147.

145. G. Was, Proc. Adv. in frac. and fail. Preven. Trans tech publications, (2004) 885.

146. C. Bailat, A. Almazouzi, M. Victoria, J. Nucl. Mater., 283-287 (2000) 446.

147. T. S. Byun, E. H. Lee, J. D. Hunn, J. Nucl. Mater. 321 (2003) 20.

148. G. Alexandreanu, G. S. Was, Corrosion. 59 (2003) 705.

149. E. Lehockey Proc. 13th Int. Conf. on Env. Deg. of Mat. in Nuc. Pow. Sys., (2007)

150. S. Teysseyre, Q. Peng, G. Was, J. Nucl. Mater., 371 (2007) 98–106.

151. R. Zhou, E.A. West, Z. Jiao, G. Was, J. Nucl. Mater., 395 (2009) 11–22.

152. K. Sridharan, A. Zillmer, J. R. Licht, L. ICAPP, (2004) 4136.

153. Y. Chen, K. Sridharan, T. Allen, (2005) 05391.

154. I. Betova, M. Bojinov, S. Penttila, T. Saario, Proc. ICAPP, (2007).

155. J. Kaneda, Proc. 12th Int. Conf. on Env. Deg. of Mat. in Nuc. Pow. Sys., (2005)1342-1351.

156. T. Allen, D. Guzonas, G. S. Was, E. A. West, J. Nucl. Mater., (2010).

157. P. Ampornrat, G. Gupta, G. Was, J. Nucl. Mater., 395 (2009) 30–36.

158. G. S. Was, T. R. Allen, Proc. American Nuclear Society-ICAPP, 6 (2005) 3460.

159. D. Guzonas, Proc. 13th Int. Conf. on Env. Deg. of Mat. in Nuc. Pow. Sys., (2007)

160. W.L. Pearl, E.G. Brush, S. Leistikow, J. Nuc. Applica., 3 (1967) 418- 432.

161. V.P. Deodeshmukh, Oxid. of Metal., 79 (2013) 567-578.

162. X. Zhang, D. W. Shoesmith, Corros. Sci., 76 (2013) 424-431.

163. W.E. Ruther, R.R.Schlueter, R.H. Lee, R.K. Hart, Corrosi., 22 (1966) 147-155.

164. K.A Burrill, Proc. 8th BNES Conf. on Wat. Chemi. of Nuc. Rea. Sys., (2000) 357-363.

165. R.L. Klueh, J. Int. Mat. Rev., 50 (2005) 287-310.

166. J. Bichoff, Pennsylvania State University, (2011) 57-62.

Appendix

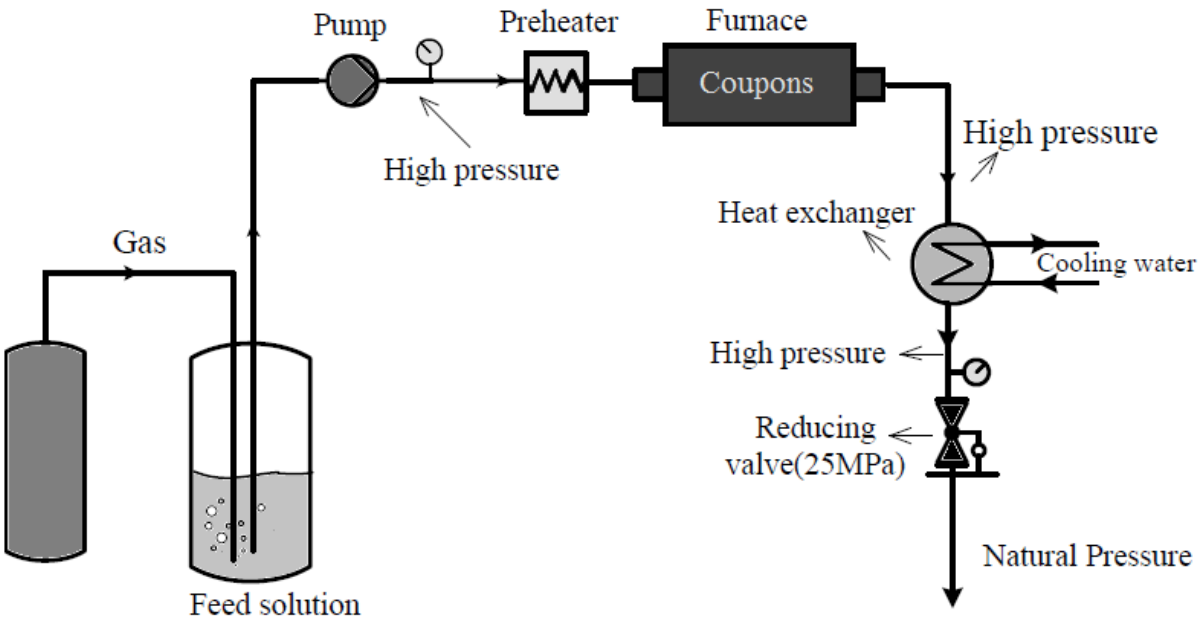

In order to resemble the operating condition in supercritical water-based reactors, an opened loop water flowing system was designed. The high temperature test environment included 500 ^{o}C, 650 ^{o}C, and 800 ^{o}C at a pressure of 25 MPa. Coupon size was 20 mm × 100 mm and the surface was prepared by mechanical grinding following by thorough rinsing.

This testing facility was mainly composed of three sections; 1) water chemistry unit and controller, 2) the heating cell, and 3) gas pressure controlling system.

Two liter tank containing Mili-Q water was connected to a High Pressure Liquid Chromatographic (HPLC) pump capable of flow rates to 100 ml/min. The tank was continuously stirred for consistent supply of water to the heating cell. A gas line fed into the bottom of the main tank in which Ar gas was bubbled to deoxygenate the water down to 20 ppb O_2. The opened loop system operated at a flow rate of 2 ml/min.

A pre-heater setup was installed before the main chamber to bring the water temperature close to the desired level. The water was pumped into a pre-heater, which raised the temperature of the water from room temperature to approximately 500 °C. The pre-heater water flowed through an insulated section of tube to autoclave. The preheating unit itself was composed of three ThermoLine 48000 tubular furnaces. The pressurized water flowed through the thermodynamic critical point of water. When the desired temperature was reached, the pressurized water passed through 3/4" tubes located in the main chamber (Autoclave) where the temperature was adjusted by temperature controllers and monitored by three thermocouples. The main furnace was positioned such that the temperature within the autoclave remained uniform and stable. The alloy 625 tubes were provided by Rolled Alloys Company and had a 0.083" wall thickness. It is worth mentioning that the loop tubes were shielded through the total heating cell by insulating jacket. The preheating and main chamber tubes were connected using stainless steel fitting. The old fitting was exchanged with new ones on a regular basis to maintain safety of the testing facility.

The coupon sample was inserted in the larger diameter tubes located in the main chamber. Before each test, three similar coupon samples were located at different spots throughout the main chamber. They were hung on opposite sides of the autoclave to detect any lack of uniformity in internal autoclave conditions. Corrosion coupons were hung from an internal tree by Inconel holder that kept each coupon and wrapped around a branch of the tree. The tree was capable of supporting up to 12 samples at a time, allowing each sample to be exposed on all surfaces except the small area clamped by the holder. The tested coupon samples were assessed

for microstructural features, SEM observation, thickness measurements and gravimetric calculations.

While flowing through the autoclave, the internal water pressure was measured by a pressure sensor placed at the inlet line of main chamber and controlled by back-pressure regulator placed at the outlet of main chamber tube. The constant feedback of temperature controllers from the thermocouples allowed both heating cells to be maintained at stable temperature throughout the test, and were crucial for increasing and decreasing temperature at system startup and shutdown. The temperature inside the autoclave was controlled with a variation ±0.5 °C and the pressure fluctuation was below ±0.09 MPa. The temperature was measured by thermocouples located in the center of the pre-heater coils, at the inlet line, attached to the external side of the main chamber, and close to the center of the main chamber. The inlet and internal thermocouples were applied primarily to monitor and record the temperatures of water entering and inside the autoclave. The thermocouples in the pre-heater unit and on the outside of the autoclave were used by temperature controllers located next to the system.

After flowing though the autoclave, the temperature of water was brought down to room temperature before it exited the end-line. This was achieved by passing the water through a regenerative stainless steel heat exchanger that absorbed the water heat before leaving the autoclave.

Once the room temperature was reached, the water pressure was lowered using a reducing valve. The water which was reached to the natural state, i.e. ambient temperature and atmosphere pressure, was collected in a glass container for the chemical composition and dissolved ions analysis. After each test run for a desired amount of time, the heating cell temperature was

decreased to room condition, and subsequently opened. Shortly, the corrosion coupon surfaces were photographed with a camera to record appearance, surface changes and features.

It should be mentioned that the pressure and temperature of water was monitored during testing condition, specifically for 800 $^{\circ}$C. Any leakage during testing resulted in complete shutdown of the loop system and assessment of fitting and connections which required to be exchanged. Once it was installed, the loop system w verified and calibrated using three similar coupon samples of same testing material for a period of 24 hours.